Explorative Approach to the Dust Evolution in Binary Star Systems

vorgelegt von Diplom-Physiker
Carsten Köllein
Berlin

von der Fakultät II - Mathematik und Naturwissenschaft
der Technischen Universität Berlin
zur Erlangung des akademischen Grades
Doktor der Naturwissenschaft
Dr. rer. nat.

genehmigte Dissertation

Promotionsausschuss:

Vorsitzender: Prof. Dr. rer. nat. T. Brandes
Berichter: Prof. Dr. rer. nat. E. Sedlmayr
Berichter: Prof. Dr. rer. nat. H. Rauer

Tag der wissenschaftlichen Aussprache: 27.03.2009

Berlin 2009
D 83

Contents

Zusammenfassung 11

Summary 15

1 Phenomenological fundaments of dust forming stars 17
- 1.1 The birth of stars . . . 17
- 1.2 Stellar evolution . . . 18
- 1.3 The Hertzsprung - Russell diagram . . . 19
  - 1.3.1 Example . . . 21
- 1.4 Brown Dwarfs . . . 23
- 1.5 Red Giant stars . . . 24
- 1.6 Mira stars and Long-Period Variables . . . 25
  - 1.6.1 The circumstellar region around Mira stars . . . 28
  - 1.6.2 Pulsation through $\kappa-$ mechanism . . . 30
  - 1.6.3 Evolution and pulsation . . . 31
  - 1.6.4 Mira stars in binaries - orbiting Brown Dwarf . . . 32
- 1.7 Observations of eclipsing binary stars . . . 33
- 1.8 Evolution of close binary stars . . . 34
  - 1.8.1 Common envelope evolution . . . 35
- 1.9 Mass transfer in close binaries . . . 37
  - 1.9.1 Mass loss by wind . . . 37

2 Modelling method 39
- 2.1 Basic equations . . . 43
  - 2.1.1 Binary star problem . . . 43
  - 2.1.2 Hydrodynamical equation . . . 43
  - 2.1.3 Radiative transfer problem . . . 51
  - 2.1.4 Equation of state . . . 51
  - 2.1.5 Chemistry of the gas phase . . . 52
  - 2.1.6 Time evolution of dust grains . . . 52
- 2.2 Boundary conditions for the modelling . . . 52

3 Dynamics in a binary star system 55
- 3.1 Force field in binaries . . . 55
- 3.2 Roche Lobe geometry . . . 57
  - 3.2.1 The Jacobi integral . . . 58

3.2.2 Lagrange points . . . 59
3.2.3 Location of equilibrium points . . . 60
3.2.4 Motion of test particles . . . 64

4 Hydrodynamics **67**
4.1 Governing equation hydrodynamics . . . 67
4.2 Numerical approach - SPH method . . . 68
4.2.1 Basic concepts . . . 68
4.2.2 Approximation of governing equations . . . 69
4.2.3 Numerical test: shock tube . . . 74

5 Radiative transfer **75**
5.1 Fundamental definitions . . . 75
5.2 Equation of radiative transfer . . . 78
5.2.1 Transport coefficients . . . 80
5.2.2 Eddington moments . . . 81
5.3 Principle of Monte Carlo method . . . 83
5.3.1 Basic concepts . . . 83
5.3.2 Sampling from probability distribution functions . . . 85
5.3.3 Example: a plane parallel atmosphere . . . 86
5.4 Radiative equilibrium for a single star . . . 92
5.4.1 Monte Carlo simulation - radiative equilibrium assuming LTE . . . 93
5.4.2 Radiative equilibrium temperature . . . 93
5.4.3 Monte Carlo code description . . . 97

6 Chemistry **103**
6.1 Fundamental relations . . . 103
6.1.1 Dissociation equilibrium . . . 104
6.1.2 Equilibrium in the gas phase - carbon rich case . . . 105
6.2 Dust formation . . . 110
6.2.1 Condensation processes . . . 110
6.2.2 Nucleation . . . 111
6.2.3 Net rate of growth and evaporation . . . 112
6.2.4 Nucleation and growth of grains . . . 114
6.3 Dust formation in the binary star system . . . 115
6.4 Preparation of initial data- modelling for the donor star . . . 116
6.4.1 Model parameter . . . 117

7 Numerical simulation **123**
7.1 Modelling of a stellar wind in a binary system . . . 123
7.2 Model 1 - stationary dust driven wind . . . 125
7.2.1 Roche lobe fill up . . . 125
7.2.2 Roche lobe overflow . . . 128
7.2.3 Extended envelope . . . 130
7.3 Model 2 - non-stationary dust driven wind . . . 131
7.3.1 Roche lobe fill up . . . 131
7.3.2 Roche lobe overflow . . . 132

7.3.3 Extended envelope 134
7.4 Time sequence of the evolution 137

8 Summary and Conclusions 141

A Used quantities 143

B Stellar atmosphere element abundances 145

C Hydrodynamics 147
C.1 Hydrodynamical tests 147
C.1.1 Equation for pressure and velocity 148
C.1.2 Example - initial data shock tube 155

D Monte Carlo principle 157
D.1 Monte Carlo integration - basic concepts 157
D.1.1 Background and probability review 157
D.1.2 The Monte Carlo estimator 160
D.1.3 Sampling random variables 162

Danksagung 179

Curriculum Vitae 181

List of Figures

1.1 Hubble telescope image of Eagle Nebula 17
1.2 Hertzsprung-Russell diagram 18
1.3 Temperature time evolution of an example C-star 22
1.4 Luminosity time evolution of an example C-star 22
1.5 Time sequence of C-stars on the HR diagram 23
1.6 Location of C-Miras and O-Miras in the Hertzsprung-Russell diagram . . 26
1.7 R Cas aperture image 28
1.8 Sketch of the global shell structure of a pulsating Mira star 29
1.9 Chandra X-ray image of Mira star 33
1.10 Hubble observations of a red giant star Mira 34
1.11 Isopotential surface through the Lagrange point $\mathbb{L}_1$ 36

2.1 Physical problem description 39
2.2 Principle of the modelling approach 42
2.3 Isothermal wind 49
2.4 Density profile for an isothermal wind 50
2.5 Location of boundaries in the model binary system 53

3.1 Inertial reference frame of a binary system 55
3.2 Zero velocity curves for the Jacobi constant 59
3.3 Langrange equilibrium points 63
3.4 Roche Lobe - 3d 63
3.5 Roche Lobe surface at $\mathbb{L}_1$ 64
3.6 Particle trajectories in the xy-plane 65
3.7 Particle trajectories in the xyz-plane 66

4.1 Shock tube Test 74

5.1 Principle of the Monte Carlo integration method 87
5.2 Principle program flow of the integrating Monte Carlo method 87
5.3 Example 1 - Intensity 90
5.4 Moments - J and H 91
5.5 Moments - K and Edington factor 91
5.6 Parametrisation of the common envelope 93
5.7 SED example 94
5.8 Opacity curve 95
5.9 Dust emissivity after temperature correction 96
5.10 Normalised Probability 98

5.11 Normalised Planck function 98
5.12 Stereographic projection 99
5.13 Parametrisation sketch 99
5.14 Temperature distribution 1d 101
5.15 Shadow distribution on a binary system 101
5.16 Binary Star system 101
5.17 Temperature in Binary Stars 102

6.1 Carbon abundances 106
6.2 Hydrogen and Helium abundances 106
6.3 Iron abundances 107
6.4 Magnesium abundances 107
6.5 Oxygen abundances 108
6.6 Sulphur abundances 108
6.7 Silicon abundances 109
6.8 Expansion Velocity 118
6.9 Gas Temperature 119
6.10 Gas mass density 119
6.11 Scaled nucleation rate per second and Hydrogen atom 120
6.12 Scaled number of dust grains per Hydrogen atom 120
6.13 Degree of condensation 121
6.14 Mean particle radius 121

7.1 Roche potential in the xy plane 124
7.2 Model 1, Slow wind - Density and velocity for Roche lobe fill up 126
7.3 Model 1, Fast wind - Density and velocity for Roche lobe fill up 126
7.4 Model 1, Slow wind - Nucleation rate - Roche lobe fill up 127
7.5 Model 1, Fast wind - Nucleation rate - Roche lobe fill up 127
7.6 Model 1, Slow wind - Density and velocity - Roche lobe overflow 128
7.7 Model 1, Fast wind - Density and velocity - Roche lobe overflow 128
7.8 Model 1, Slow wind - Nucleation rate - Roche lobe overflow 129
7.9 Model 1, Fast wind - Nucleation rate and velocity - Roche lobe overflow 129
7.10 Model 1, Slow wind - Nucleation rate and velocity - Extended envelope . 130
7.11 Model 1, Fast wind - Nucleation rate and velocity - Extended envelope . 130
7.12 Model 2 - Density - Roche lobe fill up 131
7.13 Model 2- Nucleation rate - Roche lobe fill up 132
7.14 Model 2 - Density - Roche lobe overflow 133
7.15 Model 2 - Nucleation rate - Roche lobe overflow 133
7.16 Model 2 - Density - Extended envelope 134
7.17 Model 2 - Density - Extended envelope 135
7.18 Model 2 - Velocity - Extended envelope 135
7.19 Model 2 - Nucleation rate - Extended envelope 136
7.20 Model 1 - Density - Time sequence 137
7.21 Model 1 - Nucleation Rate - Time sequence 138
7.22 Model 1 - Velocity - Time sequence 139

C.1 Riemann 1 148

C.2 Riemann 2 149
C.3 Strategy for solving the Riemann 150
C.4 shock wave 150

D.1 PDF 163
D.2 discrete PDF 163
D.3 Inversion Method 164
D.4 Probability density function 166

Zusammenfassung

Diese Arbeit diskutiert die Staubentwicklung in einem binären Stern-System. Dieses System besteht aus einem Mira-artigen Stern und einem braunen Zwerg. Ein Mira-artiger Stern ist ein Stern mittlerer Masse, der sich in einer späten Phase der Sternentwicklung auf dem asymptotischen Riesen Ast (AGB) befindet. Ein brauner Zwerg ist ein substellares Objekt mit einer Masse, die unterhalb der Grenze zur Aufrechterhaltung einer Wasserstoff-Fusionsreaktion liegt. In ihren radial pulsierenden, erhöhten und konvektiven Atmosphären entwickeln Mira-Sterne oft starke stellare Winde, die durch den Strahlungsdruck auf den Staub zu einem erheblichen Massenverlust des Sterns führen.

Stellare Winde sind von zentraler Bedeutung für die Entwicklung von mittelschweren AGB-Sternen. Ebenfalls sind sie eine zuverlässige Quelle für die Produktion von Staub-Partikeln und schweren Elementen für das interstellare Medium sowie die chemische Entwicklung von Galaxien. In der Tat, die meisten Sterne befinden sich im Binär -oder multiplen Stern-Systemen.

Für eine hinreichende Beschreibung dieser Phänomene besteht daher die Notwendigkeit, die Staubbildung eines Sternes auf den Störeinfluss eines zweiten Sternes zu erweitern, der sich in der Nähe eines AGB-Sternes mit einem stark stellaren Wind befindet. Diese Zielsetzung steht in einer langen Tradition der wissenschaftlichen Untersuchung der Staubbildung am Zentrum für Astronomie und Astrophysik (ZAA) an der technischen Universität Berlin.

Die in dieser Arbeit verwendete methodische Beschreibung der Korngrößenverteilungs-Funktion anhand von Momenten, soll neben anderen wissenschaftlichen Arbeiten eine wichtige Grundlage für die Umsetzung einer zeitabhängigen Beschreibung von Staubnukleationen, Wachstum und Verdunstung innerhalb einer selbst-konsistenten hydrodynamischen Modellrechnung von AGB-Sternen sein.

Auf der Basis profitabler wissenschaftlicher Quellen der Einzel-Sternentwicklung diskutieren wir unter anderem die drei wichtigsten Komponenten für die Staubentwicklung in Hinblick auf eine höher dimensionale Erweiterung, die für die Untersuchung von stellaren Winden in einem binären Sternsystemen von Bedeutung ist.

Die wichtigsten hierbei zu nennenden Komponenten sind der Strahlentransport in der stellaren Atmosphäre und in der sich entwickelnden Atmosphäre des binären Sternsystems, die hydrodynamische Komponente, die den Massentransport zwischen den Sternen beschreibt und die chemische Komponente, die den Staubentwicklungsprozess charakterisiert.

Diese Arbeit konzentriert sich hierbei insbesondere auf die Eigenschaften der Mira-artigen Sterne, die sich in ihrer Entwicklung in der letzten und hellsten Phase befinden, bevor sie ihre äußeren Schichten als planetarischen Nebel abstoßen. Die Eigenschaften der Pulsation, die chemische Zusammensetzung ihrer Atmosphären und die möglichen

Schlussfolgerungen aus jüngsten Beobachtungen sind daher wichtig für die weitere Betrachtung innerhalb dieser Arbeit. Hierbei diskutieren wir insbesondere die relevanten physikalischen Begriffe der stellaren Atmosphäre und ihrer Dynamik hinsichtlich der Entwicklung und des Wachstums von Staub, unter dem Einfluss eines strahlungsgetriebenen Windes innerhalb eines binären Sternsystems.

Diese Arbeit ist wie folgt strukturiert:

Kapitel 1 beschreibt die phänomenologischen Grundlagen von staubbilden Sternen. Anhand des Hertzsprung-Russel-Diagramms wird hierbei der Lebenszyklus der Mira-artigen Sterne hinsichtlich der Häufigkeitsverteilung der Elemente innerhalb ihrer Atmosphären und der für die Staubbildung notwendigen Kondensationsprozesse erörtert und diskutiert. In Bezug auf lang periodische Sterne sowie Mira-artige Sterne hinsichtlich ihres Pulsationsverhaltens, ihrer spektralen Erscheinung und ihrer räumlichen Ausdehnung wird es eine erste Übersicht geben.

In Verbindung der oben genannten Sterne mit Binären-Stern-Systemen folgt eine Auswahl an Beobachtungen. Dabei wird insbesondere der Einfluss eines begleitenden Sterns kategorisiert. Eine besondere Beachtung findet hierbei der Fall der geringen Separation des binären Sternsystems bezüglich eines möglichen Masseübertrages in Verbindung mit Sternwinden.

Kapitel 2 gibt einen grundlegenden Zugang zu den relevanten physikalischen Phänomenen, deren Zusammenhänge und mathematischen Beschreibungen.

Kapitel 3 befasst sich mit der Beschreibung der Gravitationskräfte und der Dynamik innerhalb eines binären Stern-Systems in Bezug auf die sich entwickelnde gemeinsame Atmosphäre beider Sterne. Hierbei werden die notwendigen Bewegungsgleichungen innerhalb des Roche-Potentials beschrieben sowie die den Massenüberfluss beschreibenden Lagrange-Punkte berechnet. Eine erste exemplarische Simulation für das Verhalten eines Einzelpartikels in der Umgebung des binären Sternsystems soll einen ersten Aufschluss bezüglich möglicher Schock-Fronten innerhalb einer vollen hydrodynamischen Entwicklung geben.

Kapitel 4 behandelt die numerische Umsetzung der zugrundeliegenden hydrodynamischen Gleichungen innerhalb eines SPH Ansatzes, unter Berücksichtigung der künstlichen Viskosität und der Eigengravitation der stellaren Atmosphäre. Die Qualität der numerischen Entwicklung wird anhand von Test-Rechnungen überprüft.

Kapitel 5 stellt die entscheidenden physikalischen Begriffe und Quantitäten des Strahlungstransportes hinsichtlich des hier betrachteten strahlungsgetriebenen stellaren Windes zusammen. Zur Validierung der numerischen Monte-Carlo-Approximation anhand der Eddington Momente wird zusätzlich die Strahlungstransport-Gleichung vorgestellt. Ein Unterkapitel ist der oben genannten numerischen Approximation gewidmet, in welchem anhand von etablierten Ergebnissen für das Strahlungsgleichgewicht bezüglich der Temperatur-und Strahlungsverteilung im Einzelstern-System die Gültigkeit und Erweiterbarkeit des Monte-Carlo-Ansatzes hinsichtlich eines binären Sternsystems überprüft wird.

Kapitel 6 stellt die fundamentalen Gleichungen zur Beschreibung der hier betrachten Gleichgewichts-Chemie dar, welche innerhalb eines Newton-Raphson approximiert werden. Hierbei werden insbesondere die chemischen Gegebenheiten der in dieser Arbeit betrachteten kohlenstoffreichen Mira - Atmosphäre hinsichtlich der molekularen Verteilung untersucht und anhand von Test-Rechnungen überprüft. Auf diesen Ergebnissen aufbauend, werden im weiteren die Grundlagen für Staubbildung und dessen Wachstum innerhalb der klassischen Nukleationstheorie erörtert und mittels Momenten-Gleichung für die numerische Berechnung dargestellt.

Die in Kapitel 7 verwendeten Initialdaten zur Beschreibung des strahlungsgetriebenen Windes des hier betrachteten Mira-artigen Sterns werden anhand des CHILD-Code für das binäre Sternsystem vorbereitet.

Kapitel 7 fasst das in dieser Arbeit entworfene Konzept der höher-dimensionalen Modellierung von staubgetriebenen Winden innerhalb eines binären Sternsystems zusammen. Hierbei wird exemplarisch der Fall eines stationären als auch der Fall eines pulsationsveränderlichen Sternwindes berechnet und hinsichtlich der Unterschiede zu einem Einzelsternsystems untersucht.

Im Ergebnis steht eine veränderte Dynamik des expandierenden Windes durch den hauptsächlich gravitativen Einfluss des begleitenden Sterns, dass heißt, die Formation von zusätzlichen Schock-Fronten.

Das abströmende strahlungsgetriebene Staub-Gas-Gemisch wird in der Umgebung hauptsächlich entlang des Roche-Potential des begleitenden Sterns durch sich ausbildende Schocks verdicht. Desweiteren ergeben sich zusätzliche Schockfronten durch die den begleitenden Stern umlaufenden Fluidpartikel, welche nach dem Umlauf dem abströmenden Gas-Staub-Gemisch entgegengerichtet sind.

Wie im Fall des Einzelsterns verstärken die sich ausbildenden Schockfronten effektiv die Nukleation und das Staubwachstum.

Summary

This thesis discusses dust formation in binary systems, in particular for binary systems consisting of a Mira like star and a brown dwarf. A Mira-like star is an intermediate mass star in a late stage of their stellar evolution on the Asymptotic Giant Branch (AGB), and a brown dwarf, is a sub-stellar object with a mass below that necessary to maintain hydrogen-burning nuclear fusion reactions in their cores. In their radial pulsating elevated convective atmospheres, Mira-stars often develop strong stellar winds, which are driven by radiation pressure on the dust and lead to a substantial mass-loss of the star. Stellar winds are of central importance for the development of medium-heavy-AGB stars. Also, they are a reliable source for the production of dust particles and heavy elements for the interstellar medium and the chemical evolution of galaxies. In fact, most stars are in binary or multiple star systems. For a complete description of the processes of dust formation in binary star systems it is necessary to study the perturbative influence of a second star in the vicinity of a AGB-star with a strong stellar wind.

This endeavour is embedded in a long standing tradition of scientific investigation of dust formation at the Zentrum für Astronomie und Astrophysik (ZAA) at the Technical University of Berlin. In this work we use a method which describes the dust complex by moments of the grain size distribution function, which among other works is a key stone for implementation of a time dependent description of dust nucleation, growth, and evaporation into self-consistent hydrodynamical model calculations of AGB-stars.

Based on this profitable scientific source of single star evolution, we discuss, among others, the three main components relevant to dust formation in terms of a higher dimensional extension, necessary for the investigation of stellar winds in a binary system. These main components are the radiative transfer processes occurring in the stellar atmosphere and in the final resulting common envelope, the hydrodynamical part, relevant for the mass transfer between the stars and the chemistry component which characterises the dust development.

This work focuses in particular on the properties of the Mira-like stars that are in their development in the last and brightest stage, before they release their outer layers as planetary nebulae. The properties of the pulsation, the chemical composition of their atmospheres and the possible conclusions from recent observations are therefore important for further consideration within this work. Here we will discuss in particular the relevant physical concepts of the stellar atmosphere and its dynamics, in terms of the development and growth of dust, under the influence of a radiation-driven wind in a binary star system.

This work is structured as follows:

Chapter 1 describes the phenomenological foundations of dust-forming stars. Based on the Hertzsprung-Russell diagram, the life cycle of the Mira-type stars will be dis-

cussed in terms of the chemical composition of their atmospheres and the condensation processes necessary for dust formation. We will present a first overview of the pulsation processes, spectra, space-like extension of long period variables and Mira-like stars. A collection of observations of binary systems, in which one of the stars is a Mira-like star, is given. In particular, the influence of an accompanying star is categorised. Special attention is given to the case of binary star systems with small separations, in terms of a possible mass transfer related to stellar winds.

Chapter 2 gives a fundamental introduction to the relevant physical phenomena, their relations and their mathematical descriptions.

Chapter 3 describes the gravitational forces and the dynamics in a binary star system in relation to the evolving common atmosphere of both stars. Here we describe the necessary equations of motion within the Roche potential, and the Lagrange points, which are related to the description of mass overflow. A first example simulation describing the motion of a single particle in the binary star system, will provide a first insight on possible shock fronts in the numerical hydrodynamic evolution.

Chapter 4 contains a description of the numerical implementation of the hydrodynamic equations within a SPH approach, taking into account the artificial viscosity and the self-gravitation of the stellar atmosphere. The quality of the numerical development is determined by test calculations.

Chapter 5 presents the key concepts and physical quantities of the radiation transfer, in relation to the radiation-driven stellar winds. To validate the use of the numerical Monte-Carlo approach with the Eddington moments, the radiative transfer equation will be introduced. Based on the established results for the radiation equilibrium in a single star (temperature and spectral power distribution), we will discuss the extensibility and validity of the use of the Monte Carlo approach for the binary system.

Chapter 6 presents the fundamental equations describing the here considered chemical equilibrium, which is approximated by a Newton - Raphson method. Here we will focus in particular, on the chemical composition of the C-rich Mira stars considered in this work. The results of the numerical approach for the molecular abundances will be tested. Based on these results, we can describe the dust formation and growth within the classical nucleation theory. Furthermore, we can establish the here used dust-momentum equations.

In chapter 7 we introduce the initial data used for the description of the radiative driven winds of Mira-like stars. These are obtained with the CHILD code. Chapter 7 summarises the developed concept of a high dimension model for dust driven winds in a binary star system. Here we present the numerical simulation results for a stationary and a non-stationary dust driven wind, and we discuss the differences to a single star case.

The result is a change in momentum of the expanding wind, mainly through the gravitational influence of the accompanying star, that is, the formation of additional shock fronts. The expanding radiative driven dust-gas mixture, will be concentrated around the Roche potential of the gainer star, due to evolving shocks. Furthermore, additional shock fronts will evolve due to the fluid particles which revolve around the gainer star, and collide with the new in-streaming fluid particles. Like in the case of a single star the evolving shock fronts effectively amplify the dust nucleation and growth.

Chapter 1

Phenomenological fundaments of dust forming stars

1.1 The birth of stars

All stars form from clouds of gas and dust condensing in deep space. Only the chemical composition of this cloud, and the amount of material in the cloud that condenses into the actual star, determines what will happen to the star over its entire lifetime. Very few stars with masses M_*, above 100 solar masses ($M_\odot$) are known to exist, and those that do show instabilities in their outer layers. At the other end of the mass scale, a mass of about 0.1 $M_\odot$ is required to produce core temperatures and densities sufficient to provide a significant amount of energy from nuclear processes [Collins, 2003]. Thus, we can take the range of stellar masses to span roughly 10^3 $M_\odot$ with the sun somewhat below the geometric mean. If we include the white dwarfs, which may be the size of the earth or less, the range of observed stellar radii R_*, is about 10^6 with the Sun again near the geometric mean.

The observed range of stellar surface temperatures T_*, is by far the smallest being from about 2000 K for the coolest M - star, to perhaps 50000 K for some O - stars, here M and O stars, refer to the notation used in the Hertzsprung-Russell diagram (which will be discussed in more detail in the following section). If the temperature range is combined with the range in radii, it is clear that we could expect a range as great as 10^{17} in the luminosity L_*. In practice, the largest stars do not have the

Figure 1.1: Image of the Hubble telescope known as pillars of creation, where stars are forming in the Eagle Nebula [4].

highest temperatures, such that the range in luminosity is nearer to 10^{10}. A reasonable range of these parameters is then:

$$\begin{aligned} 10^{-1}\ \mathrm{M}_\odot \leq \mathrm{M}_* \leq 10^{2}\ \mathrm{M}_\odot \\ 10^{-3}\ \mathrm{R}_\odot \leq \mathrm{R}_* \leq 10^{3}\ \mathrm{R}_\odot \\ 10^{-4}\ \mathrm{L}_\odot \leq \mathrm{L}_* \leq 10^{6}\ \mathrm{L}_\odot \end{aligned} \tag{1.1.1}$$

1.2 Stellar evolution

Understanding stellar evolution is to understand the complex changes which happen in the interior structure of the star, a self - gravitating mass, in which a contest between energy loss and energy generation occurs while attempting to maintain mechanical equilibrium.

In the beginning, the collapse of a giant molecular cloud of gas and dust in the local interstellar medium gives rise to a protostar. Its initial composition is homogeneous throughout, consisting of about 70% hydrogen, 28% helium and trace amounts of other elements. These local conditions within the cloud will influence the mass of the star. During the initial collapse, this pre-main sequence star generates energy through gravitational contraction. Upon reaching a suitable density, energy generation starts at the core using an exothermic nuclear fusion process.

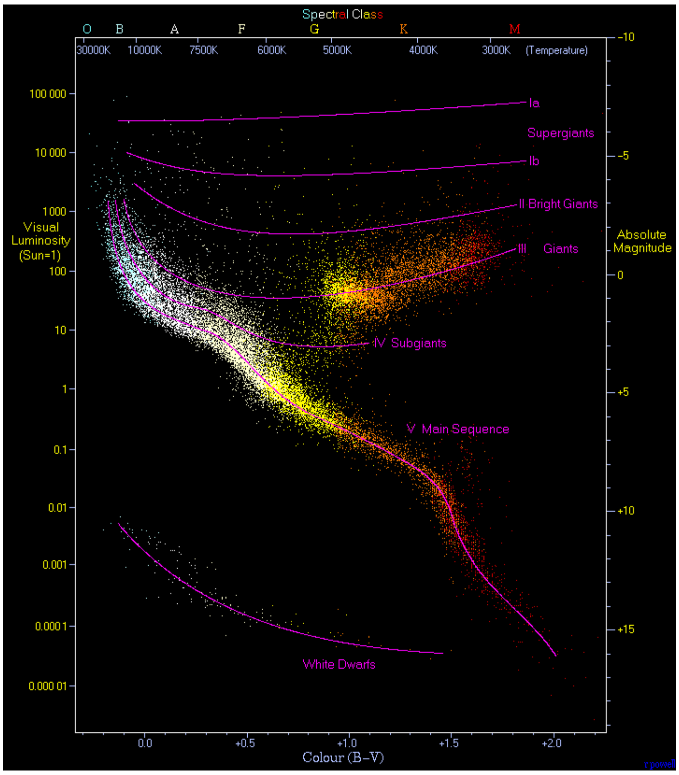

Figure 1.2: Hertzsprung-Russell diagram according to [5].

Once nuclear fusion of hydrogen becomes the dominant energy production process and the excess energy gained from gravitational contraction has been lost, the star lies along a curve on the Hertzsprung-Russell diagram (HR-diagram) called the standard main sequence.

Figure 1.2 shows a version of the Hertzsprung-Russell diagram containing stars from the Hipparcos and Gliese catalogues of nearby stars. It shows that stars tend to fall only into certain regions on the diagram. The most predominant being the main sequence, shown as the diagonal, going from the upper-left (hot and bright) to the lower-right (cooler and less bright). White dwarfs are found in the lower left, and above the main sequence are the subgiants, giants and supergiants. The Sun is found on the main sequence at luminosity 1 (absolute magnitude 4.8) and B-V colour index 0.66 (temperature 5780 K, spectral type G2).

1.3 The Hertzsprung - Russell diagram

In this section we give a brief description of the different stages of stellar evolution. The time like approximation of the evolution of the star life cycle was obtained according to [3].

- **Main Sequence**

  Stars spend about 90% of their lives in the main sequence. During this time they are in hydrostatic equilibrium and thermonuclear fusion, this means that hydrogen is being turned into helium and energy in the core. Until the core hydrogen fusion ceases, the star is very stable and remains in the main sequence.

  A low mass star ($1\ \mathrm{M}_\odot \leq\ \mathrm{M}_* \leq 2\ \mathrm{M}_\odot$) will increase in luminosity as well as temperature as it fuses its hydrogen, causing it to move slightly up along the main sequence (to the upper left). On the other hand, a high-mass star will increase in luminosity but decrease in temperature, causing it to slowly move off the main sequence to the right on the HR-diagram.

  The initial location of a star on the main sequence, is also correlated to the star's mass. A star with higher mass has a higher luminosity and temperature and is therefore higher on the main sequence.

- **Hertzsprung Gap or Subgiant Branch**

  The next step in the evolution of the star is the leaving of the main sequence. It starts after most of the hydrogen in a star's core has been fused to helium. Due to self-gravity the helium core begins to contract, which makes the hydrogen in the above layers fuse more rapidly because of increased temperature. This increase in hydrogen-shell burning causes the outer layers of the star to expand and cool and thus redden.

  The star is now becoming a red giant star, and it moves to the right of the main sequence on the HR-diagram [Chaisson and McMillan, 2002, Lattanzio, 1989]. In this moment, just as the star leaves the main sequence and before it becomes a red giant, it enters the Hertzsprung gap or subgiant branch.

  This is a very rapid process, which usually takes less than a million years. It is difficult to actually observe stars in this phase of evolution, since it occurs at almost constant luminosity [Hurley et al., 2000].

- **Asymptotic Giant Branch and Red Supergiants**

  The helium fusion process doesn't last as long as the original hydrogen fusion process that occurred on the main sequence. Since the temperature in the core during helium fusion is higher than during the hydrogen fusion, the rate of burning is also higher during this process [Chaisson and McMillan, 2002].

The luminosity is similar to what it was on the main sequence, even though helium fusion only releases one tenth of the energy per unit mass that hydrogen fusion does. After all the helium has been fused in the core of the star, it undergoes the same type of changes it went through after the main sequence phase. The core of carbon/oxygen begins to contract under its own gravity and the outer layers of the star again expand and cool.

The star has now reached a phase in its evolution known as the asymptotic-giant branch (AGB). In the HR-diagram, the path of the star moves away from the horizontal branch towards a region of lower temperature and in the case of lower mass stars, higher luminosity. The star is now becoming a red supergiant [Chaisson and McMillan, 2002, Hurley et al., 2000].

The next step in the stellar evolution depends critically on the mass of the star. In our work the more important stars are those with medium to low masses.

- **Carbon/Oxygen White Dwarfs - the Fate of Medium Mass Stars**

  The star will end as a carbon/oxygen white dwarf if its mass is within the range: $0.3\ \mathrm{M}_\odot \leq\ \mathrm{M}_* \leq 8\ \mathrm{M}_\odot$ [Hurley et al., 2000, Iben, 1981]. The carbon/oxygen core continously contracts and the outer layers become more and more unstable [Iben and Renzini, 1983]. In the end they will expand off the star completely and create what is known as a planetary nebula.

  The remaining carbon/oxygen core contracts to the point at which electron degeneracy pressure counteracts the inward pull of gravity. This degeneracy pressure only occurs at very high density ($> 10^6$ g/cm^3). It is not any kind of gas pressure and it is independent of temperature.

  The core of the dead star now becomes a white dwarf. This extremely dense star has a high temperature but a low luminosity. In the HR-diagram the white dwarf region is at the lower left, below the main sequence [Chaisson and McMillan, 2002, Hurley et al., 2000].

- **Helium White Dwarfs - the Fate of Low Mass Stars**

  Stars with less than about 0.3 $\mathrm{M}_\odot$ never reach high enough central temperatures to fuse helium into carbon and oxygen. Nevertheless, after a long time and due to the low gravitational pull, the outer layers will dissipate into a planetary nebula. This leaves mainly a helium core that is known as a helium white dwarf [Chaisson and McMillan, 2002].

- **Neutron stars, supernovae and black holes - the Fate of High Mass Stars**

  Stars with high mass (more than about 8 $\mathrm{M}_\odot$), will have a core too massive to be supported by electron degeneracy pressure after the carbon/oxygen core contracts. The star undergoes more fusion processes, until the core becomes primarily ion. As the star goes through these different fusion processes, it moves on the HR-diagram somewhat horizontally away from and to the right of the main sequence. Once the core becomes iron, no fusion process can counteract the gravitational pull of the core on itself. Thus, the iron core collapses due to its own gravity. The inner core is now a proto neutron star, and the neutron degeneracy pressure rebounds the outer material. This rebound sends a shockwave up through the rest of the star, exploding the outer layers of the core as well as the outer layers of the star itself in a violent event known as a type II supernova [Hurley et al., 2000].

The fate of the core which remains after the explosion, depends on its mass. In a core with mass less than about 3 solar masses, the neutron degeneracy pressure continues to counteract the inward pull of gravity, stabilising it into a neutron star. Neutron stars are dimmer than white dwarfs and are therefore lower in the HR-diagram. Some of the neutron stars, with strong magnetic fields collect infalling matter at and radiate out of their magnetic poles. They are observed as pulsars.

If the core's remaining mass is greater than about 3 $M_\odot$, the inward pull of gravity will force the core to collapse into a black hole from which no electromagnetic radiation can escape [Chaisson and McMillan, 2002].

1.3.1 Example

In this section we follow the life cycle of a C-star, starting at zero-age main-sequence with a mass of 1.55 $M_\odot$ and a metalicity of 0.0182 by showing a time sequence of its evolution, according to [3]. The initial values of mass and metalicity are in agreement with [Groenewegen et al., 1995].

Indicated in table 1.1 are the mass and time steps at the different stages of evolution. The time steps are in units of millions of years (10^6 yr), and the mass in units of solar mass ($M_\odot$).

Evolution type	Time ($10^6 \times$ year)	Mass ($M_\odot$)
Main sequence Star	0.0	1.550
Hertzsprung Gap	2422.6	1.550
Giant Branch	2478.8	1.550
Core Helium Burning	2607.0	1.500
First AGB	2737.7	1.473
Second AGB	2741.5	1.441
Carbon/Oxygen WD	2743.0	0.589

Table 1.1: Stellar evolution time and mass parameters.

The following figures show the time evolution of the temperature (figure 1.3) and luminosity (figure 1.4) for the example star described above. The relation between these two quantities is given by:

$$L_* = 4\pi R_*^2 \sigma_B T_*^4 \tag{1.3.1}$$

with σ_B being the Stefan-Boltzmann constant (see table A).

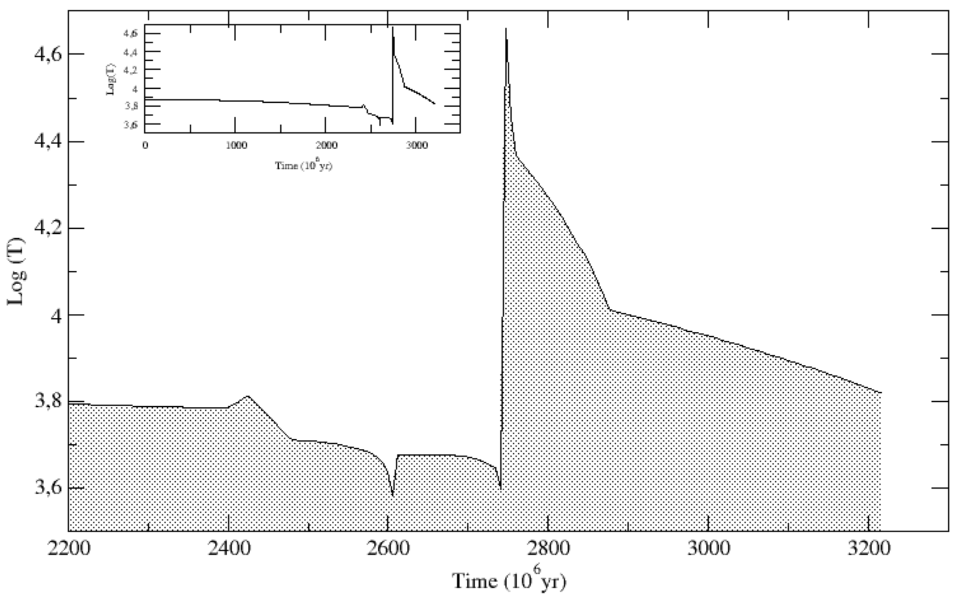

Figure 1.3: Temperature time evolution of an example C-star from the end of the main-sequence until the white dwarf phase. The smaller plot shows the full time evolution.

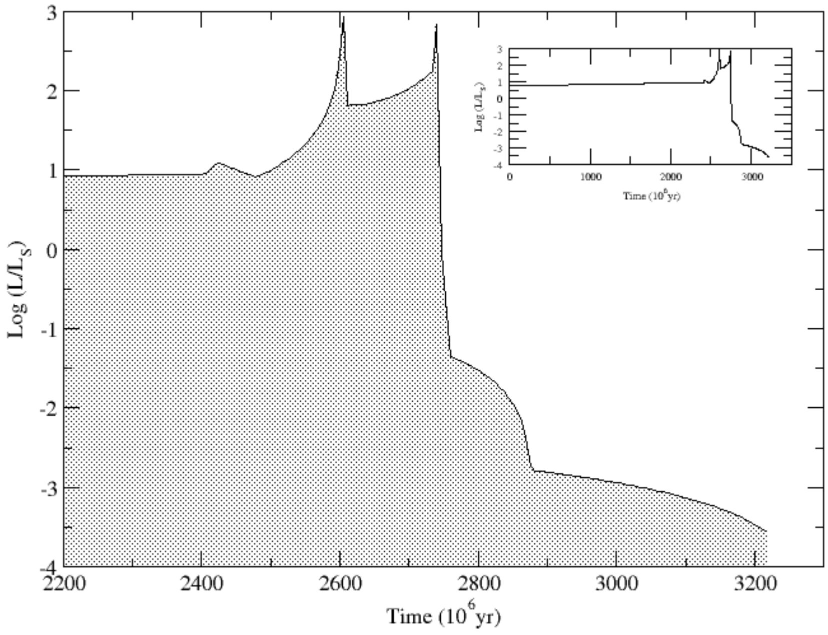

Figure 1.4: Luminosity time evolution of an example C-star. Same format as in figure 1.3.

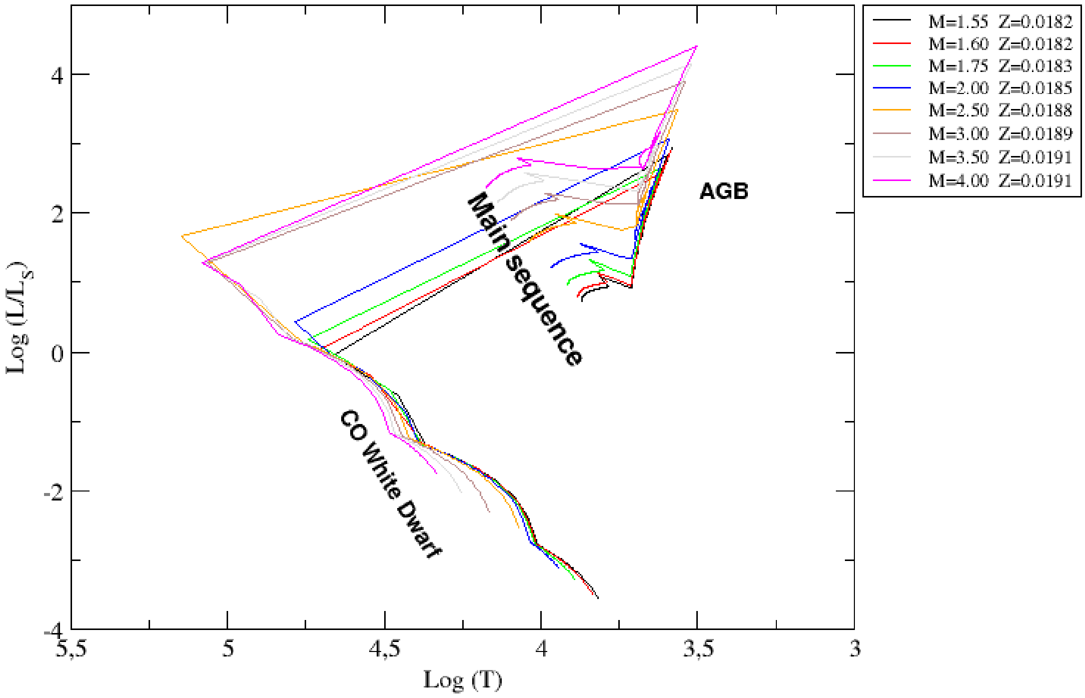

Figure 1.5: Time sequence of C-stars in the HR diagram. Indicated are the masses of the C-stars in $\mathrm{M}_\odot$ and the metalicity Z.

Figure 1.5 shows the resulting time evolution on the HR-diagram, of C-stars with masses in the range $1.55\ \mathrm{M}_\odot \leq \mathrm{M}_* \leq 4.0\ \mathrm{M}_\odot$, and with the indicated metalicities (Z). Noted are the location of the main sequence, the AGB branch and the Carbon/Oxygen white dwarfs.

1.4 Brown Dwarfs

Brown Dwarfs are sub-stellar objects, with masses between that of a star and a planet. They are assumed to form in the same way as star, that is, through the gravitational collapse of matter from an interstellar cloud, and in this way are distinct from the massive giant planets (10 times Jupiter's mass $\mathrm{M}_{\jupiter}$[1]) which have recently been discovered. It is known that Brown Dwarfs do not burn hydrogen in their cores, which is associated with their low masses, giving us an estimated upper mass between 0.075 and 0.080 $\mathrm{M}_\odot$. A lower limit for the mass is placed at 13 $\mathrm{M}_{\jupiter}$.

A classification of the different types of Brown Dwarfs has been made based on their temperature. Brown Dwarfs with high mass and temperature are known as ultra-cool dwarfs. They have dusty atmospheres and are of spectral type M7. Brown Dwarfs with temperatures as low as 2200 K are late M-types. For Brown Dwarfs cooler and smaller than type M, another spectral category L, was defined. These have temperatures of about 1500 K to 2000 K. Two additional spectral classes were also added, the spectral class T, for Brown Dwarfs with surface temperatures ranging from about 1500 K to 1000 K or even 800 K, that show strong absorption by methane and water, and the spectral class Y for Brown Dwarfs with even lower temperatures.

---

[1] $\mathrm{M}_{\jupiter} = 1.8986 \times 10^{27}$ kg $= 0.0009546\ \mathrm{M}_\odot$

Brown Dwarfs do not glow for very long. As soon as they have used up their supply of deuterium, which takes about 10 million years, they fade from dark red to black. Their luminosity is approximately $\leq 10^{-5}$ $L_{\odot}$.

The first observed Brown Dwarf [Nakajima et al., 1995, Oppenheimer et al., 1995], was Gliese 229B, a T dwarf part of a binary system. Since then several Brown Dwarfs have been observed in young clusters and in binaries [Burrows et al., 2001]. Interesting observations in a binary system constituted by a Brown Dwarf and a red giant show evidence of the Brown Dwarf surviving the common envelope evolution and remaining as a companion star [Maxted et al., 2001, Liebert, 2007].

Spectral observations show that the temperature and density structure of Brown Dwarfs offers ideal conditions for the formation of dust, e.g. [Kirkpatrick et al., 1999], and are therefore interesting for this work.

1.5 Red Giant stars

Of particular importance to this work are the Red Giant type stars, because it is assumed that dust production can occur in their atmospheres [Gail and Sedlmayr, 2009].

As we discussed previously, Red Giants are stars that exhaust the hydrogen at their core altering their appearance as they reconfigure themselves to burn helium, carbon, and oxygen. A Red Giant tends to be massive because only stars more massive than about 0.4 $M_{\odot}$ can consume their core hydrogen supply in less than the age of the universe (no more than 18 billion years). A Red Giant is physically larger than it was during its main-sequence phase, hence being called giant, and its surface temperature is lower than during the main-sequence phase to counter the effect of a larger surface area during the cooling of the star, therefore being red.

They are short-lived stars, and once thermonuclear fusion ceases in them, they cool to blackness as degenerate dwarfs and neutron stars, or they collapse into black holes.

A Red Giant star can be powered by a variety of thermonuclear processes at its core and within shells surrounding the core, in contrary to main sequence stars, which are powered by a single process. At the beginning of its Red Giant phase, the star burns helium at its core. Once this is exhausted, the star burns carbon. After the carbon is exhausted, the star burns oxygen. This march through the products of the previous stages of thermonuclear fusion continues until either electron degeneracy pressure stabilises the star as a degenerate dwarf or until all of the nuclear fuel has burned to iron, at which point the star collapsed to either a neutron star or a black hole. Regardless of the fuel burned at its core, most of the energy produced by the star comes from burning hydrogen in the star's outer envelope.

Massive stars in transition from core hydrogen burning to core helium burning have cooler photospheres than during their main-sequence phase, but they can still be hotter and bluer than the Sun. This is particularly true of very massive stars, which in their Red Giant phase form a class of objects called supergiants. These stars generate ten thousand times the power of the Sun, but can range in spectral colour from very blue to very red relative to the Sun.

The radius of a star's photosphere during the Red Giant phase is dramatically larger than it was during the main-sequence phase. For stars less than a couple of solar masses, this increase in radius counters the increase of a factor of 10 or more in brightness.

The low mass stars do not become dramatically redder in their giant phase, so the larger surface area is simply to counter the greater power generation. A solar mass star increases its radius by roughly a factor of 6 as it moves into its giant phase, while its temperature drops by only about 35%. This gives a solar-mass star a radius of about 0.03 AU. When the Sun becomes a Red Giant star in four billion years, its photosphere will extend until the orbit of Mercury. Seen from Earth, the Sun in this phase would have a diameter of 3° on the sky, versus the current 0.5°.

Large stars change more dramatically in appearance as they evolve into Red Giants than do the small stars. In the transition from the main sequence to core helium burning, a star of 9 $M_\odot$ becomes red quite fast, going from a photospheric temperature of 30000 K to a temperature of 2500 K. This minimum temperature of around 2500 K is a feature of giant stars of all masses. Unlike a low-mass star, a high mass star becomes only modestly more luminous, so the factor of 12 in temperature for a 9 $M_\odot$ star is accompanied by a factor of 4 increase in photospheric radius.

The transition of a massive star from high temperature to low temperature produces the variety of colours seen among the supergiants.

At the main sequence, due to either high atmospheric temperatures or due to the existence of chromospheres producing significant UV radiation, efficient dust formation is inhibited for most spectral types. For these reasons the presence of circumstellar or atmospheric dust seems to be limited to very cool main sequence objects of late spectral type M. As we mentioned, dust formation is also observed in atmospheres of brown dwarfs.

1.6 Mira stars and Long-Period Variables

Mira stars and Long-Period Variables are important in modern astrophysics and in particular to this work since they are low mass stars in the last and most luminous phase of their evolution, before they eject their outer layers as planetary nebula shells. At present it is not understood how matter gets lost from the surfaces into space, nor how the solid grains present in the outflow are formed. This last process is the focal point of this work.

Mira variables are cool, giant, pulsating stars with periods in the range $\sim$ 100 to $\sim$ 500 days, which can extend to $\sim$ 2000 days if one includes the OH/IR variables [Feast, 2001]. The fact that they are cool stars means that their surface temperature is lower than $\sim$ 3500 to 3000 K. They have well defined periods with visual light ranges of 2.5 mag or more. The Mira class has well defined physical properties. The majority of Mira stars has a maximum in the energy distribution, in the infrared near 1.6 μm. The visual region of the spectra is in the short wavelength tail of the energy distribution. For the wavelength range mentioned before, the light range is typically 1.0 mag or less.

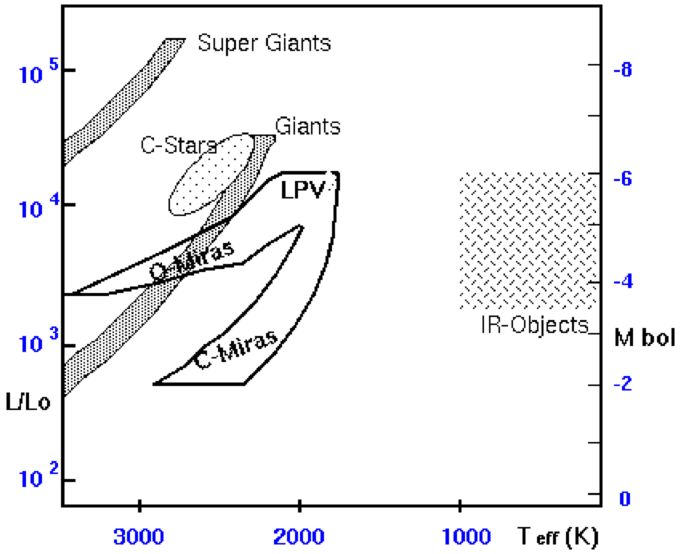

Figure 1.6: Location of C-Miras and O-Miras in the Hertzsprung-Russell diagram. Adapted from [Sedlmayr, 1985].

The visual brightness is therefore subject to large differences, even with small changes in the surface temperature. The visual region of the Mira spectra is dominated by molecular absorption bands. These become stronger when the surface temperature decreases during the pulsation cycle. The total luminosity (i.e. the bolometric luminosity) can be inferred from spectral measurements in the near infrared between 1.0 and 3.0 μm, where most of the energy is radiated.

The location of O- and C-Miras in the Hertzsprung-Russell diagram is shown in figure 1.6. In the following we describe some of the main features pertinent to the stellar evolution of Mira stars and LPVs.

Dredge-up: Dredge-up is the convective mixing into the upper atmosphere of the star, of material that has undergone nuclear processing in its interior.

An important indication that nuclear processing and the production of complex nuclei takes place in some of the stars, was given by the discovery of technetium atomic absorption lines in some S-Miras. The most stable isotope has a half-life of 4×10^6 years, while the predicted production mechanism in these stars has a half-life of only 2×10^5 years. Technetium lines have been subsequently found in many O- and C-Miras and semiregular variables [Feast, 2001].

Shock wave: Observations of the infrared spectra of Mira stars, in particular lines of the absorption bands of the CO molecule are particularly important to the understanding of the variability of the Mira stars.

By observing the variation of the radial velocity of CO lines of relatively high excitation potential, which are formed deep in the atmosphere of the star, it was seen that once per pulsation cycle a shock wave is generated which moves outwards through the stellar atmosphere. Since it was observed that at certain pulsation phases a doubling of these absorption lines occurred, it became clear that as one such shock wave is dying out in the higher atmosphere another is being generated lower down.

These observations strongly indicate that the variation of Mira stars is due to a pulsation mechanism of some kind. In order to obtain a self-sustaining pulsation, there needs to be a layer in the star which will act as an "Eddington" valve, absorbing energy when the star contracts and releasing it when the star expands. For the Mira stars this is most likely a region in which hydrogen is ionised on compression, recombination and release of energy taking place on expansion [Feast, 1989].

Spectra: The presence of emission lines of the hydrogen Balmer series in the spectra of the Mira stars makes them distinct from most lower-amplitude red variables. The intensity of these lines varies systematically in the pulsation period of the star. At present it is thought that these lines are excited by the shock waves [Feast, 2001].

Observations reveal that the lines have very unusual relative intensities ($H\delta$ much stronger than $H\gamma$, for instance), as the brightness of the star increases towards maximum light. This is due to the emission being excited by the shock deep in the stellar atmosphere. Absorption in the outer atmosphere (e.g. by molecules of TiO) causes the line strengths to be strongly modified.

During the pulsation cycle the shock wave moves outwards through the atmosphere and the emission lines which are generated suffer less from the effects of overlying absorption. Emission lines of neutral and ionised metals (e.g. lines of Fe I, Fe II, Mg I, Si I, In I) and even forbidden lines (i.e. lines with very low transition probabilities) of ionised iron (Fe II) have been observed at certain phases of the pulsation cycles in many of the better known Mira stars.

Diameter - extension: The atmospheres of Mira stars are very extended. Contrarily to most stars, where the depth of the atmosphere is only a small fraction of the stellar diameter, the atmosphere occupies most of the Mira stars. It is therefore important to define the diameter, since it is needed for the comparison with theoretical models and for a discussion of Mira stars pulsations. The diameter is measured at the wavelength in which most of the energy is radiated. For the wavelength of 1.6 μm the models suggest the diameter being measured is that of the stellar photosphere. For example, for Mira stars with a period of 300 days a linear diameter of ~ 400 $R_\odot$ is measured. For longer periods the diameters are even larger.

The images of Mira stars - asymmetric, noncircular: Due to interferometric measurements (aperture synthesis) done in recent years, it has been possible to reconstruct the images of Mira stars. The results show that the reconstructed image at optical wavelengths is non-circular. Figure 1.7 shows the aperture synthesis image of R Cas with its non-circular profile [Haniff, 1989]. This applies to the outer layers, as this is the region seen at optical wavelengths. For deep layers, such as those seen in the infrared, it has not been possible to say if this is also the case.

Three possibilities have been suggested to explain this result: the flattening of the outer atmosphere due to rotation, the non-radial pulsation of the star, and large star spots on the stellar surface which are not fully resolved with current instrumentation and lead to an apparent non-circular profile for the star.

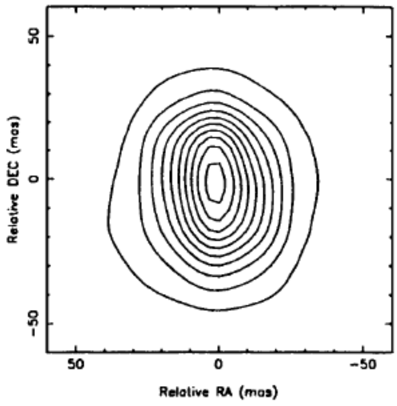

Figure 1.7: Aperture synthesis image of R Cas with its non-circular profile [Haniff, 1989].

The last of these possibilities has generally been favoured, since the atmospheres of cool red giants are expected to have large convection cells, which means that large over-hot or over-cool regions on the surface might be expected.

Some recent work indicates that the diameter of the outer regions (as seen in the visible) can vary in a way which is not connected with the pulsation. One should keep in mind that the outer regions are very tenuous and possibly consist of rising and falling clouds with little or no material between them.

1.6.1 The circumstellar region around Mira stars

Knowing the outer atmosphere structure of Mira stars is very important to understanding the process by which they loose mass. This knowledge is also extremely important to fully comprehend how solid grains are formed in the circumstellar environment and therefore essential for this work.

1.6.1.1 Atmosphere of Mira stars

According to the chemical composition of their atmospheres, there are three classes of Mira stars:

- The M-type Miras or M-Miras are the largest class. The dominant absorption bands in the optical region of the spectrum are by of the TiO molecule.

- For the S-Miras, the dominant absorption bands in the optical spectrum are those of the ZrO molecule. Often the TiO bands are strong as well. These two classes are grouped together as O-rich Miras (or O-Miras), which indicates an excess of oxygen in the atmosphere.

- In the third class, C-type Miras or C-Miras, the spectra are dominated by molecules containing carbon (C_2 etc). Stars with an excess of carbon in their atmospheres belong to this class.

For all of these stars, most of the carbon and oxygen in the atmospheres is locked up in the stable molecule CO. The differences between the two classes of O-Miras are due to different "dredge-up" rates.

1.6.1.2 Stellar Atmospheres

Stellar atmospheres are regions of relative high temperature and low density. Therefore, the gas consists mainly of single ions, and free electrons. In cooler stars molecule formation occurs. Because of the low density, the gas can always be treated as a perfect gas [Mihalas, 1970].

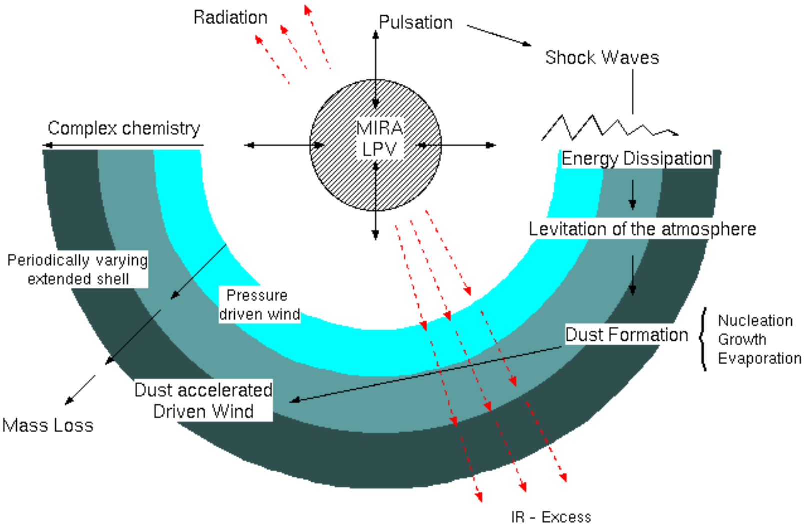
Radiation
Pulsation
Shock Waves
Complex chemistry
MIRA
LPV
Energy Dissipation
Levitation of the atmosphere
Periodically varying extended shell
Pressure driven wind
Dust Formation
Nucleation
Growth
Evaporation
Dust accelerated Driven Wind
Mass Loss
IR - Excess

Figure 1.8: Sketch of the global shell structure of a pulsating Mira star. Adapted from [Gail and Sedlmayr, 2009].

Figure 1.8 shows the global shell structure of a pulsating Mira star. Due to the nature of the pulsating star, shock fronts move outwards through the atmosphere, influencing the thermal and chemical state of each shell [Millar, 2003]. Due to the different components, such as the pulsation and the dynamics of the dust shell, dust formation and growth will be induced.

Mira stars mass loss rates are typically in the range from $\sim 10^{-7}$ to $\sim 3{\times}10^{-5}$ $M_{\odot}yr^{-1}$. This rate is related to the stars pulsation since it is correlated to the period and pulsation amplitude. Due to the pulsation, matter can be raised sufficiently above the star such that condensation into grains takes place. The fact that matter can concentrate into clouds in the atmosphere will clearly contribute to the grain formation. The existing grains are then driven from the star by radiation pressure and drag gas with them.

Since there are different types of Mira stars the dust composition will vary accordingly. Around O-Miras, dust is expected to be mostly composed of silicates, while around C-Miras there will be mostly carbon compounds.

In some C-Miras a large decrease in visual and near infrared brightness has been observed. These are similar to dust obscuration events of the RCB type (R Coronae Borealis stars). It seems that the dust formation process is non-uniform over the stellar surface and is possibly connected to clouds in the stellar atmosphere. Although it is likely that non uniform dust formation also takes place in the circumstellar envelopes of O-Miras, this will not be so obvious in optical observations due to the lower opacity of silicate grains.

The OH/IR Miras show at best how complex the circumstellar environment of Mira stars can be. These stars have a mass loss rate of $\sim 10^{-4}$ $M_{\odot}yr^{-1}$. They are long period O-Miras. Normally these are very faint objects at optical wavelengths, which is caused by circumstellar dust obscuration and low temperature of the star. The stars are bright at far infrared wavelengths (10 μm and longer). The heating of the circumstellar dust by the star causes the infrared radiation. In addition to the thermal emission from dust, these stars also show thermal emission from some molecules (e. g. mm and sub-mm lines of CO and SiO) and maser emission from molecules such as H_2O, OH, SiO.

Further relevant information on the dust formation process on Mira stars can be obtained from interferometric studies in the infrared (11 μm). These studies show that the dust formation process occurs at about two stellar radii (2 R_*) of the surface of the star. At the same distance SiO masers are also excited. This region covers a shell which is only 50 % greater in radius than the outer radius of the star's atmosphere (at visual wavelengths). Considering a typical Mira star, with a 350 days period and a photospheric radius of ~ 450 $R_{\odot}$ ($\sim 3 \times 10^{13}$ cm), one obtains an inner radius of the dust shell and a radius of the ring of SiO masers of the order of 10^{14} cm. This distance is 10^{15} cm for H_2O masers and for the OH masers it is a factor of ten further away. Thermal emission of CO, which is formed deep in the star, can be detected in the outflowing gas if enough sensitivity is given. Observations of outer radii of thermal CO emission around Mira stars are typically 10^{16} to 10^{17} cm and have large angular extent near Miras, e. g. for o Ceti an angular diameter of $\sim$ 14 arcsec was determined [Feast, 2001].

For the OH/IR Mira stars observations indicate spherical symmetry since the circumstellar masers are seen as circular rings in the sky. However, an asymmetric outflow, or a concentration of outflowing matter into clouds is observed in the less extreme Mira stars. Furthermore, asymmetrical scattering by grains in the dust shell has been confirmed by optical polarisation measurements.

The H_2O maser distribution in O-Miras can be asymmetric (e.g. as observed in the R Cas Miras) and in certain O-Miras observation of OH masers indicated that the mass loss is clumped in a small scale when compared with the OH shell radius and is chaotic.

Together with the previous mentioned characteristics, such as, the non-circular outer atmospheres of O-Miras and the RCB like decline of some C-Miras, these observations suggest that cool regions, clumps or clouds, in the upper atmosphere can be important to mass loss and grain formation processes.

1.6.2 Pulsation through $\kappa-$ mechanism

The $\kappa-$ mechanism (κ being the opacity), is a mechanism that accounts for star pulsation [Lattanzio and Wood, 2003]. In the interior of a star the opacity peaks in zones of most abundant species. In such areas equilibrium between the gravitational force and the radiation pressure (due to nuclear fusion) is not always achieved, which leads to pulsations of the star [Feast, 2001].

The pulsations are the result of cyclical changes in temperature and pressure. Let us consider a layer of the star compressed by the external layers, we know that this will cause it to move towards the centre of the star. This results in an increase of temperature and pressure and therefore an increase in the opacity. Due to the higher opacity, the radiation cannot escape and it accumulates bellow this layer. The increase in radiation pressure under this layer will lead to an expansion of the layer, which cools down and achieves a lower pressure. Now the layer has a lower opacity and the radiation can escape. The pressure bellow the layer will increase again and the gravitational force causes the layer to compress, starting the cycle from the beginning.

1.6.3 Evolution and pulsation

O-Miras in globular clusters evolve off the main sequence, climb the red giant branch (RGB). They then drop to the horizontal branch and then climb through the red giant region again in the asymptotic giant branch (AGB).

Mira stars are the brightest and coolest of the stars in the clusters in which they occur. Their luminosities are above the predicted for the RGB stars and therefore they are at the tip of the AGB. Once they leave this stage they will eject their atmospheres and become planetary nebulas.

The Mira stars belong to the thermal pulsing stage in which the stars burn helium and hydrogen in a nuclear active zone, which surrounds an inner core (a white dwarf).

A thermal pulse occurs every $\sim 10^5$ years in a solar mass star by a helium flash (a thermonuclear runaway) which lasts $\sim$ 500 years. During this period the structure of the star changes considerably, and this changes can affect the pulsation period. Some of the known Mira stars, R Hya, R Aql and W Dra [2] for example, show evidence for such changes. For example, the period of R Hya changed from $\sim$ 500 days in 1700 to 388 days at present.

Observations of globular clusters show Mira stars with short periods, which indicates that they are old objects with near solar masses. In cases where there are more than one Mira star in a cluster their periods are close to one another.

The periods of Mira stars in clusters are also related to the metalicity of the cluster, with longer period Mira stars indicating high metalicity clusters. One cannot establish such a relationship between period and metalicity for Mira stars in the general field due to the complexity of their atmospheres, which has not allowed for a detailed chemical abundance analysis.

However, for Mira stars in the general field a correlation has been established between their galactic kinematics and period.

- The short period stars, $\sim$ 200 days, belong to an old thick disk or intermediate halo population.
- Longer period Mira stars belong to a more metal rich, younger population.

The sequence of Mira periods is a sequence of the different ages and chemical abundances of the AGB branches.

---

[2] Coordinates (right ascension, declination): R Hya: (13h29m42.80s, -23°16'53.0"); R Aql: (19h06m22.2522s, +08°13'48.006"); W Dra: (18h05m35.2s, +65°57'12").

For C-Miras the stellar evolution is not so well known. It is thought that they can evolve from O-Miras due to dredge-up processes, without changing their period.

Observations of Mira stars in the Large Magellanic Cloud (LMC) can give valuable information on their period-luminosity relationship. In order to determine the absolute magnitude of Mira stars (the zero point of the period-luminosity relationship) one needs to:

- use either the distance to the LMC,
- the distance of globular clusters that contain Mira stars,
- the absolute magnitudes of main-sequence companions to Mira stars in visual binary systems, or
- the trigonometric paralaxes of Mira stars.

A defined linear relationship has been found between the bolometric or infrared magnitude and $\log \mathrm{P}$ for periods between $\sim$ 100 and $\sim$ 400 days. For O and C Mira stars the relations are almost the same at 2.2 μm (K-band) and only slightly different in bolometric luminosity.

The bolometric luminosity of a Mira star with a 200 day period is 4000 times that of the Sun, and for a Mira star with a 400 day period, the luminosity goes up to 9000 times the Sun's. Knowing the absolute magnitude and the angular diameter it is possible to estimate the linear diameter. In turn this information can be used, together with the masses and periods of the Mira stars, to determine the mode in which Miras pulsate.

Abstract Mira stars and Long-period Variables (LPVs) are highly evolved stars on the Asymptotic Giant Branch. Due to the peculiar physical conditions of these luminous pulsating objects, their cool, extended atmospheres are distinguished sites for the formation of small solid particles (dust). A massive outflow or wind develops, which is driven by radiation pressure on dust. Dust particles influence both, the internal structure of the circumstellar shell as well as the optical appearance of Mira stars and LPVs.

1.6.4 Mira stars in binaries - orbiting Brown Dwarf

Mira stars are known in interacting binary systems. These stars normally show a rich mission spectrum which is due to the infalling gas from the Mira star onto a disk around the companion.

The nearest system, with the Mira R Aqr (period of 387 days), is resolved as a bipolar nebula on the plane of the sky. In other systems, the Mira star cannot be seen in optical observations but it is clear in the infrared (e. g. RR Tel, with a period of 387 days). Another example where mass transfer is observed is in the binary system including the o Cet Mira, which transfers mass to a white dwarf companion. Another Mira, QX Pup, with a 700 day period, is observed in a complex bipolar nebula with velocity outflows of $\sim$ 200 km s^{-1}. Although it doesn't show the characteristic symbiotic line spectrum, this also seems to be part of an interacting binary system. This system is known as the Calabash Nebula or the Rotten Egg Nebula [3], due to the strong H_2S emission lines.

---

[3] Right ascension: 07h2m16.83s; Declination: 14°42'52.1'

Figure 1.9 shows the X-ray image of a Mira star binary system in the constellation of Cetus, taken by the Chandra satellite. It shows on the right a red giant Mira star and on the left a white dwarf. The red giant is loosing its upper atmosphere through stellar wind, due to the gravitational attraction of the white dwarf. The system has a distance to the Earth of 420 light years. The stars have a distance of approximately twice the distance of Pluto to the Sun.

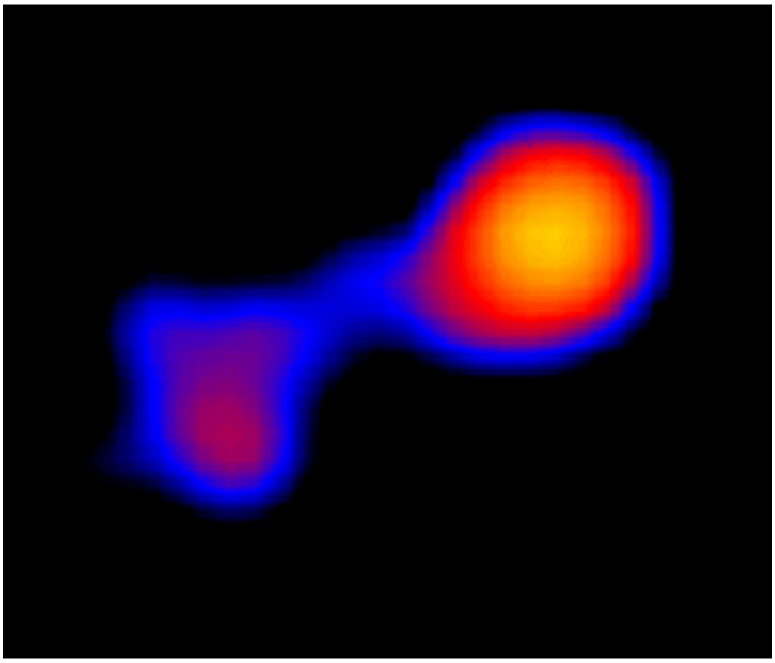

Figure 1.9: Chandra X-Ray image of a Mira star binary system [1].

1.7 Observations of eclipsing binary stars

We have discussed how Mira stars are often observed as part of binary systems. In fact these are quite common, and most stars are in binary or multiple star systems.

Observations of the orbital plane of a binary star shows the stars nearly edge-on, this means that the stars will alternately eclipse each other. These binary stars are so far away from the Earth that they look like single stars in photographs, but their brightness varies in a particular way due to the eclipses - these are known as eclipsing binary stars. About 6000 stars of this type are known in our galaxy and other nearby galaxies.

Eclipsing binary stars are a valuable source of information about the physical properties (mass, size, luminosities, internal structure, etc.) of stars and their evolution through time. They allow us to determine the fundamental physical properties with very high accuracy. Often the masses and sizes of the stars are known to better than 1% accuracy.

The study of eclipsing binary stars is done through a number of stages. The first stage is the discovery phase. This stage has evolved from the use of photographic plates in the late 19th century and early 20th century, to the more recent use of CCD cameras such as those in the MACHO project [6].

This project surveyed the Large Magellanic Cloud, looking for gravitational micro-lensing events over a period of years. As a byproduct, they found a large number (611) of eclipsing binary stars [6]. The observations obtained during the discovery phase are often not all that accurate, so this phase is usually followed by a refinement phase with different measurement techniques for stars of particular interest. One of these techniques is to observe the brightness with improved precision near predicted times of eclipse to determine accurate dates of minima in order to improve the predictions of eclipses. New techniques, such as spectroscopy, are used in this phase to measure the radial velocities of each star over the orbit. The data which is then obtained, is necessary to determine the absolute masses and sizes of the stars. Finally, combining the photometry and radial velocity data gives a complete picture of the binary star, i.e. the masses, sizes, and luminosities of a pair of stars, both of which have the same age. The study of eclipsing binary stars provides the needed constrains for the theoretical models that describe our understanding of stars.

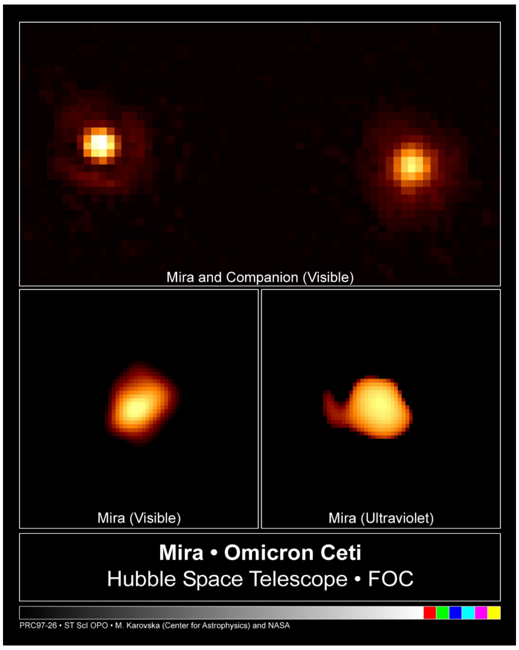
Mira and Companion (Visible)
Mira (Visible)
Mira (Ultraviolet)
Mira • Omicron Ceti
Hubble Space Telescope • FOC
PRC97-26 • ST ScI OPO • M. Karovska (Center for Astrophysics) and NASA

Figure 1.10: Top panel: NASA Hubble Space Telescope image of the cool red giant star Mira A (right), officially called Omicron Ceti in the constellation Cetus and its near-by hot companion (left) [2].

Figure 1.10 shows a false-colour picture of the Omicron Ceti Mira[4] binary star system, with the stars separated by an angular size of only 0.6 arcseconds, i.e. 70 AU. Hubble measurements show that the red giant star is 700 times larger than our Sun. In the lower right panel, observations in UV light resolve a small hook-like appendage extending from the Mira star, in the direction of the companion that could be material being gravitationally drawn toward the smaller star. Alternately, it could be that material in the Mira star upper atmosphere is being heated due to the companion's presence [2].

1.8 Evolution of close binary stars

As we mentioned above there is evidence from observations, that mass transfer occurs in a binary system. To discuss under which conditions this can occur we have to introduce some basic notions.

In particular we want to address the evolution of a close binary system. From the study of the stages of evolution it is presumed that there are no limits on both stars radius. However, the existence of a Roche surface, i.e. an equipotential surface around a star within which particles remain trapped, changes this assumption (see following sections). On reaching the Roche surface, the stellar envelope is presumed to become unbound and the mass loss or transfer is initiated on a hydrodynamic time scale. The star is generically referred to as the loser or donor, these terms are usually applied in the case of mass transfer between the binary components. The companion is called the gainer, which implies some amount of accretion. The taxonomic distinctions for the different evolutionary cases are based on the stage at which the nomenclature applies.

---

[4] Right ascension: 02h 19m 20.7927s; Declination: $-02^\circ\ 58'\ 39.513''$

Case A: occurs before the terminal main sequence, when the loser is still undergoing core hydrogen burning. This is a slow nuclear stage and not very sensitive to the stellar mass. For mass transfer to occur it requires very small orbital separation A because of the small stellar radii, and the timescale for stellar expansion is very slow.

Case B: occurs after hydrogen core exhaustion and during a relatively rapid stage of radial expansion, either in the traverse across the Hertzsprung gap or on first ascent of the giant branch but before helium core ignition.

Case C: is a late stage, when the star has developed a helium core and is on or near the giant branch or **AGB** [5].

In conservative mass transfer, the process can be studied in a straightforward way because any net mass or angular momentum losses are neglected. The Roche surface would recede into the loser were it not for the increase in the separation between the components that results from the change in the mass ratio. The loser maintains contact with the Roche lobe R_{RL}, until contact is broken by the expansion of the system and thereafter the more evolved star continues as if it were a single star. In the event of mass loss from the gainer, the process of mass transfer may be re-initiated at some later stage, but this is unlikely.

1.8.1 Common envelope evolution

Since the Roche surface represents the limit of a set of bounding equipotentials, it is a surface along which flows can occur but that a star can maintain as an equilibrium shape. If the radius of the outer layers exceeds R_{RL} and if both stars are in contact with the Lagrange point $\mathbb{L}_1$, a low-speed circulation can, in principle, be established because of the pressure reaction from the companion's outer layers. The resulting optically thick common envelope behaves as if the layer sits on top of a very strange equipotential surface, one where the surface gravity depends on both colatitude and colongitude.

There is an outer bounding surface through which some mass is lost through the Lagrange points $\mathbb{L}_2$ and $\mathbb{L}_3$, but this is small compared with the flow that must pass through $\mathbb{L}_1$ to maintain thermal balance. A sketch of a binary system with the location of the Lagrange points is shown in figure 1.11 (the Lagrange points will be discussed in more detail in chapter 3).

This is the observed situation in the W Ursae Majoris [Yang et al., 2001] variable, a type of eclipsing binary variable star (W UMa stars). Marked by continuous light variations, these stars appear to be surrounded by a common atmosphere, but they have otherwise stable cores that place them on the main sequence. This gives rise to a paradoxal situation. The mass-radius ($M - R$) relation for main sequence stars is approximately $R \sim M^{1/2}$, while a star in contact with its Roche surface will satisfy the approximate relation $R \sim M^{1/3}$. In a common envelope system, the two stars will need to simultaneously satisfy both conditions. Their equilibrium radii given by the nuclear burning conditions must be the same as their respective Roche surfaces, $(M_1/M_2)^{1/2} = (M_1/M_2)^{1/3}$, within a correction factor that depends on $q = M_2/M_1$. So the stars should have equal masses and, on the main sequence, they should also have equal luminosities [Lucy, 1968]. This however, is not what is seen. The envelopes have uniform temperature, and the B-V variation through an orbit is vanishingly small, but their luminosities and masses differ by up to a factor of 10. Such a large difference in the luminosity implies that heat transport must be occurring in the common envelope but that the overall interior structure of the star is otherwise unaffected. This is further complicated due to the fact that the coolest W UMa stars [Yang et al., 2001], [Lifang et al., 2004] must have common convective envelopes, where the temperature gradient adjusts to the large variation in the surface gravity due to the angular gradients in the equipotential. How this happens has been a controversial question for decades and remains an open question in stellar hydrodynamics. The consensus presently is that the envelopes are never precisely in thermal equilibrium and that the mass transfer fluctuates between the components. One way to picture this is that the mass transfer rate exceeds the thermal timescale for the entire envelope that drives thermal oscillations that periodically overfill the Roche lobe of the gainer, or rather the star that is accreting at that moment. Main sequence contact systems are only one example of evolutionary stages where common envelopes occur. Any circumstellar matter that completely engulfs the companion and is optically thick is, in effect, a common envelope. If the accreting material completely envelopes the gainer such that it is optically thick in all directions when the gas is confined within the Roche lobe of the gainer, than one can refer to the environment as a common envelope or a very thick accretion disk.

---

[5] The designations are originally due to [Kippenhahn and Weigert, 1967].

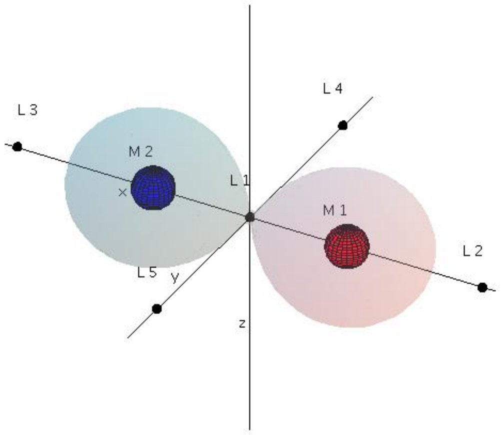

Figure 1.11: Isopotential surface through the Lagrange point $\mathbb{L}_1$ (Roche Lobe). Here M_1, M_2 are the location of the two equal mass stars, and $\mathbb{L}_2, \mathbb{L}_3, L_4$ and $\mathbb{L}_5$ the other Lagrangian points. The rotation occurs around the z-axis.

1.9 Mass transfer in close binaries

The Roche surface has acquired enormous significance as the limiting factor in the evolution of close binary stars. As a star gets closer to R_{RL} its mass becomes less stable and begins to flow. For real stars, this happens long before the photosphere comes into contact. Stars may show mass transfer effects even when their photospheres are well within the Roche radius provided they have sufficiently distended atmospheres, and this transfer can power accretion effects even before the major mass loss occurs.

1.9.1 Mass loss by wind

The role of radiation pressure in driving the winds of massive stars is similar to the tidal interactions between the stars. Either way, the star is stripped down to a bare core. There is growing evidence, for instance, that the final structure is virtually the same for a wide range of initial binary separations and mass ratios. When we add radiation pressure to the Roche problem, it has the same effect as a reduction in the mass of the luminous star. Whether or not there is a wind, the size of the Roche lobe decreases proportional to $M_{\mathsf{eff}} = (1 - \Gamma)M$, where Γ is the now familiar ratio of radiative to gravitational accelerations, g_{rad}/g. Several new effects have to be considered when treating mass loss by a stellar wind in a close binary [Shore, 2003]:

- One is that the total mass of the system changes because the material that is capable of leaving the surface of one of the stars is also able to leave the system as a whole, thus reducing the gravitational binding energy.

- On the other hand, depending on how the mass is lost, it may transport angular momentum, and this also alters the separation of the components. Isotropic mass loss at high speed will have little effect on total angular moment J, while altering the mass M.

- This is also true for jet-like mass outflows, especially if they are aligned with the orbital and rotational angular momentum axes. If, however, the mass is lost mainly from the orbital plane or if there is significant disk formation, then the torque may be important. Either effect ultimately enters into the calculation of the Roche radius, resulting in, feedback. Proximity ensures interaction if both stars happen to possess strong stellar winds.

- The shock thickness increases with distance from the orbital plane and, because each wind emerges spherically from the stellar surface, there is a dynamical pressure along the front that accelerates the flow outward.

In Chapter 3 we discuss in detail the dynamics of a binary system.

Chapter 2

Modelling method

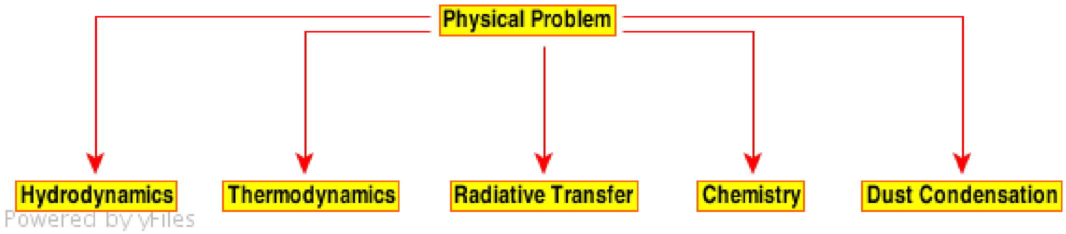

Figure 2.1: Physical problem

A realistic description of a common envelope dust shell has to take into account at least five physically and technically rather different subgroups (hydrodynamics, thermodynamics, radiative transfer, chemistry, dust condensation) as indicated in figure 2.1, which by their combined action determine its local physical behaviour and global spectral appearance.

In this chapter we would like to give a schematic description of the basic equations used in our studies of dust formation in a binary system. Before we do so we need to have an understanding of the theory of dust formation in the envelope of a single star. This has been the topic of several publications, e.g., [Gail et al., 1984, Gail and Sedlmayr, 1988, Fleischer et al., 1992, Fleischer, 1994, Winters, 1994].

The "classical" stellar atmosphere problem for a single star consists of finding the solution to the coupled system of differential equations describing the hydrodynamical and thermodynamical structure, as well as the chemical stratification of the atmosphere. The additional presence of dust, also introduces some decisive factors which have to be taken into account in the description of a dusty atmosphere.

Most importantly one has to address the basic interaction processes in a mixture of gas and particles, which are the collisions between the particles. Due to collisions an exchange of momentum and energy, as well as new chemical reactions will occur which will influence the densities of the species involved. The collisions will cause momentum exchange which impacts the hydrodynamics of the system, since there is a difference in the dynamical coupling between the particles from the different components of the stellar wind, and between the dust and gas components. Very important to the dust formation process are the chemical reactions that occur on the surface of the grains.

These reactions are responsible for the formation and growth of the condensed phases, and cause the change of chemical energy between the gaseous components and the condensed phases. The exchange of energy during collisions occurs by excitation and de-excitation of internal degrees of freedom. Furthermore, chemical energy is also exchanged between the gaseous components and the condensed phases through chemical reactions.

In summary, the main points to address when studying the influence of dust in the common atmosphere are:

- large cross section of dust particles, which affects the local transport coefficient and thus the global structure of the atmosphere;
- thermalization of energy, which results in the decoupling of the particles from the gas, which influences the thermodynamical structure;
- transmission of radiative momentum to the surrounding gas, which influences the hydrodynamical structure;
- influence on the absorption coefficient, on the IR-emission as well as the characteristic spectral appearance of the object, e.g. IR-excess;
- occurrence of further chemical reactions on the surface of the grain and possible catalysation leading to the formation of complex molecules.

A realistic description of the atmosphere containing dust, in our case the evolving common envelope of the donor and gainer star, also requires the treatment of the phase transition from the gas phase to the solid phase.

The solution of the chemical equations gives the particle densities for all species including, e.g., molecules and ions, and provides in particular the densities of the species relevant for dust formation. Starting from the nucleating species, critical clusters can be formed which will grow into macroscopic particles. The formation and growth of dust also has an impact on the gas phase. By adequately describing the dust growth process one obtains the chemical composition of the particles as well as their size distribution function. As mentioned in [Fleischer, 1994] the interaction of solids and radiation is best described by the Mie-Theory.

The radiation pressure, calculated as the product of the extinction coefficient χ_ν (equation **(5.2.7)**), of the envelope material and the frequency-integrated radiation flux, is the important contribution to the hydrodynamical equation of motion. As discussed by [Fleischer, 1994], for a single star even in the presence of other energy sources, this term completely determines the equation of motion and hence the dynamical behaviour of the circumstellar shell. Under the influence of an additional gravitational force (due to the companion star), other terms will contribute to the equation of motion (equations **(2.1.8)** and **(2.1.9)**).

Another important factor is the nucleation rate, i.e. the quantity which describes the formation of new dust grains. It depends very sensitively on the temperature, and therefore the thermodynamical structure determines where and how efficiently new dust grains are formed. The growth process of dust is also regulated by both the density stratification and the velocity structure. The first results from the equation of continuity and essentially affects the instant of time when new dust is formed and how effectively it subsequently grows. The second determines how long the material rests at a certain position in the atmosphere. Furthermore, the velocity limits the dust forming region since it causes a depletion effect in the chemistry and hence a reduced concentration of the dust forming molecules.

Based on the knowledge obtained from the previously mentioned studies, and using the CHILD-code, a profitable and proven scientific source code for a single star atmosphere evolution in one dimension, we will build up a higher dimension numerical approach to investigate the influence of an orbiting body on the dust formation in the evolving common envelope of a binary system, as sketched in figure 2.2.

In this work, we particularly focus on the behaviour of matter subjected to gravity and radiation, which are both assumed to be extraneous entities. Furthermore we include the presence of an orbiting companion star, which acts on the gravitation and radiation fields. As a consequence we loose the spherical symmetry, such that we have to chose a higher spatial dimension for the numerical evolution. The resulting dynamics of the system due to the inclusion of the companion star also have to be considered, this means taking into account a time dependent gravitational field due to the revolution of the stars around the centre of mass of the binary system.

The hydrodynamical structure of the system, resulting from extending the single star environment to a binary star one, is described in Chapter 4. For the higher dimensional numerical evolution, we select the smooth particle hydrodynamic (**SPH**) approach and the Monte Carlo method, as an adaptive higher dimensional extension based on the CHILD-code. We will use the CHILD-code time evolution of the fundamental quantities as input parameters for the higher dimensional inner boundary condition at the donor star (Mira-type). The radius of the inner boundary must be selected in such a way that the perturbative influence of the second star (brown dwarf) is negligible.

The thermodynamical structure and radiative transfer processes will be described by a Monte Carlo-type approach, in Chapter 5. This code has to be able to determine the thermal structure in the expanding common envelope during our simulation. At the inner boundary, the time-like parameter temperature $T_{\mathrm{g}}(t)$ from the CHILD-code, is used as an input source for the Monte Carlo code. In this approach we thus consider two sources of radiation, the donor star and the common envelope.

We assume Local Thermal Equilibrium (LTE) on the evolving common envelope, which is also determined by the Monte-Carlo approach during every hydrodynamical time step (SPH) and will be accounted for in the next hydrodynamical time step.

The chemistry of dust formation is discussed in Chapter 6. We use a damped Newton-Raphson method for the derivation of the local chemical equilibrium, and based on this we derive the essential quantities of dust formation and growth, such as the nucleation rate, the net growth rate and the dust moments K_i for $i = 0, ..., 3$.

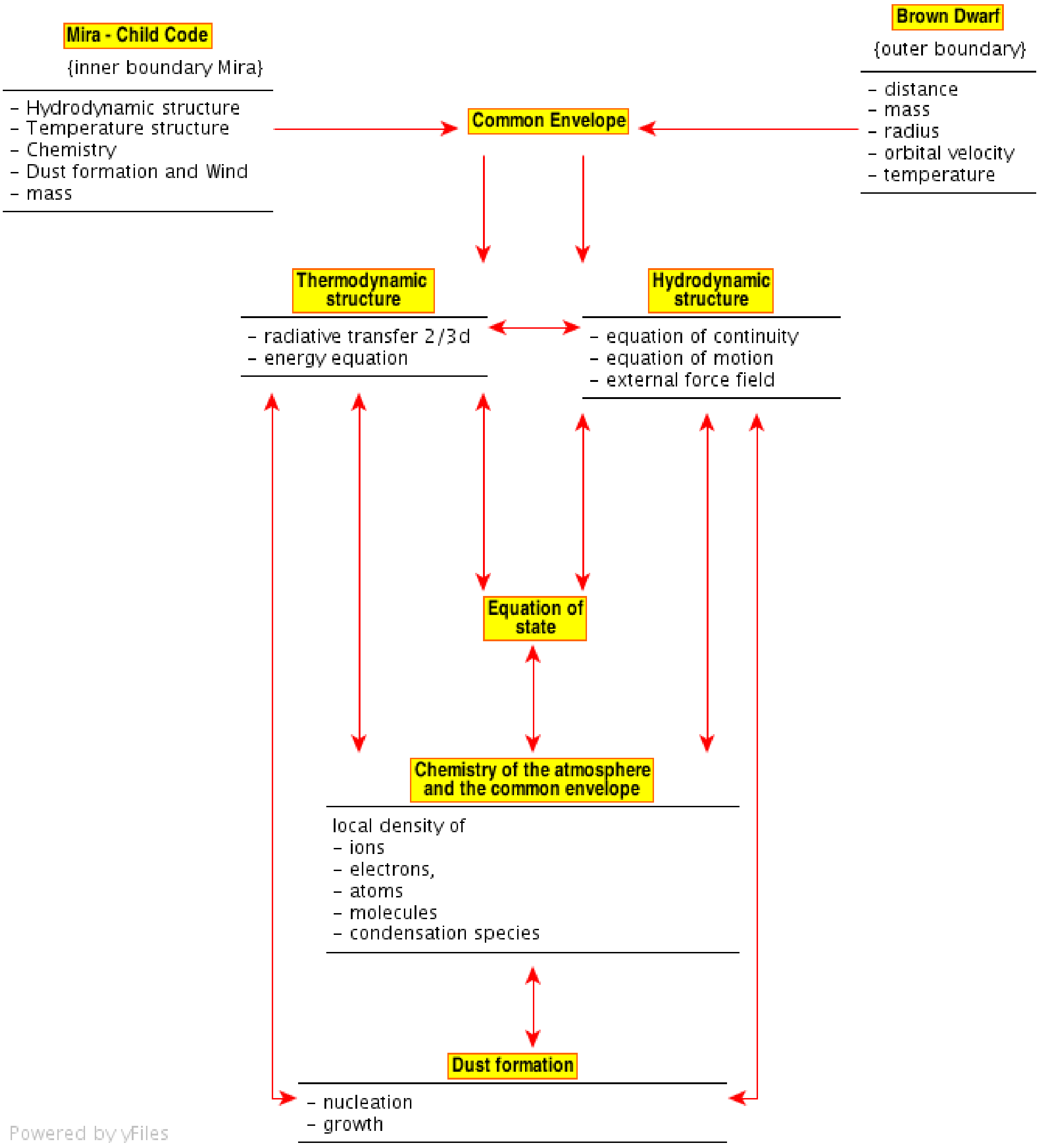
Mira - Child Code
{inner boundary Mira}
- Hydrodynamic structure
- Temperature structure
- Chemistry
- Dust formation and Wind
- mass
Brown Dwarf
{outer boundary}
- distance
- mass
- radius
- orbital velocity
- temperature
Common Envelope
Thermodynamic structure
- radiative transfer 2/3d
- energy equation
Hydrodynamic structure
- equation of continuity
- equation of motion
- external force field
Equation of state
Chemistry of the atmosphere and the common envelope
local density of
- ions
- electrons,
- atoms
- molecules
- condensation species
Dust formation
- nucleation
- growth
Powered by yFiles

Figure 2.2: Principle of the modelling approach

2.1 Basic equations

2.1.1 Binary star problem

As a main sequence star increases in size during its evolution (see section 1.3), it may at some point exceed its Roche lobe (see figure 3.4), meaning that some of its matter ventures into a region where the gravitational pull of its companion star is larger than its own. The result is that matter will transfer from one star to another through a process known as Roche Lobe overflow (RLOF), either being absorbed by direct impact or through an accretion disc. The mathematical point through which this transfer happens is called the first Lagrangian point $\mathbb{L}_1$. This is the point where the pressure gradient is not compensated by any other force. It is not uncommon that the accretion disc is the brightest (and thus sometimes the only visible) element of a binary star.

If a star grows outside of its Roche lobe too fast for all abundant matter to be transferred to the other component, it is also possible that matter will leave the system through other Lagrange points or as stellar wind, thus being effectively lost to both components.

Since the evolution of a star is determined by its mass (see section 1.2), the process of RLOF influences the evolution of both stars, and creates stages that cannot be attained by a single star, for example the mixing of atmospheres.

In Chapter 3 we give an overview on the roche lobe geometry, the Lagrange Points and the equation of motion for binary star systems.

2.1.1.1 Reduced three body problem

Here we consider the motion of the two stars and a fluid element under their mutual gravitational attraction, assuming that the mass of the fluid element is much smaller than the mass of the stars. In this is the orbit of the stars is not influenced by the fluid element.

To consider the force which acts on a fluid element in the environment of a rotating binary star system (Mira type, Brown Dwarf), we will transform the coordinate system into a reference frame (x, y, z) rotating with the binary system with its origin at the centre of donor star (Mira type). Due to the presence of the second star this is no longer an inertial system, such that it has to include non-inertial forces in the non-inertial frame of reference, such as the centrifugal fugal force or the Coriolis force. We assume a circular orbit and a synchronous rotation of the stars with the orbital rotation, i.e. $\mathbf{\Omega_1} = \mathbf{\Omega_2} = \mathbf{\Omega} = 2\pi/P_{\mathsf{orb}}$.

2.1.2 Hydrodynamical equation

A good introduction to dust formation, growth, and evaporation in a volume element of gas under time-dependent conditions can be found at [Gauger et al., 1990]. The authors use a successful approach by a Lagrangian formulation of hydrodynamics. In contrast to the field description of the Eulerian approach, the Lagrangian formulation treats the individual paths of an ensemble of small fluid elements. Thereby, the position **R** of a certain fluid parcel is described as a function of the Lagrangian variable **r**, such that at an instant of time t_1 we have $\mathbf{R} = \mathbf{R}(\mathbf{r}; t1)$, and $\mathbf{r} = \mathbf{R}(\mathbf{r}; t0)$, which denotes the initial or so called reference configuration. The time development along the path of the fluid is governed by the equation

$$\frac{\partial}{\partial t}\mathbf{R} = \mathbf{v} \tag{2.1.1}$$

which simply states, that the larger the fluid velocity $\mathbf{v}$, the larger is the change of the position of the fluid element. We denote the Lagrange - operator by:

$$\frac{d}{dt}(...) = \frac{\partial}{\partial t}(...) + \mathbf{v} \cdot \nabla(...) \tag{2.1.2}$$

2.1.2.1 Mass conservation

The local mass conservation can be expressed by:

$$\text{Eulerian: } \frac{\partial \rho}{\partial t} = -\nabla \cdot (\rho \mathbf{v}) \qquad \text{Lagrangian: } \frac{d\rho}{dt} = -\rho \nabla \cdot \mathbf{v} \tag{2.1.3}$$

Here $\mathbf{v}$ is the hydrodynamical velocity.

2.1.2.2 Stellar mass loss rate

Since during all phases of stellar evolution stars return a certain amount of their mass back into the interstellar medium by stellar wind, the mass conservation is particularly important when addressing the gain or loss of mass of the star through hydrodynamical processes. As we discussed in sections 1.6 and 1.9 the mass loss process we consider in this work is due to radiative driven winds, especially dust driven winds.

In this work we only regard the significant mass loss of the donor star, since we assume that the companion star is a compact brown dwarf and has no significant contribution to wind of the binary stellar system. We consider the donor star to have an effective mass lost rate $\dot{M}$ and that the influence of the companion star does not affect spherical symmetry in the near environment of the donor star. In this region we can adopt a spherical symmetric situation, described in spherical polar coordinates (r, θ, ϕ), with its origin at the centre of the donor star, where r is the radial coordinate and θ and ϕ are the redundant polar and azimuthal angles, respectively [Lamers and Cassinelli, 1999, Gail and Sedlmayr, 2009].

Under this considerations the mass loss rate is given by :

$$\dot{M} = 4\pi r^2 \rho v_r \tag{2.1.4}$$

where v_r is the radial component of the velocity vector $\mathbf{v}$.

2.1.2.3 Momentum conservation

From the law of momentum conservation, the equation of motion in spherical symmetry for the radial coordinate r is given by:

$$\frac{\partial v_r}{\partial t} + v_r \frac{\partial v_r}{\partial r} = \frac{1}{\rho} f_r - \frac{1}{\rho}\frac{\partial p}{\partial r} \tag{2.1.5}$$

$$\frac{dv_r}{dt} = \frac{1}{\rho} f_r - \frac{1}{\rho}\frac{\partial p}{\partial r} \tag{2.1.6}$$

where f_r is the radial component of the exterior force $\mathbf{f}$.

If we use equation **(2.1.2)** and do not assume symmetry, equation **(2.1.6)** in 3-dimensions $[x, y, z] = [x_1, x_2, x_3]$ is written:

$$\frac{\partial v_i}{\partial t} + v_i \frac{\partial v_i}{\partial x_i} = \frac{1}{\rho} f_i - \frac{1}{\rho} \frac{\partial p}{\partial x_i} \qquad i = 1, 2, 3 \tag{2.1.7}$$

such that in Lagrangian coordinates:

$$\boxed{\frac{d\mathbf{v}}{dt} = -\frac{1}{\rho} \nabla p + \frac{1}{\rho} \mathbf{f}} \tag{2.1.8}$$

where p is the pressure and $\mathbf{f}$ the exterior force density. The exterior forces acting on a fluid element are gravitational deceleration $\mathbf{f}_{\mathsf{grav}}$ **(3.2.6)** and acceleration due to radiation pressure $\mathbf{f}_{\mathsf{rad}}$ **(5.1.14)**, such that:

$$\mathbf{f} = \mathbf{f}_{\mathsf{grav}} + \mathbf{f}_{\mathsf{rad}} \tag{2.1.9}$$

2.1.2.4 Radiative driven winds

As we explained in the previous section, one of the main features of the circumstellar dust shells is the resulting stellar wind due to radiative momentum acting on the dust particles [Salpeter, 1974a, Salpeter, 1974b, Kwok, 1975].

There are however, other mechanisms which can drive winds even without radiative pressure on dust [Lamers and Cassinelli, 1999]. For completion we will present here a brief description of those mechanisms.

Radiation pressure on molecules: The question of whether radiation pressure on molecules caused atmospheric levitation, arose from the knowledge that considerable mass loss of O and B stars is caused by radiation pressure on atoms. The work of [Jørgensen and Johnson, 1992] studied the absorption and scattering of photons by molecules in the photosphere of oxygen and carbon rich giants. They found that, when compared to the solar ratio of C/O, models with higher values have higher levitation while models with lower values have lower levitation. They also found that the radiation pressure does not depend on the gravity but increases with increasing temperature. Radiation pressure can therefore support the levitation of the atmosphere.

Sound waves: The role of acoustic waves in driving winds has been studied, among others, by [Pijpers and Habing, 1989, Pijpers, 1990]. Although the authors found mass loss rates for AGB stars of the order of $10^{-7} - 10^{-4}$ $\mathrm{M}_{\odot}\mathbf{yr}^{-1}$, they did not take into account the effects of dust and these values seem to be overestimated. Sound waves therefore are more likely to have a supportive role than to a driving role in the winds.

Alfvén waves: The contribution of Alfvén waves to the winds has been studied by several authors, e. g. [Hartmann and MacGregor, 1980, Holzer and MacGregor, 1985]. The authors consider energy transport by non-compressive Alfvén waves. These waves can extend a stellar atmosphere over a large radius and cause the material to leave the gravitational field, since they are not easily dumped. Calculations indicate mass loss rates of 10^{-7} $\mathrm{M}_{\odot}\mathbf{yr}^{-1}$, without damping, but which are significantly reduced once damping is introduced. Nevertheless, the wind velocities which are obtained are still too high.

In our work we consider winds due to radiative pressure on dust with its origin on the donor star. In the following we present some of the basic equations considered, where we only evolve the wind equation in spherical symmetric coordinates, as mentioned in section 2.1.2.2.

2.1.2.5 Wind equations for the donor star

In the case of a stationary wind (where the time derivation in equation **(2.1.6)** vanishes), we introduce the isothermal sound velocity, c_{T}, given by:

$$c_{\mathsf{T}}^2 = \frac{p}{\rho} \tag{2.1.10}$$

$$v_r \frac{\partial v_r}{\partial r} = \frac{1}{\rho} f_r - \frac{1}{\rho}\frac{\partial p}{\partial r} \tag{2.1.11}$$

In this way, equation **(2.1.6)** can be written in the form of the so called wind equations:

$$\left(\frac{v_r^2 - c_{\mathsf{T}}^2}{v}\right)\frac{\partial v_r}{\partial r} = \frac{1}{\rho} f_r(r) - \frac{\partial c_{\mathsf{T}}^2}{\partial r} + \frac{2c_{\mathsf{T}}^2}{r} \qquad r \geq r_c \tag{2.1.12}$$

$$\frac{1}{p(r)}\frac{\partial p(r)}{\partial r} = \frac{2}{r}\left[\frac{r_c^4}{r^4}\frac{p_c^2}{p^2(r)} - \frac{r_c}{r}\right] \Big/ \left[1 - \frac{r_c^4}{r^4}\frac{p_c^2}{p^2(r)}\right] \qquad r < r_c \tag{2.1.13}$$

For a dust driven wind, the velocity of sound as well its radial variation are small compared to the force term (equation **(2.1.9)**). At the critical point (sonic point) $r = r_c$, we have $v(r_c) = c_{\mathsf{T}}(r_c)$, thus the radiative acceleration at the sonic point has to be large enough to be able to drive the wind. The sonic point is defined by:

$$v^2(r_c) = c_T^2(r_c) = \frac{p(r_c)}{\rho(r_c)} \tag{2.1.14}$$

with p being the gas pressure and ρ the density.

Special case - isothermal winds: For a time independent stellar wind with a constant mass loss rate, the amount of gas passing through any sphere of radius r is constant and given by equation **(2.1.4)**. The isothermal wind case is only a theoretical non realistic model to explain some of the key quantities.

In a stationary (time independent) wind, the velocity at a given distance does not change so $\partial_t v = 0$. If there are no other forces acting on the wind than the gas pressure and gravity, the equation of motion is:

$$v\frac{dv}{dr} + \frac{1}{\rho}\frac{dp}{dr} + \frac{GM_*}{r^2} = 0 \tag{2.1.15}$$

and the energy is simply $T(r) = T =$ constant (isothermal).

If the flow behaves like a perfect gas then the pressure is given by:

$$p = R\rho T/\mu \tag{2.1.16}$$

where R is the gas constant and μ is the mean atomic weight of the particle.

The force due to the pressure gradient can be written as:

$$\frac{1}{\rho}\frac{dp}{dr} = \left(\frac{RT}{\mu\rho}\right)\frac{d\rho}{dr} \tag{2.1.17}$$

The density gradient can be expressed in a velocity gradient considering equation **(2.1.4)**:

$$\frac{1}{\rho}\frac{d\rho}{dr} = -\frac{1}{v}\frac{dv}{dr} - \frac{2}{r} \tag{2.1.18}$$

Substituting equation **(2.1.18)** and equation **(2.1.17)** into equation **(2.1.15)** yields:

$$\frac{1}{v}\frac{dv}{dr} = \left(\frac{2c_{\mathsf{T}}^2}{r} - \frac{GM_*}{r^2}\right)/(v^2 - c_{\mathsf{T}}^2) \qquad \text{where} \qquad c_{\mathsf{T}} = \sqrt{\frac{RT}{\mu}} \tag{2.1.19}$$

The lower boundary condition of equation **(2.1.19)** is the bottom of the isothermal region, located at r_0 where $v(r_0) = v_0$. In general r_0 is approximately the photospheric radius, it can be a bit larger if the star is surrounded by an isothermal corona.

Equation **(2.1.19)** has a singularity at $v = c_{\mathsf{T}}$ which implies that the mass loss rate is fixed. The critical distance, r_c, is obtained when the numerator in equation 2.1.19 goes to zero:

$$r = r_c = \frac{GM_*}{2c_{\mathsf{T}}^2} \tag{2.1.20}$$

Such a distance exists in the isothermal wind at $r_c > r_0$ if:

$$\frac{GM_*}{2c_{\mathsf{T}}^2} > r_0 \qquad \text{or} \qquad \frac{GM_*}{2r_0} = \frac{v_{\mathsf{esc}}^2(r_0)}{4} > c_{\mathsf{T}}^2 \tag{2.1.21}$$

The velocity gradient at the critical distance will be zero, unless $v(r_c) = c_{\mathsf{T}}$. Similarly, the velocity gradient at the distance where $v = c_{\mathsf{T}}$ will be $\pm\infty$ because the denominator is equal to zero, unless $r = r_c$ when $c = c_{\mathsf{T}}$.

The only solution which can have a positive velocity gradient at all distances is the one that goes through the critical point, it is known as the critical solution. It satisfies:

$$v(r_c) = c_{\mathsf{T}} \qquad \text{at} \qquad r_c = \frac{GM_*}{2c_{\mathsf{T}}^2} \tag{2.1.22}$$

One finds that at the critical point, with the escape velocity $v_{\mathsf{esc}}(r) = \sqrt{2GM_*/r}$, the velocity is given by:

$$v(r_c) = c_{\mathsf{T}} = \frac{v_{\mathsf{esc}}(r_c)}{2} \tag{2.1.23}$$

The point where $v = c_{\mathsf{T}}$ is called the sonic point, the point where $v(r) = v_{\mathsf{esc}}(r)$ is called the escape point. In the isothermal wind the critical point coincides with the sonic point.

The critical solution is transonic, because it starts subsonic at small distances and reaches a supersonic velocity at large distances.

Solution: A general solution, for an isothermal wind, for the ordinary differential equation **(2.1.19)** is given by:

$$v\left(r\right) = \frac{\exp\left(-\frac{GM}{{c_{\mathsf{T}}}^2 r} - 1/2\,W_L\left(-e^{-2\,\frac{GM}{{c_{\mathsf{T}}}^2 r}-2\,\frac{C_1}{{c_{\mathsf{T}}}^2}}{c_{\mathsf{T}}}^{-2}r^{-4}\right) - \frac{C_1}{{c_{\mathsf{T}}}^2}\right)}{r^2} \tag{2.1.24}$$

where W_L is the Lambert - function:

$$W(z) = \sum_{n=1}^{\infty} \frac{-n^{n-1}}{n!} z^n \tag{2.1.25}$$

The integration constant C_1 can be isolated to :

$$C_1 = -\frac{1}{2}\,\frac{-v^2 r + 2\,\ln\left(v r^2\right){c_{\mathsf{T}}}^2 r + 2\,GM}{r} \tag{2.1.26}$$

and it can be determined by the values for the critical solution: $r_c = GM_*/(2c_{\mathsf{T}}^2)$ and $v = c_{\mathsf{T}}$, such that:

$$C_1 = -\frac{3}{2}\,{c_{\mathsf{T}}}^2 + 2\,{c_{\mathsf{T}}}^2\ln\left(2\right) - {c_{\mathsf{T}}}^2\ln\left(\frac{G^2{M_*}^2}{{c_{\mathsf{T}}}^3}\right) \tag{2.1.27}$$

It follows that the final (critical) solution is given by:

$$v(r) = \frac{1/4\, e^{-1/2\, W_L \left(-e^{-2\, \frac{GM_*}{{c_\mathsf{T}}^2 r} + \left(3\, {c_\mathsf{T}}^2 + 2\, {c_\mathsf{T}}^2 \ln \left(1/4\, \frac{G^2 {M_*}^2}{{c_\mathsf{T}}^3} \right) \right) {c_\mathsf{T}}^{-2}} {c_\mathsf{T}}^{-2} r^{-4} \right)} e^{3/2} G^2 {M_*}^2}{r^2 \left(e^{\frac{GM_*}{{c_\mathsf{T}}^2 r}} \right) {c_\mathsf{T}}^3} \tag{2.1.28}$$

Solar example: Considering the following parameters, a solution of the momentum equation of an isothermal wind with gas pressure and gravity, in terms of v/c_T versus r/r_c, can be estimated, as seen in figure 2.3.

$M_* = \mathrm{M}_\odot, \quad r_c = 8.29 \times 10^{14}\ \mathrm{m}, \quad R_* = \mathrm{R}_\odot,$

$T_* = T_{\mathsf{surface}} = 5778\ \mathrm{K}, \quad v_{\mathsf{esc}} = 565.93\ \frac{\mathrm{m}}{\mathrm{s}}, \quad c_\mathsf{T} = 282.96\ \frac{\mathrm{m}}{\mathrm{s}}$

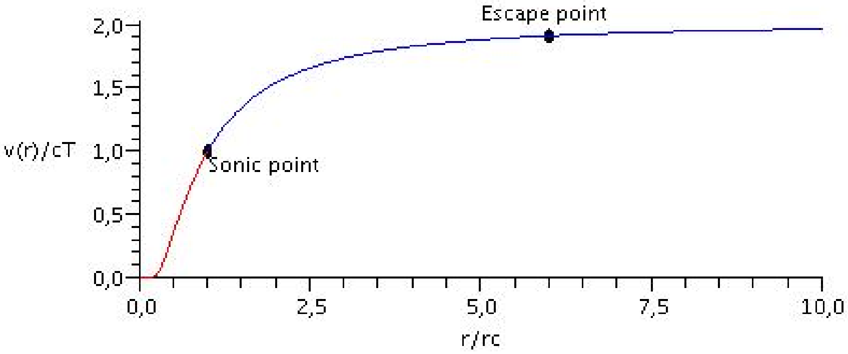

Figure 2.3: The curve shows the transonic solution (**red**: subsonic / **blue**: supersonic) with increasing velocity through the sonic point r_c (ring) where $v = c_\mathsf{T}$. The escape point, after which matter can escape, is also indicated.

The previous discussion has shown that there is only one solution for the isothermal case, which starts subsonic and ends supersonic. This critical solution occurs for only one particular value of the velocity at the lower boundary v_0. This implies that an isothermal envelope with given density ρ_0 at the bottom can only produce a transonic wind if equation **(2.1.23)** is satisfied.

This means that an isothermal wind can reach supersonic velocities for only one specific value of mass loss rate.

From equations **(2.1.4)** and **(2.1.28)** we can obtain a relation to compute the density profile for the isothermal case:

$$\dot{M} = 4\pi r_0^2 \rho_0 v_0 = 4\pi r^2 \rho(r) v(r) \tag{2.1.29}$$

with ρ_0 being the density at the surface we can derive $\rho(r)$ as:

$$\frac{\rho(x)}{\rho_0} = \frac{x_0^2 v_0}{v(x)x^2} \tag{2.1.30}$$

where v_0 is the velocity at the lower boundary, $x_0 = r_0/r_c$ and $x = r/r_c$. Figure 2.4 shows the density profile obtained with the initial data from the solar example.

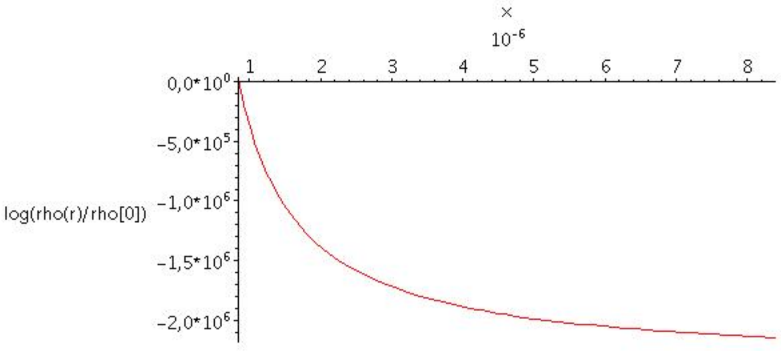

Figure 2.4: Density profile in terms of $\frac{\rho(x)}{\rho_0}$ with initial data from the solar example.

2.1.2.6 Energy conservation

This equation describes the change of energy contained in a unit volume per unit time. As previously mentioned, in this work we particularly focus on the behaviour of matter subject to gravity and radiation both assumed as extraneous entities. For this reason we introduce in equation **(2.1.31)** the effect of the radiation field and of the gravitational field, in form of the corresponding source and sink terms accounting for the exchange of energy between these external fields and the various matter constituents.

In the Eulerian frame the one-fluid total energy equation for the matter in cartesian coordinates can be written as:

$$\frac{\partial}{\partial t}\Big[\rho(e + e_{\mathsf{kin}})\Big] = -\frac{\partial}{\partial x_i}\Big[\rho(e + e_{\mathsf{kin}})v_i + p_{ij}v_j\Big] + Q_{\mathsf{rad}} + Q_{\mathsf{e}} \tag{2.1.31}$$

where Q_{rad} is the radiative net source, Q_{e} is the mechanical power input of gravitation and radiation, e is the specific energy and $e_{\mathsf{kin}} = 1/2v^2$ is the specific local kinetic energy. The two latest terms define the energy density of the matter per unit mass. The specific energy, e is given by the thermal energy e_{th} due to random particle motion, e_{int} related to the internal degrees of freedom, the latent chemical energy e_{ch}, due to exothermic and endothermic chemical reactions and the non random kinetic energy e_{rel}, associated with the systematic relative motions of the different components [Gail and Sedlmayr, 2009], such that:

$$e = e_{\mathsf{th}} + e_{\mathsf{int}} + e_{\mathsf{ch}} + e_{\mathsf{rel}} \tag{2.1.32}$$

In the lagrangian frame equation **(2.1.31)** can be written in the one - fluid approach as:

$$\boxed{\rho\frac{de}{dt} = -p\nabla\cdot\mathbf{v} + Q_{\Sigma} \qquad (2.1.33)}$$

where $Q_{\Sigma} = Q_{\mathrm{rad}} + Q_{\mathrm{vis}}$ is the net energy input rate. It describes the net energy gain of the gas per unit mass and time, with Q_{rad} being the net radiative heating rate (equation **(5.1.9)**), that describes the energy exchange between the gas and the radiation field, and Q_{vis} being the heating rate due to artificial viscosity (introduced in section 4.2). This term is needed in the numerical treatment of shock waves to avoid discontinuities. The term itself is chosen in such a way that will have no effect on the physical results outside the discontinuity.

2.1.3 Radiative transfer problem

The radial acceleration due to radiation pressure for a single star can be described by:

$$f_{\mathrm{rad}} = \frac{4\pi}{c}\int_0^{\infty}\chi_\nu H_\nu d\nu = \frac{4\pi}{c}\xi_{\mathrm{F}}H \qquad (2.1.34)$$

where χ_ν is the extinction coefficient (equation **(5.2.7)**), H_ν is the spectral Eddington flux and c the speed of light. ξ_{F} denotes the mean extinction coefficient and is given by:

$$\xi_{\mathrm{F}} = \frac{\int_0^{\infty}\chi_\nu H_\nu d\nu}{\int_0^{\infty}H_\nu d\nu} \qquad (2.1.35)$$

In section 5.3.3 we make a Monte-Carlo example calculation, for a plane parallel atmosphere, for the Eddington moments, J_ν, H_ν and K_ν. In our higher dimensional Monte-Carlo approach to the radiative transfer problem, we will instead use equation **(5.1.14)**.

2.1.4 Equation of state

In a circumstellar dust shell the thermodynamic conditions are such that the interaction energy of the gas particles is small when compared with their kinetic energy. In this way the gas pressure is that of an ideal gas:

$$p = \frac{\rho}{\mu m_H}k_{\mathrm{B}}T_g \qquad (2.1.36)$$

where k_{B} is the Boltzmann constant (table A) and μ is the mean molecular weight, calculated for the dominant species H, H_2 and He (table B), such that:

$$\mu = \frac{n_{\mathrm{H}} + 2n_{\mathrm{H_2}} + 4n_{\mathrm{He}}}{n_{\mathrm{H}} + n_{\mathrm{H_2}} + n_{\mathrm{He}}} \qquad (2.1.37)$$

Since the density of the dust particles is several orders of magnitude smaller then the particle density of gas. the dust particles are neglected in the equation of state.

2.1.5 Chemistry of the gas phase

To describe the chemical structure of a reacting gas one can normally use a system of rate equations, to represent the evolution of the particle density n_i with time, for each chemical species i.

$$\frac{dn_i}{dt} = \frac{\partial n_i}{\partial t} + \nabla \cdot (\mathbf{v}\ n_i) = Q_i \tag{2.1.38}$$

where Q_i is the net rate of production of species i, and includes all gain and loss processes due to kinetic and photo interactions. For our model we assume local thermodynamical equilibrium (LTE) and chemical equilibrium (CE) such that we can replace the general ansatz **(2.1.38)** by the law of mass action. A detailed description will be given in chapter 6.

2.1.6 Time evolution of dust grains

To describe the two step process of grain nucleation and growth we consider in our model the classical nucleation theory and the successful approach by a master equation for the grain size distribution function f, expressed in terms of its moments K_i [Gail et al., 1984, Gail and Sedlmayr, 1988]. We include in our model K_i up to the third moment $(i = 3)$ to describe the particle density, the average grain radius and the number density of monomers. The time evolution of K_i in the comoving Lagrangian frame in our one fluid approach is given by [Gauger et al., 1990]

$$\frac{dK_i}{dt} = \frac{\partial K_i}{\partial t} + \nabla \cdot (\mathbf{v}\ K_i) \qquad i = 0...3 \tag{2.1.39}$$

In section 6.2 we give the full set of equations describing nucleation and growth of carbon grains, under the assumption of the small particle limit of the Mie - theory. By using the moment method we can obtain the complete information about the carbon dust component for the description of the dust shell.

2.2 Boundary conditions for the modelling

A sketch showing the different boundaries to which our modelling of the binary system is subjected is given in figure 2.5. It shows the location of the inner boundary near the donor star (Mira type star), and the region around it where spherical symmetry can still be considered, that is, where the influence of the companion star is negligible. The outer boundaries, one at the companion star and another around the binary system, which constitutes the end of the evolution area, are shown in blue.

For the inner boundary we set the following conditions: The inner boundary radius (R_i) is located a few scale heights below the photosphere of the donor star. We consider two cases, a stationary dust driven wind (Model 1) and a second case, with a non stationary wind (Model 2), for which we chose the piston model [Bowen, 1988a, Bowen, 1988b]. In this case the inner boundary radius and the local velocity vary sinusoidally with time

$$R_i = R_0 + \Delta v_p \frac{P}{2\pi} \sin(\frac{2\pi}{P} t) \tag{2.2.1}$$

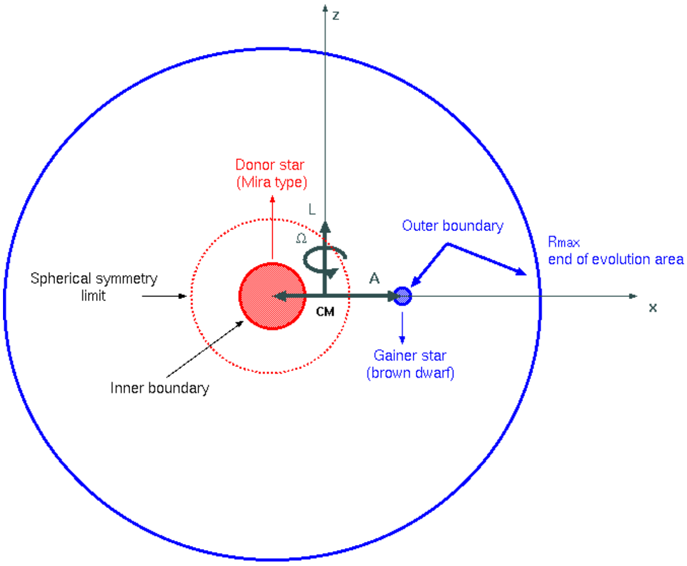

Figure 2.5: The sketch shows the location of the inner (R_*) and outer boundary settings of our numerical approach for the orbiting binary system build up by a donor star (Mira type) and a gainer star (brown dwarf type). The two stars are separated by a distance A along the x -axes in the corotating frame and have an orbital frequency Ω.

this gives for the velocity at the inner boundary v_i,

$$v_i = \Delta v_p \cos(\frac{2\pi}{P}t) \tag{2.2.2}$$

where P is the pulsation period. Both Δv_p and P are given as input parameters to the model, as can be later seen in section 6.4. The beginning of the hydrodynamical cycle is defined as the time when the inner boundary is at position R_0, for time $t = nP$ with $n = 0, 1, 2, \ldots$.

The treatment of the outer boundary of the evolution area, implies establishing a discretisation scheme with an imaginary pressure for the region outside the outer boundary [Richtmyer and Morton, 1967].

For the boundary at the gainer star we use a free fall condition which removes particles across the surface of the gainer star, instead of smoothing gravity very close to the gainer star [Mastrodemos and Morris, 1998]. This means that the gainer accretes at its maximum rate.

Another boundary condition, which defines the photosphere radius (R_*), comes from requiring that $T(R_*) = T_*$, which gives for the optical depth (see section 5.3, equation **(5.3.6)**):

$$\tau_L(R_*) = \frac{2}{3} \tag{2.2.3}$$

Further considerations regard the solving of the moment equations for the dust component. We start with a dust free atmosphere of a hydrostatic stellar model. In order for condensation to occur the supersaturation ration (S, equation **(6.2.2)**) has to be greater than one. This means that the partial pressure of carbon in the gas phase is greater than the vapour pressure of solid carbon.

In chapter 7, we will implement these boundary conditions into our modelling approach (see figure 2.2) for the above mentioned models.

Chapter 3

Dynamics in a binary star system

3.1 Force field in binaries

As we discussed in chapter 1, mass transfer is likely to occur in a binary system when the donor star is expanding over the Roche lobe. In this section we describe how we calculate the force field of rotating binary stars, taking into account distortion due to tidal forces. For this we consider the forces that impact on a probe particle in a binary system, with masses M_1 and M_2. Both stars are assumed to be spherically symmetric, the gravitational attraction to each star depends on the distance with r^{-2}. When one considers the stars to be at a certain distance such that tidal forces can distort the shape of one or both stars, the gravitational attraction will not depend on the distance as r^{-2} but will contain other terms. These additional terms will cause the orbit to stop being a closed eclipse.

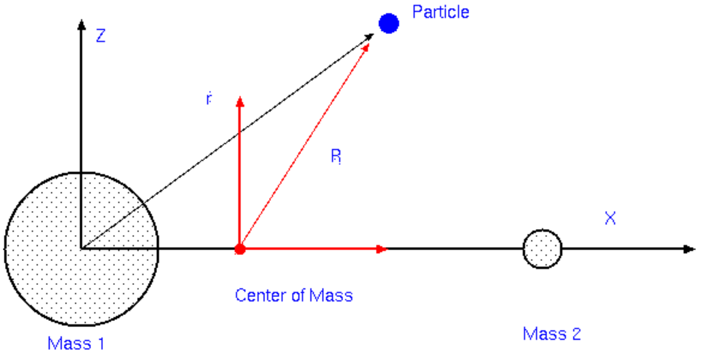

Figure 3.1: The sketch shows the inertial reference frame with origin at centre of mass (x, y, z) (red) and the reference frame rotating with the binary system (black) and with origin at the centre of star 1.

However, due to the tidal interaction the orbit will be circular and the rotation of each star is synchronous with the orbital rotation $\boldsymbol{\Omega}$.

In the following discussion a circular orbit and the synchronous rotation of the stars with the orbital rotation will be assumed, i.e., $\boldsymbol{\Omega_1} = \boldsymbol{\Omega_2} = \boldsymbol{\Omega} = 2\pi/P_{\text{orb}}$, where P_{orb} is the orbital period. Two cartesian coordinate systems are used, as indicated in figure 3.1. One (X, Y, Z) is an inertial reference frame with origin at the binary's centre of mass, the second (x, y, z) is a reference frame rotating with the binary system and with origin at the centre of star 1.

The x-axis is along the line connecting the components centres, the z-axis is perpendicular to the orbit and parallel to $\mathbf{\Omega}$ and the y-axis produces a right hand coordinate system.

Let the position of a particle be set by the vector $\mathbf{r}$ in the rotating coordinate system, and by the vector $\mathbf{R}$ in the inertial system. The acceleration $\ddot{\mathbf{r}}$, in the coordinate system (x, y, z) can be expressed in terms of the acceleration $\ddot{\mathbf{R}}$ corresponding to the inertial coordinate system (X, Y, Z) as:

$$\frac{d^2\mathbf{r}}{dt^2} = \frac{d^2\mathbf{R}}{dt^2} - \frac{d^2\mathbf{R_1}}{dt^2} - \mathbf{\Omega} \times (\mathbf{\Omega} \times \mathbf{r}) - 2\mathbf{\Omega} \times \frac{d\mathbf{r}}{dt} \tag{3.1.1}$$

where $\mathbf{R_1}$ is the radius vector of the centre of mass of star 1 in the inertial coordinate system and $\ddot{\mathbf{R}}_\mathbf{1}$ is the acceleration of the (x, y, z) coordinate system's origin with respect to the inertial frame (X, Y, Z). The term $\mathbf{\Omega} \times (\mathbf{\Omega} \times \mathbf{r})$ is the acceleration due to the **centrifugal force** and the term $-2\mathbf{\Omega} \times \dot{\mathbf{r}}$ is the acceleration due to the **Coriolis force**.

A probe particle in the inertial system, is acted upon by three forces, the gravitational forces to each star and the pressure gradient. The particle acceleration can then be represented as:

$$\frac{d^2\mathbf{R}}{dt^2} = -\nabla\Phi_1 - \nabla\Phi_2 - \frac{1}{\rho}\nabla p \tag{3.1.2}$$

where Φ_1 and Φ_2 are the gravitational potentials produced by star 1 and star 2, ρ is the density and p the pressure of the environmental matter. Considering additionally that for a circular orbit:

$$-\frac{d^2\mathbf{R_1}}{dt^2} = -\mathbf{\Omega} \times (\mathbf{\Omega} \times \mathbf{R_1}) \tag{3.1.3}$$

equation **(3.1.1)** can be written as:

$$\frac{d^2\mathbf{r}}{dt^2} = -\nabla\Phi_1 - \nabla\Phi_2 - \frac{1}{\rho}\nabla p - \mathbf{\Omega} \times (\mathbf{\Omega} \times \mathbf{R_1}) - \mathbf{\Omega} \times (\mathbf{\Omega} \times \mathbf{r}) - 2\mathbf{\Omega} \times \frac{d\mathbf{r}}{dt} \tag{3.1.4}$$

Using vector analysis the expressions $-\mathbf{\Omega} \times (\mathbf{\Omega} \times \mathbf{R_1})$ and $-\mathbf{\Omega} \times (\mathbf{\Omega} \times \mathbf{r})$ can be written as:

$$\begin{aligned} -\mathbf{\Omega} \times (\mathbf{\Omega} \times \mathbf{R_1}) &= \Big(-\Omega^2 R_1, 0, 0\Big) = -\nabla(\Omega^2 R_1 x) \\ -\mathbf{\Omega} \times (\mathbf{\Omega} \times \mathbf{r}) &= -\nabla\Big(-1/2\Omega^2(x^2 + y^2)\Big) \end{aligned}$$

where $\mathbf{\Omega} = (0, 0, \Omega)$.

The equation of motion of a probe particle in a rotating coordinate system is then:

$$\boxed{\frac{d^2\mathbf{r}}{dt^2} = -\frac{1}{\rho}\nabla p - 2\mathbf{\Omega} \times \frac{d\mathbf{r}}{dt} - \nabla\Phi \qquad (3.1.5)}$$

with the total potential Φ being:

$$\Phi = \Phi_1 + \Phi_2 + \Omega^2 R_1 x - \frac{1}{2}\Omega^2(x^2 + y^2) \tag{3.1.6}$$

In the case of synchronous rotation of a star and a binary system, an arbitrary particle has zero velocity and acceleration $\dot{\mathbf{r}} = \ddot{\mathbf{r}} = 0$ and equation **(3.1.5)** becomes:

$$\frac{1}{\rho}\nabla p = -\nabla\Phi \tag{3.1.7}$$

This equation describes the hydrostatic equilibrium of matter in a star. The surface on which the density matter is zero determines the boundary of a star. As a consequence the iso-surfaces of density, pressure and potential coincide. In this way, to determine the form of the star, one has to find the iso-surface $\Phi =$ constant, where the density of matter of a star is zero.

3.2 Roche Lobe geometry

Since the potential Φ depends on the distribution of density inside each component of the system, the gravitational potentials, Φ_1 and Φ_2 mentioned above, can be determined from Poisson's equations. However, in the majority of cases the Roche approximation is used to determine the gravitational potential. This approximation allows us to consider the stars as point masses, since it assumes that all the mass of the star is concentrated in the centre. In this case the gravitational potentials are described by the classical Newton law:

$$\phi_1 = -\frac{GM_1}{r_1} \tag{3.2.1}$$

$$\phi_2 = -\frac{GM_2}{r_2} \tag{3.2.2}$$

with $r_1 = \sqrt{x^2 + y^2 + z^2}$, $r_2 = \sqrt{(x-A)^2 + y^2 + z^2}$ being the distances from the considered point **r** to the centres of the components, A being the binary separation, G being the gravitational constant, and M_1, M_2 being the masses of the components. Using the gravitational potentials given above in equation **(3.1.6)**, and knowing that the motion of the components follows Kepler's third law:

$$\boxed{G(M_1 + M_2) = A^3\Omega^2} \tag{3.2.3}$$

and that the position of the centre of mass is given by:

$$R_1 = \frac{M_2}{M_1 + M_2}A \tag{3.2.4}$$

the total potential of the system can be represented in the (x, y, z)-coordinate system by:

$$\boxed{\Phi = -\frac{GM_1}{\sqrt{x^2 + y^2 + z^2}} - \frac{GM_2}{\sqrt{(x-A)^2 + y^2 + z^2}} - \frac{1}{2}\Omega^2\left\{\left(x - A\frac{M_2}{M_1 + M_2}\right)^2 + y^2\right\}} \tag{3.2.5}$$

This equation is known as the Roche potential. The Roche potential has five stationary points that are known as the Lagrangian points. We use this potential to define the effective gravitational force density by

$$\mathbf{f}_{\mathsf{grav}} = -\nabla\Phi \tag{3.2.6}$$

3.2.1 The Jacobi integral

The Jacobi integral is the only integral of the circular restricted three-body problem. This means that the problem cannot be solved in closed form for general cases.

The integral cannot be used to provide an exact solution for the orbital motion, but it can be used to determine regions from which the particle is excluded.

To determine this integral for a single particle ($\frac{1}{\rho}\nabla p = 0$) we use equation **(3.1.5)**, i.e.

$$\ddot{\mathbf{r}} = -2\,\boldsymbol{\Omega}\times\dot{\mathbf{r}} - \nabla\Phi \tag{3.2.7}$$

Scalar multiplying equation **(3.2.7)** with $\dot{\mathbf{r}}$ such that

$$\ddot{\mathbf{r}}\cdot\dot{\mathbf{r}} = \underbrace{\left(-2\,\boldsymbol{\Omega}\times\dot{\mathbf{r}}\right)\cdot\dot{\mathbf{r}}}_{=0} - \nabla\Phi\cdot\dot{\mathbf{r}} \tag{3.2.8}$$

gives for the components

$$\dot{x}\,\ddot{x} + \dot{y}\,\ddot{y} + \dot{z}\,\ddot{z} = \left(\frac{\partial\Phi}{\partial x}\right)\dot{x} + \left(\frac{\partial\Phi}{\partial y}\right)\dot{y} + \left(\frac{\partial\Phi}{\partial z}\right)\dot{z} = -\frac{d\Phi}{dt} \tag{3.2.9}$$

and we can integrate this equation with respect to time i.e.,

$$\frac{1}{2}\frac{d}{dt}\left(\dot{x}^2 + \dot{y}^2 + \dot{z}^2\right) = -\frac{d\Phi}{dt} \tag{3.2.10}$$

The integral is then given by:

$$\dot{x}^2 + \dot{y}^2 + \dot{z}^2 = -2\,\Phi - C_J \tag{3.2.11}$$

where C_J is a constant of integration. Since $\dot{x}^2 + \dot{y}^2 + \dot{z}^2 = v^2$, is the square of the velocity of the particle in the rotating frame, we have:

$$\boxed{v^2 = -2\,\Phi - C_J \qquad (3.2.12)}$$

This is the Jacobi Integral or Jacobi constant, sometimes called the integral of relative energy. The importance of the Jacobi constant is seen when considering the locations where the velocity of the particle is zero. In this case we have:

$$2\,\Phi = -C_J \tag{3.2.13}$$

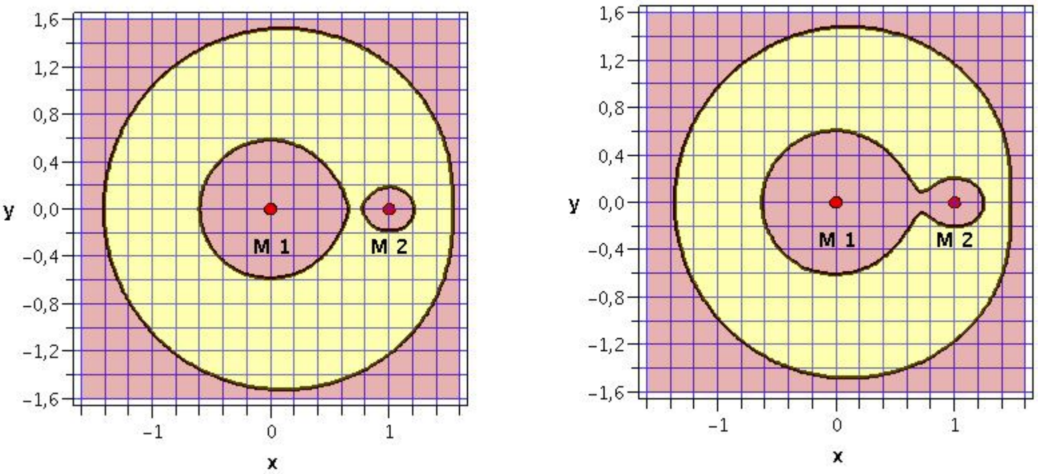

Figure 3.2: Zero-velocity curves for the Jacobi integral, with $M_1 = \mathrm{M}_\odot, M_2 = 1/10\,\mathrm{M}_\odot$, $A = 1$ AU, $\Omega = 1.0488\,2\pi$/yr. **Left panel**: $C_J = 157.2$ AU^2/yr^2; **Right panel:** $C_J = 153.2$ AU^2/yr^2. The yellow areas denote the excluded regions described in the text.

Equation **(3.2.13)** defines a set of surfaces for the particle values of C_J. These surfaces, known as the zero-velocity surfaces, play an important role in placing bounds on the motion of the particle.

For simplicity the following discussion is restricted to the $x-y$ plane (see figure 3.2). In this case the intersection of the zero-velocity surfaces with the $x-y$ plane produces a set of zero-velocity curves. From the expression for the Jacobi constant (see equation **(3.2.11)**) it is clear that one must always have $2\,\Phi \geq C_J$ since otherwise the velocity v would be complex. Thus equation **(3.2.13)** defines the boundary curves of the regions where particle motion is not possible, i.e. excluded regions. The yellow shaded areas in figure 3.2 denote regions where motion is impossible. We can see from the left panel of figure 3.2, for example, that if a particle with that value of C_J is in orbit in the unshaded region (pink) around M_1 then it can never orbit the mass M_2, or escape from the system since this would imply crossing the excluded region.

Similarly, in the right panel of figure 3.2, if the particle is originally orbiting the mass M_1 then it is possible that it could eventually orbit the mass M_2 but never escape from the system. This is the concept of Hill's stability.

3.2.2 Lagrange points

The problem for finding the Lagrange points is fairly straightforward. We need to find the solutions to the equation of motion which maintain a constant separation between three bodies.

If M_1 and M_2 (see figure 3.1) are the two masses, and $\mathbf{R}_1$ and $\mathbf{R}_2$ are their respective positions along the x-axis, then the total force exerted on a third mass m, at a position $\mathbf{R}$, will be:

$$\mathbf{F} = -\frac{GM_1 m}{|\mathbf{R}-\mathbf{R}_1|^3}(\mathbf{R}-\mathbf{R}_1) - \frac{GM_2 m}{|\mathbf{R}-\mathbf{R}_2|^3}(\mathbf{R}-\mathbf{R}_2) \tag{3.2.14}$$

The interesting point is that both $\mathbf{R}_1$ and $\mathbf{R}_2$ are functions of time since M_1 and M_2 are orbiting each other.

We can now insert the orbital solution for $\mathbf{R}_1(t)$ and $\mathbf{R}_2(t)$ (obtained by solving the two body-body problem for M_1 and M_2) and look for the solutions to the equations of motion that keep the relative positions of the three bodies fixed:

$$\mathbf{F} = m\frac{d^2\mathbf{R}(t)}{dt^2} \tag{3.2.15}$$

The stationary solutions are know as Lagrange points. The easiest way to find these solutions is to adopt a co-rotating frame of reference in which the two masses hold fixed positions. The new frame of reference has its origin at the centre of mass, and an angular frequence Ω given by Kepler's third law (see equation **(3.2.3)**).

3.2.3 Location of equilibrium points

Although the circular restricted three-body problem is not integrable we can find a number of special solutions. This can be achived by searching for points where the particle has zero velocity and zero acceleration in the rotating frame. Such points are equilibrium points of the system. We assume that the motion is confined to the $x-y$ plane.

For the sake of simplicity we choose a unit system for the mass MU $= M_1+M_2$, length LU $= A$ and time TU $= \sqrt{A^3/G(M_1+M2)}$ such that we have $\mu = G(M_1+M_2) = 1$.

$$\mu = G(M_1+M_2)\left[\frac{\mathsf{m}^3}{\mathsf{kg}\cdot\mathsf{s}^2}\right]\left[\mathsf{kg}\right] = 1 \times \left[\frac{\mathsf{LU}^3}{\mathsf{MU}\cdot\mathsf{TU}^2}\right]\left[\mathsf{MU}\right] \tag{3.2.16}$$

If we set in this system

$$\bar{\mu} = \frac{M_2}{M_1+M_2}, \quad \mu_1 = G\,M_1 = 1-\bar{\mu}, \quad \mu_2 = G\,M_2 = \bar{\mu} \tag{3.2.17}$$

It follows in system that $\mu_1+\mu_2 = 1 = G(M_1+M_2)$ and for equation **(3.2.3)** that $\Omega^2 = G(M_1+M_2) = \mu$.

The direction of the x axis is chosen such that the two masses always lie along it with coordinates: $(x_1, y_1, z_1) = (-\mu_2, 0, 0)$ and $(x_2, y_2, z_2) = (\mu_1, 0, 0)$.

For a co-rotating reference frame at the center of mass (figure 3.1) we get for the location of two mass μ_1, μ_2:

$$R_1^2 = (x+\mu_2)^2 + y^2 + z^2 \tag{3.2.18}$$
$$R_2^2 = (x-\mu_1)^2 + y^2 + z^2 \tag{3.2.19}$$

$$\mu_1 R_1^2 + \mu_2 R_2^2 = x^2 + y^2 + \mu_1\mu_2 \tag{3.2.20}$$

and for the potential $\Phi = \Phi_{\mathsf{CM}}$ in this center of mass coordinate system:

$$\boxed{\Phi_{\mathsf{CM}} = -\mu_1\left(\frac{1}{R_1} + \frac{R_1^2}{2}\right) - \mu_2\left(\frac{1}{R_2} + \frac{R_2^2}{2}\right) + \frac{1}{2}\mu_1\mu_2 \qquad (3.2.21)}$$

The advantage of this expression for Φ is that the explicit dependence on x and y is removed, such that the partial derivatives in **(3.2.7)** become simpler.

We now consider the equations of motion, given by equations with: $\ddot{x} = \ddot{y} = \ddot{z} = \dot{x} = \dot{y} = \ddot{z} = 0$. To find the location of the equilibrium points we must solve simultaneously the nonlinear equations:

$$\frac{\partial \Phi_{CM}}{\partial x} = \frac{\partial \Phi_{CM}}{\partial R_1}\frac{\partial R_1}{\partial x} + \frac{\partial \Phi_{CM}}{\partial R_2}\frac{\partial R_2}{\partial x} = 0 \tag{3.2.22}$$

and

$$\frac{\partial \Phi_{CM}}{\partial y} = \frac{\partial \Phi_{CM}}{\partial R_1}\frac{\partial R_1}{\partial y} + \frac{\partial \Phi_{CM}}{\partial R_2}\frac{\partial R_2}{\partial y} = 0 \tag{3.2.23}$$

Evaluating the partial derivatives, we can write the equations for the location of the equilibrium points as:

$$\mu_1\left(-\frac{1}{R_1^2} + R_1\right)\frac{x+\mu_2}{R_1} + \mu_2\left(-\frac{1}{R_2^2} + R_2\right)\frac{x-\mu_1}{R_2} = 0 \tag{3.2.24}$$

and

$$\mu_1\left(-\frac{1}{R_1^2} + R_1\right)\frac{y}{R_1} + \mu_2\left(-\frac{1}{R_2^2} + R_2\right)\frac{y}{R_2} = 0 \tag{3.2.25}$$

Inspection of equations **(3.2.22)** and **(3.2.23)** shows the existence of the trivial solution:

$$\frac{\partial \Phi_{CM}}{\partial R_1} = \mu_1\left(-\frac{1}{R_1^2} + R_1\right) = 0 \tag{3.2.26}$$

$$\frac{\partial \Phi_{CM}}{\partial R_2} = \mu_2\left(-\frac{1}{R_2^2} + R_2\right) = 0 \tag{3.2.27}$$

which gives $R_1 = R_2 = 1$ in this system of units. Using equations **(3.2.18)** and **(3.2.19)** this implies:

$$(x+\mu_2)^2 + y^2 = 1 \text{ and } (x-\mu_1)^2 + y^2 = 1 \tag{3.2.28}$$

with the two solutions:

$$x = \frac{1}{2} - \mu_2, \qquad y = \pm\frac{\sqrt{3}}{2} \tag{3.2.29}$$

Since $R_1 = R_2 = 1$, each of the two points defined by these equations forms a equilateral triangle with the masses μ_1 and μ_2. These are the triangular Lagrangian equilibrium points referred as $\mathbb{L}_4$ and $\mathbb{L}_5$. By convention the leading point triangular point is taken to be $\mathbb{L}_4$ and the trailing point $\mathbb{L}_5$.

It is clear from equation **(3.2.25)** that $y = 0$ is a simple solution of equation **(3.2.23)**, implying that the remaining equilibrium points lie along the x-axis and satisfy equation **(3.2.22)**. There are three such solutions corresponding to the collinear Lagrangian equilibrium points denoted by: $\mathbb{L}_1$, $\mathbb{L}_2$ and $\mathbb{L}_3$. The $\mathbb{L}_1$ point lies between the masses μ_1 and μ_2, the $\mathbb{L}_2$ lies outside the mass μ_2 and the $\mathbb{L}_3$ point lies on the negative x-axis. We now derive an approximate location for each of the collinear point.

- At $\mathbb{L}_1$ we have:

$$R_1 + R_2 = 1, \quad R_1 = x + \mu_2 \quad R_2 = -x + \mu_1, \quad \frac{\partial R_1}{\partial x} = -\frac{\partial R_2}{\partial x} = 1 \quad (3.2.30)$$

Hence substituting in equation **(3.2.24)** gives us:

$$\mu_1\left(-\frac{1}{(1-R_2)^2} + 1 - R_2\right) - \mu_2\left(-\frac{1}{R_2^2} + R_2\right) = 0 \qquad (3.2.31)$$

- At $\mathbb{L}_2$ we have:

$$R_1 - R_2 = 1, \quad R_1 = x + \mu_2 \quad R_2 = x - \mu_1, \quad \frac{\partial R_1}{\partial x} = \frac{\partial R_2}{\partial x} = 1 \qquad (3.2.32)$$

Hence substituting for R_1 in equation **(3.2.24)** we have:

$$\mu_1\left(-\frac{1}{(1+R_2)^2} + 1 + R_2\right) - \mu_2\left(-\frac{1}{R_2^2} + R_2\right) = 0 \qquad (3.2.33)$$

- At $\mathbb{L}_3$ we have:

$$R_2 - R_1 = 1, \quad R_1 = -x - \mu_2 \quad R_2 = -x + \mu_1, \quad \frac{\partial R_1}{\partial x} = \frac{\partial R_2}{\partial x} = -1 \qquad (3.2.34)$$

Hence substituting for R_1 in equation **(3.2.24)** we have:

$$\mu_1\left(-\frac{1}{R_1^2} + R_1\right) - \mu_2\left(-\frac{1}{(1+R_1)^2} + 1 + R_1\right) = 0 \qquad (3.2.35)$$

At the langrangian points the absolut value of Φ (in units AU^2/yr^2) is derived to be:

$$\begin{aligned}\Phi(\mathbb{L}_1) &= 77.527\\ \Phi(\mathbb{L}_2) &= 74.949\\ \Phi(\mathbb{L}_3) &= 67.110\\ \Phi(\mathbb{L}_{4,5}) &= 63.349\end{aligned}$$

In figures 3.3 and 3.4 we show the equi-potential surfaces of Φ for these values.

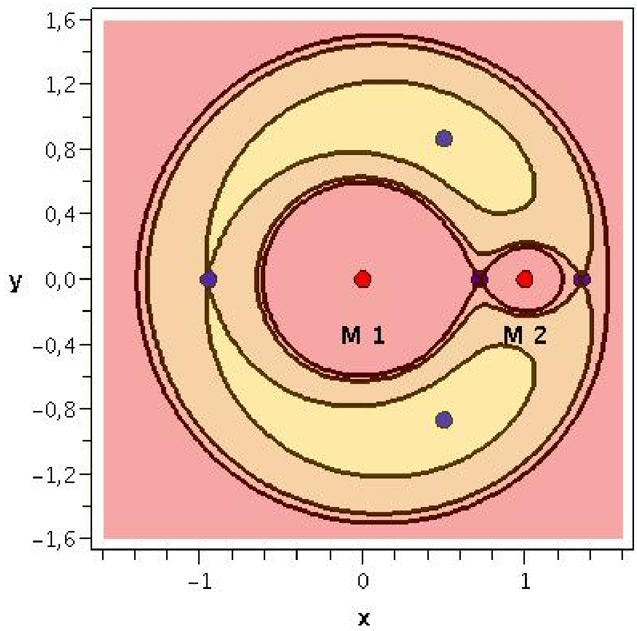

Figure 3.3: Location of the langrangian equilibrium points computed along the x-axis: $\mathbb{L}_1 = [0.717, 0]$, $\mathbb{L}_2 = [1.346, 0]$, $\mathbb{L}_3 = [-.946, 0]$, $\mathbb{L}_4 = [1/2, 1/2\sqrt{3}]$ and $\mathbb{L}_5 = [1/2, 1/2\sqrt{3}]$. The axes are scaled in units of AU. The same setting is used as in figure **(3.2)**.

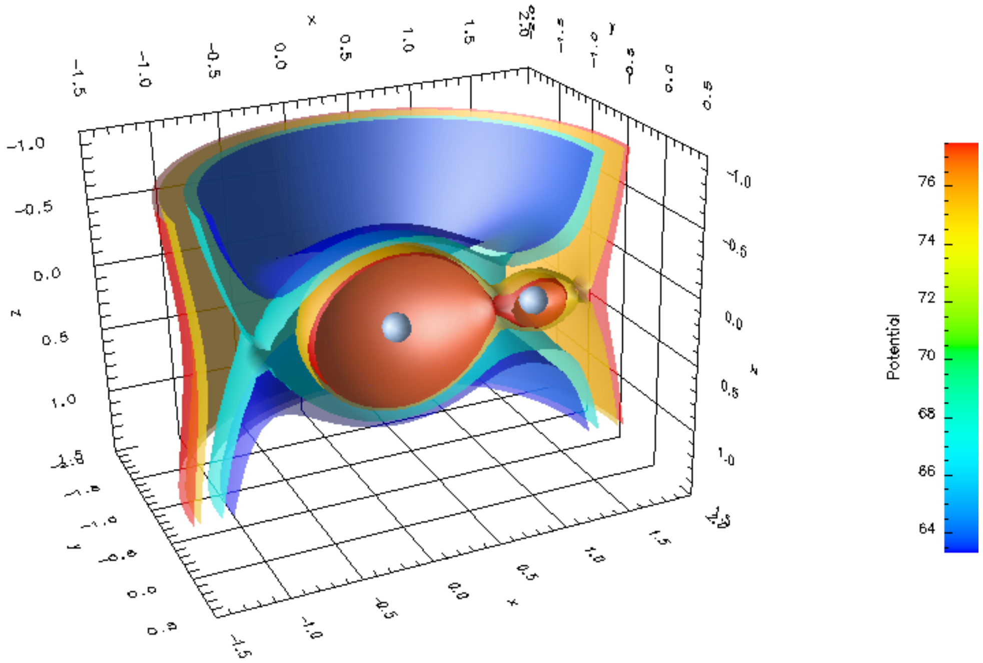
x
-1.5
-1.0
-0.5
0.0
0.5
1.0
1.5
2.0
y
z
-1.0
-0.5
0.0
0.5
1.0
1.5
Potential
76
74
72
70
68
66
64

Figure 3.4: Iso-potential sufaces at the lagrangian points $\mathbb{L}_1, ..\mathbb{L}_4$, with the values $\Phi = \{77.527, 74.949, 74.949, 67.110, 63.349\}$ $\mathsf{AU}^2/\mathsf{yr}^2$. The lenght scale in the plot is AU. The initial setting is the same as in figure **(3.2)**.

3.2.4 Motion of test particles

In preparation of our numerical simulation we present here a single particle motion within the Roche potential Φ. We consider the equation of motion **(3.1.5)** in a binary mass system with a separation $A = 5$ AU, $M_1 = 0.7$ $\mathrm{M}_\odot$ and $M_2 = 0.08$ $\mathrm{M}_\odot$, where for a single particle the gas pressure is neglected in that equation. For the calculation we choose the unit system described in section **(3.2.3)**, such that for the potential **(3.2.5)** with the origin at the donor star it follows

$$\Phi = -\frac{\mu_1}{\sqrt{x^2+y^2+z^2}} - \frac{\mu_2}{\sqrt{(x-1)^2+y^2+z^2}} - \frac{1}{2}\left\{(x-\mu_2)^2+y^2\right\} \qquad (3.2.36)$$

with $\mu_1 = 0.89$ and $\mu_2 = 0.11$ for the given mass M_1, M_2 respectively. For the following numerical test we transform the potential to inertial frame (x, y, z) at the centner of mass of the system as shown in figure 3.1, i.e.

$$\tilde{\Phi} = -\frac{\mu_1}{\sqrt{(x+\mu_2)^2+y^2+z^2}} - \frac{\mu_2}{\sqrt{(x-\mu_1)^2+y^2+z^2}} - \frac{1}{2}\left\{x^2+y^2\right\} \qquad (3.2.37)$$

We assume that the mass overflow occurs at time $t = 0$ in the vicinity of the inner Lagrange point $\mathbb{L}_1$ and is similar to the gas expansion from a cavity with a dot aperture into vacuum. This mean that the gas velocity at $\mathbb{L}_1$ is approximately equal to the sound velocity in the atmosphere of the mass-loosing star ($|\mathbf{v}| \sim c_\mathrm{T}$).

For the numerical test the direction of the velocity vector **v** at $\mathbb{L}_1$ is chosen to lay on the cone given by the tangential vectors of the Roche potential at $\mathbb{L}_1$ as seen in figure 3.5. To determine the opening angle of the cone, we have to compute the tangential vectors of the constant Roche potential surface $\tilde{\Phi}(\mathbb{L}_1)$ (blue surface in figure 3.5). This can be done by calculating the eigen vectors and eigen values of the Hessian matrix

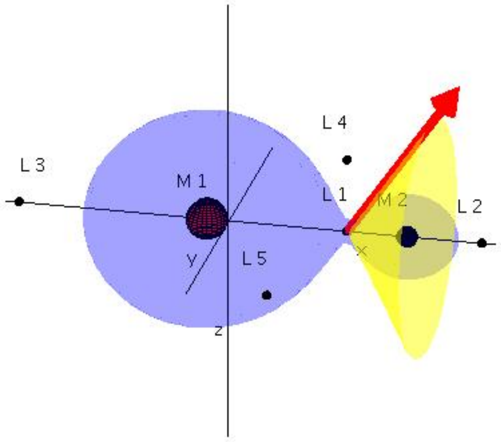

Figure 3.5: Roche Lobe surface at $\mathbb{L}_1$ (blue). The yellow cone is given by the tangential vectors (one example is seen in red). Indicated are the Lagrangian points $\mathbb{L}_1$ to $\mathbb{L}_5$.

$H_e(\tilde{\Phi})$ of the Roche potential at $\mathbb{L}_1$.

$$H_e(\tilde{\Phi}) = \begin{pmatrix} \tilde{\Phi}_{xx} & \tilde{\Phi}_{xy} & \tilde{\Phi}_{xz} \\ \tilde{\Phi}_{yx} & \tilde{\Phi}_{yy} & \tilde{\Phi}_{yz} \\ \tilde{\Phi}_{zx} & \tilde{\Phi}_{zy} & \tilde{\Phi}_{zz} \end{pmatrix}$$

where $\tilde{\Phi}_{ij}$ represents the partial derivation in direction of the i, j-coordinate. Here, we will only consider the vacuum equation, i.e. the gravitational interaction of the particle and exclude the interaction with the radiative field or gas pressure as in the full equation of motion **(2.1.8)**.

Since we are interested in determining the trajectories of the single particle as it leaves the system, we do not consider an evolving accretion disk for the binary system. Furthermore, we are interested in trajectories which rotate around the gainer star and eventually cross its own path. This is important because the presence of the cross trajectories indicates the existence of strong gas interactions (shocks) in the system which can lead to efficient molecule formation and subsequent grain condensation [Gail and Sedlmayr, 2009, Woitke et al., 1996].

In figure 3.6, we show the trajectories of a single particle simulation for different initial velocities. The red arrow indicates the infalling direction at $\mathbb{L}_1$ in the xy - plane, which numerical simulations indicate is the preferred infalling direction, as the particle enters the Roche lobe of the gainer star for the first time [Flannery, 1975, Lubow and Shu, 1975, Pringle, 1985, Boyarchuk et al., 2002].

The particle's injection velocity varies between 3.64 and 22.35 kms^{-1}. Up to a certain velocity the particle will either remain in a stable orbit in the xy - plane or it will fall in one of the stars. After this velocity (in our case, 8.35 kms^{-1}) the kinetic energy of the particle is high enough that it is capable of leaving the system.

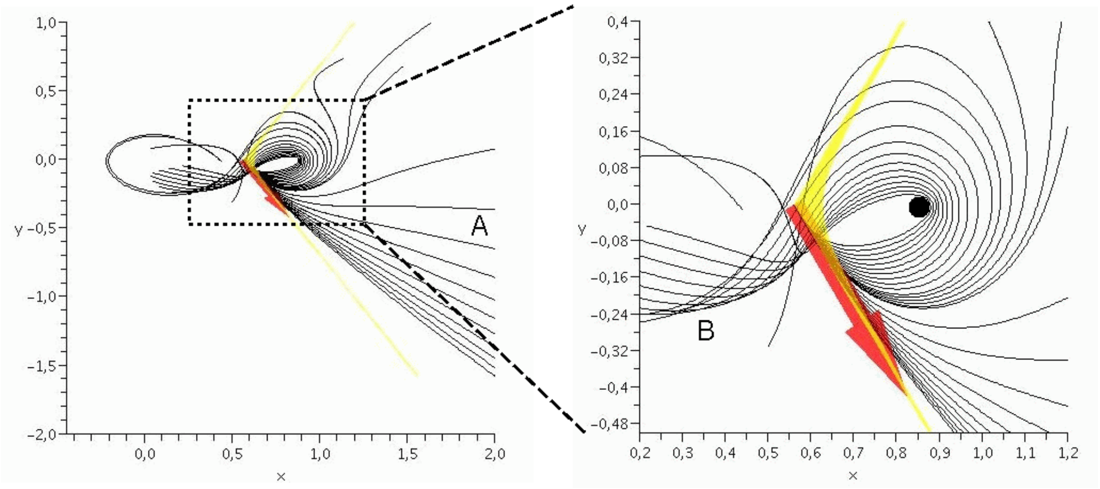

Figure 3.6: Particle trajectories in the xy-plane. The black circle indicates the gainer star. **A** - Particle trajectories which leave the system; **B** - Particle trajectories which cross itself.

For the numerical test in figure 3.7 we fixed the particle velocity (13.5 kms^{-1}) at $\mathbb{L}_1$ such that the particle is capable of leaving the system. The injection vector (red arrow at $\mathbb{L}_1$, figure 3.7) lays on the upper half of the cone ($z \geq 0$) and will be rotated for the different trajectories around the x - axis.

Due to interaction with the gainer star the particle leaves the system with a negative z component, as can be seen by the red arrow pointing down in figure 3.7. This behaviour is symmetric in relation to the xy-plane, i.e. a particle injected through the lower half of the cone ($z < 0$), will leave the system through the upper part (positive z component).

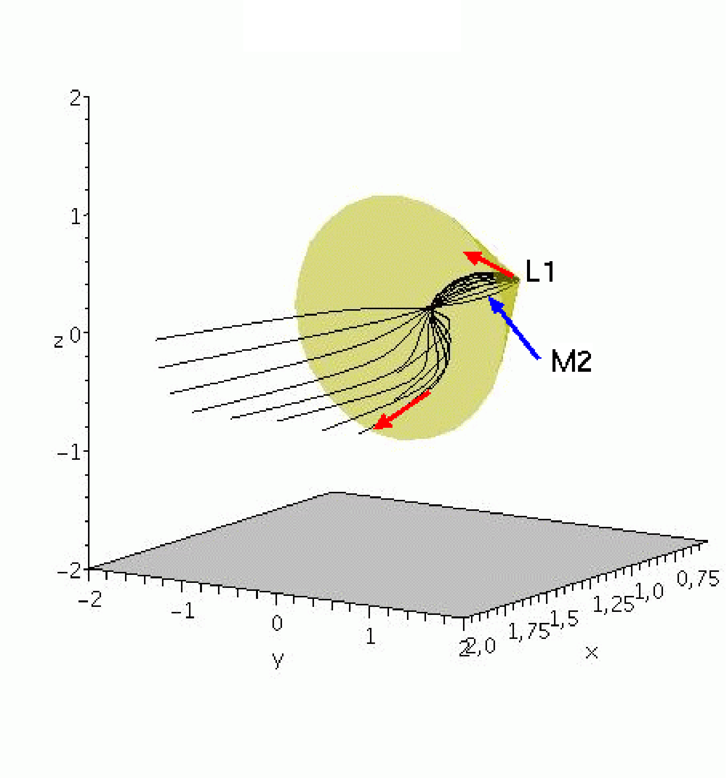

Figure 3.7: Particle trajectories in the xyz-plane. Indicated are the location of the $\mathbb{L}_1$ point and the gainer star (M_2).

Chapter 4

Hydrodynamics

4.1 Governing equation hydrodynamics

To analyse the hydrodynamical evolution in the binary star system and describe the flow of a compressed non viscous fluid, we will use the Lagrangian formulation in a one fluid approach instead of the Eulerian system of equations.

The one fluid approach is appropriate to describe a circumstellar dust shell / envelope in the case of tight collisional coupling between the components of the matter, which is considered as a single entity of both dust and gas components. As a consequence of this condition all drift effects are neglected. Furthermore, the radiative momentum is transfered to the matter by the grains through grain - gas collisions, which are described by the radiative volume force $\mathbf{f}_{\text{rad}}$ **(5.1.14)**. The matter has a total mass density ρ described by the equation of mass conservation **(2.1.3)**, a hydrodynamical velocity $\mathbf{v}$ defined by the barycentric motion, common to all material elements obeying the equation of motion **(2.1.8)** and a specific energy e given by **(2.1.33)**. In the matter reference system the system of equations is closed by a equation of state **(2.1.36)** referring to a common local temperature T.

The Euler equations can be written in the Lagrangian frame as indicated below, where to close the system the equation of motion for the Euler variable $\mathbf{r}$ is given by **(2.1.1)**:

$$\boxed{\begin{aligned} \frac{d\rho}{dt} &= -\rho\nabla\cdot\mathbf{v} \\ \frac{d\mathbf{v}}{dt} &= -\frac{1}{\rho}\nabla p + \frac{1}{\rho}\Big(\mathbf{f}_{\text{rad}} + \mathbf{f}_{\text{grav}}\Big) \\ \frac{de}{dt} &= -\frac{p}{\rho}\nabla\cdot\mathbf{v} + \frac{1}{\rho}\Big(Q_{\text{rad}} + Q_{\text{vis}}\Big) \qquad (4.1.1) \end{aligned}}$$

Where we use for the gravitational volume force $\mathbf{f}_{\text{grav}} = -\nabla\Phi$, with Φ given by **(3.2.5)**, the radiative energy transfer rate Q_{rad} is given by **(5.1.9)** and Q_{vis} represents the heating via artificial viscosity.

Additionally we have to consider, during the SPH evolution, the equations **(2.1.39)** for the time evolution of the dust moments K_i $(i = 0...3)$. The corresponding source terms are given by equations **(6.2.19)** and **(6.2.20)**.

4.2 Numerical approach - SPH method

In this section we give a short overview of the numerical realization of the Lagrangian operators **(2.1.2)** in equation **(4.1.1)** by a smoothed particle hydrodynamics (SPH) approach. The method of SPH was proposed by [Lucy, 1977] and developed in later studies by [Gingold and Monaghan, 1977, Gingold and Monaghan, 1982, Monaghan, 1988, Monaghan and Gingold, 1983].

The principal idea of this method consists in substituting a continuous medium by a set of mutually overlapping particles. The method makes use of gas dynamical equations in Lagrange variables and does not necessitate the introduction of a difference grid.

4.2.1 Basic concepts

Consider an arbitrary function $f(\mathbf{r})$. We can represent its smoothed approximation$\langle f(\mathbf{r})\rangle$ as

$$\langle f(\mathbf{r})\rangle = \int f(r')W(\mathbf{r} - \mathbf{r}', h)dr' \tag{4.2.1}$$

where the function W is called the kernel **(4.2.8)** and h is the smoothing length. The function W should meet the conditions:

$$\int W(\mathbf{r}, h)d\mathbf{r} = 1, \tag{4.2.2}$$

and

$$W(\mathbf{r}, h) \rightarrow \delta(\mathbf{r}) \qquad \text{as} \qquad h \rightarrow 0, \tag{4.2.3}$$

where δ is the Dirac delta-function. One can readily see that, as $h \rightarrow 0$, the smoothed approximation evolves towards the original function $\langle f(\mathbf{r})\rangle \rightarrow f(\mathbf{r})$. When going on to a discrete representation of the function, the integral must be replaced by the sum over all particles and $d\mathbf{r}$ must be replaced by: $\langle n(\mathbf{r}_j)\rangle^{-1} \sim m_j/\rho(\mathbf{r}_j)$. As a result we obtain:

$$\langle f(\mathbf{r})\rangle = \sum_{j=1}^{N} \frac{m_j}{\rho(\mathbf{r}_j)} f(\mathbf{r}_j)W(\mathbf{r} - \mathbf{r}_j, h) \tag{4.2.4}$$

where N is the number of particles. The smoothed approximation for density ρ has then the form:

$$\langle \rho(\mathbf{r})\rangle = \sum_{j=1}^{N} m_j W(\mathbf{r} - \mathbf{r}_j, h) \tag{4.2.5}$$

The form of this expression explains the origin of the name of the SPH method since the mass of each particle is smeared out over the support of the kernel function. In the SPH approach the gradient of the function is defined as:

$$\begin{aligned}\langle \nabla f(\mathbf{r})\rangle &= \int \nabla f(\mathbf{r}')W(\mathbf{r}-\mathbf{r}',h)d\mathbf{r}' \\ &= \int \nabla\Big(f(\mathbf{r}')W(\mathbf{r}-\mathbf{r}',h)\Big)d\mathbf{r} - \int f(\mathbf{r}')\nabla W(\mathbf{r}-\mathbf{r}',h)d\mathbf{r} \\ &= \int_\Sigma f(\mathbf{r}')W(\mathbf{r}-\mathbf{r}',h)\mathbf{n}d\mathbf{s} + \int f(\mathbf{r}')\nabla W(\mathbf{r}-\mathbf{r}',h)d\mathbf{r}' \end{aligned} \tag{4.2.6}$$

Since the surface integral is taken over a surface as distant as one wishes, where the values of function W tend to zero, the integral is equal to zero and the expression for the gradient of the function can be transformed to the following form:

$$\langle \nabla f(\mathbf{r})\rangle = \sum_{j=1}^{N} \frac{m_j}{\rho(\mathbf{r}_j)} f(\mathbf{r}_j)\nabla W(\mathbf{r}-\mathbf{r}_j,h) \tag{4.2.7}$$

Note that the differential derivative is not replaced by a finite-difference derivative since in the SPH method all quantities are represented as continuous (and even smooth) distributions, not as sets of discrete values used in finite-difference schemes. The kernel form most currently in use is the spline-kernel with compact support proposed by [Monaghan and Lattanzio, 1985]:

$$W(\mathbf{r}-\mathbf{r}',h) = \frac{1}{\pi h^3}\begin{cases} 1 - 3/2\cdot y^2 + 3/4\cdot y^3, & \text{if } 0\le y\le 1 \\ 1/4\cdot(2-y)^3, & \text{if } 1\le y\le 2 \\ 0, & \text{otherwise}\end{cases} \tag{4.2.8}$$

where

$$r = |\mathbf{r}-\mathbf{r}'| \qquad y = \frac{r}{h} \tag{4.2.9}$$

4.2.2 Approximation of governing equations

4.2.2.1 Continuity equation

In the SPH formalism the continuity equation **(2.1.3)** is implied automatically. Indeed, it follows from equation **(4.2.5)** (from here on for the sake of simplicity we omit the angle brackets designating averaging) that:

$$\frac{d}{dt}\rho_i = \sum_{j=1}^{N} m_j \nabla_i W(\mathbf{r}_{ij},h)\left(\frac{d}{dt}\mathbf{r}_i - \frac{d}{dt}\mathbf{r}_j\right) = \sum_{j=1}^{N} m_j \mathbf{v}_{ij}\nabla_i W(\mathbf{r}_{ij},h) \tag{4.2.10}$$

where we introduce the designations $\mathbf{v}_{ij} = \mathbf{v}_i - \mathbf{v}_j, \mathbf{r}_{ij} = \mathbf{r}_i - \mathbf{r}_j$ and i, j indicate the i'th and j'th SPH - particle, respectively.

4.2.2.2 Momentum equation

By applying the basic concepts of the SPH method it is easy to construct the expression for 'grad p', and consequently, to get the approximation of the momentum equation:

$$\begin{aligned}(\rho\nabla p)_i &= (\nabla\rho p)_i - (p\nabla\rho)_i \\ &= \sum_{j=1}^{N} m_j(p_j - p_i)\nabla_i W(\mathbf{r}_{ij}, h).\end{aligned} \tag{4.2.11}$$

An advantage of this form is that the pressure gradient disappears if and only if the pressure is constant. However, this expression suffers from a serious drawback: the pressure of the i'th on j'th SPH - particle is not equal to the pressure particle j on particle i (this is connected with the antisymmetry form of the expression $p_j - p_i$). The result is that the laws of conservation of momentum and angular momentum are violated. Therefore a specific approach should be used for estimating the pressure gradient, namely:

$$\left(\frac{\nabla p}{\rho}\right)_i = \left(\nabla\frac{p}{\rho}\right)_i + \left(\frac{p}{\rho^2}\nabla\rho\right)_i = \sum_{j=1}^{N} m_j\left(\frac{p_j}{\rho_j^2} + \frac{p_i}{\rho_i^2}\right)\nabla W(\mathbf{r}_{ij}, h)$$

The equation for the momentum can be written in this case as:

$$\frac{d}{dt}\mathbf{v}_i = -\sum_{j=1}^{N} \underbrace{m_j\left(\frac{p_j}{\rho_j^2} + \frac{p_i}{\rho_i^2}\right)}_{f(\rho_i,\rho_j,p_i,p_j)}\nabla W(\mathbf{r}_{ij}, h) \tag{4.2.12}$$

The function $f(\rho_i, \rho_j, p_i, p_j)$ is symmetric in relation to the particle indices i and j. The pressure of one particle on another can be expressed in this case as:

$$\mathbf{F}_{ij} = \left(m_i\frac{d}{dt}\mathbf{v}_i\right)_j = m_i m_j\left(\frac{p_j}{\rho_j^2} + \frac{p_i}{\rho_i^2}\right)\mathbf{r}_{ij}W(r, h)'/r$$

meaning that in this case the pressure gradient produces a centrally symmetric force between a pair of particles, hence both the momentum and orbital momentum are preserved. Because the symmetry of the function f and the antisymmetry of the $\nabla_i W = -\nabla_j W$ the third Newton Axiom (*action = reaction*) is obtained. This means that $\mathbf{F}_{ij} = -\mathbf{F}_{ji}$, by this the momentum equation is always fulfilled since the time derivative of the total momentum is vanishing.

$$0 = \sum_i m_i\frac{d\mathbf{v}_i}{dt} = \sum_j\sum_i \mathbf{F}_{ij} = \frac{1}{2}\sum_{i,j}(\mathbf{F}_{ij} + \mathbf{F}_{ji}) \tag{4.2.13}$$

For a kernel in the form 4.2.8 the expression for $W'(r, h)/r$ can be written as:

$$W'(r, h)r^{-1} = \frac{1}{\pi h^4}\begin{cases}(-3 + 9/4\cdot y)\cdot h^{-1}, & \text{if } 0 \le y \le 1\\ -3/4\cdot(2-y)^2\cdot r^{-1}, & \text{if } 1 \le y \le 2\\ 0, & \text{otherwise}\end{cases}$$

Modified expressions for the gradient of a kernel are also known (see [Thacker et al., 1998], [Thomas and Couchman, 1992], [Steinmetz, 1996] and [Schüssler and Schmitt, 1981]).

4.2.2.3 Energy equation

From the derivation

$$-\frac{p}{\rho}\nabla\cdot\mathbf{v} = -\frac{p}{\rho^2}\nabla\Big(\rho\mathbf{v}\Big) + \frac{p}{\rho^2}\mathbf{v}\cdot\nabla\rho \tag{4.2.14}$$

In the SPH formalism the energy equation is written in the form:

$$\frac{d}{dt}e_i = -\sum_{j=1}^{N} m_j\frac{p_i}{\rho_i^2}\,\mathbf{v}_{ij}\nabla W(\mathbf{r}_{ij},h) \tag{4.2.15}$$

Or from the relation

$$-\frac{p}{\rho}\nabla\cdot\mathbf{v} = -\nabla\left(\frac{p}{\rho}\mathbf{v}\right) + \mathbf{v}\cdot\nabla\left(\frac{p}{\rho}\right) \tag{4.2.16}$$

its SPH form can be written:

$$\frac{d}{dt}e_i = -\sum_{j=1}^{N} m_j\frac{p_j}{\rho_j^2}\,\mathbf{v}_{ij}\nabla W(\mathbf{r}_{ij},h) \tag{4.2.17}$$

The implementations of the SPH method involve, as a rule, the use of the half-sum of expressions **(4.2.15)** and **(4.2.17)** which makes the energy equation to take the form:

$$\frac{d}{dt}e_i = -\frac{1}{2}\sum_{j=1}^{N} m_j\left(\frac{p_j}{\rho_j^2}+\frac{p_i}{\rho_i^2}\right)\mathbf{v}_{ij}\nabla W(\mathbf{r}_{ij},h) \tag{4.2.18}$$

Note that this equation has the same symmetrical factor as the equation for momentum **(4.2.12)**.

4.2.2.4 Treatment of viscosity

The equations derived above were assumed applicable to the smooth flow of a nonviscous gas, that is to the case when the transition of kinetic energy to thermal energy is reversible. Considering the SPH approach, in some cases (for instance, when the Mach number is large) the thermal pressure $\sim \rho c^2$ might be found insufficient to prevent mutual penetration of particles and the breaks of flow fail to be reproduced. The way to cope with this difficulty is to prevent the penetration of particles at the breaks without changing the solution in the smooth flow regions. This can be achieved by artificially increasing the pressure only in the vicinity of the break. One of the most effective ways of increasing pressure is to introduce artificial viscosity $Q_{\text{vis}} \sim \Pi_{ij}$. We define this term in agreement with the classical Neumann-Richtmyer viscosity approach [Neumann and Richtmyer, 1950, Bowen, 1988b].

Artificial viscosity is introduced in order to simulate gas dynamical phenomena (for which one considers that the scale is of the order of the free length of 'liquid particles'), in the same way that for real gases molecular viscosity is used to prevent the penetration of particles in the case where the scale is comparable with the free path length of atoms or molecules. For shock waves, in which the velocity changes significantly, artificial viscosity is effective. The form of the artificial viscosity in the SPH method has been proposed by several authors, e.g. [Monaghan and Gingold, 1983, Loewenstein and Mathews, 1986, Lattanzio et al., 1986, Hernquist and Katz, 1989, Balsara, 1995, Steinmetz, 1996]. The most commonly used form is given by [Monaghan, 1992]:

$$\Pi_{ij} = \begin{cases} \frac{-\alpha c \mu_{ij} + \beta \mu_{ij}^2}{\rho_{ij}}, & \text{if } \mathbf{v}_{ij} \cdot \mathbf{r}_{ij} \le 0 \\ 0, & \text{otherwise} \end{cases}$$

$$\mu_{ij} = \frac{h\,\mathbf{v}_{ij} \cdot \mathbf{r}_{ij}}{r_{ij}^2 + \eta^2 h^2} \quad , \rho_{ij} = \frac{\rho_i + \rho_j}{2}.$$

Here α, β, and η are dimensionless constants, usually adopted as to $\alpha = 1$, $\beta = 2$, $\eta = 0.01$. It is seen that the artificial viscosity in the SPH method includes both a term, linear with respect to velocity, describing the shear and volume viscosities, and a term representing quadratic viscosity which is similar to von Neumann-Richtmyer viscosity. With account of the artificial viscosity, the equations for momentum 4.2.12 and energy 4.2.18 are written as follows:

$$\frac{d}{dt}\mathbf{v}_i = -\sum_{j=1}^{N} m_j \left(\frac{p_j}{\rho_j^2} + \frac{p_i}{\rho_i^2} + \Pi_{ij} \right) \nabla W(r_{ij}, h) \tag{4.2.19}$$

$$\frac{d}{dt}e_i = -1/2 \sum_{j=1}^{N} m_j \left(\frac{p_j}{\rho_j^2} + \frac{p_i}{\rho_i^2} + \Pi_{ij} \right) \mathbf{v}_{ij} \nabla W(r_{ij}, h)$$

4.2.2.5 Treatment of self-gravitation

With the SPH method, self-gravitation, i.e. the mutual attraction of particles, can be taken into account rather easily. For this purpose a term $\mathbf{F}^{\text{grav}}$ is introduced into the equation for momentum for describing the gravitational attraction of each particle to all other particles:

$$\frac{d}{dt}\mathbf{v}_i = \mathbf{F}^{\text{hydro}} + \mathbf{F}^{\text{grav}}$$

where $\mathbf{F}^{\text{hydro}}$ is defined by formulas **(4.2.12)** or **(4.2.19)**. Then the specific force of attraction of particle i to particle j is expressed as:

$$\mathbf{F}_{ij}^{\text{grav}} = -\frac{G m_j}{r_{ij}^3} \mathbf{r}_{ij}$$

where G, as usual, is the gravitational constant and $r_{ij} = |\mathbf{r}_{ij}|$.

Note that the expression for the specific force has a peculiarity that manifests itself when the positions of particles i and j coincide (or are very close). It was shown that the way to bypass this peculiarity is to use a 'softened' gravity attraction take over $-\frac{m_i m_j}{r_{ij}^2 + \varepsilon^2}$ instead of the standard expression $\sim -\frac{m_i m_j}{r_{ij}^2}$ [Hernquist and Katz, 1989]. Another approach was also proposed by [Bate, 1995] with the specific force of gravitational attraction determined as:

$$\mathbf{F}_{ij}^{\text{grav}} = -\frac{G m_{ij}}{r_{ij}^3} \mathbf{r}_{ij}$$

where $m_{ij} = M^j(r_{ij})$ has the form:

$$M^j(r_{ij}) = 4\pi \int_0^{r_{ij}} r^2\rho(r)\ dr = m_j 4\pi \int_0^{r_{ij}} r^2 W(r,h)\ dr.$$

Considering a specific kernel in the form 4.2.8, the expression for $M^j(r_{ij})/r_{ij}^3$ is written as:

$$M^j(r)r^{-3} = m_j \begin{cases} (4/3 - 6/5\cdot y^2 + 1/2\cdot y^3)\,h^{-3}, & \text{if } 0 \le y \le 1 \\ (1/15 - 8/3\cdot y^3 + 3\cdot y^4 - 6/5\cdot y^5 + 1/6\cdot y^6)\cdot r^{-3}, & \text{if } 1 \le y \le 2 \\ r^{-3}, & \text{if otherwise} \end{cases}$$

4.2.2.6 Variable smoothing length

The term smoothing length was previously used for designating the size of the kernel support, i.e. the domain wherein the function W is not equal to zero, see among others [Miyama et al., 1984], [Evrard, 1988], [Benz, 1990], [Steinmetz and Müller, 1993], [Nelson and Papaloizou, 1993], [Nelson and Papaloizou, 1994]. The physical meaning of this quantity is the size of a particle in the SPH method [Evrard, 1988]. Initially, the SPH method operated with a smoothing length h common for all particles:

$$h^3 = \zeta\cdot\langle\frac{m}{\rho}\rangle$$

where ζ is a numerical factor ~ 1, and $\langle\rangle$ as usual designates averaging. The length h defines the spatial resolution of the scheme in terms of the number of neighbour particles. This is why, when dealing with problems requiring a high (and/or variable) resolution, other variants of the SPH method were advanced, with the smoothing length h varying in space and/or in time [Hernquist and Katz, 1989]. Let us introduce the equations for momentum and energy for the SPH method in the case when the smoothing length varies from particle to particle:

$$\frac{d}{dt}\mathbf{v}_i = -\sum_{j=1}^{N} m_j\left(\frac{p_j}{\rho_j^2} + \frac{p_i}{\rho_i^2} + \Pi_{ij}\right)\nabla W(r_{ij},h_{ij}) - \frac{Gm_{ij}}{r_{ij}^3}\mathbf{r}_{ij},$$

$$\frac{d}{dt}e_i = -1/2\sum_{j=1}^{N} m_j\left(\frac{p_j}{\rho_j^2} + \frac{p_i}{\rho_i^2} + \Pi_{ij}\right)\mathbf{v}_{ij}\nabla W(r_{ij},h_{ij}),$$

$$h_{ij} = 1/2(h_i + h_j)$$

Note that these equations can be written in other forms as well,[Monaghan, 1992]. For instance, the kernel W can be made symmetrical as $1/2\cdot(W(r_{ij},h_i) + W(r_{ij},h_j))$ ([Hernquist and Katz, 1989, Rasio and Lombardi Jr., 1998]). The smoothing length h can be expressed in terms of the initial density distribution ρ_0 as follows:

$$h_i^3 = \zeta\cdot\frac{m_i}{\rho_i^0}$$

In order to obtain a more accurate representation of the solution the smoothing length should be made variable also in time so that the number of neighbour particles remains the same. In this case:

$$h_i^3 = \zeta\cdot\frac{m_i}{\rho_i}$$

4.2.3 Numerical test: shock tube

To test our SPH - code we use a standard hydrodynamical test, i.e. the one dimensional shock tube problem. This benchmark is a common test for the accuracy of computational fluid codes [Toro, 1997]. The experiment consists of a tube divided by a diaphragm in which a gas at low (left side) and high pressure (right side) are separated.

At time $t = 0$, the diaphragm will be broken and the shock wave will travel down the low pressure section of the tube, such that the temperature and pressure of the gas in direction of the shock wave increase. At the same time a rarefraction wave travels back to the left side.

The numerical results can be compared to the analytic solution for this problem. A detailed description of this problem as well as a derivation of the analytic solution can be found in **Appendix C**.

In figure 4.1 we see the time evolution of the density profile, for the one dimensional Riemann problem with the following initial data for the left (l) and right (r) sight.

$$\begin{pmatrix} \rho_l \\ p_l \\ v_l \end{pmatrix} = \begin{pmatrix} 1 \\ 1 \\ 0. \end{pmatrix}, \qquad \begin{pmatrix} \rho_r \\ p_r \\ v_r \end{pmatrix} = \begin{pmatrix} 1/8 \\ 1/8 \\ 0. \end{pmatrix}$$

The time sequence of the density profile is indicated by the different colors in figure 4.1. As can be seen on the left hand side a rarefraction wave travels back into the high pressure region, and on the right hand side the shock wave travels down the low pressure section. For our solution we find that our numerical SPH solution converges to the analytic solution, within an error of 1%.

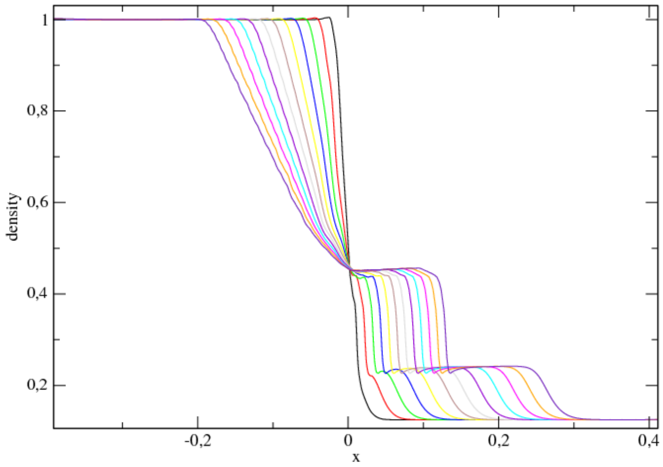

Figure 4.1: Time evolution of the density in the shock tube problem.

Chapter 5

Radiative transfer

In the previous chapters we have focused on the aspect of matter in our problem. The radiative field was considered as an external quantity, i.e. a suitable defined source term, which influences the thermodynamical and hydrodynamical state due to momentum and energy coupling between matter and radiation.

For a correct calculation, we have to consider that these quantities depend explicitly on the local actual state of the present radiation field, such that we require simultaneous consideration of the radiative transfer problem as well as the hydrodynamical and thermodynamical quantities.

5.1 Fundamental definitions

We consider the radiation field to be carried by massless particles called photons. Each photon has an associated frequency, ν, such that the photon energy, E_{ph}, is equal to $h\nu$ where h is the Planck constant (see table **(A)**). It is known that a massless particle has a momentum E_{ph}/c where c is the vacuum speed of light, and hence the momentum of a photon is:

$$\mathbf{p}_{\text{ph}} = \frac{h\nu}{c}\mathbf{k} \tag{5.1.1}$$

where $\mathbf{k}$ is the unit vector pointing into the solid angle d^2k around $\mathbf{k}$. When not colliding with matter, a photon is supposed to travel in a straight line with speed c and with no change in frequency $\nu \in [\nu, \nu + d\nu]$. To specify the position of the photon in phase space $(\mathbf{r}, \nu, \mathbf{k})$, at a given time t, six variables are needed. These are three position variables, $\mathbf{r}$, and three momentum variables, $\mathbf{p}_{\text{ph}}$.

The fundamental quantities, needed for the treatment of the radiation field are introduced bellow.

Photon density $n_{\text{ph},\nu}$: The spectral photon density, $n_{\text{ph},\nu}(t, \mathbf{r}, \mathbf{k})\ dV\ d^2k\ d\nu$, is the number of photons with frequency ν, at time t, around $\mathbf{r}$, in a differential volume element dV and frequency interval $d\nu$, and travelling in a direction $\mathbf{k}$ in a solid angle element d^2k. According to the photon distribution function, f, the dimension of $n_{\text{ph},\nu}$ is [number of photons/$\text{m}^2 \cdot \text{sr} \cdot \text{Hz}$]

Photon flux $\mathbf{j}_{\text{ph},\nu}$: The spectral photon flux, $\mathbf{j}_{\text{ph},\nu}(t,\mathbf{r},\mathbf{k})$, can be derived by multiplication of $n_{\text{ph},\nu}$ with the photon speed c in direction $\mathbf{k}$,

$$\mathbf{j}_{\text{ph},\nu} = n_{\text{ph},\nu} c\mathbf{k} \tag{5.1.2}$$

Energy flux $\mathbf{j}_{\text{rad},\nu}$: The spectral energy flux of radiation, $\mathbf{j}_{\text{rad},\nu}(t,\mathbf{r},\mathbf{k})$, can be determined by the energy of the photon E_{ph} and $\mathbf{j}_{\text{ph},\nu}$, i.e.:

$$\begin{aligned} \mathbf{j}_{\text{rad},\nu} &= c\mathbf{j}_{\text{ph},\nu} h\nu\mathbf{k} \\ &= I_\nu \mathbf{k} \end{aligned} \tag{5.1.3}$$

where for the second line we have used the expression of the spectral specific intensity I_ν

Specific intensity I_ν: The spectral specific intensity $I_\nu = I_\nu(t,\mathbf{r},\mathbf{k})$, is commonly used in radiative transfer in place of the distribution function f and has a dimension [radiation energy/m^2 · s · sr · Hz]. I_ν is defined per solid angle d^2k, such that it does not depend on the distance of a considered object and it describes the propagation of radiation energy within the interval $(\nu, \nu + d\nu)$ through a unit surface area dA oriented normal to $\mathbf{k}$ at a certain time interval dt.

$$I_\nu = \frac{dE_\nu}{\cos\theta \, dA \, dt \, d\nu \, d^2k} \tag{5.1.4}$$

Momentum flux $\mathbf{j}_{\text{m},\nu}$: If we use, instead of E_{ph}, the amount of photon momentum $\mathbf{p}_{\text{ph}}$ in equation **(5.1.3)** as a factor, we can derive the spectral specific momentum flux of radiation:

$$\mathbf{j}_{\text{m},\nu} = \frac{1}{c} I_\nu \mathbf{k} \tag{5.1.5}$$

Energy density: The spectral specific energy density of radiation (per volume), $\bar{e}_{\text{rad},\nu}$, is given by the relation:

$$\bar{e}_{\text{rad},\nu} = \frac{1}{c} I_\nu \tag{5.1.6}$$

and by solid angle integration, the related spectral energy density $e_{\text{rad},\nu}$ is derived:

$$\mathbf{e}_{\text{rad},\nu} = \frac{1}{c} \int_\Omega I_\nu d^2k \tag{5.1.7}$$

From the definition of the spectral mean intensity $J_\nu(t,\mathbf{r})$, we can express $e_{\text{rad},\nu}$ as:

$$J_\nu = \frac{1}{4\pi} \int_\Omega I_\nu d^2k = \frac{c}{4\pi} e_{\text{rad},\nu} \tag{5.1.8}$$

Radiative energy transfer rate: This quantity represents both the gain rate due to the transfer of radiation energy to the internal energy of matter (by photo excitation and photo ionisation), and the loss rate due to the transfer of internal energy of gas and dust to the radiation field (by photo emission). It is given by:

$$Q_{\mathsf{rad}} = 4\pi \int_0^\infty [\hat{\kappa}_\nu J_\nu - \eta_\nu^{\mathsf{sp}}] d\nu \tag{5.1.9}$$

In the case of radiative equilibrium $Q_{\mathsf{rad}} = 0$.

Radiation flux: If we integrate the directional energy fluxes $\mathbf{j}_{\mathsf{rad},\nu}$ over all directions we get the spectral radiation flux, $\mathbf{F}_\nu$, with a dimension of [energy/m$^2 \cdot$ s $\cdot$ Hz]., i.e.:

$$\mathbf{F}_\nu = \int_\Omega d^2k \, \mathbf{j}_{\mathsf{rad},\nu} = \int_\Omega d^2k \, I_\nu \mathbf{k} = \int_0^{2\pi} d\phi \int_0^\pi \sin(\theta) d\theta \, I_\nu \, \mathbf{k} \tag{5.1.10}$$

If the specific intensity is independent of both $\mathbf{r}$ and $\mathbf{k}$, the radiation field is said to be homogeneous and isotropic.

One of the most relevant example of a homogeneous, isotropic radiation field is that in which radiation and matter are in complete thermodynamic equilibrium at a given temperature T. In this case the specific intensity of radiation I_ν is given by the Planck function, B_ν:

$$I_\nu = B_\nu = \frac{2h}{c^2} \frac{\nu^3}{\left(e^{(h\nu/k_{\mathsf{B}}T)} - 1\right)} \tag{5.1.11}$$

where k_{B} is the Boltzmann constant (see table **(A)**) and it yields $\mathbf{F}_\nu = \mathbf{0}$. This result is not surprising, since in complete thermodynamic equilibrium there is no net flow of radiative energy in any direction.

Radiation pressure tensor $P_{ij,\nu}$**:** The spectral pressure tensor due to radiation is defined as the rate of momentum flow across a surface, as usual in the kinetic theory of (photon) gases. It results from the second velocity moment of the particle distribution function as symmetrical second rank tensor. By a straight forward application to the radiation field (photon gas) we can write $P_{ij,\nu}$ as a second moment of the specific intensity I_ν with regard to the directional vector **k**:

$$P_{ij,\nu} = \frac{1}{c} \int_\Omega I_\nu \mathbf{k}_i \mathbf{k}_j d^2k \tag{5.1.12}$$

The total radiation pressure is obtained from the integration of the spectral radiation pressure tensor over the frequency, i.e.:

$$P_{ij} = \frac{1}{c} \int_0^\infty P_{ij,\nu} \, d\nu \tag{5.1.13}$$

Radiation force density: The radiation force density describes the force exerted on matter due to transfer of momentum by photon absorption, scattering and emission

$$\mathbf{f}_{\mathsf{rad}} = \frac{1}{c}\int_0^\infty \xi_\nu \mathbf{F}_\nu d\nu \tag{5.1.14}$$

where ξ_ν is the momentum transfer coefficient. In the case where the asymmetry parameter Ω_ν vanishes, ξ_ν can be replaced by the extinction coefficient χ_ν. Ω_ν is given by:

$$\Omega_\nu k'_\mu = \int_\Omega d^2k k_\mu \omega_\nu(\mathbf{k}' \rightarrow \mathbf{k}) \tag{5.1.15}$$

5.2 Equation of radiative transfer

When radiation is propagating through matter, the time and space evolution in phase space $(\mathbf{r}, \nu, \mathbf{k})$ of the specific intensity (I_ν) can be described by a kind of Boltzmann - equation [Mihalas, 1970, Peraiah, 2002], i.e. a transport equation for the specific intensity I_ν:

$$\underbrace{\frac{\partial I_\nu}{\partial t} + ck_i\left(\frac{\partial I_\nu}{\partial x_i}\right)}_{\text{change by free flow of photon}} = \underbrace{\left(\frac{\delta I_\nu}{\delta t}\right)_{\mathsf{COLL}}}_{\text{change by photon}-\text{matter interaction}} \tag{5.2.1}$$

where $(\frac{\delta I_\nu}{\delta t})_{\mathsf{COLL}}$ indicates the Boltzmannian collision operator of the interacting material components. With suitably defined transport coefficients $\chi_\nu, \kappa_\nu, \eta_\nu$, and $q_{\mathsf{ch,rad},\nu}$ for the elementary radiation-matter interactions we have:

$$\left(\frac{\delta I_\nu}{\delta t}\right)_{\mathsf{COLL}} = c\left\{-\chi_\nu I_\nu + \eta_\nu + q_{\mathsf{ch,rad},\nu} + \int_\Omega s_\nu(\mathbf{k} \rightarrow \mathbf{k}')I_\nu(\mathbf{k}')d^2k'\right\} \tag{5.2.2}$$

Here we have set for the transport coefficients the bellow indicated coefficients. A detailed description of the use of these coefficients in our calculations is given in section 5.2.1.

Absorption κ_ν: denotes the isotropic monochromatic absorption coefficient at frequency ν of the matter, whereas the net absorption coefficient $\hat{\kappa}_\nu$ is defined by:

$$\hat{\kappa}_\nu = \kappa_\nu - \eta_\nu^{\mathsf{ind}} \tag{5.2.3}$$

Scattering $s_\nu(\mathbf{k} \rightarrow \mathbf{k}')$: denotes the angle average scattering coefficient, which accounts for both absorption and elastic scattering of photons. The angular dependence of photon scattering due to gas particles and dust grains can be expressed by a suitable normated scattering function $\omega_\nu(\mathbf{k} \rightarrow \mathbf{k}')$, i.e.:

$$\int_\Omega \omega_\nu(\mathbf{k} \rightarrow \mathbf{k}')d^2k = 1 \tag{5.2.4}$$

Herewith we can take into account the angular dependence of scattering for the individual matter constituents by defining differential scattering coefficients:

$$s_\nu(\mathsf{k} \rightarrow \mathsf{k}') = \bar{s}_\nu \, \omega_\nu(\mathsf{k} \rightarrow \mathsf{k}') \tag{5.2.5}$$

with $\bar{s}$ being the total scattering coefficient. In the case of isotropic scattering for gas (index g) and dust grains (index d) we have:

$$\omega_{g,\nu} = \omega^{\alpha}_{d,\nu} = \frac{1}{4\pi} \tag{5.2.6}$$

where α is the size parameter of the grains.

Extinction χ_ν: denotes the loss of radiation along its trajectory of propagation,

$$\chi_\nu = \kappa_\nu + \bar{s}_\nu \tag{5.2.7}$$

We define the net extinction coefficient $\hat{\chi}_\nu$ by:

$$\hat{\chi}_\nu = \chi_\nu - \eta^{\mathsf{ind}}_\nu \tag{5.2.8}$$

Emission η_ν: denotes the spectral emission coefficients. Caused by interaction with the local radiation field it consists of the spontaneous emission, η^{sp}_ν, (independent of radiation field) and the induced emission[1], η^{ind}_ν:

$$\eta_\nu = \eta^{\mathsf{sp}}_\nu + \eta^{\mathsf{ind}}_\nu I_\nu \tag{5.2.9}$$

Chemical photon production $q_{\mathsf{ch,rad},\nu}$: denotes the spectral photon emission probability by chemical reaction and will be formally contracted with the spontaneous emission coefficient.

The total transport coefficients in equation **(5.2.2)** are given formally by the sum of all contributing gaseous and dust species, where for all frequencies the induced emission of dust grains can be neglected, since macroscopic grains usually possess a large optical depth for all dust components. Hence, η^{ind} is only derived from the induced gaseous emission. If we insert these expressions into equation **(5.2.1)** it yields for the radiative transfer equation in a gas-dust system:

$$\boxed{\frac{\partial I_\nu(\mathsf{k})}{c\,\partial t} + k_i \frac{\partial I_\nu(\mathsf{k})}{\partial x_i} = -\hat{\chi}_\nu I_\nu(\mathsf{k}) + \eta^{\mathsf{sp}}_\nu + \bar{s}_\nu \int_\Omega \omega(\mathsf{k} \rightarrow \mathsf{k}') d^2k' I_\nu(\mathsf{k}') \qquad (5.2.10)}$$

For further consideration we compare the characteristic time scale for a change of the physical quantities of a system contained at the r.h.s. of equation **(5.2.10)**, with the characteristic time controlling the corresponding change of the specific intensity (I_ν), in order to judge in which situation the partial time derivative at the l.h.s. of equation **(5.2.10)** can be neglected, such that we can treat the radiation transfer problem as stationary. If $t_{\text{ph}} = s/c$ is the typical time required for the radiation to travel a distance s, and t_{tc} the characteristic time required for a significant change of the transport coefficients due to hydrodynamical, thermodynamical and chemical evolution of the considered system, the following condition has to be fulfilled, in order to neglect all effects due to finite propagation velocity of radiation.:

---

[1] Usually macroscopic grain possess large optical depth for all dust components therefore induced emission in all frequencies can be neglected,$\eta^{\mathsf{ind}}_\nu = 0$ [Gail and Sedlmayr, 2009].

$$t_{\text{ph}} \ll t_{\text{tc}} \tag{5.2.11}$$

Thus, if we apply this condition to a Mira (the donor star) with a typical pulsation period of 1yr and a spatial extension of some stellar radii 10^{13}cm, it results that the travel time of light is small compared to the time displayed for a significant change of its macroscopic properties. For this reason we consider the specific intensity, I_ν, to be only a function of $\mathbf{r}, \nu$ and $\mathbf{k}$, with the effect that the corresponding time derivation can be neglected and we can furthermore consider the equation **(5.2.12)** of the stationary radiation transport problem.

$$\boxed{k_i \frac{\partial I_\nu(\mathbf{k})}{\partial x_i} = -\hat{\chi}_\nu I_\nu(\mathbf{k}) + \eta_\nu^{\text{sp}} + \bar{s}_\nu \int_\Omega \omega(\mathbf{k} \rightarrow \mathbf{k}') d^2k' I_\nu(\mathbf{k}') \qquad (5.2.12)}$$

An implicit dependence on time will be considered via a variation of the transport coefficients, which due to hydrodynamics vary with time t.

5.2.1 Transport coefficients

In the previous section we defined the transport coefficients, absorption, scattering, extinction (which is the sum of the previous two) and emission. In this section we discuss how the coefficients are treated when applied to the gas (index g) and dust particles (index d) in our problem, in which we consider the one-fluid approach and one kind of dust.

Gas: For the case of gas we consider that the light scattering by the molecules is negligible and we do not explicitly consider the frequency dependency of the gas opacity. In this case the gas opacity is represented only by its Rosseland mean absorption coefficient, such that:

$$\chi_g^{-1} = \int_0^\infty d\nu \frac{1}{\chi_g} \frac{\partial B_\nu}{\partial T} / \int_0^\infty d\nu \frac{\partial B_\nu}{\partial T} \tag{5.2.13}$$

Dust: For the case of dust the size of the particles has to be considered, since the absorption and scattering properties of grains strongly depend on the ratio of the grain size to the wavelength of the interacting wave. This is important because these properties strongly influence the dynamics of the common envelope, namely in relation to the momentum transfer coefficient ξ between the radiation and the dust grains.

The here considered stars and circumstellar dust shells have typical wavelengths of radiation which considerably exceed the size of most grains such that we can examine the extinction properties in the limit of small particles. This assumption is supported by observations of the visual and infrared wavelength region which indicate that circumstellar grains seem not to strongly scatter radiation in this region, but become important in the UV [Kruszewski et al., 1968, Serkowski and Shawl, 2001].

For small size parameter $x \ll 1$ the angular distribution of the scattered radiation has the simple shape typical for dipole scattering and the angular distribution is symmetric between forward and backward direction.

Although the shape of the circumstellar grains is not accurately determined from observations, we will consider in this work carbon dust grains with a spherical shape, as considered by other authors [Croat et al., 2005]. Additionally we assume that the particles are formed from a homogeneous, isotropic material.

By considering this assumption one can calculate the absorption and scattering efficiencies of carbon grains, by solving the appropriate boundary value problem for Maxwell equations, using the Mie-theory [Mie, 1908].

$$\omega(\mathbf{k}' \rightarrow \mathbf{k}) = \frac{3}{16\pi}(1 + \cos^2\theta) \tag{5.2.14}$$

where θ is the angle between the unit vectors $\mathbf{k}'$ and $\mathbf{k}$.

5.2.2 Eddington moments

The Eddington moments, which we describe bellow, will be used to validate the results of the Monte Carlo code, with the known solutions for a single star (see section 5.3.3).

They are obtained by the expansion of I_ν into an orthogonal basis $k_{j_1}k_{j_2}...k_{j_m}$ of spherical harmonics is given by:

$$I_\nu = \sum_{m=0}^{\infty} M^m_{\nu,j_1\cdots j_m} k_{j_1\cdots j_m} \tag{5.2.15}$$

where $k_{j_1\cdots j_m} = k_{j_1}k_{j_2}...k_{j_m}$ is a series of tensors of rank $m = 0, 1, 2...$ and $M^m_{\nu,j_1\cdots j_m}$ is the m -fold tensor product:

$$M^m_{\nu,j_1\cdots j_m} = \frac{1}{4\pi}\int_\Omega I_\nu k_{j_1\cdots j_m} d^2k \tag{5.2.16}$$

In this way, and according to equations **(5.1.8)**,**(5.1.10)** and **(5.1.12)** we can identify the first three particular moments of I_ν, known as the Eddington moments. These are, the spectral mean intensity, J_ν, the spectral radiation flux, $\mathbf{F}_\nu$ and the spectral radiation pressure tensor, $\mathbf{P}_{\nu,i,j}$. They are defined as follows:

m=0: Spectral mean intensity

$$J_\nu = M_\nu^0 \tag{5.2.17}$$

m=1: Spectral Eddington flux

$$H_{\nu,\mathrm{i}} = M_{\nu,\mathrm{i}}^0 = \frac{1}{4\pi} F_{\nu,\mathrm{i}} \tag{5.2.18}$$

m=2: Spectral Eddington tensor

$$K_{\nu,\mathrm{ij}} = M_{\nu,\mathrm{ij}}^0 = \frac{1}{4\pi} P_{\nu,\mathrm{ij}} \tag{5.2.19}$$

The expansion of I_ν into moments enables us to consider the radiation field in terms of the angle dependency. Such that instead of treating the problem of radiative transfer explicitly by using the microscopic quantity I_ν, an equivalent system of macroscopic moments can be considered.

A conventional way of solving the problem of radiation transfer by means of moments would give a coupled system of integro-differential equations which is non-closed. Therefore in practical applications an additional closure relation has to be introduced, which allows us to express the highest moment taken into account in the treatment of radiative transfer, by lower moments. A usually closure relation is given by the variable Eddington factor f_ν, defined as the frequency dependent local factor of the zeroth moment J_ν to yield the second moment K_ν

$$K_\nu = f_\nu J_\nu \tag{5.2.20}$$

In the case of an isotropic radiation field the Eddington factor approaches $f_\nu = 1/3$.

5.3 Principle of Monte Carlo method

Monte Carlo methods are not based on a single technique, but are a class of rather loosely related techniques. They are defined by the use of statistical sampling to determine the likely outcome of an interaction, and have been extensively used in astrophysical problems [Kling et al., 2000].

Applying a Monte Carlo method to radiation transport means tracing the history of a statistically meaningful random sample of photons from points of emission to the points of absorption. The method consists of simulating a finite number of representative photons histories. For each photon, random numbers are generated and used to sample appropriate probability distributions for scattering angles and the path lengths between collisions [Oran and Boris, 1987, Garrod, 1995, Lapeyre et al., 2003].

A computation is started by assigning a set of values to the photon, such as initial energy, position and direction. The number of mean free paths that the photon propagates is determined stochastically. Then the cross - section data are sampled and these are used to determine whether the collided photon is absorbed or scattered by the gas molecules or dust particles in the medium.

If the photon is scattered, the distribution of the scattering angles is sampled and a new direction is assigned to the photon, depending on whether the scattering is elastic or inelastic. For elastic scattering, a new energy is determined by conservation of energy and momentum. With the newly assigned energy, position and direction, the procedure is repeated for successive collisions until the photon is absorbed or escapes from the system.

Monte Carlo solutions fluctuate statistically around the "real" answer. The answer is expected to converge to the exact solution of the problem as the number of the photons increases, which causes an increase of computational cost. The advance of the method is that it can correctly solve the radiative transfer problem in case of complex geometry, with relatively uncomplicated programming.

The Monte Carlo method directly simulates the physical process of the radiation transport. It is accurate when the opacity is small and it may decrease drastically for moderate-to-large opacities. It traces and collects the scattering and absorption behaviour of a large number of independent radiative energy particles, namely, photon packages, which are emitted from each point in the system. Numerical computations are then performed to determine the incident radiation from the surroundings to the system and the absorption distribution of self-radiation emitted from each position with in the system.

5.3.1 Basic concepts

We start this section with the assumption that a photon has been emitted and determine how far it will travel in a medium. Once this distance has been reached we discuss what can happen next.

In simulating the transfer of radiation, photon packets are followed as they are scattered and absorbed within a medium. An initial total energy is given, and it is then split equally among the photon packets that are followed. Each packet, which has a direction of travel, then possesses a definite total energy (and partial polarisation) and these packets are related to the specific intensity, I_ν (equation **(5.1.4)**).

The photons interact according to probabilistic interactions determined by the scattering and absorption cross sections of the particles within the medium. These cross sections are related to the difference between the incoming and outgoing energy (or number of photons) at a point. A cross section, σ is defined by the energy per second, per frequency and per solid angle (number of photons) that is removed from the direction of travel, by either scattering or absorption, such that:

$$\textbf{Energy removed per second per frequency} = I_\nu \sigma \tag{5.3.1}$$

A cross section thus has dimensions of area [cm^{-2}].

Considering now a homogeneous medium filled with scatters or absorbers of number density, n, and cross section σ, it follows that the number of photons scattered per second by an infinitesimal volume is $I_\nu\ \sigma\ n\ A\ dl$, so the number of photons scattered per second per area is $I_\nu\ \sigma\ n\ dl$. Therefore the intensity differential along a length dl is given by:

$$dI_\nu = -I_\nu n \sigma dl \tag{5.3.2}$$

We then obtain the known relation between the incident and outgoing intensity (Beer's Law):

$$I_\nu(l) = I_\nu(0) e^{-n\sigma l} \tag{5.3.3}$$

The fraction of photons scattered or absorbed per unit length is thus $n\sigma$ and this quantity is called the volume absorption coefficient. It is related to the opacity or mass absorption coefficient, κ (equation 5.2.3), by:

$$n\sigma = \kappa\rho \tag{5.3.4}$$

where ρ is the mass density of scatterers or absorbers.

A related quantity is the photon mean free path, $1/n\sigma$, which is the average distance a photon travels between interactions. The probability that a photon interacts (is scattered or absorbed by the particles) over a length dl is thus $n\sigma dl$, so the probability of travelling dl without interacting is therefore $1 - n\sigma dl$. Dividing a length l into N sections of equal length indicates that the probability of travelling the distance l without an interaction occurring is:

$$P(l) = (1 - n\sigma l/N)^N = e^{-n\sigma l} = e^{-\tau} \tag{5.3.5}$$

where the notion of optical depth, $\tau = n\sigma l$, is introduced. Physically, the optical depth over a distance l in a given direction is the number of photon mean free paths over that distance. In general the optical depth is defined as:

$$\tau = \int_0^l n\sigma ds \tag{5.3.6}$$

The optical depth will in general be wavelength dependent due to continuum and line opacity depending on the the absorbing and scattering species present.

After the photon has travelled the interaction length one of two things can occur, it is either absorbed or scattered. The photon's destiny is determined by the albedo ϖ which is the probability that the photon is scattered. The albedo is defined as:

$$\varpi = \frac{n_s \sigma_s}{n_s \sigma_s + n_a \sigma_a} \tag{5.3.7}$$

where the subscripts refer to the number densities and cross sections of scatters and absorbers respectively. There are several different types of absorption (continuous absorption, line absorption, resonance line scattering, etc.) and in general the photon will be absorbed at a certain frequency and will be re-emitted at another frequency in a different direction of travel.

For our current discussion we assume that if a photon is absorbed it will be terminated and a new photon will be emitted from the source. In this way the absorbed photon contributes to the mean intensities as it scatters throughout the atmosphere until it is absorbed. If a photon is scattered it then travels in a new direction that is determined by the angular phase function of the scattering particle.

Two of the most common scattering functions ω used for modelling scattering atmospheres are the isotropic scattering function (equation **(5.2.6)**), and the dipole-like scattering function (equation **(5.2.14)**).

5.3.2 Sampling from probability distribution functions

In the previous section we have discussed all the necessary notions to establish a Monte Carlo radiation transfer code. A photon is emitted, sent into a distance l, it is then either absorbed (terminated) or scattered into a new direction.

However, the distances travelled and scattering angles are not uniformly chosen from all space $l \in [0, \infty]$ or all angles $\theta \in [0, \pi]$ and $\phi \in [0, 2\pi]$, since there are probability distribution functions associated with the interaction length and scattering angle as described above. Therefore the optical depths and scattering angles must be sampled, such that the chosen τ's, ϕ's and θ's "fill in" the respective probability distribution function $P(x)$. In order to randomly sample the quantities (l, θ and ϕ) from a probability distribution function there are several techniques which will now be explained.

5.3.2.1 Sampling from the cumulative distribution function

To sample a quantity x_0 from a probability distribution function $P(x)$, which is normalised over all x, we use the fundamental principle which is:

$$\xi = \int_a^{x_0} P(x)dx = \psi(x_0) \tag{5.3.8}$$

where ξ, is a random number sampled uniformly from the range 0 to 1, a is the lower limit of the range over which x is defined, and $\psi(x_0)$ is thecumulative probability distribution function.

The probability that a photon travels an optical depth τ without an interaction is $e^{-\tau}$. The probability of scattering prior to τ is $1 - e^{-\tau} = \psi(\tau)$. Therefore we can sample from the cumulative probability according to $\xi = 1 - e^{-\tau}$, giving:

$$\boxed{\tau = \log(1 - \xi) \qquad (5.3.9)}$$

Having sampled a random optical depth in this manner we then calculate the physical distance l that the photon travels from:

$$\tau = \int_0^l n\sigma dl \qquad (5.3.10)$$

In general l cannot be found analytically from equation **(5.3.10)**, so one must use numerical techniques which can be computationally intensive and time consuming.

Luckily, l can be found analytically for certain densities and this allows the generation of large numbers of photons in a fraction of the time required if we had to solve equation **(5.3.10)** numerically. Geometries which allow this include spherically symmetric $(1/r^2)$ density laws, ellipsoidal envelopes, and any homogeneous (constant density) medium.

5.3.3 Example: a plane parallel atmosphere

We now apply the concepts and definitions presented in section 5.3.1 to radiation transfer within a plane parallel isotropic scattering atmosphere. For comparison and validation of the solution we use the results for the angular dependence of the intensity and polarisation of the emergent radiation from a semi-infinite slab of constant density, which was presented by [Chandrasekhar, 1960]. In the following we discuss the main points of the developed code that determines the emergent energy and intensity from a slab illuminated from below, as well as the mean intensities of the radiation field within the slab.

Principle flow of the code: A principle flow of the Monte Carlo approximation is shown in figure **(5.2)**. A photon will be released at the starting point $(0, 0, 0)$ in random direction $(\mathbf{k}_x, \mathbf{k}_y, \mathbf{k}_z)$ (see also section 5.1) and with a probable optical depth $\tau = -\log(\xi)$. until it will be scattered or until it leaves the slab at $\mathrm{Z_{max}}$ (forward scattered) or $\mathrm{Z_{min}}$ (backward scattered) where it will be detected as the output result (see figure 5.1).

The monochromatic photons are injected from the origin such that the flux in any direction of emission is isotropic. In this way, the specific intensity is independent of direction and the lower limit is 0 since we are injecting photons in only upward directions. This then gives $\mu = \cos\theta = \sqrt{\xi}$ and $\phi = 2\pi\xi$ such that the direction cosines of the photon are $\mathbf{k}_x = \sin(\theta)\cos(\phi), \mathbf{k}_y = \sin(\theta)\sin(\phi)$ and $\mathbf{k}_z = \cos(\theta)$.

At the scatter point the moments $J(z)^{\pm}, H(z)^{\pm}$ and $K(z)^{\pm}$ (given by equations **(5.3.21)**, **(5.3.22)** and **(5.3.23)**) will be stored, and a new optical depth τ, as well as a new pair of scatter angles (θ, ϕ), will be generated until the photon package leaves the slab at $\mathrm{Z_{max}}$ or $\mathrm{Z_{min}}$.

Propagation of the photons: here we address the propagation of photons within the homogeneous planar slab of height $\mathrm{Z_{max}} = 1$. The slab may be parametrised by its

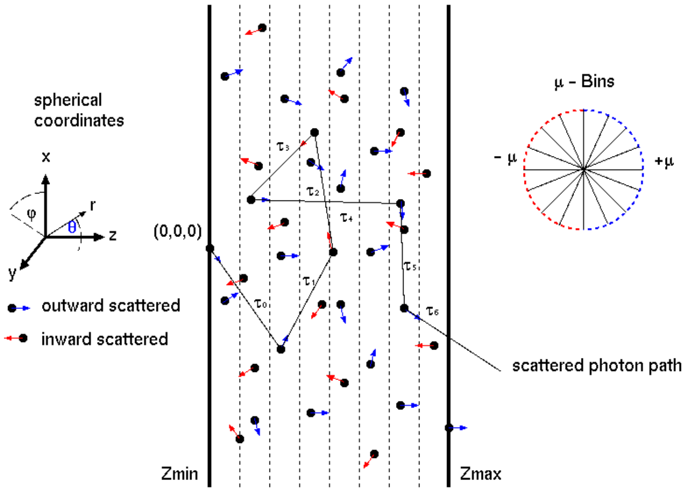
spherical coordinates
x
y
z
r
φ
θ
(0,0,0)
outward scattered
inward scattered
τ0
τ1
τ2
τ3
τ4
τ5
τ6
μ - Bins
- μ
+μ
scattered photon path
Zmin
Zmax

Figure 5.1: Sketch showing the principle of the Monte Carlo integration method. The photon will be released at $(x_0, y_0, z_0) = (0, 0, 0)$ and is scattered after an optical depth τ_i. At each scattering event the newly determined scatter angle $\mu = \cos(\theta)$ is stored into the associated μ - bin.

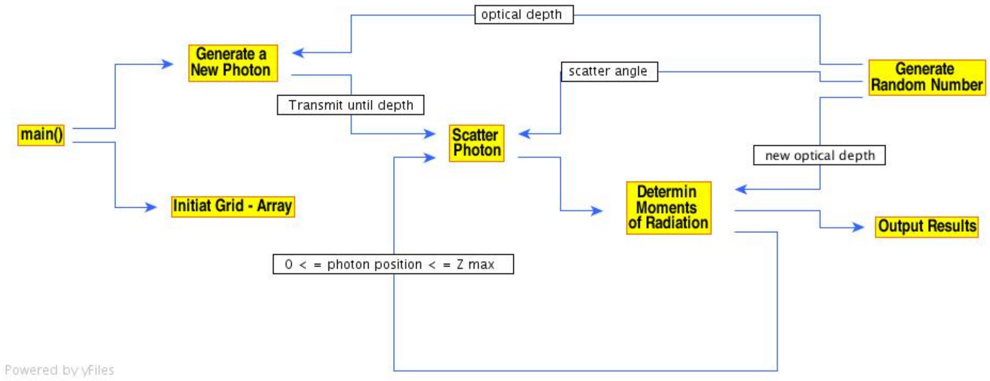
optical depth
Generate a New Photon
scatter angle
Generate Random Number
Transmit until depth
main()
Scatter Photon
new optical depth
Determin Moments of Radiation
Initiat Grid - Array
Output Results
0 < = photon position < = Z max
Powered by yFiles

Figure 5.2: Diagram showing the principle program flow of the integrating Monte Carlo method.

total vertical optical depth $\tau_{\mathsf{max}} = n\sigma \mathsf{Z}_{\mathsf{max}}$, where σ is the scattering cross section. The distance, l, travelled by a photon along any ray is then simply:

$$l = \frac{\tau \mathsf{Z}_{\mathsf{max}}}{n\sigma \mathsf{Z}_{\mathsf{max}}} = \frac{\tau \mathsf{Z}_{\mathsf{max}}}{\tau_{\mathsf{max}}} \tag{5.3.11}$$

The photon's position is then updated according to:

$$x = x' + l\sin(\theta)\ \cos(\phi) \qquad y = y' + l\sin(\theta)\sin(\phi) \qquad z = z' + l\cos(\theta) \tag{5.3.12}$$

where x', y' and z' are the coordinates of emission. At this point the photon may be absorbed, scattered, or escape from the atmosphere (i.e., $z > \mathsf{Z}_{\mathsf{max}}$ or $z < 0$). Since we are considering a pure scattering atmosphere the albedo ϖ is equal to 1 and every interaction will be a scattering event.

Isotropic scattering of photons: In an isotropic scattering atmosphere the photons are scattered uniformly into 4π steradians. We generate the new direction by sampling uniformly for ϕ in the range 0 to 2π and μ in the range 0 to 2π, thus:

$$\phi = 2\pi\xi \qquad \mu = 2\xi - 1 \tag{5.3.13}$$

Binning photons: Once the photon exits the slab they are placed into a "μ-Bin" (see figure 5.1) depending on its direction of travel. We measure continuous distributions such as the emergent flux or intensity by using a discrete set of events. This means we are sampling (in the statistical sense) the distribution function we measure. This is done by binning the photons to produce histograms of the distribution function.

Binning in μ and ϕ ensures that each bin is of equal solid angle since $d^2k = \sin(\theta)d\theta d\phi = d\mu d\phi$. The number of bins depends on the symmetry of the radiation source and the scattering medium, and for fully three dimensional systems we must choose enough bins to give resolution on scales of the smallest variation with solid angle.

In the case of the plane parallel slab, each ϕ direction of exit is equally probable (the system is axisymmetric) so we only need to bin in μ. In addition, since we are interested in the radiation emerging from the top of the slab, we bin the photons in the range $0 < \mu < 1$ i.e. $0 < \theta < \pi/2$.

Flux normalisation: We now discuss how to compute the output flux or intensity of our time-independent and mono-chromatic simulation. Since Monte Carlo works in flux/energy units the computation of intensity is only needed when comparing to other radiation transfer methods. The outgoing energy in the i'th bin, normalised to the total energy, is just:

$$\frac{dE_i}{dE} = \frac{N_i}{N_0} \tag{5.3.14}$$

where N_i is the number of photons in the i'th bin and N_0 is the total number of photons. In order to calculate the emergent intensity from the top of our slab we note that the energy per area through the slab surface is:

$$\frac{dE}{dA} = F_\nu = \pi B_\nu \tag{5.3.15}$$

where B_ν is the physical flux. Supposing that the energy in the i'th bin is $dE_i = N_i dE/N_0$, then taking equation **(5.1.4)** relating the energy per area per solid angle we get the intensity in the i'th bin as:

$$I_\nu = \frac{dE_i}{\mu d^2k dA} = \frac{N_i \pi B_\nu}{N_0 \mu d^2 k} \tag{5.3.16}$$

For our plane parallel slab our elemental solid angle is $d^2k = 2\pi d\mu$ and $d\mu = 1/N_\mu$, with N_μ being the number of μ bins. This then gives:

$$\frac{I_\nu}{B_\nu} = \frac{N_i N_\mu}{2 N_0 \mu_i} \tag{5.3.17}$$

where μ_i is the μ value at the centre of the i'th bin.

Error estimation: Since the Monte Carlo method employs a stochastic approach, the results for the emergent energies in each bin contain random sampling errors. Consequently, in all Monte Carlo simulations, a large number of events (i.e. photons) must be generated until the physical properties under investigation have small statistical fluctuations. It is therefore necessary to estimate the errors on the results stored in each bin.

For this example we calculate the total energy for each direction bin. The number of photons in each bin obeys Poisson statistics, so the error in the total energy in each direction bin is simply $\sigma_E = dE_i/\sqrt{N_i}$, where dE_i is the energy andN_i is the number of photons in the i'bin.

Intensity moments: As we have outlined in the previous sections, the Monte Carlo technique tracks each and every photon package as it propagates through an atmosphere ([Chandrasekhar, 1960], page 233-248). Astrophysically important quantities are the intensity moments i.e., spectral mean intensity J_ν (equation **(5.2.17)**), spectral Eddington flux H_ν (equation **(5.2.18)**) and spectral Eddington tensor K_ν **(5.2.19)** which are measure at every point throughout the medium, here (equation **(5.3.18)**) expressed for the one-dimensional case.

$$J_\nu = \frac{1}{4\pi}\int_\Omega I_\nu \, d^2k, \quad H_\nu = \frac{1}{4\pi}\int_\Omega I_\nu \, \mu d^2k, \quad K_\nu = \frac{1}{4\pi}\int_\Omega I_\nu \, \mu^2 d^2k \quad (5.3.18)$$

Keeping with the plane parallel slab, we compute the intensity moments as a function of optical depth through the slab. First of all we split the slab into layers of equal width (see figure 5.1), then count the number of photons, weighted by powers of their direction cosines, to obtain the three moments.

$$\mu = \begin{cases} \mu^+ = \cos(\theta) & 0 \le \theta \le \pi/2 \\ \mu^- = \cos(\theta) & \pi/2 \le \theta \le \pi \end{cases} \quad (5.3.19)$$

We note that the contribution to the specific intensity from a single photon is:

$$\Delta I = \frac{\Delta E}{|\mu|\Delta A d^2k} = \frac{F_\nu}{|\mu| N_0 d^2k} = \frac{\pi B_\nu}{|\mu| N_0 d^2k} \quad (5.3.20)$$

which may be substituted into the intensity moment equations **(5.3.18)**. Converting the integral to a summation and substituting **(5.3.20)** thus we then get an expression for moments and its out and inward components, i.e.:

$$\begin{aligned} J_\nu(\tau) &= \frac{1}{4\pi}\int_\Omega I_\nu d^2k = \frac{1}{2}\int I_\nu d\mu = \frac{1}{4}\int \frac{\pi B_\nu}{|\mu| N_0 \pi d\mu} d\mu \approx \left(\frac{B_\nu}{4N_0}\right)\sum_i^{\mu_{\mathrm{max}}} \frac{1}{|\mu_i(\tau)|} \\ &= \left\{\left(\frac{B_\nu}{4N_0}\right)\sum_i^{\mu^+_{\mathrm{max}}} \frac{1}{|\mu_i(\tau)|}\right\} + \left\{\left(\frac{B_\nu}{4N_0}\right)\sum_i^{\mu^-_{\mathrm{max}}} \frac{1}{|\mu_i(\tau)|}\right\} \\ &= J^+_\nu(\tau) + J^-_\nu(\tau) \end{aligned} \quad (5.3.21)$$

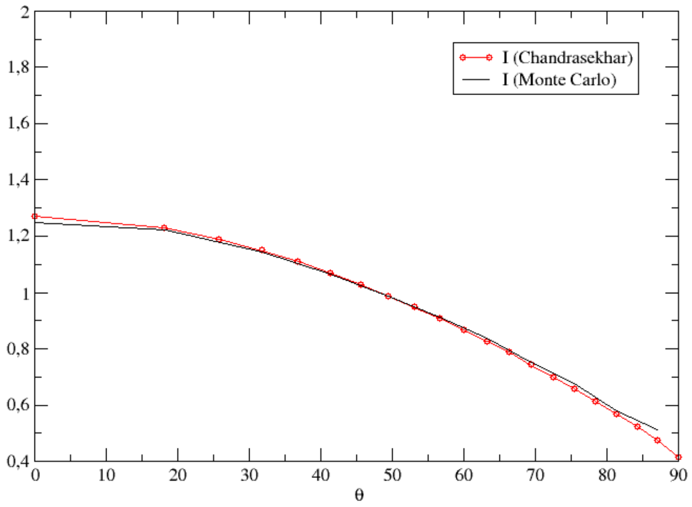

Figure 5.3: The plot shows the result of our numerical approach (Monte Carlo) and the corresponding solution given by [Chandrasekhar, 1960] for the Intensity $I_\nu(\theta)$

and analogue for H_ν and K_ν:

$$H_\nu(\tau) \approx \left\{ \left(\frac{B_\nu}{4N_0}\right) \sum_i^{\mu^+_{\mathrm{max}}} \frac{\mu_i(\tau)}{|\mu_i(\tau)|} \right\} + \left\{ \left(\frac{B_\nu}{4N_0}\right) \sum_i^{\mu^-_{max}} \frac{\mu_i(\tau)}{|\mu_i(\tau)|} \right\} = H^+_\nu + H^-_\nu \tag{5.3.22}$$

$$K_\nu(\tau) \approx \left\{ \left(\frac{B_\nu}{4N_0}\right) \sum_i^{\mu^+_{max}} \frac{\mu_i(\tau)^2}{|\mu_i(\tau)|} \right\} + \left\{ \left(\frac{B_\nu}{4N_0}\right) \sum_i^{\mu^-_{max}} \frac{\mu_i(\tau)^2}{|\mu_i(\tau)|} \right\} = K^+_\nu + K^-_\nu \tag{5.3.23}$$

One should note that the mean flux, H, is simply the net energy (number of photons travelling up minus the number travelling down) passing each level. These summations is implemented in the Monte Carlo code and demonstrates how Monte Carlo techniques return the same quantities as the more traditional methods.

Results of the numerical simulation: Figures 5.3, 5.4 and 5.5 show the results of our numerical approach (Monte Carlo) for a plane parallel slab with $\tau = 10$. In figure 5.3 we have compared the computed intensity $I_\nu(\theta)$ with the results from [Chandrasekhar, 1960] for this problem. The related moments $J^\pm$, $H^\pm$ and $K^\pm$ as given by equations **(5.3.20)** - **(5.3.23)** are shown in figure 5.4 and 5.5, where we have additionally computed the value for the variable Eddington factor f_ν (equation **(5.2.20)**).

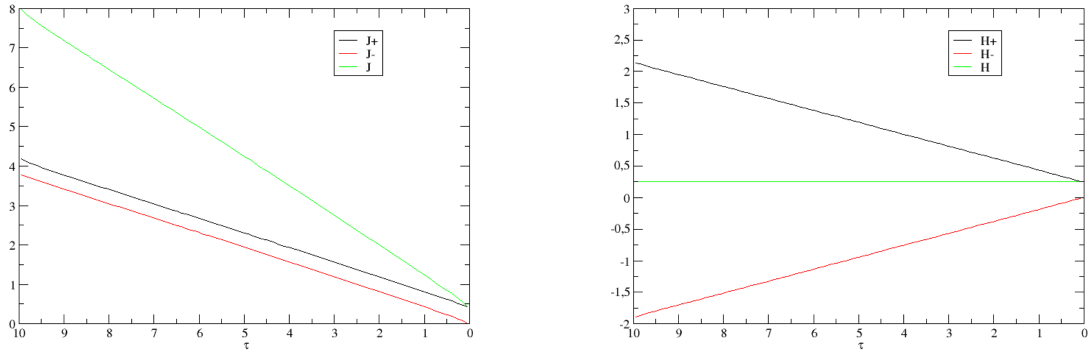

Figure 5.4: The plot shows the result of the Monte Carlo approximation for the moment of radiation for forward and backward scattering for J (left panel) and H (right panel) .

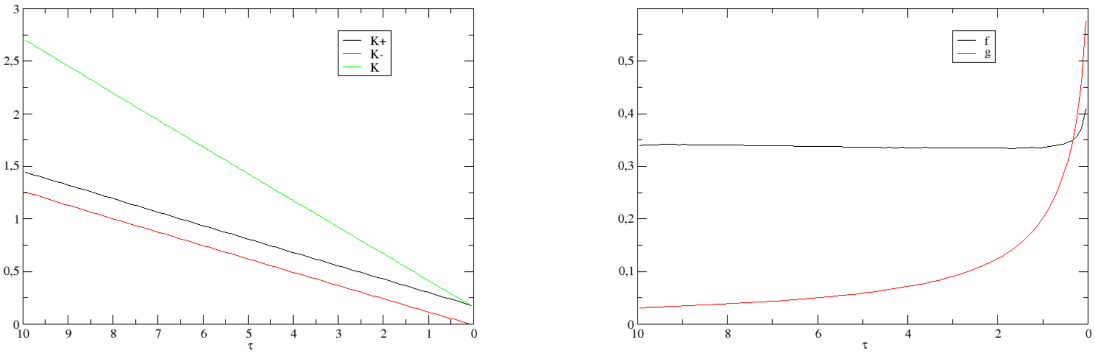

Figure 5.5: The plot shows the result of the Monte Carlo approximation for the moment of radiation for forward and backward scattering for K (left panel) and the Eddington factor $f = K(\tau)/J(\tau)$ and $g = H(\tau)/J(\tau)$ (right panel). The Monte Carlo approach fullfills clearly the Eddington closure relation at $\tau = 10$, i.e. $f \approx 1/3$.

5.4 Radiative equilibrium for a single star

For a single star with an extended atmosphere the radiative transfer problem can be treated by a semi-analytic method [Lucy, 1971, Lucy, 1976] which is based on the coupled system of moment equations **(5.2.15)** for the radiation field and an appropriate closure relation, given by the Eddington approximation **(5.2.20)** at $r = R_*$, where r is the radial coordinate and R_* is the stellar radius.

By assuming radiative equilibrium, the system of moment equations can be integrated analytically and yield an expression for the temperature structure such that the local radiative equilibrium temperature T_{eq} at r is determined by:

$$T_{\text{eq}}^4(r) = T_*^4\left(W + \frac{3}{4}\tau_L\right) \tag{5.4.1}$$

where

$$W = \frac{1}{2}\left(1 - \sqrt{1 - \left(\frac{R_*}{r}\right)^2}\right) \tag{5.4.2}$$

is the geometrical dilution factor and

$$\tau_L(r) = -\int_{\infty}^{r}\left(\frac{R_*}{r}\right)^2 \kappa_H \rho dr' \tag{5.4.3}$$

is the modified optical depth with $\tau_L(\infty) = 0$.

Since scattering is neglected, we can replace the extinction coefficient χ (equation **(5.2.7)**) by the mean mass absorption coefficient κ_H. It is given by the sum of the dust opacity κ_d and the gas opacity κ_g. For our computation κ_g is assumed to be constant with a value of 2×10^{-4} cm^{2}g^{-1} [Alexander et al., 1983]. The dust coefficient is calculated by assuming that the size of the grains are small compared to the mean wavelength of the radiation field. This means that we can use the Mie theory [Mie, 1908] to calculate κ_d in the small particle limit, by using the following equation [Gail and Sedlmayr, 2009]:

$$\kappa_d = \frac{3}{4}V_0 K_3 Q'(T) \tag{5.4.4}$$

V_0 is the volume per monomer of the grains, K_3 is the third moment of the grain size distribution function f [Gail et al., 1984] (see section 6.2) and $Q'(T)$ is the extinction efficiency of the grain material divided by the grain radius [Lucy, 1976].

To simplify the calculations the flux weighted mean absorption coefficient κ_H is replaced by the Rosseland mean κ_R. According to [Fleischer, 1994], the extinction data of amorphous carbon can be used, such that the temperature dependence of the Rosseland mean can be approximated by [Gail and Sedlmayr, 2009]:

$$Q'(T) \approx Q'_R = 5.9T \tag{5.4.5}$$

5.4.1 Monte Carlo simulation - radiative equilibrium assuming LTE

In this section we discuss the development of a method to calculate the temperature distribution throughout an extended dusty environment for use with Monte Carlo simulations of the radiation transfer. The basic idea is to divide the luminosity of the radiation source into equal-energy, monochromatic "photon packets" that are emitted stochastically by the source. These packets are followed to random interaction locations, determined by the optical depth, where they are either scattered or absorbed with a probability given by the albedo (equation **(5.3.7)**).

If the packet is scattered, a random scattering angle is obtained from the scattering phase function. If instead the packet is absorbed, its energy is added to the envelope, raising the local temperature. To conserve energy and enforce radiative equilibrium, the packet is re-emitted immediately at a new frequency determined by the envelope temperature. These re-emitted photons comprise the diffuse radiation field. After either scattering or absorption plus re-emission, the photon packet continues to a new interaction location. This process is repeated until all the packets escape the envelope. Since all the injected packets eventually escape (either by scattering or absorption followed by re-emission), this method implicitly conserves total energy. Furthermore it automatically includes the diffuse radiation field when calculating both the temperature structure and the emergent spectral energy distribution.

5.4.2 Radiative equilibrium temperature

We start by dividing the stellar luminosity L_* of the donor star, into N_γ photon packets emitted over a time interval Δt. Each photon packet has the same energy E_γ, so:

$$E_\gamma = \frac{L_* \Delta t}{N_\gamma} \tag{5.4.6}$$

It should be noted that the number of physical photons in each packet is frequency dependent. When the monochromatic photon packet is injected into the envelope, it will be assigned a random frequency chosen from the spectral energy distribution of the source, as seen in figure 5.7. This frequency determines the dust absorptive and scattering opacities, as well as the scattering parameters for the following random walk of the packet through the envelope. The envelope is divided into spatial grid cells with volume V_i , where i is the cell index (see figure 5.6).

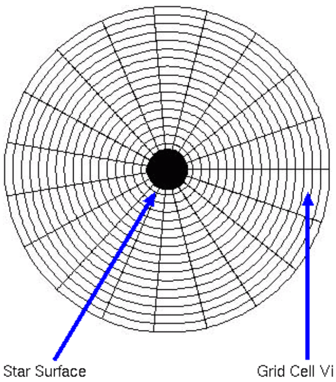

Figure 5.6: Parametrisation of the envelope by division into spatial grid cells of volume V_i. At the centner is the donor star with luminosity L_*.

As we inject source photon packets, we keep a total N_i, of how many packets are absorbed in each grid cell.

Whenever a packet is absorbed in a grid cell, we deposit its energy in the cell and recalculate the cells temperature. The total energy absorbed in the cell is:

$$E_i^{\mathsf{abs}} = N_i E_\gamma \tag{5.4.7}$$

We assume a local thermodynamic equilibrium (LTE), and for simplicity we adopt a single temperature for the dust grains and gas. In radiative equilibrium, the absorbed energy, E_i^{abs}, must be re-radiated. The thermal emissivity of the dust $\eta_{d,\nu} = \hat{\kappa}_{d,\nu} B_\nu(T)$, where $B_\nu(T)$ is the Planck function **(5.1.11)** at temperature T, so the emitted energy is:

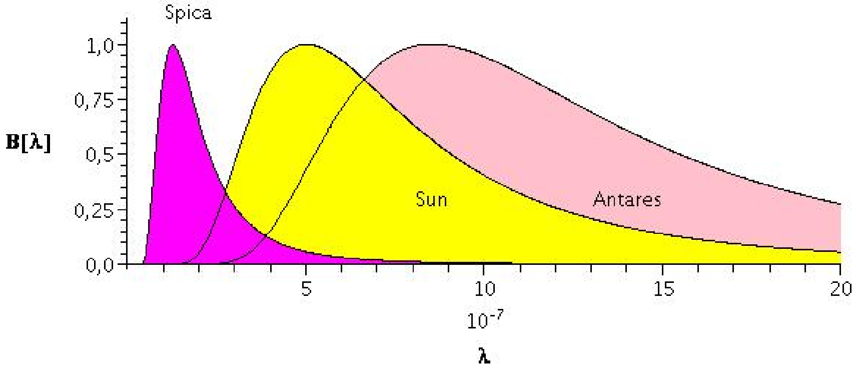

Figure 5.7: Illustration of the spectral energy distribution of three different stars (Spica 23000K , Sun 5800K , Antares 3400K) with different surface temperatures. The strong shift of the spectrum to shorter wavelengths (in units m) with increasing temperatures is apparent in this illustration. For convenience in plotting, these distributions have been normalised to unity at the respective peaks by the Stefan-Boltzmann Law, the area under the peak for the hot star Spica is in reality 2094 times the area under the peak for the cool star Antares.

$$E_i^{\mathsf{em}} = 4\pi\Delta t \int dV_i \int d\nu \; \hat{\kappa}_{d,\nu} B_\nu(T) = 4\pi\Delta t \int dV_i \int d\nu \; \rho\kappa'_{d,\nu} B_\nu(T) \tag{5.4.8}$$

where $\kappa'_{d,\nu}$ is the absorption coefficient per mass unit of the gas-dust mixture.

$$E_i^{\mathsf{em}} = 4\pi\Delta t \int dV_i \; \rho\kappa_{\mathsf{P}}(T) B(T) \tag{5.4.9}$$

with

$$\kappa_{\mathsf{P}} = \frac{\int d\nu B_\nu \kappa_{d,\nu}}{B} \tag{5.4.10}$$

being the Planck mean opacity and $B = \sigma T^4/\pi$ is the frequency integrated Planck function. If we adopt a temperature T_i that is constant throughout the grid cell, then:

$$E_i^{\mathsf{em}} = 4\pi\Delta t \; m_i \kappa_{\mathsf{P}}(T_i) B(T_i) \tag{5.4.11}$$

where m_i is the mass of the cell.

Equating the absorbed and emitted energies, we find that after absorbing N_i packets the dust temperature is given by:

$$\sigma T_i^4 = \frac{N_i L_*}{4 N_\gamma \kappa_{\mathrm{p}}(T_i) m_i} \qquad (5.4.12)$$

The Planck mean opacity κ_{p}, is a function of temperature and equation **(5.4.12)** is actually an implicit equation for the temperature, which must be solved every time a packet is absorbed.

To do so, we pretabulate the Planck mean opacity for the dust species, for a large range of temperatures and evaluate $\kappa_{\mathrm{P}}(T_i)$ by interpolation, using the temperature from the previous guess.

For this calculation we have taken the physical description of the dust properties from the work of [Kim et al., 1994]. This work provides albedos, scattering functions and the opacity appropriate for the range of known interstellar dust extinction curves.

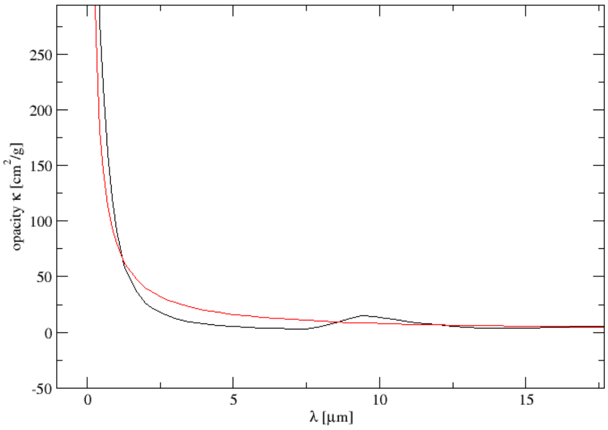

Figure 5.8: Interpolated opacity $\kappa_{d,\nu}$, based on data (black curve) and an analytical approach, $\kappa \propto \lambda^{-p}$, here $\kappa = 80/\lambda$ (red curve).

Figure 5.8 shows the interpolated opacity data adopted from [Kim et al., 1994] and analytic approach.

5.4.2.1 Temperature correction

Monte Carlo radiative transfer is a numerically demanding method, and several authors have attempted to either accelerate or avoid completely the iteration process in the method. [Lucy, 1999] proposed a device to optimise the iteration. The author argues that a much faster convergence can be achieved by applying a temperature correction and re-emission immediately after each individual absorption event. Thus, every single time a packet is absorbed, the temperature $T_i - \Delta T$ of the cell is updated to a new temperature T and a new packet is re-emitted with the new emissivity of the cell $\hat{\kappa}_\nu B_\nu(T)$. This packet is then followed until either it leaves the system or it is absorbed again. In this way the temperature distribution and the radiation field, after the last packet leaves the system are closer to the equilibrium state, and fewer iterations are necessary to reach convergence. However, this method still needs iterations. Another problem arises from the fact that as the temperature in each cell gradually increases, the packets re-emitted in the beginning of the simulation are emitted from an incorrect frequency distribution.

An extension of the idea of [Lucy, 1999] has been proposed with the aim to correct, during each re-emission event, for the incorrect frequency distribution of the packets that have been re-emitted before [Bjorkman and Wood, 2001]. If this happens, the system is in radiative and thermal equilibrium at all moments during the simulation, and after the last packet leaves the system, the correct temperature distribution and spectrum are obtained without any iteration at all. Let us consider some stage in the Monte Carlo process, when k packets have already been absorbed and re-emitted in a certain cell. The temperature of the cell has been gradually increasing from zero to $T_i - \Delta T$, and we assume that the re-emission frequencies correspond to the emissivity $\hat{\kappa}_\nu B_\nu(T_i - \Delta T)$.

Now assuming that a $(k+1)$'th packet is absorbed, increasing the dust cell temperature to T_i, the emissivity changes to $\hat{\kappa}_\nu B_\nu(T_i)$. To preserve radiative equilibrium, a new packet must be emitted. Its frequency is chosen such that the ensemble of the $(k+1)$ re-emitted packets from this cell correspond to the new emissivity $\hat{\kappa}_\nu B_\nu(T_i)$. [Bjorkman and Wood, 2001] argue that this can be satisfied if the $(k+1)$'th frequency corresponds to the difference emissivity

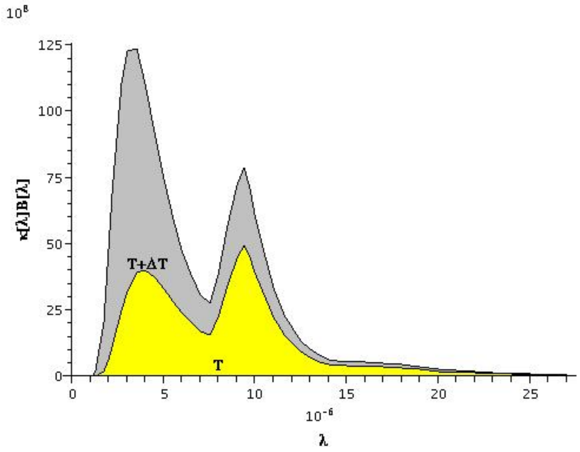

Figure 5.9: Dust emissivity before and after absorption of a single photon packet.

$$\Delta\eta_\nu = \hat{\kappa}_\nu \bigg(B_\nu(T_i) - B_\nu(T_i - \Delta T) \bigg) \tag{5.4.13}$$

Figure 5.4.2.1 shows the dust emissivities, j_ν, prior to and after the absorption of a single photon packet. The spectrum of the previously emitted packets is given by the emissivity at the old cell temperature (bottom curve). To correct the spectrum from the old temperature to the new temperature (upper curve), the photon packet should be re-emitted using the difference spectrum (shaded area).

As long as the packet energy E_γ is not too large the temperature change ΔT is small, so the temperature correction spectrum is:

$$\Delta\eta_\nu \approx \hat{\kappa}_\nu \Delta T \frac{dB}{dT} \tag{5.4.14}$$

$\Delta\eta_\nu$ is everywhere positive because $\Delta T > 0$, and the Planck function is a monotonically increasing function of temperature.

Therefore, to correct the previously emitted spectrum, we immediately re-emit the packet (to conserve energy), and we choose its frequency using the shape of $\Delta\eta_\nu$. This procedure statistically reproduces $\Delta\eta_\nu$ for the distribution of the re-emitted packets.

Normalising this distribution, we find the temperature correction probability distribution:

$$\frac{dP_i}{d\nu} = \frac{\hat{\kappa}_\nu}{C_N} \left(\frac{dB_\nu}{dT} \right)_{T=T_i} \tag{5.4.15}$$

where $\frac{dP_i}{d\nu}$ is the probability of re-emitting the packet between frequencies ν and $\nu + d\nu$, and the normalisation constant C_N is:

$$C_N = \int_0^\infty \hat{\kappa}_\nu \left(\frac{dB_\nu}{dT} \right) d\nu \tag{5.4.16}$$

5.4.3 Monte Carlo code description

When modelling the transfer of radiation through optically thick material, we pretabulated the mean opacity tables before photon emission, as mentioned in the previous section, because performing computationally costly calculations of the frequency-dependent opacity may not be doable [Ferguson et al., 2002] [Maarten et al., 2002].

Therefore in the first step we compute for a defined range of frequency ν and temperature T the Planck mean opacity κ_P, the normalisation constant C_N **(5.4.16)** and the temperature correction probability distribution P by using the data from[Kim et al., 1994].

For the parametrisation of the temperature T and frequency ν - [Pinte et al., 2006] we use a logarithmically spaced grid ranging, for $T \in [0.1\ \mathsf{K}, 6000\ \mathsf{K}]$ and for $\nu \in [10^9\ \mathsf{Hz}, 10^{14}\ \mathsf{Hz}]$.

$$\ln(T_i) = \ln\left(T_\mathsf{min}\right) + (i-1)\ln\left(\frac{T_\mathsf{max}}{T_\mathsf{min}}\right)\left(N_T - 1\right)^{-1} \tag{5.4.17}$$

or

$$T_i = T_\mathsf{min}\left(\frac{T_\mathsf{max}}{T_\mathsf{min}}\right)^{\frac{i-1}{N_T-1}} \tag{5.4.18}$$

where $T_\mathsf{min}, T_\mathsf{max}$ are the minimal and maximal temperature respectively of computed grid and N_T is the total number of grid points. The frequency bins are parametrised by:

$$\nu_i = \nu_\mathsf{min} + \frac{(i+1)\left(\nu_\mathsf{max} - \nu_\mathsf{max}\right)}{N_\nu} \tag{5.4.19}$$

where N_ν are the number of uniform frequency bins.

5.4.3.1 Emitting a photon package

We consider a 3-dimensional spatial grid, within $r \in [R_*, R_\mathsf{max}], \theta \in [0, \pi], \phi \in [0, 2\pi]$ where r, θ and ϕ are spherical coordinates. A cell is then specified by the three indices (i, j, k). Further assumption about the physical quantities within the cells are as follows:

- the temperature $T(\mathbf{r})$ is constant in each cell;
- the extinction, absorption and scattering mass coefficient are constant throughout one cell (see section 5.2);
- the mass density $\rho(\mathbf{r})$ may have a arbitrary spatial dependence;
- the albedo ϖ **(5.3.7)** and the scattering function $\omega_\nu(\mathbf{r})$ **(5.2.6)** are constant in each cell.

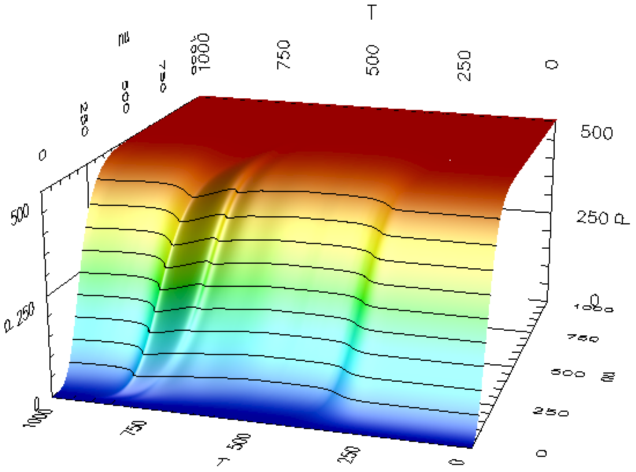

Figure 5.10: The image shows the pre-tabulated temperature correction probability function $P(\nu, T)$ for a temperature frequency grid $[\nu, T] = [10^9\text{Hz}, 10^{14}\text{Hz}, 0.1\text{K}, 2100\text{K}]$. The probability function $P(\nu, T)$ is scaled in the image by a factor 500. The number of grid point were $[N_\nu N_T] = [1025, 1000]$.

To begin the simulation, we release the photon package with a black body frequency distribution, given by the normalised Planck function (figure 5.11):

$$b_\nu = \left(\frac{15}{\pi^4}\right)\frac{x^3}{e^x - 1} \qquad \text{with} \qquad x = \frac{h\nu}{kT_*} \tag{5.4.20}$$

We use the method described by [Carter and Cashwell, 1975, page 12] for sampling

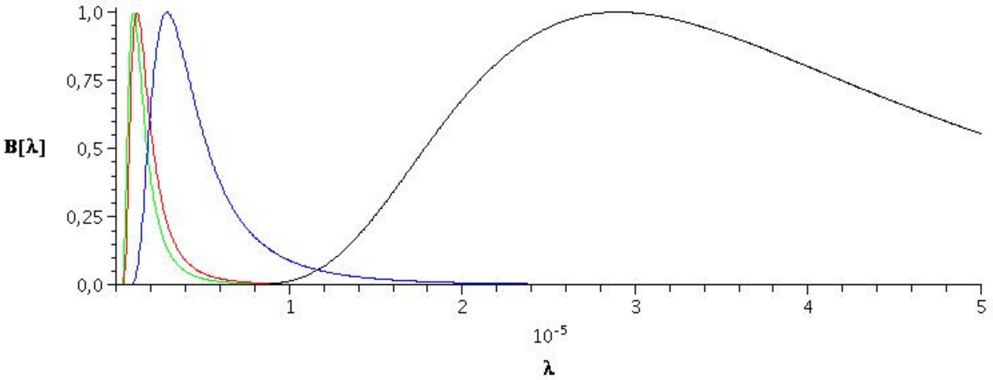

Figure 5.11: Plot of normalised Planck function for the typical temperature T at stellar surface 3000K (green) / 2500K (red) , dust temperature at the inner edge 1000K (blue) and at the outer edge of the circumstellar dust shell 100K (black).

the black body distribution. We derive the emission point and the emission direction in a two-step process. In our calculations we consider the donor star to have radius $R_* = \text{R}_\odot$, luminosity L_* and temperature $T_* = 3000\ K$. The star is embedded in a dusty environment with density ρ decreasing with r^{-2}.

Emission point: The first step consists in determining the emission point $\mathbf{r} = \mathbf{r}(R_*, \theta, \phi)$ of the photon package, at the inner boundary of a cell adjacent to the star (figure 5.6).

For this we select two aleatory numbers $\xi_1, \xi_2 \in [0,1]$, which give the possibility to randomly choose the emission point $P = P(R_*, \theta_p, \phi_p)$ inside the cell, as depicted in the stereographic projection of the stellar surface seen in figure 5.12. The coordinates of point P in the cell $[\theta_j, \theta_{j+1}]$ and $[\phi_k, \phi_{k+1}]$ are defined as follows, where N_θ, N_ϕ are the number of grid points for θ, ϕ respectively:

$$\begin{array}{lll} \theta_p = \theta_j + \xi_2(\theta_{j+1} - \theta_j), & \theta_p \in [\theta_j, \theta_{j+1}], & j = 1..N_\theta \\ \phi_p = \phi_k + \xi_3(\phi_{k+1} - \phi_k), & \phi_p \in [\phi_k, \phi_{k+1}], & k = 1..N_\phi \end{array}$$

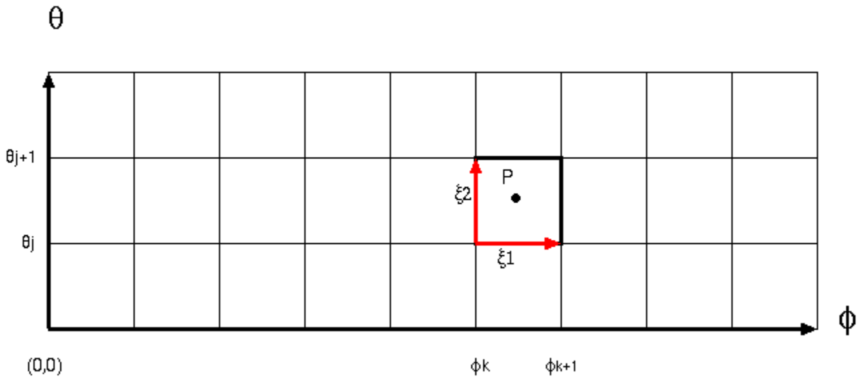

Figure 5.12: Stereographic projection of the stellar surface.

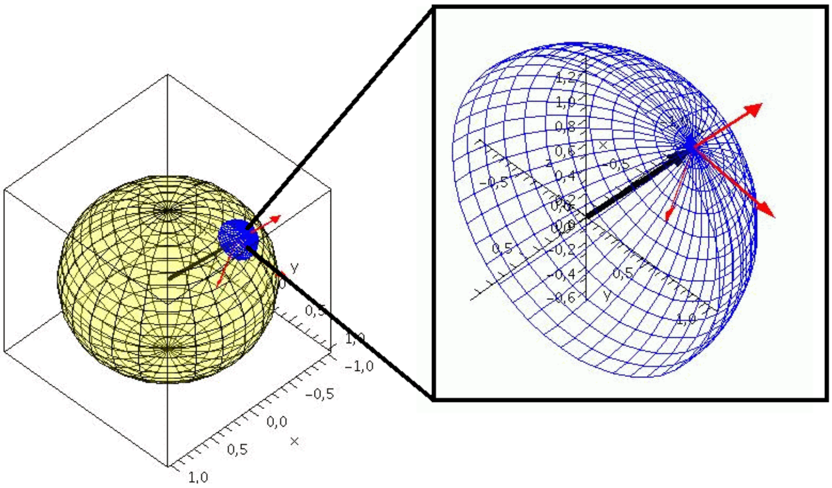

Figure 5.13: The picture shows the emission cells of the star (yellow) and the unit half sphere (blue). For each grid cell emission the direction of the photon is chosen randomly from this half sphere.

Emission direction: The photon package will be emitted in the direction $\mathbf{n} = (n_x, n_y, n_z)$. For this we choose two more random numbers $\xi_3,\ \xi_4 \in [0,1]$ to determine isotropically a point on the unit half sphere, indicated by the vector $\mathbf{n}'$.

$$\mathbf{n}' = \begin{pmatrix} \sin(\theta_n)\sin(\phi_n) \\ \sin(\theta_n)\cos(\phi_n) \\ \cos(\theta_n) \end{pmatrix}, \text{where} \quad \theta_n = (\frac{1}{2} - \xi_3)\frac{\pi}{2}, \quad \phi_n = (\frac{1}{2} - \xi_4)\frac{\pi}{2}$$

To place the emission direction at the intended emission point $P(R_*, \theta_p, \phi_p)$, we additionally have to use the rotation matrices $\mathbf{R}_x(\phi_p)$, $\mathbf{R}_z(\theta_p)$ (equation **(5.4.21)**), which transform from the basis of $\mathbf{n}'$ to the basis of P, according to $\mathbf{n} = \mathbf{R}_x\mathbf{R}_z\mathbf{n}'$, as seen in figure 5.13.

$$\mathbf{R}_x = \begin{pmatrix} \cos(\phi_p) & \sin(\phi_p) & 0 \\ -\sin(\phi_p) & \cos(\phi_p) & 0 \\ 0 & 0 & 1 \end{pmatrix}, \quad \mathbf{R}_z = \begin{pmatrix} 1 & 0 & 0 \\ 0 & \cos(\theta_p) & -\sin(\theta_p) \\ 0 & \sin(\theta_p) & \cos(\theta_p) \end{pmatrix} \tag{5.4.21}$$

5.4.3.2 1-dim test: single star

In the optically thin limit, the mean intensity $J_\lambda(\mathbf{r})$ of the radiation field around a black body sphere of radius R_* and temperature T_* is given by:

$$J_\lambda(\mathbf{r}) = W(\mathbf{r})B_\lambda(T_*) \tag{5.4.22}$$

where $W(r)$ is the radial dilution factor **(5.4.2)**. For the absorption coefficient we use the following power law dependence (see also figure 5.8):

$$\kappa_\lambda^{\mathsf{abs}} \propto \lambda^{-p} \tag{5.4.23}$$

The radiative equilibrium:

$$\int_0^\infty \kappa_\lambda^{\mathsf{abs}} B_\lambda(T(\mathbf{r}))d\lambda = \int_0^\infty \kappa_\lambda^{\mathsf{abs}} J_\lambda(\mathbf{r})d\lambda \tag{5.4.24}$$

can be solved analytically, resulting in a equilibrium solution:

$$T_{\mathsf{eq}}(\mathbf{r}) = W(\mathbf{r})^{\frac{1}{4+p}}T_* \tag{5.4.25}$$

We use this analytical solution to validate our Monte Carlo code in the case of radiative equilibrium.

We choose $T_* = 3000$ K and $p = 1$ as initial data for the star. The following spatial and wavelength grids are considered: $N_\lambda = 40$ equidistant wavelength grid points between 0.1 μm and 100 μm, $\mathsf{N_r} = 100$ equidistant radial grid points between $1R$ and $20R$, $N_\theta = 10$ equidistant latitude angular grid points between 0 and π and $N_\phi = 20$ equidistant altitude angular grid points between 0 and 2π. A total number of 9×10^6 stellar photon packages is used. The resulting temperature distribution of this computation is shown in figure 5.14.

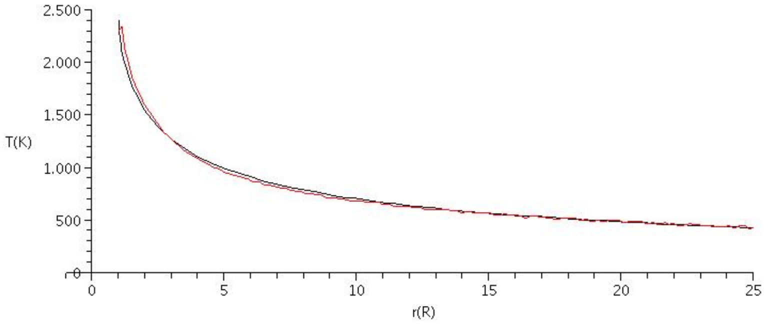

Figure 5.14: Computed temperature distribution of the 1d test (red line). The black line represents the analytic solution T_{ref}. The units are T inK and r in solar Radius $\mathrm{R}_{\odot}$

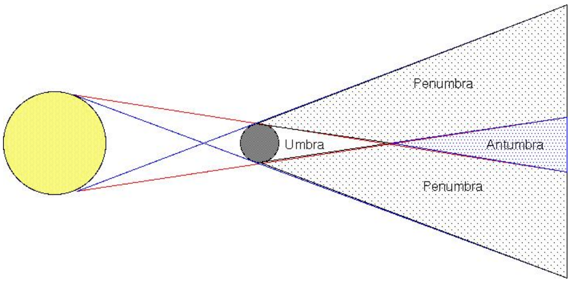

Figure 5.15: Sketch of the shadow distribution in a binary system.

5.4.3.3 3-D test: radiative equilibrium in a binary system assuming LTE

In the next computation example, we investigate the radiative equilibrium distribution in the environment of a binary star system (figure 5.16). Figure 5.15 presents a sketch of a theoretical radiation (shadow) distribution in a binary system. The theoretical expectation predicts that three regions of different shadow strengths form behind the cool star. These are the umbra, the region with the darkest shadow; the penumbra, in which only a part of the star is occulting the light coming from the main star and the antumbra, which is the region totally contained in the disc of the light source, with a darker shadow than the penumbra.

This configuration will affect the radiation distribution in the binary system and therefore we took it into consideration when modelling the radiation in a binary system where the massive central star represents a Red Giant like star which is orbited by small body (brown dwarf), with a thick atmosphere and a negligible radiation.

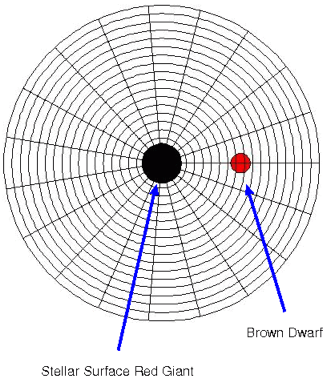

Figure 5.16: Sketch of parametrisation in spherical coordinates of the binary stellar system.

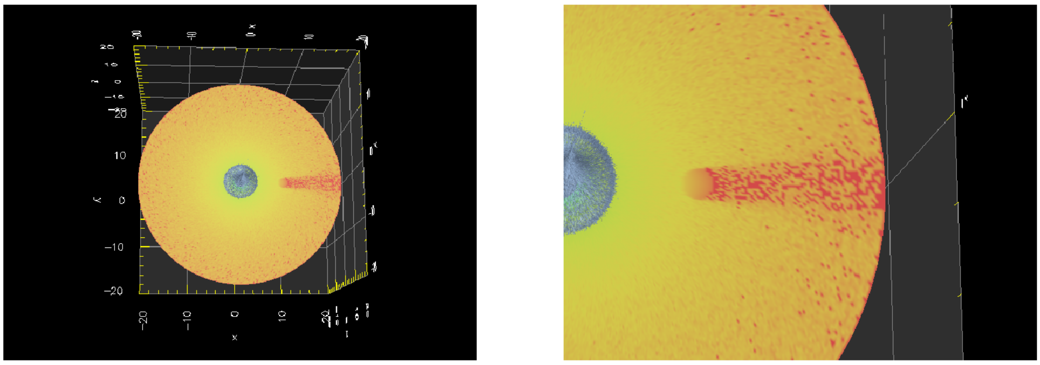

Figure 5.17: Results of the computation for the temperature distribution in a binary star system. **left**: Full system **right**: Zoom of the brown dwarf.

In this test calculation, the common envelope is assumed to have a density decay of r^{-2} around the central star. In our first simulation we set for the number of grid points $[N_r, N_\theta, N_\phi] = [100, 100, 600]$. We used 1×10^8 photon packets and an frequency distribution like for the 1d -example (see section 5.4.3.2). The maximal radius of the numerical evolution area is $r = 20\mathrm{R}_\odot$. The results of this computation are shown in figure 5.17. The temperature difference between the day and the night side (core shadow, in red representing a lower temperature) could be a preferential area for the evolution of dust particles. In the case of a mass overflow from the red giant to the brown dwarf and a hence resulting disk (around the brown dwarf) this cool and dens area may give an ideal environment for the temperature and density sensible evolution of bigger dust particle. We will investigate this case in more detail in section 7 on the full set of equations, i.e. by inclusion of the hydrodynamical , chemical and the dust components.

Chapter 6

Chemistry

6.1 Fundamental relations

This chapter describes the essential chemical network which can occur in the envelope of a C-giant star as well as in the further evolving common envelope of the binary system. Here we assume that the atmosphere of the companion star is non-expanding and represents one of the outer computational boundaries of our binary system (see figure 2.3), such that the chemical components of this atmosphere do not intermixture with those of the donor star. This means, that in the close environment of the donor star we can benefit from the well known spherical symmetric solution for a single star.

For this approximation we consider a solar composition of the gas in the atmosphere (see Appendix B), with exception of the carbon abundance ϵ_c, which in order to account for a C-rich mixture is taken as a parameter.

As previously mentioned the time evolution of the particle density n_i, is generally described by a system of rate equations **(2.1.38)**, so that it represents the net rate for the production of species i. These equations give the chemical structure of the reacting gas.

The molecular gas composition determines the gas opacity (Rosseland mean absorption coefficient) which enters the radiation hydrodynamic equation, and the concentration of those species which contribute to the dust formation and growth. In the here assumed carbon-rich element mixture, these are primarily the species C, C_2, C_2H_2, C_2H (see figure 6.1).

For our computation we assume the gas to be in LTE and the concentration of the atoms, ions and molecules are calculated by assuming CE, such that the general form of the above mentioned rate equations can be replaced by the law of mass action (equation **(6.1.7)**). In all situations where the expansion velocity is small and there are no ionizing photons, as in the here considered case of cool giants, chemical equilibrium is a reasonable assumption [Jura, 1986, Beck et al., 1992]. Moreover, [Mamon et al., 1988] indicated that photo reactions can be neglected in the dust forming region because no interstellar UV photons can penetrate into the inner layers of the dust shell.

Following our assumption, the chemical equilibrium between several species in a mixture with a given temperature T, total pressure p, and n_i number of moles of elements, corresponds to the minimum of the Gibbs function $G(p, T, n_i)$.

$$G = E + pV - TS \tag{6.1.1}$$

It expresses a congruence between the minimisation of the energy E and the maximisation of the entropy S.

6.1.1 Dissociation equilibrium

In this section we will describe the equation system for the situation of CE. The numerical method for solving this system is based on a damped Newtonian algorithm.

For a given elemental abundance (table B) in the gas phase, the conservation of charge and the vanishing ensemble lead to the number density of free electrons n_e, which is given by summation over the particle densities of all ions with respect to the degree of ionisation Z:

$$n_e = \sum_{j=1}^{N_{\text{ions}}} Z_j n_j \tag{6.1.2}$$

Further it yields for element i from the conservation of elements, that

$$n_{<i>} = \epsilon_i n_{<\mathtt{H}>} = n_i + \sum_{m=1}^{N_{\text{molecules}}} a_{i,m} n_m \tag{6.1.3}$$

where ϵ_i is the relative abundance of the element i with respect to the total number density of Hydrogen $n_{<\mathtt{H}>}$ and $n_{<i>}$ denotes the total number density of the element i. The right hand side of the equation is given by the element i's number density of free atoms and the summation over all $N_{\mathtt{molecules}}$ molecules in the gas phase. $a_{i,m} \in N_o$ represents the stoichiometric factor.

Considering the law of mass action the partial pressure p_{AaBb} of molecules containing a atoms of element A and b atoms of element B is given by:

$$\frac{p_{AaBb}}{p_A^a p_B^b} = \frac{1}{(p^\ominus)^{a+b-1}} \exp\left(\frac{\Delta_f G^\ominus(T)}{R\,T}\right) = K_P(T) \tag{6.1.4}$$

where $p_{A,B}$ denotes the partial pressure of the free atoms of the corresponding elements, R the gas constant, and T the temperature of the gas phase. The standard reference pressure is given by: $p^\ominus = 1\text{bar} = 106$ dyn/cm^2. $K_P(T)$ denotes the equilibrium constant.

One can determine the Gibbs free energy (or free enthalpy) for the molecule at the reference pressure using the equation:

$$\Delta_f G^\ominus = \Delta_f G^\ominus(A_a B_b^{\mathsf{gas}}) - a\Delta_f G^\ominus(A^{\mathsf{gas}}) - b\Delta_f G^\ominus(B^{\mathsf{gas}}) \tag{6.1.5}$$

By combining equation **(6.1.4)** with the ideal equation of state $p_i = n_i k_B T$ we obtain the number densities of the corresponding molecules.

To simplify the numerical solution we express the equations with the logarithms of the densities:

$$\ln(n_{AaBb}) = \ln(K_P(T)) + a\ln(n_A) + b\ln(n_B) + (a+b-1)\ln(k_B T) \qquad (6.1.6)$$

In general the partial pressure for all polyatomic molecules $m = A^1_{a_1} A^2_{a_2} ... A^{N_{\text{elements}}}_{a_{N_{\text{elements}}}}$ consisting of a_i atoms of element A_i is given by the following equation:

$$p_m = K_P(m) \prod_{i=1}^{N_{\text{elements}}} p_i^{a_i} \qquad (6.1.7)$$

In a similar way to equation **(6.1.6)**, the logarithm of the particle density for the molecule m is given by:

$$\ln(n_m) = \ln(K_P(m)) + \sum_{i=1}^{N_{\text{elements}}} a_{i,m}\ln(n_i) + \left\{\left(\sum_{i=1}^{N_{\text{elements}}} a_{i,m}\right) - 1\right\}\ln(k_B T) \quad (6.1.8)$$

We define the generalised equilibrium constant K_P as:

$$K_P(m) = \frac{1}{(p^{\ominus})^{(N_A(m)-1)}} \exp\left(\frac{\Delta_f G^{\ominus}}{RT}\right) \qquad (6.1.9)$$

with the number of atoms in molecule N_A given by:

$$N_A(m) = \sum_{i=1}^{N_{\text{elements}}} a_{i,m} \qquad (6.1.10)$$

This results in the following Gibbs free energy for the molecule at the reference pressure:

$$\Delta_f G^{\ominus} = \Delta_f G^{\ominus}(m) - \sum_{i=1}^{N_{\text{elements}}} a_{i,m}\Delta_f G^{\ominus}(i) \qquad (6.1.11)$$

For the further computation of the chemical equilibrium we use the available molecular data of the JANAF tables.

6.1.2 Equilibrium in the gas phase - carbon rich case

In this section we show some representative results of our computation for the chemical equilibrium.The numerical evolution is based on a damped Newtonian algorithm, such that we can determine the particle densities of the most abundant compounds in a circumstellar envelope of a C-giant.

We choose a giant on the AGB, with a carbon rich element mixture C/O $= 1.2$ in its stellar atmosphere, and a fixed pressure of $P = 10^{-10}$ bar. The element abundances correspond to the surface abundances after the third dredge-up on a thermal pulsing AGB brought the products of He burning to the surface.

Based on equation **(6.1.8)** we obtain the particle densities for different compounds in the relevant temperature range, following the methods defined in [Gail and Sedlmayr, 2009]. The compounds shown in the following pictures are just a few of those resulting from the chemical reactions in the stellar atmosphere (see table B).

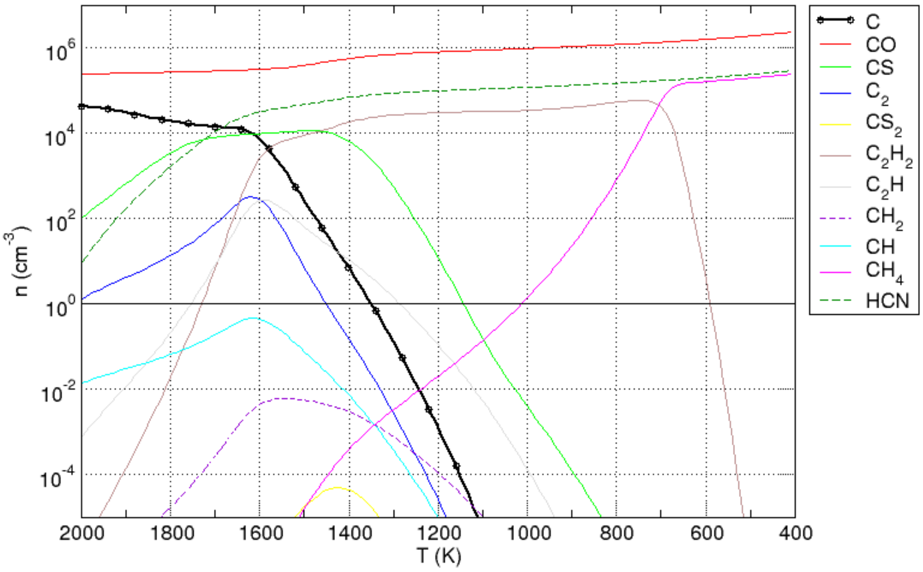

Figure 6.1: Abundances for Carbon compounds in a carbon rich element mixture with C/O $= 1.2$ and a fixed pressure of $P = 10^{-10}$ bar.

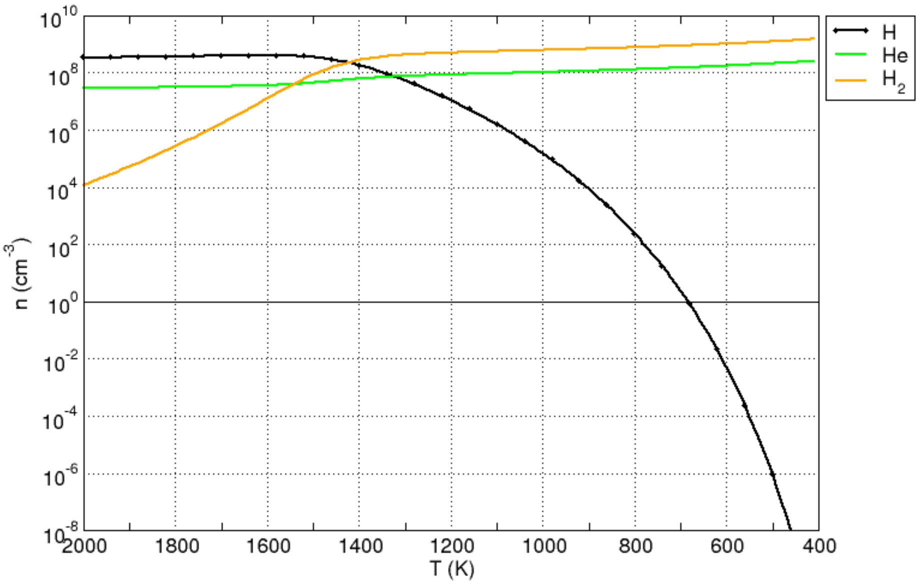

Figure 6.2: Abundances for Hydrogen and Helium compounds in a carbon rich element mixture with C/O $= 1.2$ and a fixed pressure of $P = 10^{-10}$ bar.

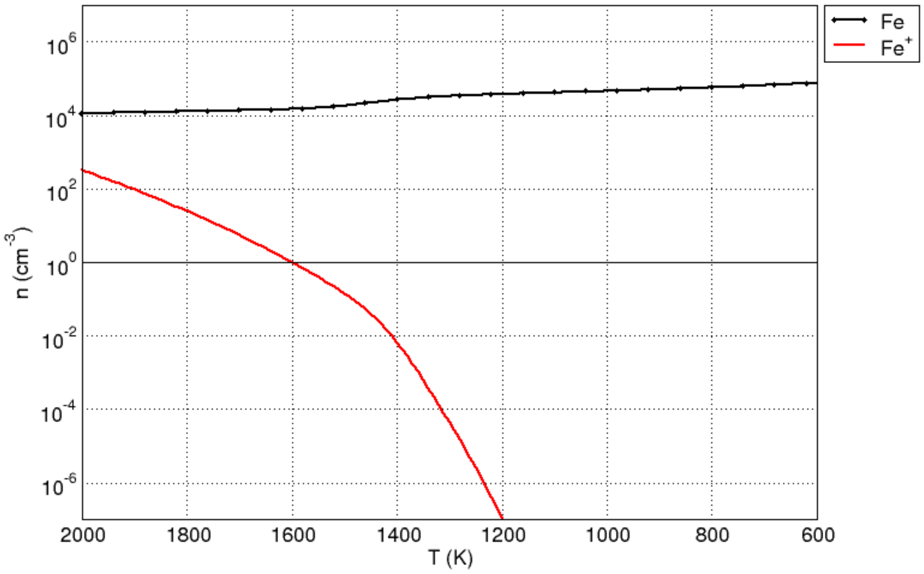

Figure 6.3: Abundances for Iron compounds in a carbon rich element mixture with C/O = 1.2 and a fixed pressure of $P = 10^{-10}$ bar.

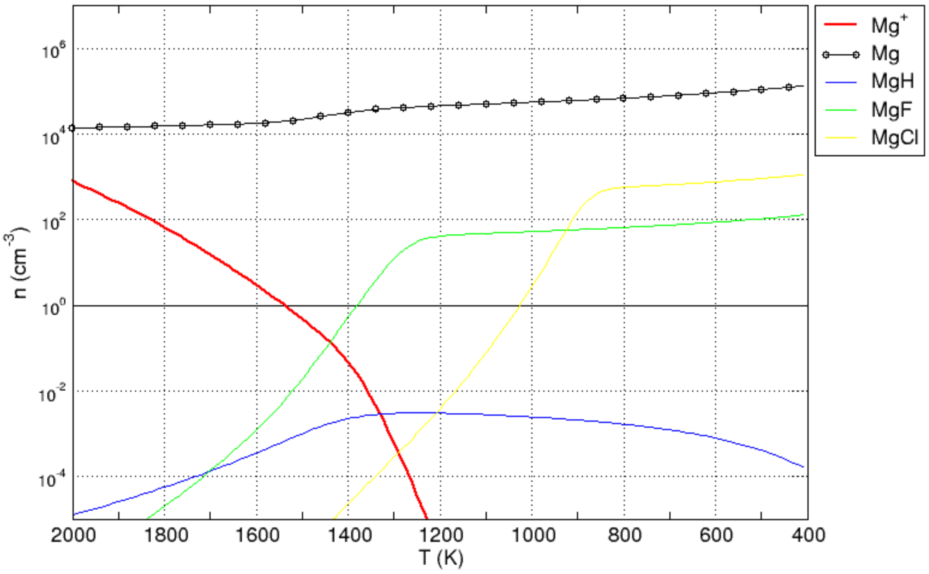

Figure 6.4: Abundances for Magnesium compounds in a carbon rich element mixture with C/O = 1.2 and a fixed pressure of $P = 10^{-10}$ bar.

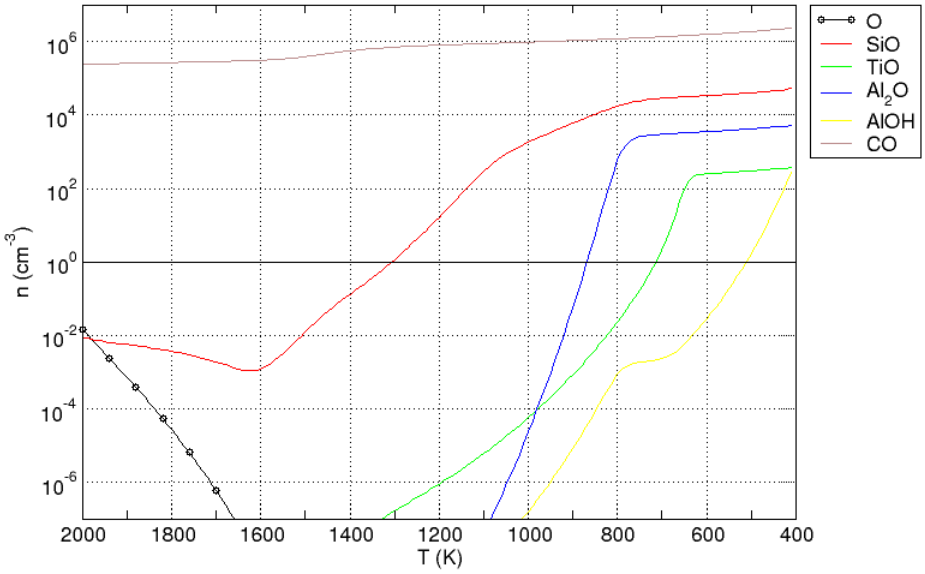

Figure 6.5: Abundances for Oxygen compounds in a carbon rich element mixture with C/O = 1.2 and a fixed pressure of $P = 10^{-10}$ bar.

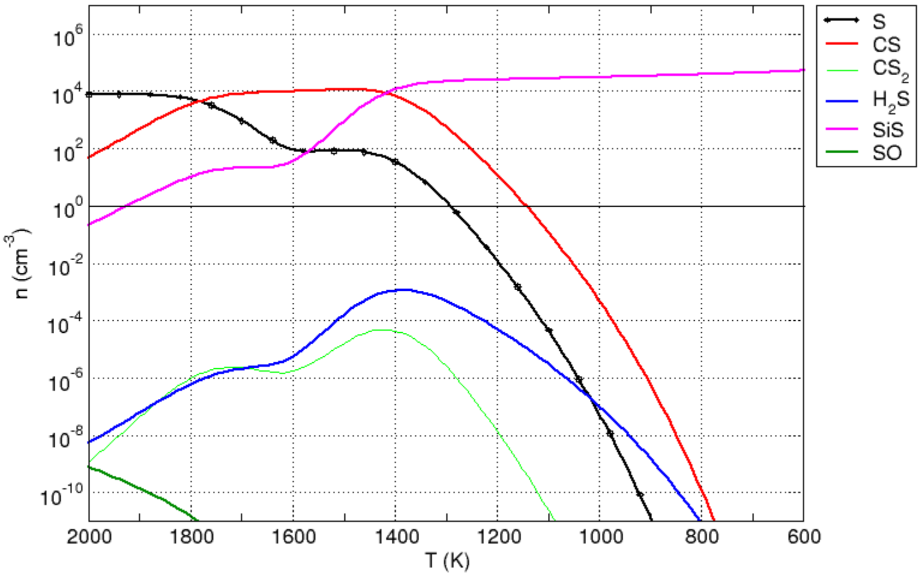

Figure 6.6: Abundances for Sulphur compounds in a carbon rich element mixture with C/O = 1.2 and a fixed pressure of $P = 10^{-10}$ bar.

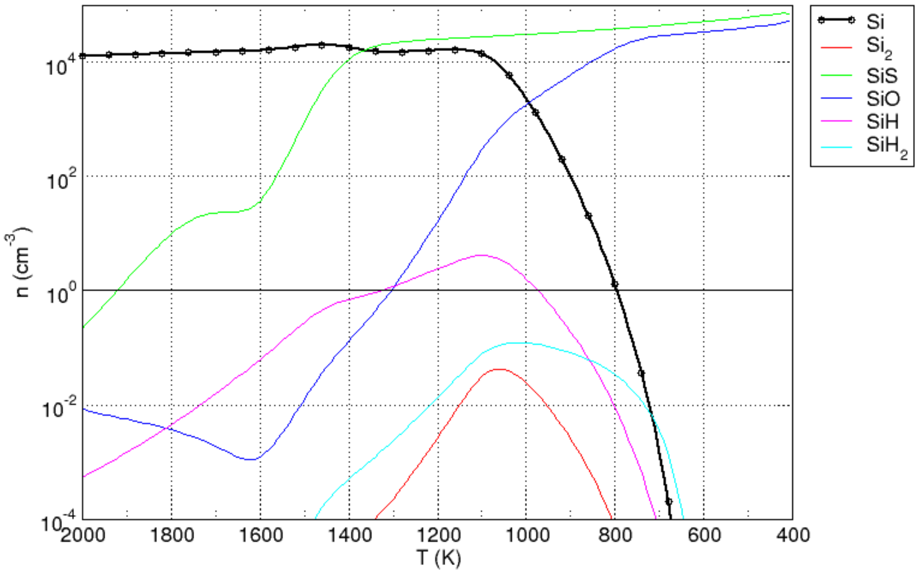

Figure 6.7: Abundances for Silicon compounds in a carbon rich element mixture with C/O = 1.2 and a fixed pressure of $P = 10^{-10}$ bar.

6.2 Dust formation

The formation of dust is described as a two step process consisting in grain nucleation and subsequent growth to macroscopic particles. We use in this work the method developed by [Gail et al., 1984, Gauger et al., 1990]. In this section we introduce the microphysical model and its fundamental quantities i.e., the dust moments K_i (equation **(6.2.20)**), the nucleation rate J_N (equation **(6.2.3)**) and the net growth rate τ^{-1} (equation **(6.2.11)**) as they are computed throughout this work for the assumed case of a carbon rich star. In this situation the number density of carbon atoms is higher than that of oxygen atoms and due to the high binding energy of the CO-molecule (about 11 eV), the oxygen will be effectively locked in CO and is therefore not available for the formation of high temperature condensates, which could condense to solid grains. Only the excess of carbon, which is not locked in CO will form the grains. This can be described by the time evolution of the particle size distribution function $f(N, t)$, which characterizes the formation, growth and evaporation of the dust particles.

To decribe the dust complex by a one dimensional distribution function, we include the assumption that the grains actually consist of a number of identical monomers that condensate into graphite clusters from the non locked carbon. We consider in this work not only C - atoms as species contributing to the nucleation and growth via chemical reactions, but also C_2 ,C_2H and C_2H_2.

6.2.1 Condensation processes

In thermal equilibrium the saturation pressure p_{sat} over a curved surface is determined by the Thomson-Helmholtz equation [J. Feder et al., 1966, Mitrović and Stephan, 1980]:

$$\ln\left(\frac{p_{\mathsf{sat}}(r)}{p_\infty}\right) = \frac{2\sigma_{\mathsf{surf}}\,\mu m_u}{r\,\rho\,k_{\mathsf{B}}\,T} \tag{6.2.1}$$

here, $p_{\mathsf{sat}}(r)/p_\infty$ is the ratio of the pressure over a curved surface to that over a plane surface, σ_{surf} is the surface tension of the grains material, r is the radius of the curvature and μm_u is the mass of the monomer (see table A). This means that, for a given temperature and density, there is a grain size, r_{crit}, for which the grains will be in stable equilibrium with the gas phase. Grains with this size are known as critical clusters. Depending on their size relative to the critical cluster, grains can either evaporate, if they are smaller than the critical cluster, or grow by catching monomers from the gas phase, if they are bigger. The condensable material in the gas is depleted by those particles larger than r_{crit}. In this way the increase in r_{crit} is given by equation **(6.2.1)** and it leads to the evaporation of more grains. This process will stop when an equilibrium between the new solid phase and the depleted gas is reached. When an equilibrium is established the partial pressure of the monomers equals the saturation pressure over the solid surface. The monomers are in chemical equilibrium with the partial pressure of the remaining i-mers.

The supersaturation ratio between the partial pressure of monomers p_1 and the pressure of a saturated vapour over a flat surface p_∞, is defined by equation **(6.2.2)** [Vehkamäki, 2006]:

$$\mathbf{S} = \frac{p_1}{p_\infty} \tag{6.2.2}$$

where S is the supersaturation ration. By this defintion a value of $\mathbf{S} = 1$ means that the size of the critical cluster would be infinite and no particles could go through self-nucleation from the gas phase. In order for nucleation to occur the supersaturation rate should be bigger than 1. This would allow the critical cluster size to be reached by a chemical fluctuation process. This situation is however, thermodynamically unstable since the growth of the seeds will lead to a depletion of condensable monomers. This could lead to difficulties in the description of this state using equilibrium quantities.

6.2.2 Nucleation

The nucleation process is regarded, in the framework of classical nucleation theory (e.g. [Feder et al., 1966]), as a random walk problem of clusters in the cluster size space. A cluster that has reached the critical cluster size will most probably continue to grow to macroscopic dimensions. Smaller clusters are more likely to reevaporate. Therefore, the nucleation rate, J_*, is assumed to be the formation rate of critical clusters in a quasi stationary equilibrium situation. Stationary in this case means, that the clusters are assumed to grow fast from the critical size N_* to the size N_l, the minimum size of a macroscopic particle.

$$J_*^s = \beta \; A_N \; Z \; \overset{\circ}{c} \tag{6.2.3}$$

where A_N denotes the surface of a grain of size N, A_1 the hypothetical monomer surface $A_1 = 4\pi r_0^2$, d denotes the dimension of the spatial structure of the microcopic cluster. (see table A).

$$A_N = A_1 \cdot N^{\frac{d-1}{d}} \tag{6.2.4}$$

The quantity β describes the rate of i-mers growing onto a cluster of size N. It is given by:

$$\beta = \sum_i^{N_0} v_{\mathsf{th}} \; \overset{\circ}{c} \; i^{2/3} s_i = \sum_i^{N_0} v_{\mathsf{th}} \; \overset{\circ}{c} \; i^{2/3} \alpha_i \quad = \quad \sqrt{\frac{k_{\mathsf{B}} T_{\mathsf{gas}}}{2\pi \; m_u}} \; \sum_{i=1}^{2} \overset{\circ}{c}(i) \; \alpha_i \; i^{7/6} \tag{6.2.5}$$

with $v_{\mathsf{th}} = \sqrt{\frac{k_{\mathsf{B}} T_{\mathsf{gas}}}{2\pi \; m_i}}$ being the thermal velocity. N_0 is the highest i-mer that plays a role in the nucleation process. In equation **(6.2.5)** the sticking coefficient $s_i(N)$ has been approximated by the evaporation coefficient a_i of the i-mer from a flat graphite-surface. Z is the Zeldovich - factor:

$$Z = \left(\frac{1}{2\pi} \frac{\partial^2}{\partial N^2} \bigg|_{N_*} \ln \overset{\circ}{c} \right)^{1/2} \tag{6.2.6}$$

$\overset{\circ}{c}(N)$ is the equilibrium distribution of dust grains of size N in thermal equilibrium:

$$\overset{\circ}{c}(N) = n_1\, \mathbf{S}^{N-1} \exp\left(-\frac{\theta_N\ (N-1)^{2/3}}{T} \right) \tag{6.2.7}$$

with

$$\theta_N = \frac{\theta_\infty}{1 + \left(\frac{N_d}{N-1} \right)^{1/3}} \qquad \text{and} \qquad \theta_\infty = \frac{4\pi r_0^2 \sigma_{\mathsf{surf}}}{k_{\mathsf{B}}}$$

N_d is the particle size for which $\sigma_{\mathsf{surf}}(N)$ reduces to one half of the value of σ_{surf} for bulk material, and N_* is the critical cluster size. It is given by:

$$N_* = 1\ +\ \frac{N_{*.\infty}}{8} \left\{ 1 + \sqrt{1 + 2\left(\frac{N_l}{N_{*,\infty}} \right)^{1/3}} - 2\left(\frac{N_l}{N_{*,\infty}} \right)^{1/3} \right\}^3 \tag{6.2.8}$$

where

$$N_{*,\infty} = \left(\frac{2\ \theta_\infty}{3T \ln(\mathbf{S})} \right)^3 \qquad \text{and} \qquad \mathbf{S} = \frac{n_1 k_{\mathsf{B}} T}{p_{\mathsf{sat}}} = \frac{p_1}{p_{\mathsf{sat}}} \tag{6.2.9}$$

where n_1 is the particle density of the monomers and p_{sat} the saturation pressure of the monomers with respect to the grain. In this work, p_{sat} is approximated by the saturation pressure of monomers in phase equilibrium over a flat surface:

$$\overset{\circ}{p}_{\mathsf{sat}}(1) = \overset{\ominus}{p} \exp\left[\frac{\Delta_f \overset{\ominus}{G}(s) - \Delta_f \overset{\ominus}{G}(1)}{RT} \right] \tag{6.2.10}$$

Here the pressure of the standard state is denoted as $\overset{\ominus}{p}$, $\Delta_f \overset{\ominus}{G}(1)$ is the standard molar Gibbs free energy of formation of the monomer and $\Delta_f \overset{\ominus}{G}(s)$ is the standard molar Gibbs free energy of formation of the solid phase (referred to the standard state). For our calculation we have assumed thermal equilibrium between solids and the gas phase, such that the temperature used in equation **(6.2.10)** corresponds to the temperature of the solid. If the condition of thermal equilibrium is violated, the gas and the solid phase can have different temperatures. In this case, the pressure p_1 of the monomers must be calculated using the gas temperature T_{gas}, while the saturation pressure $\overset{\circ}{p}_{\mathsf{sat}}$ should be calculated with the dust temperature T_{dust}.

6.2.3 Net rate of growth and evaporation

The net rate τ^{-1} can be considered [Gauger et al., 1990] as the rate of particle growth or evaporation. It is derived from the difference between the pure growth τ_{gr}^{-1} rate and the evaporation rate τ_{ev}^{-1}, where we assume C, C_2,C_2H and C_2H_2 as the growth species.

$$\tau^{-1} = \tau_{\mathsf{gr}}^{-1} - \tau_{\mathsf{ev}}^{-1} \tag{6.2.11}$$

where

$$\tau_{\text{gr}}^{-1} = \sum_{i=1}^{I} iA_1 v_{\text{th}} \alpha(i) f(i,t) + \sum_{i=1}^{I'} iA_1 \sum_{m=1}^{M_i} v_{\text{th}}(i,m) \alpha_m^c(i) n_{i,m} \tag{6.2.12}$$

and

$$\tau_{\text{ev}}^{-1} = \sum_{i=1}^{I} iA_1 v_{\text{th}}(i) \alpha(i) f(i,t) \frac{1}{\mathbf{S}^i} \frac{1}{b_i} \alpha_*(i) + \sum_{i=1}^{I'} iA_1 \sum_{m=1}^{M_i} v_{\text{th}}(i,m) \alpha_m^c(i) n_{i,m} \frac{1}{\mathbf{S}^i} \frac{1}{b_{i,m}} \alpha_*^c(i,m) \tag{6.2.13}$$

such that

$$\boxed{\begin{aligned} \tau^{-1} = & \sum_{i=1}^{I} iA_1 v_{\text{th}} \alpha(i) f(i,t) \left\{ 1 - \frac{1}{\mathbf{S}^i} \frac{1}{b_i} \alpha_*(i) \right\} \\ & + \sum_{i=1}^{I'} iA_1 \sum_{m=1}^{M_i} v_{\text{th}}(i,m) \alpha_m^c(i) n_{i,m} \left\{ 1 - \frac{1}{\mathbf{S}^i} \frac{1}{b_{i,m}} \alpha_*^c(i,m) \right\} \qquad (6.2.14) \end{aligned}}$$

Here, we have introduced the following quantities:

m : indicates the individual chemical reactions, which contributes to the grain growth;

i : is the number of monomers added to an abritrary cluster;

v_{th} : is the mean thermal velocity of corresponding species;

α, α_m^c : are the sticking coefficients of the related species;

b_i, b_m^c : refer to the departure coefficients.

6.2.3.1 Remarks:

In our calculation we assume chemical equilibrium. In a general formulation the coefficients a_*, a_*^c b_i and $b_{i,m}^c$ describe non-equlilibrium effects. Such that in our assumption, they can be simplifed to the following equations, according to [Gail and Sedlmayr, 1988]:

$$\alpha_*(i) = \sqrt{\frac{T_{\text{dust}}}{T_{\text{gas}}}} \tag{6.2.15}$$

$$\alpha_*^c(i,m) = 1 \tag{6.2.16}$$

Furthermore, in the Appendix of [Gauger et al., 1990] a calculation for the departure coefficients b_i and $b_{i,m}^c$ is given which states that for chemical equilibrium

$$b_i = \frac{D_i(T_{\text{gas}})}{D_i(T_{\text{dust}})} \frac{T_{\text{dust}}}{T_{\text{gas}}} \tag{6.2.17}$$

and

$$b^c_{i,m} = \frac{D_{i,m}(T_{\text{gas}})}{D_{i,m}(T_{\text{dust}})} \bigg/ \frac{D^r_{i,m}(T_{\text{gas}})}{D^r_{i,m}(T_{\text{dust}})} \tag{6.2.18}$$

where $D_{i,m}$ and $D^r_{i,m}$ describe the dissociation constant of the molecule formed by the backward reaction of the growth reaction m.

6.2.4 Nucleation and growth of grains

The microscopic processes of formation and destruction of carbon clusters containing N carbon atoms (N-cluster) can be described by a master equation for the grain size distribution function $f(N,t)$, where this function characterises the full information about the dust complex at a given moment t, i.e. the number of grains of size N per hydrogen core. The time evolution of $f(N,t)$ is determined by the sum of the rates of all processes which change the size N of a cluster [Gail and Sedlmayr, 1988].

By using the master equation one could in principle solve the complete distribution function for the dust grains. In reality, since a 0.1μm dust grain contains on the order of 10^9 monomers, this is impractical. To solve the grain growth and evaporation problem, we will rather use the equation system that describes the time evolution of dust moments K_i of the grain size distribution function.

According to [Gauger et al., 1990] the time evolution of the above mentioned dust moments is then given by:

$$\frac{dK_0}{dt} = J_{N_l} \tag{6.2.19}$$

$$\frac{dK_i}{dt} = N_l^{i/d} J_{N_l} + \frac{i}{d}\frac{1}{\tau} K_{i-1} \quad \text{with } i = 1...3 \tag{6.2.20}$$

where N_l is the minimum cluster size of a macroscopic particle, i.e. the lower size limit of the distribution function.. Particles are assumed to be spherical, which means for the spatial dimension $d = 3$.

For dust growth, J_{N_l} is the creation rate of clusters of size N_l. In this case J_{N_l} corresponds to the stationary nucleation rate J_*. If we consider dust evaporation then J_{N_l} is the destruction rate. τ^{-1} is the net growth rate, which includes the effects of dust destruction. In the case where efficient nucleation is possible, the reverse processes are negligible. Therefore $\tau \sim \tau_{\text{gr}}$. Furthermore, it has been shown through numerical studies, that the first term on the right hand side of equation **(6.2.20)** can be neglected. If this term is not neglected then the average grain size K_3/K_0, is equal to the critical cluster size N_* as expected, and if the term is neglected then K_3/K_0 is zero, which is in principle not correct. However, when K_3/K_0 becomes large compared to N_*, both solutions approach each other and, since this happens before significant dust formation, we can neglect the term [Gail and Sedlmayr, 1988].

If the consumption of carbon in the gas phase by condensation to the solid phase is taken into account, another equation is added to the moment K_3 which links the chemical abundance to the carbon cores in the gas phase ϵ_C:

$$\epsilon_{\mathsf{C}} = \epsilon_{\mathsf{C},0} - K_3(t) \tag{6.2.21}$$

with $\epsilon_{\mathsf{C},0}$ being the carbon-core abundance of the dust free case.

The knowledge of the moments suffices to describe both, the interaction with the radiation field and the dust component . The relation between the moments and grain size distribution function is then given by

$$K_i(t) = \sum_{N_l}^{\infty} N^{i/d} f(N, t) \tag{6.2.22}$$

The derivation of these moments gives the opportunity to obtain different physical quantities, such as the:

Particle density n_d for grains of size $\geq N_l$:

$$n_d = K_0;$$

Average grain radius:

$$\langle r \rangle = r_0 \frac{K_1}{K_0}$$

with r_0 being the radius of the monomer.

Average particle size:

$$\langle N \rangle = \frac{K_3}{K_0}$$

Number density n_c of the monomers condensed into grains of size $\geq N_l$:

$$n_c = K_3$$

6.3 Dust formation in the binary star system

The data of the stellar wind expansion velocity, the gas temperature, the gas mass density, the average number of dust grains and the mean particle radius (see also figures 6.8, 6.9, 6.10, 6.11, 6.12, 6.13 and 6.14) obtained previously with the CHILD code for a single star will now serve as the initial data for the donor star in the binary system. These data are adapted sufficiently close the donor star, in a region where we can assume that the influence of the companion star is negligible. In order to continue the evolution for the dust moments we use equations **(6.2.19)** and **(6.2.20)** as discussed in section 6.2.4, i.e.

$$\frac{dK_0}{dt} = J_{N_l} \tag{6.3.1}$$

$$\frac{dK_i}{dt} = \frac{i}{d}\frac{1}{\tau_{\mathsf{gr}}} K_{i-1}, \qquad i = 1..3 \tag{6.3.2}$$

The set of equations can be formally integrated to

$$K_0\,(t) = J_{N_l}\,t + C4 \tag{6.3.3}$$

$$K_1\,(t) = 1/6\,\frac{J_{N_l}\,t^2}{\tau} + 1/3\,\frac{C4\,t}{\tau} + C3 \tag{6.3.4}$$

$$K_2\,(t) = 1/27\,\frac{J_{N_l}\,t^3}{\tau^2} + 1/9\,\frac{C4\,t^2}{\tau^2} + 2/3\,\frac{C3\,t}{\tau} + C2 \tag{6.3.5}$$

$$K_3\,(t) = \frac{1}{108}\,\frac{J_{N_l}\,t^4}{\tau^3} + 1/27\,\frac{C4\,t^3}{\tau^3} + 1/3\,\frac{C3\,t^2}{\tau^2} + \frac{C2\,t}{\tau} + C1 \tag{6.3.6}$$

Where the integration constants $C1 \ldots C4$, will be determined by the adapted moment-solution of the CHILD-code evolution.

6.4 Preparation of initial data - modelling for the donor star

The following section discusses the use of the CHILD-code model, developed at the "Zentrum für Astronomie und Astrophysik" from the Technical University Berlin. This code was successfully used to describe dust driven winds and dust condensation in a spherical symmetric geometry. It is prepared to derive the dust evolution in a single star environment based on the principles discussed in the previous sections [Gail et al., 1984], [Gail and Sedlmayr, 1985], [Gail and Sedlmayr, 1987], [Gail and Sedlmayr, 1988], [Gauger et al., 1990], [Schirrmacher et al., 2003].

We make use of the one dimensional CHILD-code to model the onset of nucleation and dust evolution in the very close environment to R_* of the donor star (Mira type). As mentioned before we consider that in this region, the influence of the companion star is neglectable, such that we can consider a spherical symmetric problem.

The results we obtain will then serve as initial data in the following numerical evolution of the full binary system. Several model parameters are used to describe the basic features of a pulsating dust forming circumstellar shell of a Mira type donor star. In the following we give a basic description of the motivation for the values we used in our simulations.

Stellar mass - M_*: for this parameter we need to consider the total mass, which includes the mass of the circumstellar shell and the mass of the donor star. We are considering C-giants, which are AGB objects [Jura, 1991]. For these objects the central star is believed to have a minimum mass of 0.55 M$_\odot$ [Schönberner, 1983]. in this way, the minimum mass of our donor star, is such that $M_* > 0.55$ M$_\odot$. The maximum mass of our star, is given by the initial mass of the star when it is located in the main sequence. For a C-giant on the AGB this would be 4 M$_\odot$. However we have to take into account that a considerable part of the mass has already been lost by the time the dust driven winds arise (i. e., during the final AGB phases). This lowers the upper limit, such that the star should have a mass in the range: 0.55 M$_\odot < M_* \leq 1$ M$_\odot$.

Stellar luminosity - L_*: Observations of AGB stars do not give accurate measurements of the luminosity. However, some of the most considered works indicate the range: 2×10^3 L$_\odot$ $< L_* < 5 \times 10^4$ L$_\odot$ [van der Veen and Rugers, 1989].

Stellar temperature - T_*: Effective temperatures for C-giants have been determined in the range: 2400 K $< T_* < 3200$ K [Tsuji, 1981].

Mass loss rate - $\dot{M}$: For dust forming AGB stars, observations indicate mass loss rates of 10^{-7} M$_\odot$yr^{-1} to 10^{-4} M$_\odot$yr^{-1} [Knapp and Morris, 1985].

Carbon abundance - ϵ_C: Estimations of the ratio of C/O in C-rich AGB stars have given a wide range of values. [Lambert et al., 1986] indicated a C/O ratio in the range $1 \leq \epsilon_C/\epsilon_O \leq 1.6$, with the majority of the stars having $\epsilon_C/\epsilon_O < 1.2$. Higher values were found by [Gow, 1977] $1 \leq \epsilon_C/\epsilon_O \leq 10$, while the work of [Frantsman and Eglitis, 1988] indicate $\langle \epsilon_C/\epsilon_O \rangle = 1.7$. Recent works considering dust formation in the environment of C-stars, have considered ranges of $1.2 \leq \epsilon_C/\epsilon_O \leq 2.0$ [Winters, 1994].

Pulsation period - **P**: For Mira-type stars and LPVs observations indicate pulsation periods in the range: 80 d $< P < 1000$ d. Recent observations of C-rich objects indicate periods up to 750 d.

Velocity amplitude - Δv_p : Velocity amplitudes cannot be directly determined from observations and are therefore based on modelling studies. These indicate as a lower limit $\Delta v_p < 1$ kms^{-1}. For values greater than this limit the shell structure is almost independent of the velocity, as long as a maximum limit of 10 kms^{-1} is not crossed [Fleischer, 1994].

6.4.1 Model parameter

Taking into account the considerations discussed above, we choose the following parameters for our computation:

- Effective temperature: $T_{\texttt{eff}} = 3000$ K;
- Stellar Mass: $M_* = 1$ M$_\odot$;
- Stellar Luminosity: $L_* = 4.618 \times 10^3$ L$_\odot$;
- Piston characteristics: Period: $P = 700$ d; Initial velocity amplitude: $\Delta v_p = 5$ kms^{-1};
- Abundance ratio of Carbon to Oxygen: $\epsilon_C/\epsilon_O = 1.3$;
- Rosseland mean opacity for the gas: $\chi_{g,R}/\rho = 2.0 \times 10^{-4}$ cm^{-2}g^{-1}.

The dust extinction is given by the small particle limit of Mie-Theory. Spherical grains are considered, and an average is made over the grain size distribution function:

$$\chi_{d,\lambda}(r) = \frac{3}{4} V_0 K_3(r) C_\lambda^{ext} \tag{6.4.1}$$

where V_0 is the volume of a carbon monomer with hypothetical radius a_0, K_3 is the third moment of the grain size distribution function and $C_\lambda^{ext} = C_\lambda^{abs} + C_\lambda^{sca}$, which are the absorption and scattering cross-sections of small spherical particles.

The following pictures show an time evolution example of the radial profile for the hydrodynamical and dust quantities, derived on equidistant grid of time instants $t_n = t_0 + n \times 0.5P$ by the CHILD - code. The time period considered here is from 10.0 to 11.5, as indicated in the figures. As can be seen in figure **(6.12)** the onset of dust formation occurs after 2 R_*.

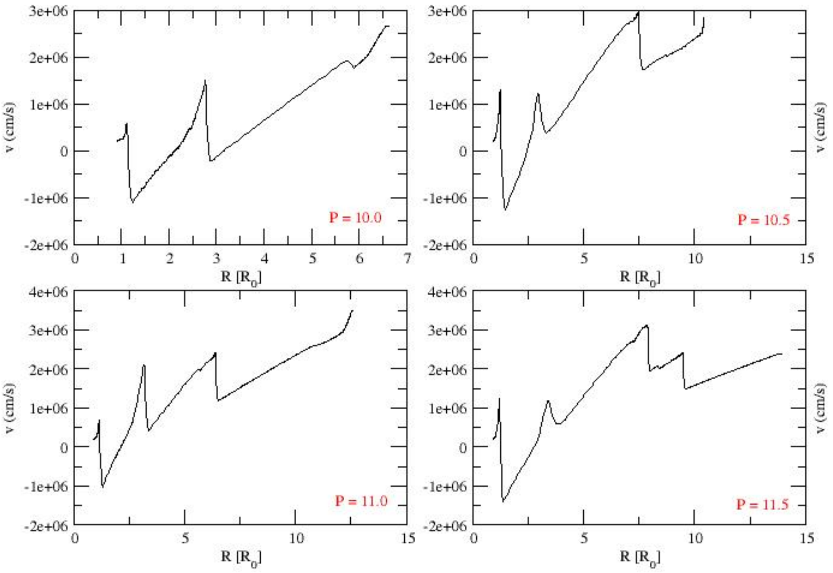

Figure 6.8: Radial profile of the expansion velocity of the gas.

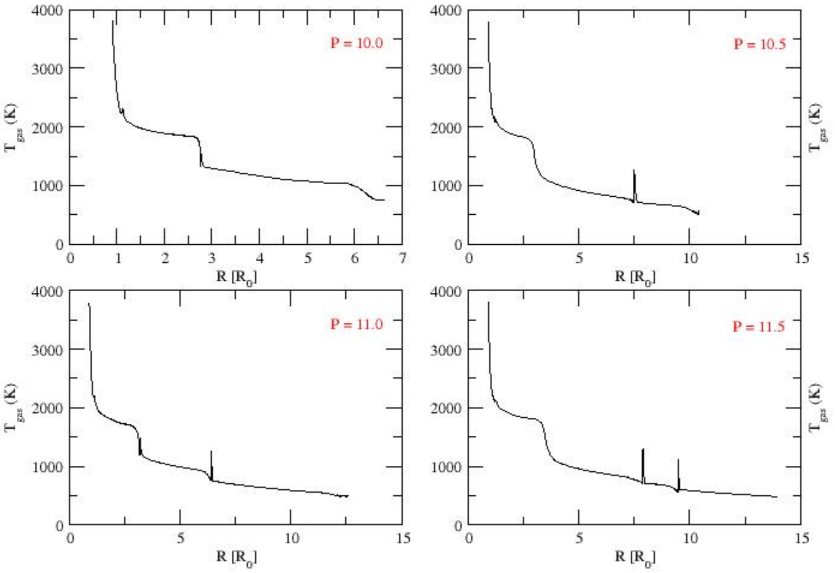

Figure 6.9: Radial profile of the gas temperature.

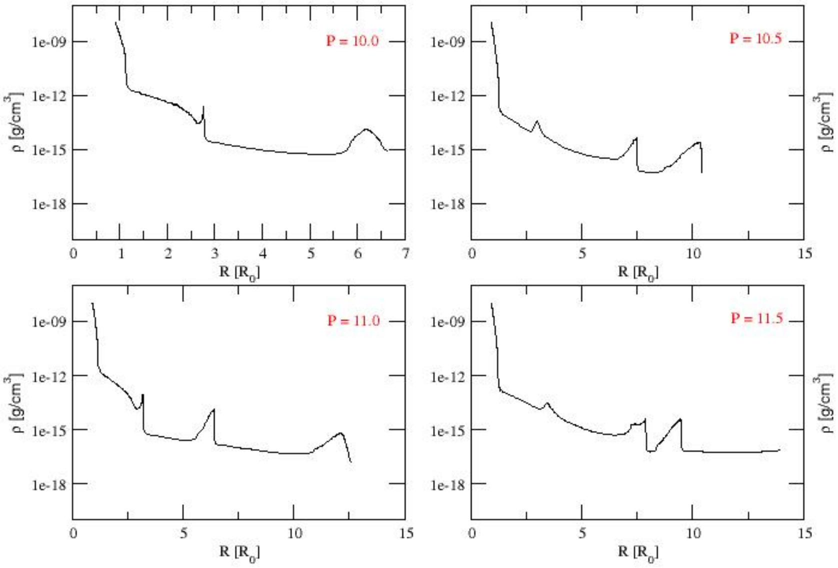

Figure 6.10: Radial profile of the gas mass density.

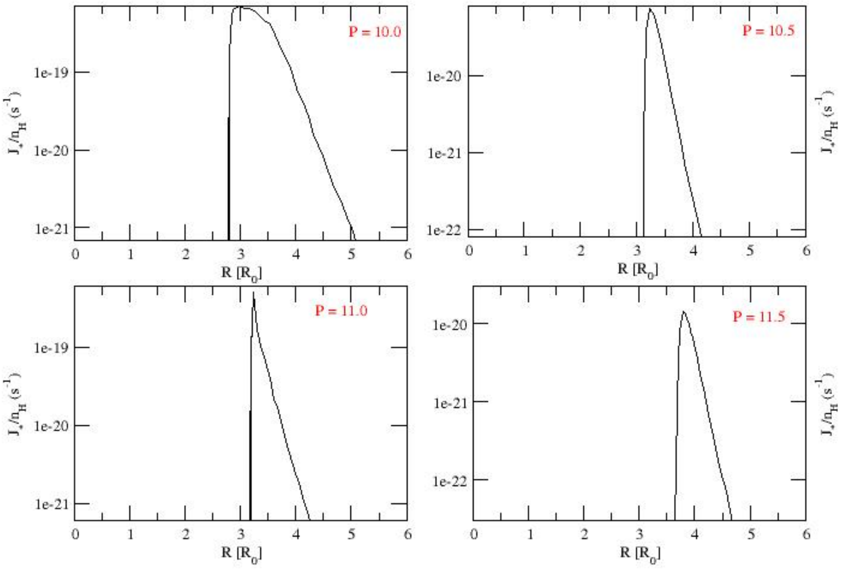

Figure 6.11: Radial profile of the scaled nucleation rate per second and Hydrogen atom.

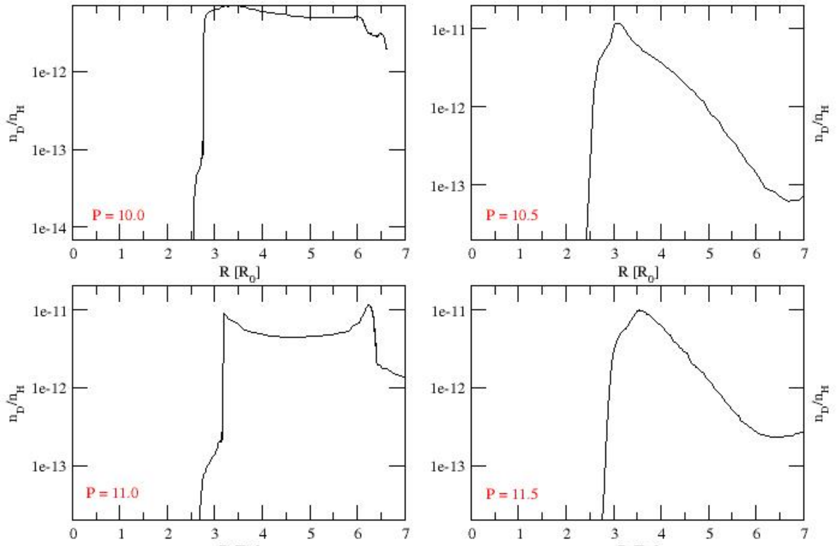

Figure 6.12: Radial profile of the scaled number of dust grains per Hydrogen atom.

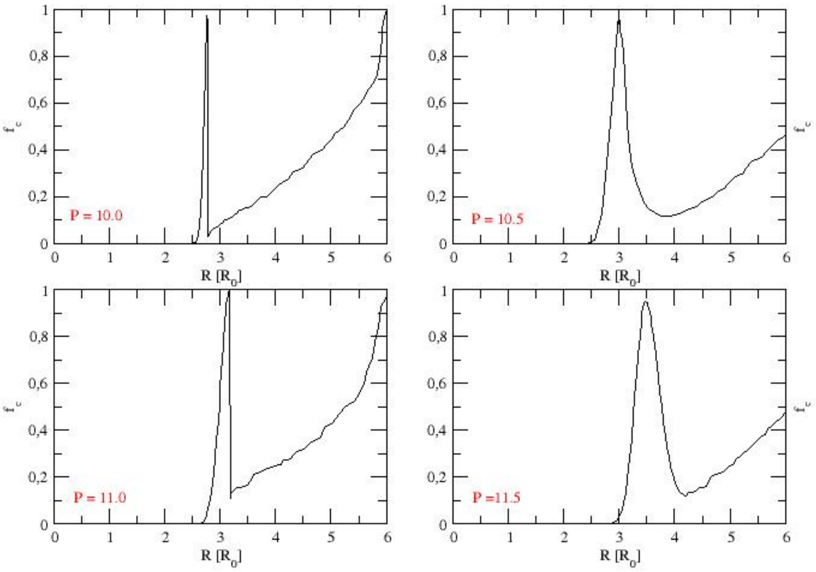

Figure 6.13: Radial profile of the degree of condensation.

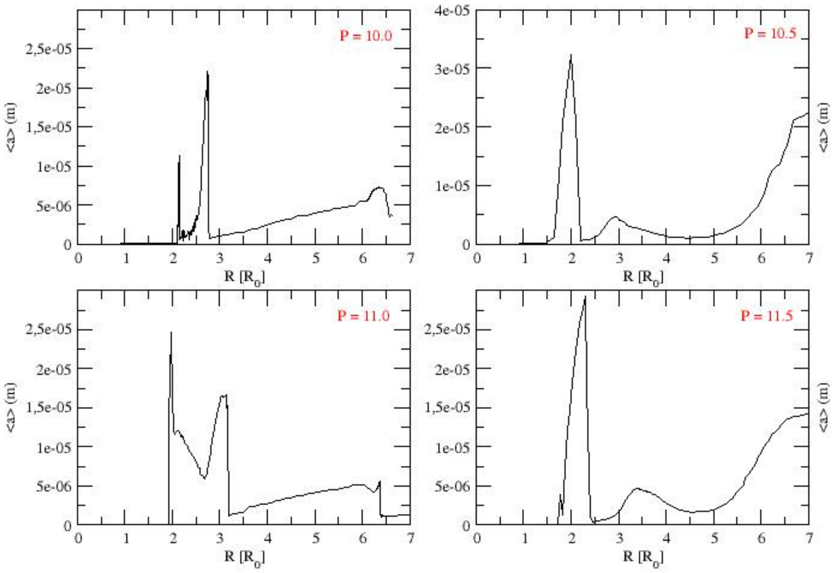

Figure 6.14: Radial profile of the mean particle radius.

Chapter 7

Numerical simulation

7.1 Modelling of a stellar wind in a binary system

In the following section we present the results of our full numerical computation. For this we include the components of the hydrodynamical, radiation transport, chemical and dust derivation discussed in the previous chapters. The relation between the different components are show in figure 2.2, where for every time step we computed the needed quantities in the following order

1. hydrodynamical evolution step of the stellar wind key quantities (i.e. density ρ, velocity field **v** and specific energy e) in a one fluid approach, by using the SPH - evolution of the equation **(4.1.1)**;

2. determination of the chemical equilibrium composition (see equation **(6.1.8)**) for a carbon rich atmosphere of the donor star, C/O $= 1.3$;

3. solving of the dust - moment equations **(6.2.19)** and **(6.2.20)** for K_i $(i = 0...3)$;

4. determination of the resulting radiation field with its temperature stratification by means of the Monte Carlo Code based on this new density distribution in a similar manner as in section 5.4.3.3, but now applied to a dynamical situation of a dust driven wind.

5. The newly computed dust complex and radiation field will couple back to the next evolution time step.

Our initial settings are based on the single star time evolution for a Mira - star presented in section 6.4, now adopted to the binary system with the second star being a brown dwarf with a mass of 0.08 M$_\odot$.

The separation A between the stars is set to 5 AU on a circular orbit such that according to **(3.2.3)** it follows for $\mid \mathbf{\Omega} \mid = 0.079 \times\ 2\pi$/yr and an orbital period $P_{\text{orb}} = 12.65\ \mathbf{yr}$. For the numerical computation we scaled the length, time and mass units according to equation **(3.2.16)**, where for this mass relation of the two stars the derived values are

$$
\begin{aligned}
MU &= 0.15522 \times 10^{30} \text{ kg} \\
TU &= 2.014 \text{ yr} \\
LU &= 7.47 \times 10^{8} \text{ km}
\end{aligned}
$$

The Lagrange points in this unit system are then derived to (see section 3.2.3):

$$
\begin{aligned}
&\mathbb{L}_1 = [0.604, 0], \quad \mathbb{L}_2 = [1.260, 0], \quad \mathbb{L}_3 = [-1.042, 0] \\
&\mathbb{L}_4 = [0.397, \frac{1}{2}\sqrt{3}], \quad \mathbb{L}_5 = [0.397, -\frac{1}{2}\sqrt{3}]
\end{aligned}
\tag{7.1.1}
$$

The here considered interaction of the gainer star (brown dwarf) on the the dust driven wind, is due to gravitational force and radiation field, i.e. by shadowing (see section 5.4.3.3) and backwarming, where luminosity and temperature of the gainer star are assumed to be negligible. For the numerical evolution we have made a boundary set up as described in section 2.2. The simulation is modelled in this way, so that the derived time sequence of the single star evolution now serves as the time dependent boundary condition at the donor star.

The jump conditions of the radial shock at this boundary are given by the equations for mass conservation, momentum and energy in a comoving frame of the shock (see also Appendix C.1.0.1).

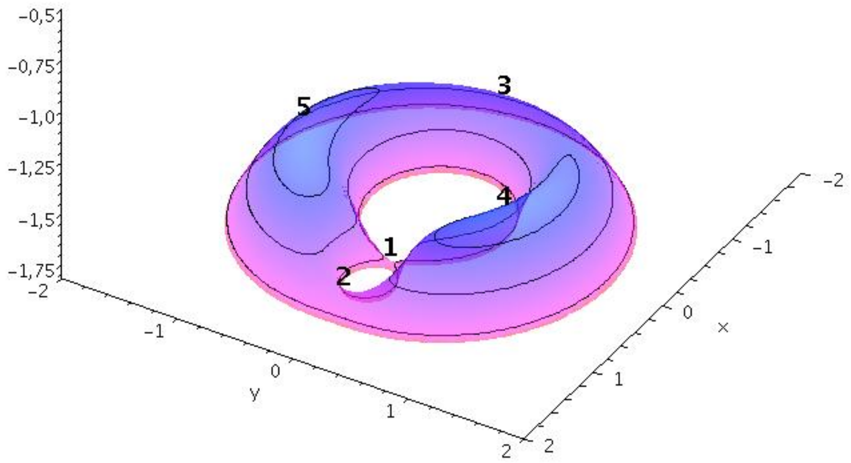

Figure 7.1: Roche potential Φ in the xy plane, $z = 0$. The Lagrange points $\mathbb{L}_1$ to $\mathbb{L}_5$ are indicated by the numbers.

Figure 7.1 shows the Roche potential $\Phi(x, y, z)$ in the xy plane for $z = 0$ and the different potential values at the Lagrange points. As we mentioned in section 1.8.1 the Roche surface can be maintained as an equilibrium shape by the star. One should note that the Roche potential only includes the gravitational interaction and no radiation force or hydrodynamical properties. In figure 7.1 we can see that the $\mathbb{L}_1$, $\mathbb{L}_2$, $\mathbb{L}_3$ all lay at the saddle points on the surface and that $\mathbb{L}_1$ has the lowest value of the potential.

The equipotential passing through the inner lagrangian point $\mathbb{L}_1$, limits two conjugated volumes which are know as the Roche lobe. For a star inside the Roche lobe a steady-state configuration is still possible, since in this case the gradient of the Roche potential is counter balanced by the gradient of the gas pressure. When the star reaches the Roche lobe the total force equals zero in the inner lagrangian point, since the pressure gradient at this point cannot be equalled the matter will start to flow. The fluid particles originating at the expanding atmosphere of the donor star will initially fill up the Roche lobe and stream through $\mathbb{L}_1$ in direction of the gainer star, where a certain number of particles would fall inside (free fall boundary condition, see section 2.2). The remaining particles will then tend to escape the system through $\mathbb{L}_2$.

In contrast to the single star case where we can assume a spherical symmetric density fall off with $\sim 1/r$, in the binary system we have a situation where the trajectories of the fluid particles are not radial as shown in section 3.2.4, but they converge towards the $\mathbb{L}_1$ point, which in the dynamic sense acts as an attractor, resulting in an increase of pressure and consequently in an increase of the nucleation rate.

In the following sections we present the results (density ρ, nucleation rate J_* and velocity field $\mathbf{v}$) of our 2 dimensional simulation for the extension of the spherical symmetric initial setup, with the initial parameters described above and in section 6.4.1. We will present 2 different models and we will separate the evolution of the common envelope in three main stages, which are the Roche lobe fill up, the Roche lobe overflow and the extended envelope. In the figures shown below, the donor and gainer stars are indicated by the grey circles. While the donor star is portrayed in a realistic scale (at the boundary where we adopt the initial data from the CHILD code), we have increased the radial extension of the gainer star not only for better visualisation purposes, but more importantly to account for the area of any possible accretion disk, which we do not consider in our simulations.

7.2 Model 1 - stationary dust driven wind

In this model we investigate the behaviour of the dust driven atmosphere for the above described binary system, in case of a stationary dust driven wind [Gail and Sedlmayr, 1985]. This means that we do not consider the piston model described in section 2.2. In place of equations **(2.2.1)** and **(2.2.2)**, we use a non-moving inner radius and a constant initial velocity, in agreement with the wind equations **(2.1.12)** and **(2.1.13)**. For comparison purposes we consider a slow (2.5 kms^{-1}) and a fast wind (5 kms^{-1}).

7.2.1 Roche lobe fill up

Here we depict the stage of the evolution where the Roche lobe is nearly filled up by the wind of the donor star, and the influence of the gainer star is no longer neglectable, therefore showing the deviation from a single star system. In figures 7.2 and 7.3 we show the simulation results for the density and for the velocity field components v_x, v_y (black arrows), in the case of the slow and fast wind, respectively.

In the slow wind case, we have up rising and infalling fluid particles, due to the slow wind velocity, which results in strong density fluctuations around the star. Additionally, from the fact that the centre of the donor star is no longer the centre of gravity, the density distribution looses its spherical symmetry, and due to the fluctuations the outer layer is scattered. We also see that the velocity field (black arrows) clearly shows an azimuthal component due to the acting Coriolis force. Evolving local eddies are seen close to the star, resulting from the up rising and infalling fluid particles. In the fast wind case, the density distribution has a more homogeneous radial fall off and the strength of the density fluctuations is considerably lower than in the slow wind case. These fluctuations are only visible in the very close environment of the donor star, such that less particles are falling inward and the outer layer is now more adjusted to the Roche lobe. This is also seen in the velocity field which now has a stronger radial component than in the previous case.

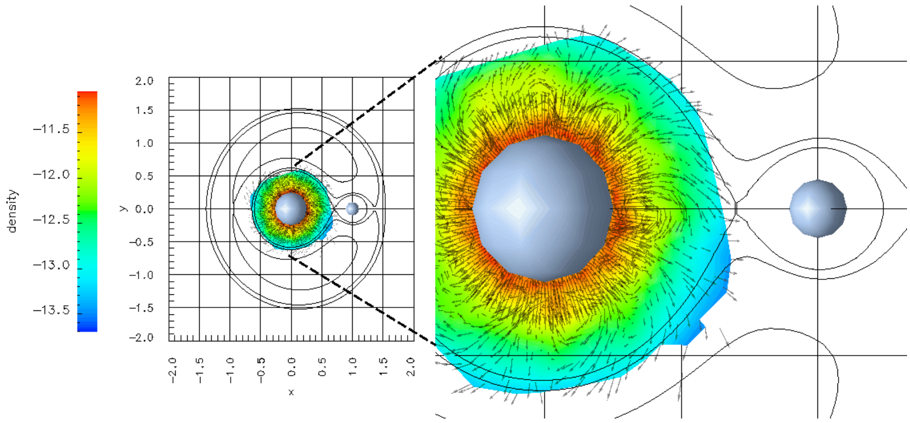

Figure 7.2: Model 1, Slow wind - Computation results for the density log(ρ) [gcm^{-3}] and the v_x, v_y components (black arrows) of the velocity field $\mathbf{v}$ (kms^{-1}) at the Roche lobe fill up. Indicated are also the equipotential surfaces, in the xy-plane, through the five lagrangian stability points $\mathbb{L}_1 ... \mathbb{L}_5$. **Left**: Full binary system; **Right**: Closer view of the system.

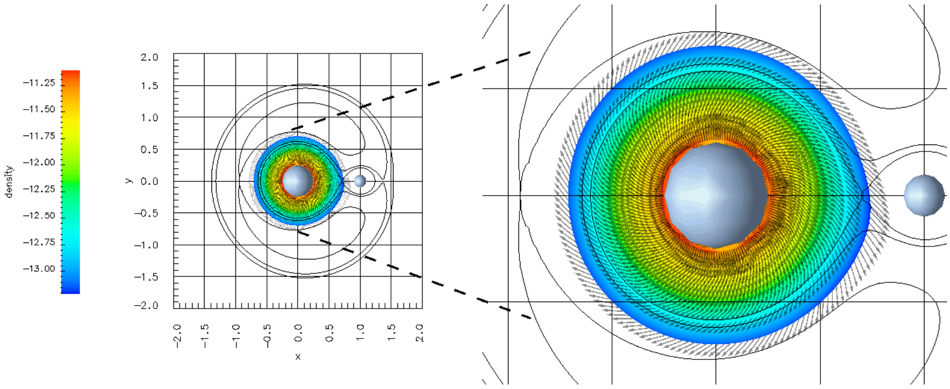

Figure 7.3: Model 1, Fast wind - Computation results for the density log(ρ) [gcm^{-3}] and the v_x, v_y components (black arrows) of the velocity field $\mathbf{v}$ (kms^{-1}) at the Roche lobe fill up. Same format as in figure 7.2.

Figures 7.4 and 7.5 show the nucleation rate for the slow and fast wind case, respectively. An effective onset of the nucleation is seen around 2 R_*, which is mainly concentrated slightly below the Roche lobe. Due to the density fluctuations in the slow wind case, the nucleation rate also displays strong fluctuations in the radial distribution. Our figures give only a snapshot of the highly dynamical stellar atmosphere and of the location of the high nucleation rate regions (observed for the slow wind case, figure 7.4). These regions will permanently change location during the time evolution.

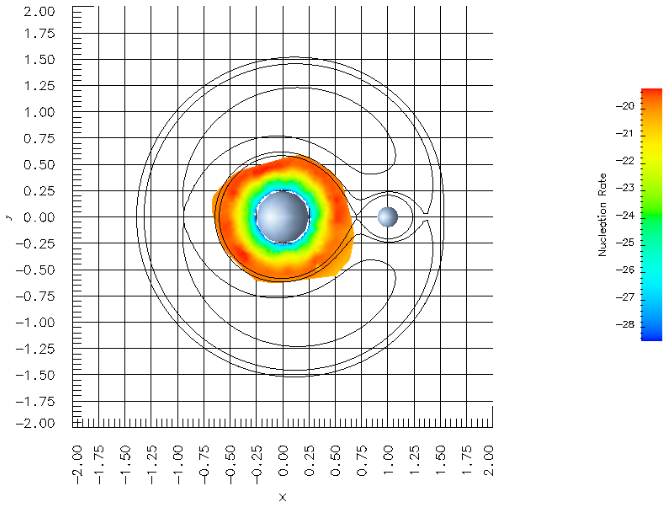

Figure 7.4: Model 1, Slow wind - Computation results for the nucleation rate $\log(J_*/n_\mathrm{H})$ $[s^{-1}]$, at the Roche lobe fill up.

For the fast wind case, the small density fluctuations close to the star do not influence the distribution of the nucleation rate. The distribution is more homogeneous and the outer and inner layers are also more clearly defined when compared to the previous case.

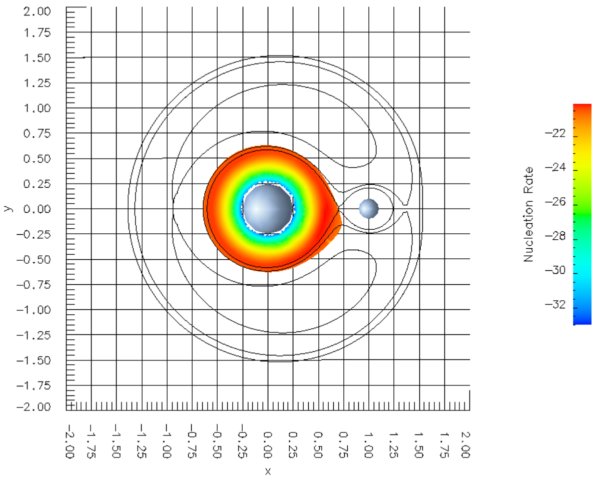

Figure 7.5: Model 1, Fast wind - Computation results for the nucleation rate $\log(J_*/n_\mathrm{H})$ $[s^{-1}]$, at the Roche lobe fill up.

7.2.2 Roche lobe overflow

In this section we show an intermediate stage of our evolution, identified as the Roche lobe overflow. In this stage the fluid particles start to overflow mainly via the $\mathbb{L}_1$ point.

In figure 7.6 (slow wind) we can see how due to the different azimuthal velocities that the particles achieve, a certain amount of the wind material will loop around the gainer star while another part is capable of leaving the system mainly via $\mathbb{L}_2$. This behaviour was clearly predicted in section 3.2.4 (see figure 3.6). The particles which form loops around the gainer could form an accretion disk, however, we have suppressed this effect by the infalling boundary conditions, which are placed at the outer boundary of a possible accretion disk.

In comparison to the previous stage (Roche lobe fill up) one can observe the continuous increase of the density inside the Roche lobe and a decrease of the fluctuations due to the increasing gravitational influence of the gainer star, and by this the stripping off effect on the atmosphere of the donor star.

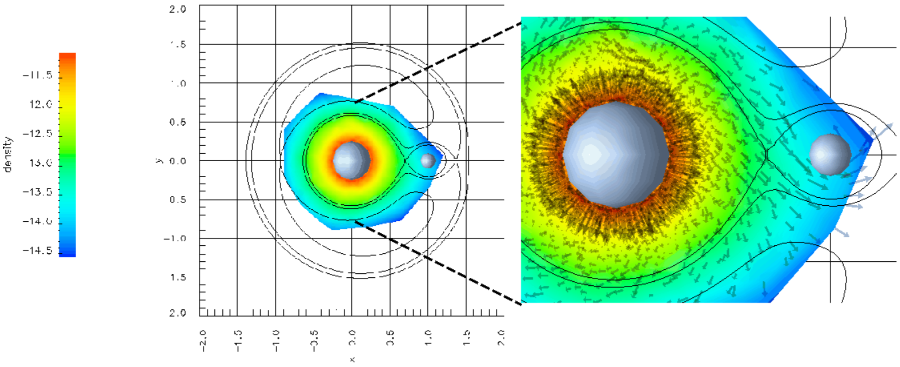

Figure 7.6: Model 1, Slow wind - Computation results at the Roche lobe overflow. Same format as in figure 7.2.

In the fast wind case (figure 7.7) we observe the same effect in the near of the gainer star, with part of the particles looping around the star and another part leaving the system via $\mathbb{L}_2$. In both cases we can see a rarefaction of density due to an increase of the velocity and gravitational influence of the gainer star.

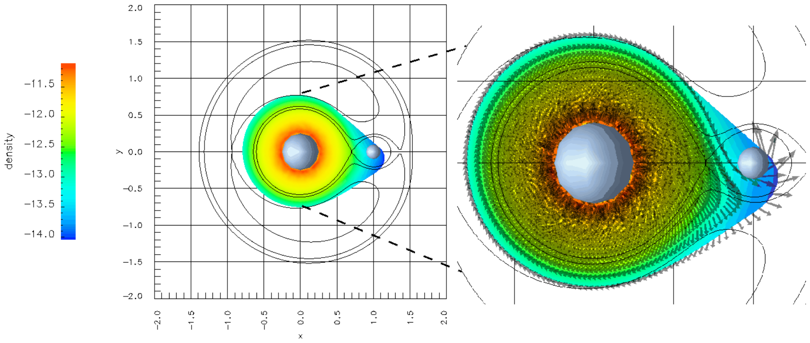

Figure 7.7: Model 1, Fast wind - Computation results at the Roche lobe overflow. Same format as in figure 7.2.

The nucleation rate seen in figure 7.8 (slow wind) shows increasing fluctuations, due to increasing velocity turbulence, which leads to a inhomogeneous distribution. As we saw in the nucleation rate distribution at the previous stage (see figure 7.4) the outer layers can locally reach high values. Since this quantity is directly related to the radiated acceleration of the wind due to the transmission of the dust grains momentum to the ambient gas by local collisions, it is easier for a small amount of fluid particles to become gravitationally unbound, in this case.

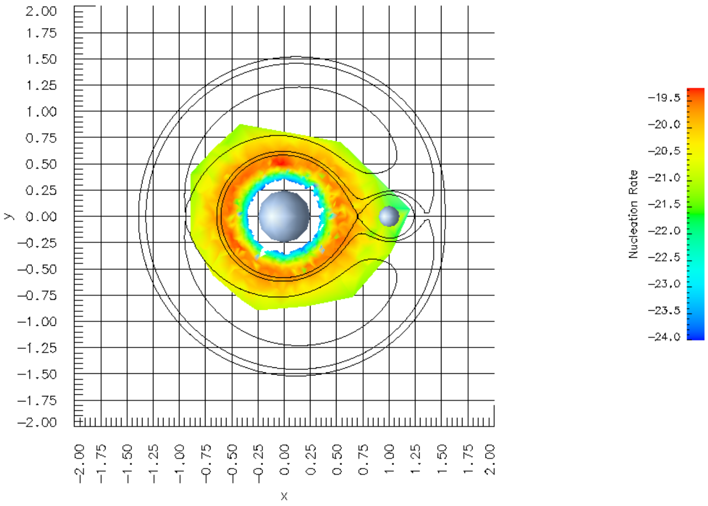

Figure 7.8: Model 1, Slow wind - Computation results for the nucleation rate $\log(J_*/n_{\mathrm{H}})$ $[s^{-1}]$, at the Roche lobe overflow.

In the fast wind case (see figure 7.9), the nucleation rate distribution is homogeneously concentrated in a ring-like structure around the donor star, which is deviated to the left of and below $\mathbb{L}_1$.

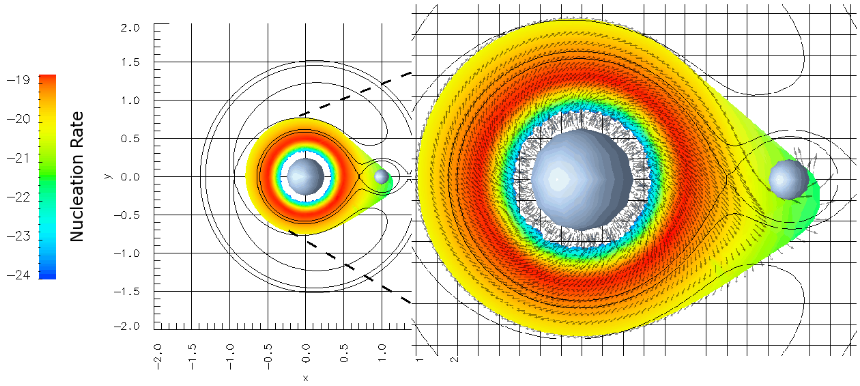

Figure 7.9: Model 1, Fast wind - Computation results for the nucleation rate $\log(J_*/n_{\mathrm{H}})$ $[s^{-1}]$ and the v_x, v_y components of the velocity field $\mathbf{v}$, at the Roche lobe overflow. **Left**: Full binary system; **Right**: Closer view of the system.

7.2.3 Extended envelope

The following figures show the nucleation rate and the velocity field components v_x, v_y, for the extended envelope case, i.e. the last stage of the simulation. We present only a closer look at the system focusing on the region around the gainer star. The colour scale is the same as in the previous stage and the contours used in both plots show the iso-surfaces for nucleation rates of -19.1, -20.0, -20.2, -20.4, -20.6, -20.8 and -21.2. For a better visualisation we do not show the potential lines of the Roche potential.

In both cases, we can mainly differentiate two regions of high nucleation rate. In region **A**, we see the part of the matter that does not interact directly with the stream from $\mathbb{L}_1$. It forms the external part of the circumbinary envelope. In region **B**, a part of the matter makes a complete revolution around the gainer star and mixes with the gas stream flowing from $\mathbb{L}_1$, as depicted by the bold black arrow. Similar situations have been described by previous authors, for the particle flow [Sawada et al., 1986a, Sawada et al., 1986b], although they did not consider radiation pressure on dust particles, nor the nucleation processes in the fluid.

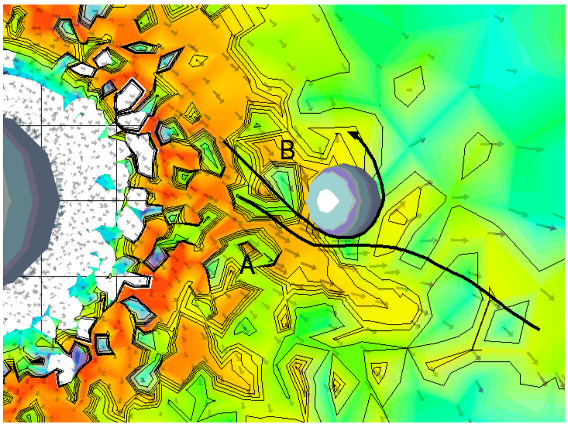

Figure 7.10: Model 1, Slow wind - Computation results for the nucleation rate $\log(J_*/n_{\mathsf{H}})$ $[s^{-1}]$ and the v_x, v_y components of the velocity field $\mathbf{v}$, in the extended envelope. Indicated are two regions of interest described in the text.

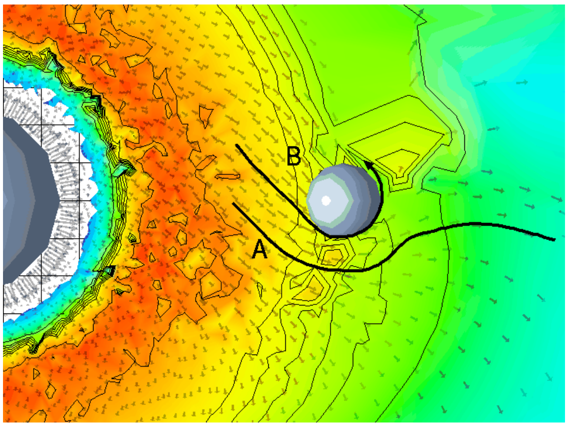

Figure 7.11: Model 1, Fast wind - Computation results for the nucleation rate $\log(J_*/n_{\mathsf{H}})$ $[s^{-1}]$ and the v_x, v_y components of the velocity field $\mathbf{v}$, in the extended envelope.

7.3 Model 2 - non-stationary dust driven wind

In this model we consider a non-stationary dust driven wind for the donor star, as a model for a C -Mira, and we include the piston model with a pulsation period of 700 d.

7.3.1 Roche lobe fill up

The distribution in this stage, shows a nearly radial symmetric decrease of the density with distance in the close environment of the donor star (figure 7.12). However the de-shaping caused by the filling up of the Roche lobe is already visible.

Due to our assumption of synchronous rotation of the stars, the onion like structure caused by the evolving shocks, seen in the one-dimensional models, are smoothed out and therefore not seen in our density distribution. Furthermore, in the one-dimensional evolution, rotation and the evolution of eddies in the expanding atmosphere are not regarded and do not influence the density profiles. Furthermore, in comparison with the slow wind case of model 1, we have here a higher radial velocity and pressure, such that the occurrence of local velocity turbulence and density fluctuations are smoothed out, similarly to the fast wind case. As a consequence, less particles are falling back to the donor star, than in the slow wind case. Furthermore, as the atmosphere expands the initially dominant radial velocity will be deviated in the clockwise rotating direction and will increase in amplitude, forming differential velocity layers, which produce eddies, in the outer atmosphere of the donor star.

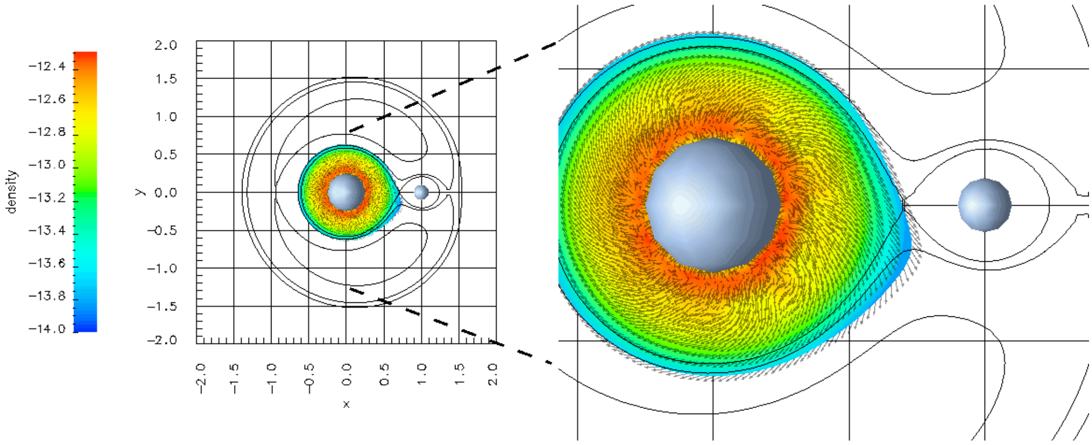

Figure 7.12: Model 2 - Computation results for the density ($\log(\rho)$ [gcm^{-3}]) and the v_x, v_y components of the velocity field $\mathbf{v}$ (kms^{-1}) at the Roche lobe fill up. The black lines indicate the equipotential surfaces through the five lagrangian stability points $\mathbb{L}_1 ... \mathbb{L}_5$. Left: Full binary system; Right: Closer view of the system.

As expected, the gainer's gravitational attraction causes an increase in the amplitude of the radial velocity field in the near of the $\mathbb{L}_1$ point. This results in a effect at $\mathbb{L}_1$, which causes an increase of the pressure and density, and consequent amplification of the nucleation rate.

In the distribution of the nucleation rate function (figure 7.13), we can see the onset of condensation located in a ring-like structure around 2.1 R_*, in our two dimensional

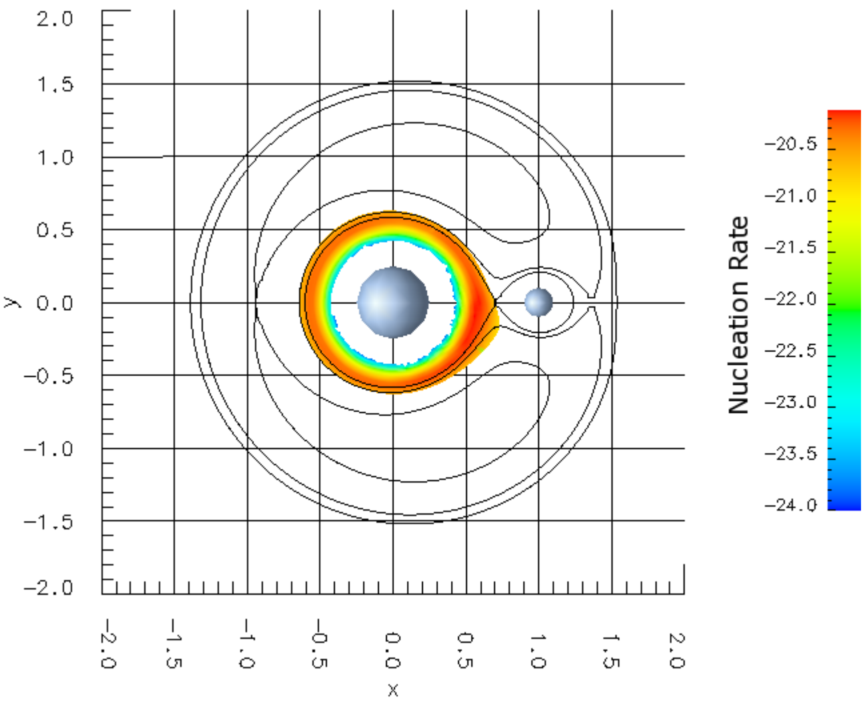

Figure 7.13: Model 2 - Computation results of the nucleation rate $\log(J_*/n_{\rm H})$ (s^{-1}) at the Roche lobe fill up.

evolution around the donor star, with a slightly enhanced nucleation rate in direction of and below $\mathbb{L}_1$. In comparison to the previous model for the fast wind, the onset of condensation occurs slightly further away, due to the energy input by the shock waves produced by the piston model. The inner ring in the nucleation rate distribution, is not as smooth as in the fast wind model, but smoother than in the slow wind simulation.

7.3.2 Roche lobe overflow

The density distribution at this stage is seen in figure 7.14. Due to strong evolved eddies, we can see the start of an inhomogeneous distribution in the environment of the Roche lobe surface where the azimuthal velocity component is strongly increased. The evolution of the inhomogeneities is better seen in figure 7.20 which shows a more detailed evolution with several time steps. The particles which accrete into the gainer star, are removed from the evolution, and only those with a high enough velocity will be capable of leaving the system through the $\mathbb{L}_2$ point, as evidenced by the small stream to the right of the gainer star. The $\mathbb{L}_2$ (which has the second lowest value of the Roche potential, see figure 7.1) and the $\mathbb{L}_3$ points act in a similar way to the $\mathbb{L}_1$ point, in this case causing the particles to leave the system.

The nucleation rate is shown in figure 7.15. We observe a shift and an extension of the effective condensation area outwards, with a maximum around the Roche lobe, due to the expanding envelope. In this stage we can see a fall off around of the nucleation rate around the gainer star due to the infalling fluid particles.

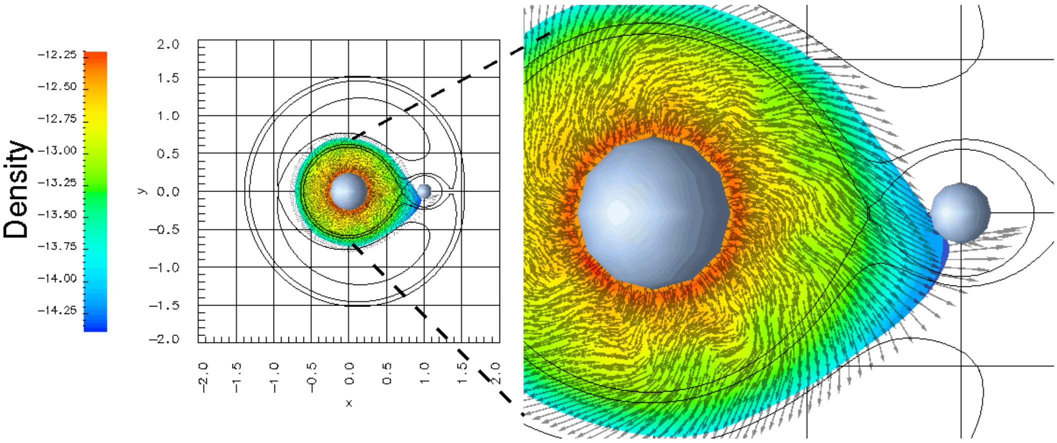

Figure 7.14: Model 2 - Computation results at the Roche lobe overflow. Same format as in figure 7.12.

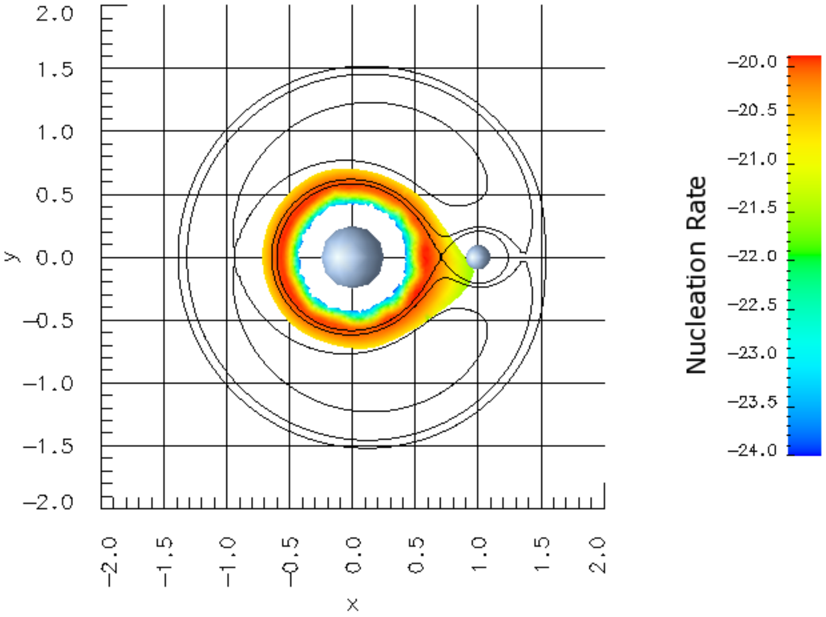

Figure 7.15: Model 2 - Computation results of the nucleation rate $\log(J_*/n_{\mathrm{H}})$ (s^{-1}) at the Roche lobe overflow.

7.3.3 Extended envelope

Figure 7.16 shows that at this stage the pressure of the matter is no longer counter balanced by the potential and the envelope is extended over the Roche potential, which results in an expanding atmosphere. The density shows strong perturbations, and deviates from the spherical shape as can be seen in the spiral-like structure evidenced by the contour lines. Small disturbances in the density distribution due to the up rising and infalling fluid particles are found to have a large impact on the dust forming system. This can be better seen in figure 7.17, showing the density distribution and the velocity field in the close environment of the donor star. The eddies present close to the star (also seen in the previous stages and in Model 1) will be amplified up to the outer layers of the donor star and seem to amplify the nucleation rate in these regions. This could be due to the interaction of fluid particles with different velocity components at different layers. The piston model continuously produces radial outward moving shock waves, at the inner boundary of the donor star. As they move outwards they will encounter previous layers which already have an azimuthal component, such that the radial outward moving particles will gain an azimuthal acceleration, while the particles in the pre-existing layer will be de-accelerated, giving rise to the evolving eddy structure.

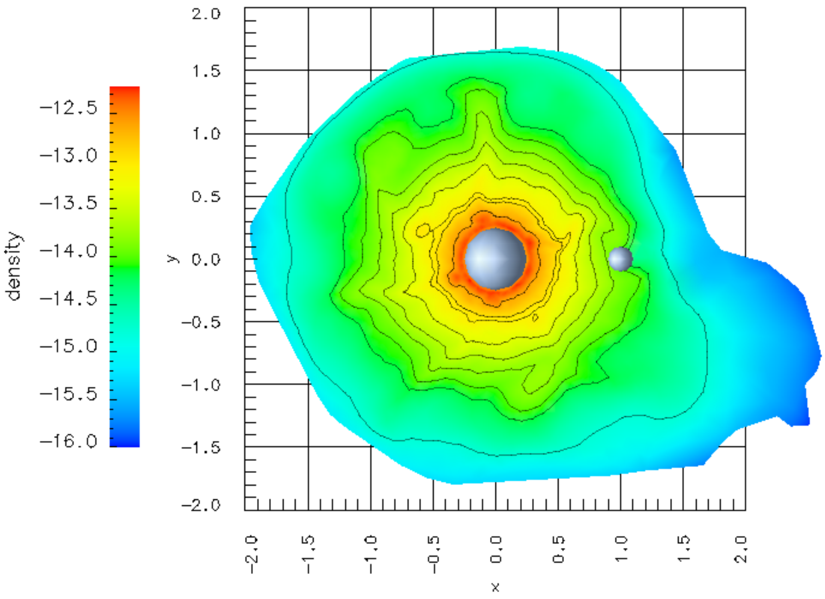

Figure 7.16: Model 2 - Computation results for the density ($\log(\rho)$ [gcm^{-3}]) in the extended envelope of the binary star system. Indicated are the contour lines for the density: −12.62, −12.97, −13.07, −13.37, −13.62, −13.82, −14.04, −14.17, −14.77.

The velocity field of the extended envelope (figure 7.18) once again shows the onset of a spiral-like structure for the particle distribution. The closer look at the gainer star (right panel) shows an increase of the velocity due to the radial infalling or revolving particles around the gainer star due to the strong gravitational attraction, resulting in nearly circular orbits for the fluid particles, which we assume would lead to the formation of an accretion disk.

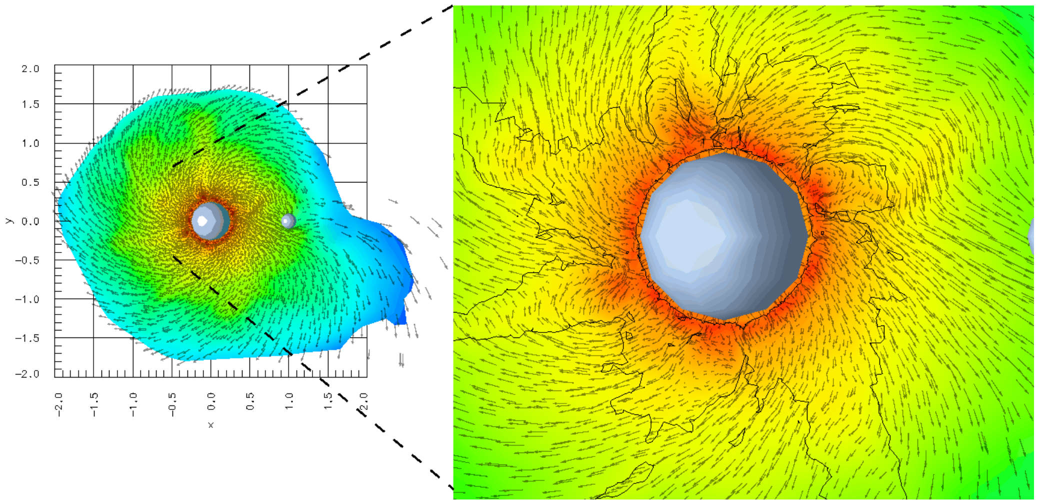

Figure 7.17: Model 2 - Computation results for the density (log(ρ) [gcm^{-3}]) and the v_x, v_y components of the velocity field $\mathbf{v}$ (kms^{-1}) in the extended envelope of the binary star system. **Left**: Full binary system; **Right**: Closer view of the system. The colour code is the same as in figure 7.16.

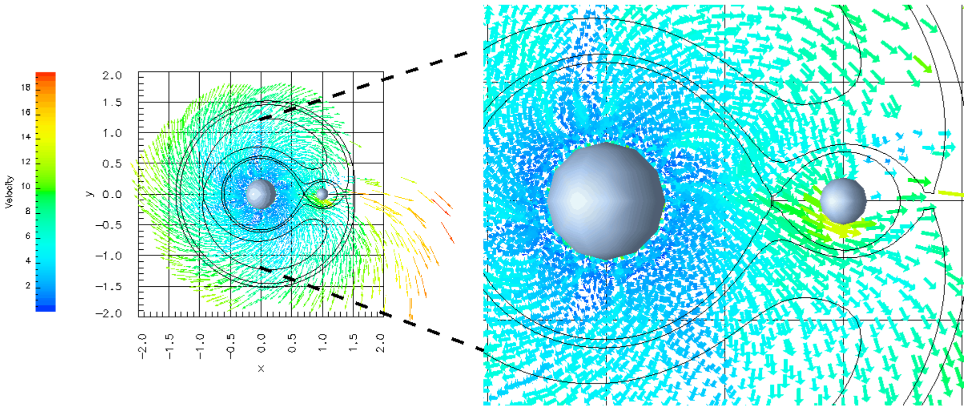

Figure 7.18: Model 2 - Computation results for the v_x, v_y components of the velocity field $\mathbf{v}$ (kms^{-1}) in the extended envelope. Same format as in figure 7.12.

Figure 7.19 shows the nucleation rate, with its contour lines and the velocity field, at this stage of the evolution. Similarly to the previous model, we can observe the development of two shock fronts (**A** and **B**), which cause a local increase of the nucleation rate. Furthermore, a trailer-like structure can be seen at this stage, to the right of the gainer star, with its origin near $\mathbb{L}_2$. Our simulation indicates that this feature could be due to an interplay of the radiation blocking properties of the gainer star, which leads to a decrease of temperature on the shadow side (umbra), and the shock front **B**, which leads to an increase of density and pressure. All three components give ideal conditions for dust formation. As a result the region of possible nucleation in a binary system is extended into the trailing region behind the gainer star. By this, the dust formation region looses the spherical symmetry seen in the models for non-rotating single star dust evolution.

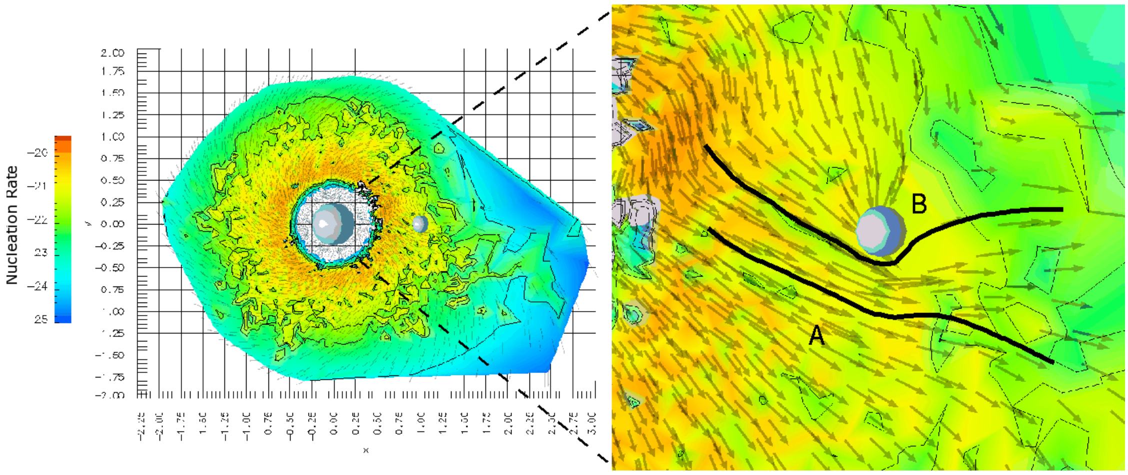

Figure 7.19: Model 2 - Computation results of the nucleation rate log($J_*/n_{\mathsf{H}} =$ (s^{-1}) and the v_x, v_y components of the velocity field **v** (kms^{-1}) in the extended envelope. **Left**: Full binary system; **Right**: Closer view of the system.

7.4 Time sequence of the evolution

The following figures show a time sequence of different stages during the numerical evolution of Model 2.

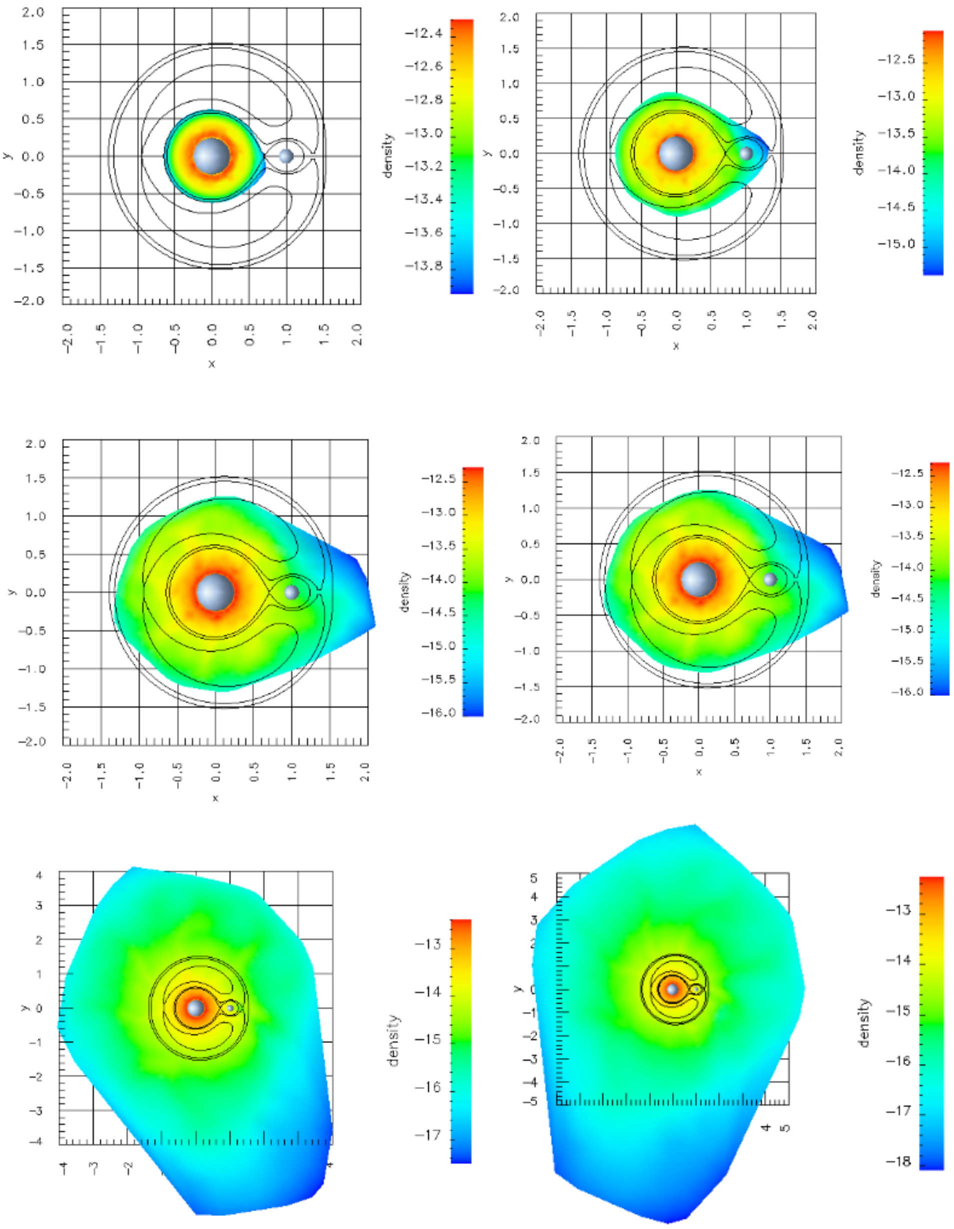

Figure 7.20: Computation results for the density at different stages of the evolution.

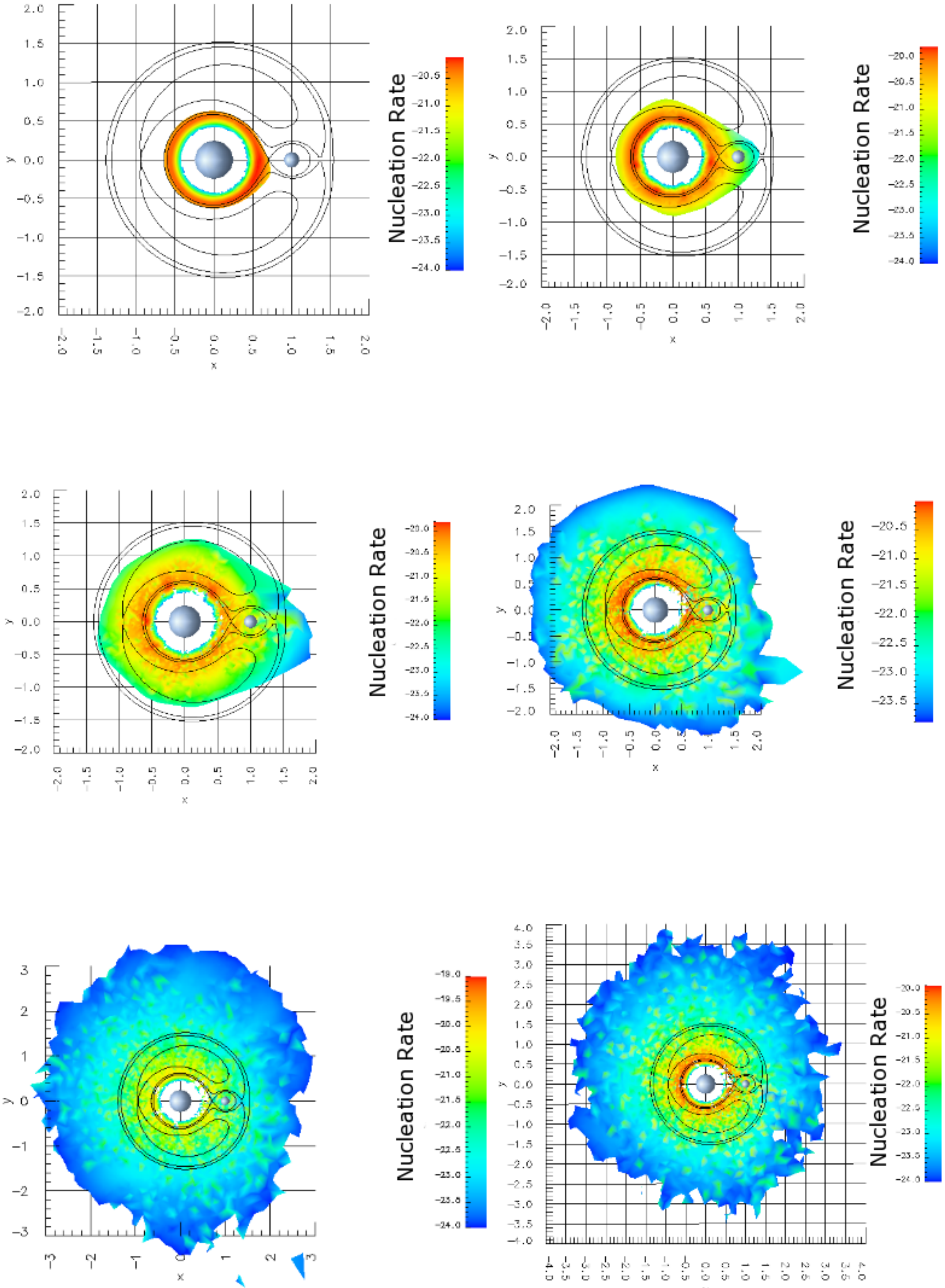

Figure 7.21: Computation results for the nucleation rate at different stages of the evolution.

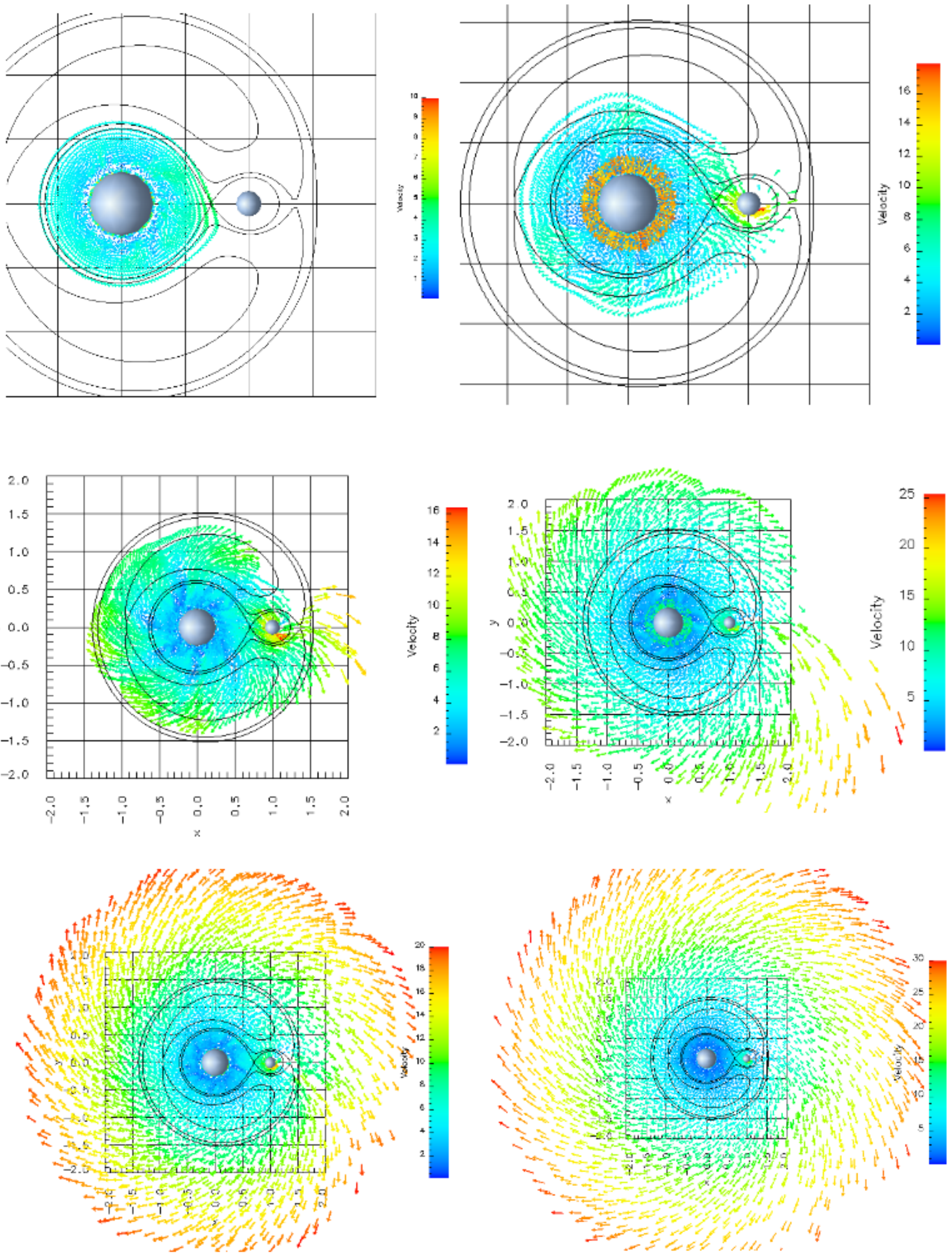

Figure 7.22: Computation results for the velocity at different stages of the evolution.

Chapter 8

Summary and Conclusions

In this work we presented an explorative approach to the perturbative influence of a second star on the dust formation in AGB - winds, in order to advance the established one dimensional models of dust formation in the envelope of a single star.

As a first step we introduced the main characteristics of a close binary system, where the donor star is a C-Mira and the gainer star is represented by a brown dwarf. These comprise the description of the force field in the environment of a rotating two body system, the resulting equation of motion and the related lagrangian equilibrium points.

We considered three main areas of investigation: the radiative transfer, the hydrodynamics and the chemistry of the system.

For the higher dimensional radiative transfer study, we chose a Monte Carlo type numerical approach, since in view of the resulting complex geometry it is the most adequate and effective method.

Using this algorithm we could derive several of the essential quantities of the problem. These are the radiative equilibrium temperature, the intensity and its moments. Our results are in agreement with the analytical solutions often used in the one dimensional approach.

For the study of the hydrodynamical evolution in the binary system, we used the smoothed particle hydrodynamical approach (SPH), which describes the governing equations of the one fluid system. We chose this type of approach because it is easy to establish the algorithm and to adjust to the boundary conditions imposed by the system. Several numerical tests regarding the time evolution of the density, velocity field, temperature of the gas and the internal energy, were performed and successfully compared to known analytical solutions.

In preparation of the computation of dust formation in a carbon rich environment, we describe the essential chemical network in the envelope of a red giant as well as in the common envelope of the binary system.

We assume local thermodynamical and chemical equilibrium to be described by a damped Newtonian algorithm the dissociation equilibrium. Our results were compared with established results. The dust formation is described as a two step process consisting in grain nucleation and subsequent growth to macroscopic particles. The nucleation was considered in the framework of the classical nucleation theory. In order to prepare the initial data for our final simulation we used the well established CHILD code, based on the moments of the distribution function, to generate the seed particles for a one dimensional time sequence in the close environment of the donor star. Due to the computational effort involves in adapting this method to a higher dimensional generalisation, we chose the simplifying assumption of the mono-disperse size spectrum, which considers that all dust grains will have the same radius.

This means that at the interface of $2\ \mathrm{R}_\odot$ we adapt the time sequence computed by the CHILD code to the three dimensional generalisation and continue the coating of dust seed particle (generated by the CHILD - Code) in a mono-disperse form.

The three components of our study are finally brought together in a numerical simulation of the full binary system. The time dependent input parameters at the inner boundary (at $2\ \mathrm{R}_\odot$ from the donor star) are adopted from the time sequence of the one dimensional CHILD code, assuming spherical symmetry. From this interface on, we evolve the system of equation in a higher dimensional manner, obtaining, among others, the density, the velocity field and the net-growth rate.

This work has obtained for the first time two additional regions of strong dust formation, in comparison to a spherical symmetrical single star approach, as a result of a long term evolution. These regions, where an increase of the net-growth rate is obtained, are in the close environment of the Roche lobe around the donor star, and another area of peak nucleation rate, in the region between the lagrangean points $\mathbb{L}_{1,5}$.

Our simulation results have been computed in such a way as to allow future comparison with real observations of dust formation in a similar binary system, which has up to know not been observed.

Appendix A

Used quantities

Symbol	Quantity	Value
$\mathrm{M}_\odot$	Solar mass	1.9891×10^{30} kg
$\mathrm{R}_\odot$	Solar radius	6.955×10^{8} m
$\mathrm{L}_\odot$	Solar luminosity	3.839×10^{26} W
h	Planck constant	6.626×10^{-34} J s
c	speed of light in vaccum	299792458 m s^{-1}
k_B	Boltzmann constant	1.3807×10^{-16} erg K^{-1}
σ_B	Stefan-Boltzmann constant	5.670×10^{-8} kg s^{-3} K^{-4}
α_i	Sticking coefficient (Carbon)	$\alpha_\mathrm{C} = 0.37$
		$\alpha_{\mathrm{C_2}} = 0.34$
		$\alpha_{\mathrm{C_2H}} = 0.34$
		$\alpha_{\mathrm{C_2H2}} = 0.34$
		$\alpha_{\mathrm{C_3}} = 0.08$
		$\alpha_{\mathrm{C_3H}} = 0.08$
m_u	Atomic mass unit	0.1660531×10^{25} g
r_0	Hypotetical monomer radius	0.128 nm
$A_1 = 4\pi r_0^2$	Hypotetical monomer surface	20.7×10^{-6} cm^2
σ_surf	Surface tension	1400 erg $\cdot$ cm^{-2}
N_d	Particle size for which σ_surf reduces to $1/2$ of the value for the bulk material	5

Appendix B

Stellar atmosphere element abundances

The following [Hoskin et al., 2001] table lists the element abundance in the solar photosphere and in meteorites. The abundances are given in the logarithmic scale usually adopted by astronomers. The value for an element "El " on the logarithmic astronomical scale is designated as $A(\mathsf{H}) = \log n(\mathsf{H}) = 12.0$, such that:

$$A(\mathsf{El}) = \log \epsilon(\mathsf{El}) = \log\left(\frac{n(\mathsf{El})}{n(\mathsf{H})}\right) + 12.0 \tag{B.0.1}$$

By definition the abundance of hydrogen is exactly $A_{\mathrm{H}} = 12.0$. Values between square brackets are not derived from the photosphere, but from sunspots, solar corona and solar wind particles. Values between parentheses are less accurate results. Here Δ gives the difference: Photosphere - Meteorite difference.

Element	Photosphere	Meteorite	Δ	Element	Photosphere	Meteorite	Δ
1 H	12.00	-	-	42 Mo	1.92 ± 0.05	1.97 ± 0.02	- 0.05
2 He	[10.93 ± 0.004]	-	-	44 Ru	1.84±0.07	1.83 ±0.04	+0.01
2 He	[10.93 ± 0.004]	-	-	44 Ru	1.84±0.07	1.83 ±0.04	+0.01
3 Li	1.10 ± 0.10	3.31 ± 0.04	-2.21	45 Rh	1.12 ± 0.12	1.10 ± 0.04	+0.02
4 Be	1.40 ± 0.09	1.42 ± 0.04	-0.02	46 Pd	1.69 ± 0.04	1.70 ± 0.04	-0.01
5 B	(2.55 ± 0.30)	2.79 ± 0.05	-0.24	47 Ag	(0.94 ± 0.25)	1.24 ± 0.04	-0.30
6 C	8.52 ± 0.06	-	-	48 Cd	1.77 ± 0.11	1.76 ± 0.04	+0.01
7 N	7.92 ± 0.06	-	-	49 In	(1.66 ± 0.15)	0.82 ± 0.04	+0.84
8 O	8.83 ± 0.06	-	-	50 Sn	2.0 ± 0.3	2.14 ± 0.04	-0.14
9 F	[4.56 ± 0.30]	4.48 ± 0.06	+0.08	51 Sb	1.0 ± 0.3	1.03 ± 0.07	-0.03
10 Ne	[8.08 ± 0.06]	-	-	52 Te	-	2.24 ± 0.04	-
11 Na	6.33 ± 0.03	6.32 ± 0.02	+0.01	53 I	-	1.51 ± 0.08	-
12 Mg	7.58 ± 0.05	7.58 ± 0.01	+0.00	54 Xe	-	2.17 ± 0.08	-
13 Al	6.47 ± 0.07	6.49 ± 0.01	-0.02	55 Cs	-	1.13 ± 0.02	-
14 Si	7.55 ± 0.05	7.56 ± 0.01	-0.01	56 Ba	2.13 ± 0.05	2.22 ± 0.02	-0.09
15 P	5.45 ± 0.04	5.56 ± 0.06	-0.11	57 La	1.17 ± 0.07	1.22 ± 0.02	-0.05
16 S	7.33 ± 0.11	7.20 ± 0.06	+0.13	58 Ce	1.58 ± 0.09	1.63 ± 0.02	-0.05
17 Cl	[5.50 ± 0.30]	5.28 ± 0.06	+0.22	59 Pr	0.71 ± 0.08	0.80 ± 0.02	-0.09
18 Ar	[6.40 ± 0.06]	-	-	60 Nd	1.50 ± 0.06	1.49 ± 0.02	+0.01
19 K	5.12 ± 0.13	5.13 ± 0.02	-0.01	62 Sm	1.01 ± 0.06	0.98 ± 0.02	+0.03
20 Ca	6.36 ± 0.02	6.35 ± 0.01	+0.01	63 Eu	0.51 ± 0.08	0.55 ± 0.02	-0.04
21 Sc	3.17 ± 0.10	3.10 ± 0.01	+0.07	64 Gd	1.12 ± 0.04	1.09 ± 0.02	+0.03
22 Ti	5.02 ± 0.06	4.94 ± 0.02	+0.08	65 Tb	(-0.1 ± 0.3)	0.35 ± 0.02	-0.45
23 V	4.00 ± 0.02	4.02 ± 0.02	-0.02	66 Dy	1.14 ± 0.08	1.17 ± 0.02	-0.03
24 Cr	5.67 ± 0.03	5.69 ± 0.01	-0.02	67 Ho	(0.26 ± 0.16)	0.51 ± 0.02	-0.25
25 Mn	5.39 ± 0.03	5.53 ± 0.01	-0.14	68 Er	0.93 ± 0.06	0.97 ± 0.02	-0.04
26 Fe	7.50 ± 0.05	7.50 ± 0.01	+0.00	69 Tm	(0.00 ± 0.15)	0.15 ± 0.02	-0.15
27 Co	4.92 ± 0.04	4.91 ± 0.01	+0.01	70 Yb	1.08 ± 0.15	0.96 ± 0.02	+0.12
28 Ni	6.25 ± 0.04	6.25 ± 0.01	+0.00	71 Lu	0.06 ± 0.10	0.13 ± 0.02	-0.07
29 Cu	4.21 ± 0.04	4.29 ± 0.04	-0.08	72 Hf	0.88 ± 0.08	0.75 ± 0.02	+0.13
30 Zn	4.60 ± 0.08	4.67 ± 0.04	-0.07	73 Ta	-	-0.13 ± 0.02	-
31 Ga	2.88 ± 0.10	3.13 ± 0.02	-0.25	74 W	(1.11 ± 0.15)	0.69 ± 0.03	+0.42
32 Ge	3.41 ± 0.14	3.63 ± 0.04	-0.22	75 Re	-	0.28 ± 0.03	-
33 As	-	2.37 ± 0.02	-	76 Os	1.45 ± 0.10	1.39 ± 0.02	+0.06
34 Se	-	3.41 ± 0.03	-	77 Ir	1.35 ± 0.10	1.37 ± 0.02	-0.02
35 Br	-	2.63 ± 0.04	-	78 Pt	1.8 ± 0.3	1.69 ± 0.04	+0.11
36 Kr	-	3.31 ± 0.08	-	79 Au	(1.01 ± 0.15)	0.85 ± 0.04	+0.16
37 Rb	2.60 ± 0.15	2.41 ± 0.02	+0.19	80 Hg	-	1.13 ± 0.08	-
38 Sr	2.97 ± 0.07	2.92 ± 0.02	+0.05	81 Tl	(0.9 ± 0.2)	0.83 ± 0.04	+0.07
39 Y	2.24 ± 0.03	2.23 ± 0.02	+0.01	82 Pb	1.95 ± 0.08	2.06 ± 0.04	-0.11
40 Zr	2.60 ± 0.02	2.61 ± 0.02	-0.01	83 Bi	-	0.71 ± 0.04	-
41 Nb	1.42 ± 0.06	1.40 ± 0.02	+0.02	90 Th	-	0.09 ± 0.02	-
				92 U	(<-0.47)	-0.50 ± 0.04	-

Appendix C

Hydrodynamics

C.1 Hydrodynamical tests

C.1.0.1 Initial value problem - shock tube

The Riemann Problem for the one - dimensional time-depentdent Euler-equations is the Inital value Problem for the conservative laws

$$\mathbf{U}_t + \mathbf{F}(\mathbf{U})_x = 0 \tag{C.1.1}$$

$$\mathbf{U} = \begin{bmatrix} \rho \\ \rho u \\ E \end{bmatrix}, \qquad \mathbf{F} = \begin{bmatrix} \rho u \\ \rho u^2 + p \\ u(E+p) \end{bmatrix} \tag{C.1.2}$$

with initial condition

$$\mathbf{U}(x,0) = \mathbf{U}^0(x,0) = \begin{cases} \mathbf{U}_L & \text{if } x < 0, \\ \mathbf{U}_R & \text{if } x > 0, \end{cases} \tag{C.1.3}$$

The domain of interest in the $x-t$ plane are the points (x,t) with $-\infty < x < \infty$ and $t > 0$. In practice one lets x vary in a finit interval $[x_L, x_R]$ around the point $x = 0$. In solving the Riemann problem we shall freuqently make use of the vector $\mathbf{W} = (\rho, u, p)$ of primitive varibles, rahter then the vector $\mathbf{U}$ of conserved varables, where ρ is the density, u is the particle velocity and p is the pressure. The Riemann problem **(C.1.1)**-**(C.1.2)** is the simplest, non-trivial **IVP** for **(C.1.1)**. Data consists of just two constant states, which in terms of primitve variables are $\mathbf{W_L} = (\rho_L, u_L, p_L)$ to the left of $x = 0$ and $\mathbf{W_R} = (\rho_R, u_R, p_R)$ to the right of $x = 0$, separeted by a discontinuity at$x = 0$.

Physically, in the context of the Euler equaitons, the Riemann problem is a slight generalisation of the so called **shock tube problem**: two stationary gases $u_L = u_R = 0$ in a tube separated by a diaphragma. The rupture of the diaphragma generates a nearly centered wave system that typically consists of a rarefaction wave, a contact discontinuity and a shock wave. In general, given the conservation equations **(C.1.1)** for the dynamics it is left to the statements about the material, the equation of state , to determin not

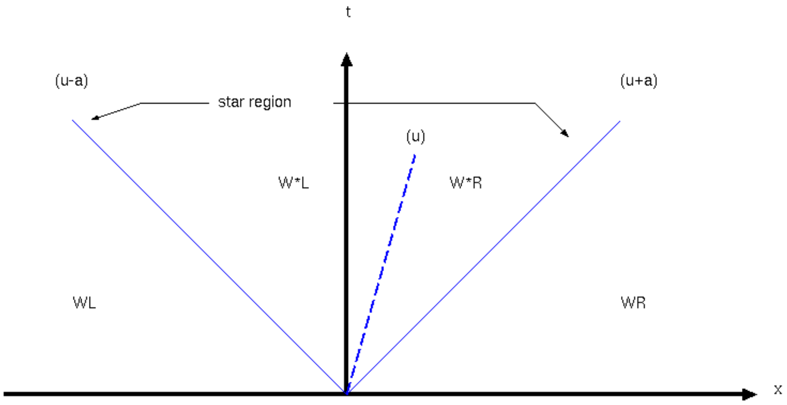

Figure C.1: Structure of solution of the Riemann problem in the $x{-}t$ plane for the one dimensional Euler euqations

only the structure of the solution of the Riemann problem but also the mathematical character of the equations. In this appoach we restrict attention to the ideal gas

$$e = \frac{p}{\rho(\gamma - 1)} \tag{C.1.4}$$

where γ is the ration of the specific heats,a constant. For the case in which no vacuum is present the exact solution of the Riemann problem **(C.1.1)**, **(C.1.2)** has three waves, which are associated with the eigenvalues $\lambda_1 = u - a$, $\lambda_2 = u$ and $\lambda_3 = u + a$ see figure **(C.1)**

Note that the sppeds of these waves are not in general, the charakteristics speeds given by the eigenvalues. The three waves separate four constant states which from left to right are $\mathbf{W_L}$ (data on the left hand side), $\mathbf{W_{*L}}$,$\mathbf{W_{*R}}$ and $\mathbf{W_R}$ (data on the right hand side).

The unknown region between the left and the right waves, the **star region**, is devided by the middle wave into the two subregions **star left** $\mathbf{W_{*L}}$ and **star right** $\mathbf{W_{*R}}$. The middle wave is always a contact discontinuity while the left and right (non linear) are either shock or rarefaction waves. Therefore, according to the type of non-linear waves there can be four possible wave patterns, which are shown in **(C.2)**

The analysis based on the eigenstructure [Toro, 1997] of the Euler equations, reveals that both pressure p_* and u_* between the left and right waves are constant, while the density takes on the two constant valuesthe value ρ_*L and ρ_*R Here we present a solution procedure which makes use of the constancy of the pressure and the particle velocity in the **star region** to derive a s single, algebraic non-linear equation for the pressure p_*.

C.1.1 Equation for pressure and velocity

Here we establish euations and solution strategies for computing the pressure p_* and the particle velocity u_* in the **star region**

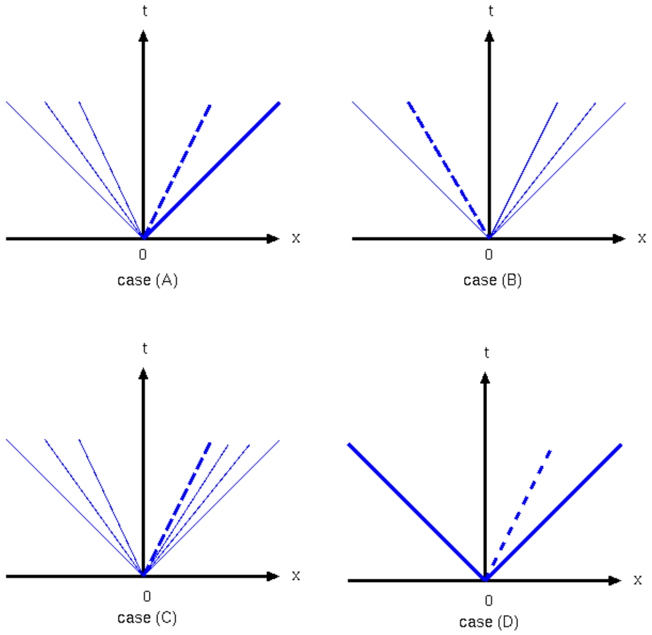

Figure C.2: Possible wave pattern in the solution of the Riemann problem : (A) left rarefaction, contact,right shock (B) left shock, contact, right rarefaction (C) left rarefaction, conatct right rarefaction (D) left shock, contact right shock

C.1.1.1 Solution for p_* and u_*

The solution for the pressure p_* of the Riemann problem **(C.1.1)**,**(C.1.2)** with ideal gas equation of state **(C.1.4)** is given by the root of the algebraic equation

$$f(p,\mathbf{W_L},\mathbf{W_R}) = f_L(p,\mathbf{W_L}) + f_R(p\mathbf{W_R}) + \Delta u = 0\ , \qquad \Delta u = u_R - u_L \quad \text{(C.1.5)}$$

where the function f_L is given by

$$f_L(p,\mathbf{W_L}) = \begin{cases} (p-p_L)\sqrt{\frac{A_L}{p+B_L}} & \text{if } p > p_L \text{ (shock) },\\ \frac{2a_L}{(\gamma-1)}\left[\left(\frac{p}{p_L}\right)^{\frac{\gamma-1}{2\gamma}} - 1\right] & \text{if } p \le p_L \text{ (rarefaction) }, \end{cases} \quad \text{(C.1.6)}$$

the function f_R is given by

$$f_R(p,\mathbf{W_R}) = \begin{cases} (p-p_R)\sqrt{\frac{A_R}{p+B_R}} & \text{if } p > p_R \text{ (shock) },\\ \frac{2a_R}{(\gamma-1)}\left[\left(\frac{p}{p_R}\right)^{\frac{\gamma-1}{2\gamma}} - 1\right] & \text{if } p \le p_R \text{ (rarefaction) }, \end{cases} \quad \text{(C.1.7)}$$

and the data-dependent constants A_L, B_L, A_R and B_L are given by

$$\begin{aligned} A_L &= \frac{2}{(\gamma+1)\rho_L} & \qquad B_L &= \frac{(\gamma-1)}{(\gamma+1)}p_L \\ A_R &= \frac{2}{(\gamma+1)\rho_R} & \qquad B_R &= \frac{(\gamma-1)}{(\gamma+1)}p_R \end{aligned} \quad \text{(C.1.8)}$$

The solution for the particle velocity u_* in the star region is

$$u_* = \frac{1}{2}(u_L + u_R) + \frac{1}{2}\Big(f_R(p_*) - f_L(p_*)\Big) \tag{C.1.9}$$

Once **(C.1.5)** is solved for p_* the solution for u_* follows as in **(C.1.9)**. The function f_L governs relations across the left non-linear wave and serves to connect the unknown particle speed u_* to the state $\mathbf{W_L}$ on the left side, see figure **(C.3)**; the relations depend on the type of wave (shock or rarefaction). The argument of f_L are the pressure p and the data state $\mathbf{W_L}$. Similarly the function f_R governs relations across the right wave connects the unknown u_* to the right data state $\mathbf{W_R}$; its arguments are p and $\mathbf{W_R}$.

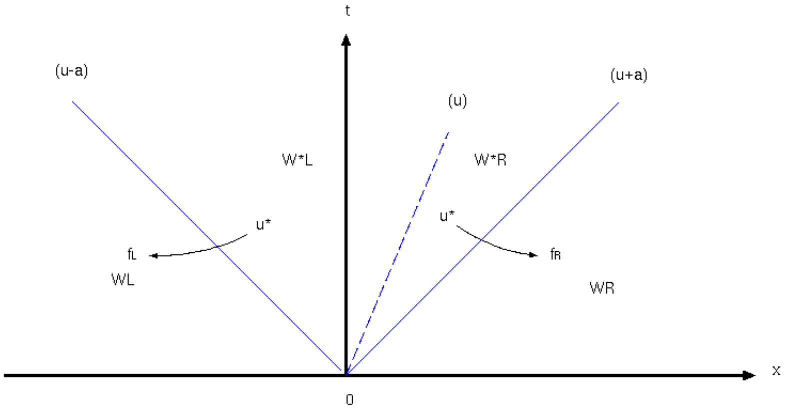

Figure C.3: Strategy for solving the Riemann problem via a pressure function. The particle velocity is connected to data on the left via function f_L and f_R

C.1.1.2 Function f_L for left shock

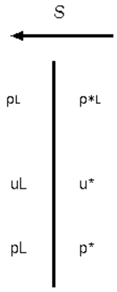

Figure C.4: Left wave is a shock of speed S_L in a stationary frame

We assume the left wave is a shock moving with speed S_L as shown in Fig. **(C.4)**. The pre-shock values are ρ_L, u_L and p_L and the post post shock values are $\rho_* L, u_*$ and p_*. We transform the equations to a frame of reference moving with the shock. In the new frame the shock speed is zeri and the relative velocitites are

$$\hat{u}_L = u_L - S_L, \qquad \hat{u}_* = u_* - S_L \tag{C.1.10}$$

The Rankine-Hugoniot Conditions give then

$$\rho_L \hat{u}_L = \rho_{*L} \hat{u}_* \tag{C.1.11}$$

$$\rho_L \hat{u}_L^2 + p_L = \rho_{*L} \hat{u}_*^2 + p_* \tag{C.1.12}$$

$$\tag{C.1.13}$$

$$\hat{u}_L(\hat{E}_L + p_L) = \hat{u}(\hat{E}_{*L} - p_*) \tag{C.1.14}$$

We introduce the mass flux Q_L, which in view of **(C.1.11)** may be written as

$$Q_L \equiv \rho_L \hat{u}_L = \rho_{*L} \hat{u}_* \tag{C.1.15}$$

From equation **(C.1.13)**

$$\left(\rho_L \hat{u}_L\right) \hat{u}_L + p_L = \left(\rho_{*L} \hat{u}_*\right) \hat{u}_* + p_*$$

Use of **(C.1.15)** and soling for Q_L gives

$$Q_L = \frac{p_* - p_L}{\hat{u}_* - \hat{u}_L} \tag{C.1.16}$$

But from erquation **(C.1.10)** $\hat{u}_L - \hat{u}_* = u_L - u_*$ and so Q_L becomes

$$Q_L = \frac{p_* - p_L}{u_* - u_L} \tag{C.1.17}$$

from which we obtain

$$u_* = u_L \frac{(p_* - p_L)}{Q_L} \tag{C.1.18}$$

We are now cloe to having related u_* to data on the left hand side. We seek to express the right hand side of **(C.1.18)** purly in terms of p_* and $\mathbf{W_L}$, which means that we need to express Q_L as a function of p_* and the data on the left side. We substitue the relations

$$u_L = \frac{Q_L}{\rho_L}, \qquad u_* = \frac{Q_L}{\rho_{*L}}$$

obtained from **(C.1.15)** into **(C.1.16)** to produce

$$Q_L^2 = -\frac{p_* - p_L}{\frac{1}{\rho_{*L}} - \frac{1}{\rho_L}} \tag{C.1.19}$$

The density ρ_{*L} is related to the pressure p_* behind the left shock via

$$\rho_{*L} = \rho_L \left[\frac{\left(\frac{\gamma-1}{\gamma+1}\right) + \left(\frac{p_*}{p_L}\right)}{\left(\frac{\gamma-1}{\gamma+1}\right)\left(\frac{p_*}{p_L}\right) + 1} \right] \tag{C.1.20}$$

Substition of ρ_{*L} into **(C.1.19)** yields

$$Q_L = \sqrt{\frac{p_* + B_L}{A_L}} \tag{C.1.21}$$

which in turn reduces **(C.1.18)** to

$$u_* = u_L - f_L(p_*, \mathbf{W_L}) \tag{C.1.22}$$

with

$$f_L(p_*, \mathbf{W_L}) = (p - p_L)\sqrt{\frac{A_L}{p + B_L}} \tag{C.1.23}$$

which is the seeked expression for f_L for the case in which left wave is a shock wave has been obtained.

C.1.1.3 Function f_L for left rarefaction

Now dreive an expression for f_L for the case in which the left wave is a rarefaction wave. The unknown state $\mathbf{W_{*L}}$ is now connected to the left data state $\mathbf{W_L}$ using the isentropic realtion and the generalised Riemann invariants for the left wave. The isentropic law

$$p = C\rho^\gamma \tag{C.1.24}$$

where C is a constant, may be used across rarefactions. C is evaluated at the initial data state by applying the isentropic law namely

$$p_L = C\rho_L^\gamma$$

and so the constant C is

$$C = p_L/\rho_L^\gamma$$

from which we write

$$\rho_{*L} = \rho_L\left(\frac{p_*}{p_L}\right)^{\frac{1}{\gamma}} \tag{C.1.25}$$

Across a left rarefaction the generalised Riemann Invariant is constant. By evaluating the constant on the left data state we write

$$u_L + \frac{2a_L}{\gamma - 1} = u_* + \frac{2a_{*L}}{\gamma - 1} \tag{C.1.26}$$

where a_L and a_{*L} denote the sound speed on left and right states bounding the left rarefaction wave. Substituion from **(C.1.25)** into the defintion of a_{*L} gives

$$a_{*L} = a_L\left(\frac{p_*}{p_L}\right)^{\frac{\gamma-1}{\gamma}} \tag{C.1.27}$$

and equation **(C.1.26)** leads to

$$u_* = u_L - f_L(p_*, \mathbf{W_L}) \tag{C.1.28}$$

with

$$f_L(p_*, \mathbf{W_L}) = \frac{2a_L}{(\gamma-1)}\left[\left(\frac{p_*}{p_L}\right)^{\frac{\gamma-1}{2\gamma}} - 1\right]$$

This is the required expression for the function f_L for the case in which the left wave is a rarefaction wave.

C.1.1.4 Function f_R for a right shock

Here we find the expression for the function f_R for the case in which the right wave is a shock wave travelling with speed S_R. The situation is entirely analogous to the case of a left shock wave. Pre-shock values are ρ_R, u_R and p_R and the post-shock values are ρ_{*R}, u_* and p_*. In the transformed frme of the reference moving frame with the shock, the shock speed is zero and the relative velocities

$$\hat{u}_R = u_R - S_R, \qquad \hat{u}_* = u_* - S_R \tag{C.1.29}$$

The Rankine-Hugoniot Conditions give then

$$\begin{aligned} \rho_{*R}\hat{u}_* &= \rho_R\hat{u}_R \\ \rho_{*R}\hat{u}_*^2 + p_* &= \rho_R\hat{u}_R^2 + p_R \\ \hat{u}_*(\hat{E}_{*R} + p_*) &= \hat{u}_R(E_R - p_R) \end{aligned} \tag{C.1.30}$$

Now the mass flux is defind

$$Q_R \equiv -\rho_{*R}\hat{u}_* = -\rho_R\hat{u}_R \tag{C.1.31}$$

By perfoming algebriac manipulation similar to those for a left shock we derive the following expression for the mass flux

$$Q_R = \sqrt{\frac{p_* + B_R}{A_R}} \tag{C.1.32}$$

Hence the particle velocity in the star region satifies

$$u_* = u_R + f_R p_*, \mathbf{W_R}) \tag{C.1.33}$$

with

$$f_R(p_*, \mathbf{W}_R) = (p_* - p_R)\sqrt{\frac{A_R}{p_* + B_R}} \tag{C.1.34}$$

C.1.1.5 Function f_R for the right rarefaction

The derivation of the function f_R for the case in which the right wave is a rarefaction wave is carried out in entirely analogous manner to the case of the left rarefaction. The isentropic law gives

$$\rho_{*R} = \rho_R \left(\frac{p_*}{p_R} \right)^{\frac{1}{\gamma}} \tag{C.1.35}$$

and the generalised Riemann invariant for a right rarefaction gives

$$u_* - \frac{2a_{*R}}{\gamma - 1} = u_R - \frac{2a_R}{\gamma - 1} \tag{C.1.36}$$

Using **(C.1.35)** into the defintion of sound speed gives

$$a_{*R} = a_R \left(\frac{p_*}{p_R} \right)^{\frac{\gamma-1}{2\gamma}} \tag{C.1.37}$$

which if substituted into **(C.1.36)** leads to

$$u_* = u_R + f_R(p_*, \mathbf{W_R}) \tag{C.1.38}$$

$$f_R(p_*, \mathbf{W_R}) = \frac{2a_R}{\gamma - 1} \left[\left(\frac{p_*}{p_R} \right)^{\frac{\gamma-1}{2\gamma}} - 1 \right]$$

The functions f_L and f_R have now been determined for all four possible wave patterns. Now by eliminating u_* from equations **(C.1.22)** or **(C.1.28)** and **(C.1.33)** or **(C.1.38)** we obtain a single equation

$$f(p_*, \mathbf{W_L}, \mathbf{W_R}) \equiv f_L(p_*, \mathbf{W_L}) + f_R(p_*, \mathbf{W_R}) + \Delta u = 0 \tag{C.1.39}$$

which is required equation **(C.1.5)** for the pressure. Assuming this single non-linear algebric equation is solved (numerically) for p_* the the particle velocity u_* can be found from equation **(C.1.22)** if the left wave is a shock ($p_* > p_L$) or from equaiton **(C.1.28)** if the wave is a rarefaction ($p_* \leq p_L$) or from equation **(C.1.33)** if the right wave is a shock ($p_* > p_R$) or from equation **(C.1.38)** if the right wave is a rarefaction wave ($p_* \leq p_R$). It can also be found from a mean value as

$$u_* = \frac{1}{2}(u_L + u_R) + \frac{1}{2}\Big(f_R(p_*) - f_L(p_*) \Big) \tag{C.1.40}$$

C.1.2 Example - initial data shock tube

N_{total}(total number of particles)	500
N_L (total number of particles - right)	400
N_R (number of particles - left)	100
x_{min} (left wall)	0
x_{max} (right wall)	100
Δx	$x_{max} - x_{min}$
x_{dia}	$(x_{max} - x_{min})/2$
dx	$(x_{max} - x_{min})/N_{total}$
h (smoothing length)	0.6
γ (adiabatic index)	1.6
ρ_L	10^5
ρ_R	0.125×10^5
e_L	$2,5 \times 10^{-5}$
e_R	2×10^{-5}
v_L	0
v_R	0
T_L	$(\gamma - 1)e_L$
T_R	$(\gamma - 1)e_R$
p_L	$\rho_L T_L$
p_R	$\rho_R T_R$

$$W(r,h) = \begin{cases} Q\left[6\left(\frac{r}{h}\right)^3 - 6\left(\frac{r}{h}\right)^2 + 1\right] & \text{if } 0 \leq r \leq \frac{h}{2} \\ 2Q\left(1 - \frac{r}{h}\right)^3 & \text{if } \frac{h}{2} \leq r \leq h \\ 0, & \text{otherwise} \end{cases} \tag{C.1.41}$$

$$Q = \begin{cases} \frac{4}{3h} & 1\text{ D} \\ \frac{40}{7\pi h^2} & 2\text{ D} \\ \frac{8}{\pi h^3} & 3\text{ D} \end{cases} \tag{C.1.42}$$

$$dx = \frac{\Delta x}{N_{total}} \tag{C.1.43}$$

$$W_{sum} = W(0,h) + \sum_{i=1}^{h/dx} 2W(idx, h) \tag{C.1.44}$$

$$M_L = \rho_L / W_{sum} \tag{C.1.45}$$

$$M_R = \rho_R / W_{sum} \tag{C.1.46}$$

Appendix D

Monte Carlo principle

D.1 Monte Carlo integration - basic concepts

D.1.1 Background and probability review

We will start by defining some basic terms and reviewing basic ideas from probability. A random variable X is a value chosen by some random process. We will generally use capital letters to denote random variables, with exceptions made for a few Greek symbols that represent special random variables. Random variables are always drawn from some domain, which can be either discrete (e.g., a fixed set of possibilities) or continuous (e.g., the real numbers R). Applying a function f to a random variable X results in a new random variable $Y = f(X)$.

For example, the result of a roll of a die is a discrete random variable sampled from the set of events $X_i = I, 2, 3, 4, 5, 6$. Each event has a probability $p_i = \frac{1}{6}$ and the sum of probabilities $\sum p_i$ is necessarily one. We can take a continuous, uniformly distributed random variable $\xi \in [0, 1]$ and map it to a discrete random variable, choosing X_i if

$$\sum_{J=1}^{i-1} p_i < \xi \leq \sum_{j=1}^{i} p_i \tag{D.1.1}$$

For lighting applications, we might want to define the probability of sampling illumination from each light in the scene based on the power Φ_i from each source relative to the total power from all sources:

$$p_i = \frac{\Phi_i}{\sum_j \Phi_j} \tag{D.1.2}$$

Notice that these p_i also sum to one.

The cumulative distribution function (CDF) $P(x)$ of a random variable is the probability that a value from the variable's distribution is less than or equal to some value x:

$$P(x) = Pr\{X \leq x\} \tag{D.1.3}$$

For the die example, $P(2) = \frac{1}{3}$, since two of the six possibilities are less than or equal to 2.

D.1.1.1 Continuous random variables

In rendering, discrete random variables are less common than continuous random variables, which take on values over ranges of continuous domains (e.g., the real numbers or directions on the unit sphere). A particularly important random variable is the canonical uniform random variable, which we will write as ξ. This variable takes on all values in its domain $[0, 1)$ with equal probability. This particular variable is important for two reasons.

- First, it is easy. to generate a variable with this distribution in software-most run time libraries have a pseudorandom number generator that does just that.
- Second, as we will show later, it is possible to generate samples from arbitrary distributions by first starting with canonical uniform random variables and applying an appropriate transformation.

The technique described previously for mapping from ξ to the six faces of a die gives a flavour of this technique in the discrete case.

Another example of a continuous random variable is one that ranges over the real numbers between 0 and 2, where the probability of it taking on any particular value x is proportional to the value $2 - x$: it is twice as likely for this random variable to take on a value around zero as it is to take one around one, and so forth. The probability density function (PDF) formalises this idea: it describes the relative probability of a random variable taking on a particular value. The PDF $p(x)$ is the derivative of the random variable's CDF,

$$p(x) = \frac{dP(x)}{dx} \tag{D.1.4}$$

For uniform random variables, $p(x)$ is a constant; this is a direct consequence of uniformity. For ξ we have

$$p(x) = \begin{cases} 1 & x \in [0, 1] \\ 0 & \text{otherwise} \end{cases} \tag{D.1.5}$$

PDFs are necessarily nonnegative and always integrate to one over their domains. Given an arbitrary interval $[a, b]$ in the domain, the PDF can give the probability that a random variable lies inside the interval:

$$P(x \in [a, b]) = \int_a^b p(x)dx \tag{D.1.6}$$

This follows directly from the first fundamental theorem of calculus and the definition of the PDF.

D.1.1.2 Expected values and variance

The expected value $E_p[f(x)]$ of a function f is defined as the average value of the function over some distribution of values $p(x)$ over its domain. In the next section, we will see how Monte Carlo integration computes the expected values of arbitrary integrals. Expected value over a domain, D, is defined as

$$E_p[f(x)] = \int_D f(x)p(x)dx \tag{D.1.7}$$

As an example, consider the problem of finding the expected value of the cosine function between 0 and π, where p [1] is uniform. Because the PDF $p(x)$ must integrate to one over the domain, $p(x) = \frac{1}{\pi}$, so

$$E[\cos x] = \int_0^\pi \frac{\cos x}{\pi} dx = \frac{1}{\pi}(-\sin\pi + \sin 0) = 0 \tag{D.1.8}$$

which is precisely the expected result. (Consider the graph of $\cos x$ over $[0, \pi]$ to see why this is so.)

The variance of a function is the expected deviation of the function from its expected value. Variance is a fundamental concept for quantifying the error in a value estimated by a Monte Carlo algorithm. It provides a precise way to quantify this error and measure how improvements to Monte Carlo algorithms reduce the error in the final result. The variance of a function f is defined as

$$V[f(x)] = E\left[(f(x) - E[f(x)])^2\right] \tag{D.1.9}$$

The expected value and variance have three important properties that follow immediately from their respective definitions:

$$1) \qquad E[af(x)] = aE[f(x)] \tag{D.1.10}$$

$$2) \qquad E\left[\sum_i f(X_i)\right] = \sum_i E\left[f(X_i)\right] \tag{D.1.11}$$

$$3) \qquad V[af(x)] = a^2 V[f(x)] \tag{D.1.12}$$

These properties, and some simple algebraic manipulation, yield a much simpler expression for the variance:

$$V[f(x)] = E[(f(x))^2] - E[f(x)]^2 \tag{D.1.13}$$

Thus, the variance is simply the expected value of the square minus the square of the expected value. Given random variables that are independent, variance also has the property that the sum of the variances is equal to the variance of their sum:

$$\sum_i V[f(X_i)] = V\left[\sum_i f(X_i)\right] \tag{D.1.14}$$

---

[1] When computing expected values with a uniform distribution, we will drop the subscript p from E_p.

D.1.2 The Monte Carlo estimator

We can now define the basic Monte Carlo estimator, which approximates the value of an arbitrary integral. It is the foundation of the light transport algorithms defined in the next chapters.

Suppose that we want to evaluate a one-dimensional integral $\int_a^b f(x)dx$. Given a supply of uniform random variables $X_i \in [a, b]$, the Monte Carlo estimator says that the expected value of the estimator [2] [3]

$$F_N = \frac{b-a}{N} \sum_{i=1}^{N} f(X_i) \qquad \text{(estimator)} \tag{D.1.16}$$

$E[F_N]$, is in fact equal to the integral. This can be demonstrated with just a few steps. First, note that the PDF $p(x)$ corresponding to the random variable X_i must be equal to $1/(b-a)$, since p must both be a constant and also integrate to one over the domain $[a, b]$. Algebraic manipulation then shows that

$$\begin{aligned} E[F_N] &= E\left[\frac{b-a}{N} \sum_{i=1}^{N} f(X_i)\right] \\ &= \frac{b-a}{N} \sum_{i=1}^{N} E[f(X_i)] \\ &= \frac{b-a}{N} \sum_{i=1}^{N} \int_a^b f(x)p(x)dx \\ &= \frac{1}{N} \sum_{i=1}^{N} \int_a^b f(x)dx \\ &= \int_a^b f(x)dx \end{aligned} \tag{D.1.17}$$

The restriction to uniform random variables can be relaxed with a small generalisation. This is an extremely important step, since carefully choosing the PDF from which samples are drawn is an important technique for reducing variance in Monte Carlo. If the random variables X_i are drawn from some arbitrary PDF $p(x)$, then the estimator

---

[2] **Estimator of the integral :**

$$\begin{aligned} \int_a^b f(x)dx &\approx (b-a)f(X_1) && \text{first approximation} \\ &\approx \frac{1}{2}\Big((b-a)f(X_1) + (b-a)f(X_2)\Big) && \text{second approximation} \\ &\approx \frac{1}{N}\Big((b-a)f(X_1) + (b-a)f(X_2) + ... + (b-a)f(X_N)\Big) && \text{N'th approximation} \end{aligned} \tag{D.1.15}$$

[3] **Example:** The exected value for a ideal die is given by $p = \frac{1}{6}$,$i = 1, 2, 3, 4, 5, 6$. From this it can computed the expected value $E = \sum_{i=1}^{n} x_i p_i$ i.e. to $E = 1\cdot\frac{1}{6} + 2\cdot\frac{1}{6} + 3\cdot\frac{1}{6} + 4\cdot\frac{1}{6} + 5\cdot\frac{1}{6} + 6\cdot\frac{1}{6} = 3.5$

$$F_N = \frac{1}{N}\sum_{i=1}^{N}\frac{f(X_i)}{p(x)} \qquad \text{(estimator)} \tag{D.1.18}$$

can be used to estimate the integral instead. The only limitation on p(x) is that it must be nonzero for all x where $\mid F(x) > 0 \mid$. It is similarly easy to see that the expected value of this estimator is the desired integral of f:

$$\begin{aligned} E[F_N] &= E\left[\frac{1}{N}\sum_{i=1}^{N}\frac{f(X_i)}{p(x)}\right] \\ &= \frac{1}{N}\sum_{i=1}^{N}\int_a^b \frac{f(X_i)}{p(x)}p(x)dx \\ &= \frac{1}{N}\sum_{i=1}^{N}\int_a^b f(X_i)dx \\ &= \int_a^b f(X_i)dx \end{aligned} \tag{D.1.19}$$

Extending this estimator to multiple dimensions or complex integration domains is straightforward. N samples X_i are taken from a multidimensional (or "joint") PDF, and the estimator is applied as. usual. For example, consider the three-dimensional integral

$$\int_{x_0}^{x_1}\int_{y_0}^{y_1}\int_{z_0}^{z_1} f(x,y,z)dxdydz \tag{D.1.20}$$

If samples $X_i = (x_i, y_i, z_i)$ are chosen uniformly from the box from (x_0, y_0, z_0) to (x_1, y_1, z_1), the PDF $p(X)$ is the constant value

$$\frac{1}{(x_0 - x_1)}\frac{1}{(y_0 - y_1)}\frac{1}{(z_0 - z_1)} \tag{D.1.21}$$

and the estimator is

$$\frac{(x_0 - x_1)(y_0 - y_1)(z_0 - z_1)}{N}\sum_i f(X_i) \tag{D.1.22}$$

Note that the number of samples N can be chosen arbitrarily, regardless of the dimension of the integrand. This is another important advantage of Monte Carlo over traditional deterministic quadrature techniques. The number of samples taken in Monte Carlo is completely independent of the dimensionality of the integral, while with standard numerical quadrature techniques the number of samples required is exponential in the dimension.

Showing that the Monte Carlo estimator converges to the right answer is not enough to justify its use; a good rate of convergence is important too. Although we will not derive its rate of convergence here, it has been shown that error in the Monte Carlo estimator decreases at a rate of $O(\sqrt{N})$ in the number of samples taken. Although standard quadrature techniques converge faster than $0(\sqrt{N})$ in one dimension, their performance becomes exponentially worse as the dimensionality of the integrand increases, while MonteCarlo's convergence rate is independent of the dimension, making Monte Carlo the only practical numerical integration algorithm for high-dimensional integrals.

D.1.3 Sampling random variables

In order to evaluate the Monte Carlo estimator in Equation **(D.1.21)**, it is necessary to be able to draw random samples from the chosen probability distribution. This section will introduce the basics of this process and demonstrate it with some straightforward examples. The next sections will develop the approach for the general multidimensional case, and will show how to use these techniques to generate samples from the distributions defined by **BSDF**s [4] and light sources.

D.1.3.1 Inversion method

The inversion method uses one or more uniform random variables and maps them to random variables from the desired distribution. To explain how. this process works in general, we will start with a simple discrete example.

Suppose we have a process with four possible outcomes. The probabilities of each of the four outcomes are given by p_1, p_2, p_3 and p_4 respectively, with the requirement that $\sum_{i=1}^{4} p_i = 1$.

The corresponding PDF is shown in Figure D.1. In order to draw a sample from this distribution, we first find the CDF $P(x)$. In the continuous case, P is the indefinite integral of p. In the discrete case, we can directly construct the CDF by stacking the bars on top of each other, starting at the left. This idea is shown in Figure D.2. Notice that the height of the rightmost bar must be one because of the requirement that all probabilities sum to one.

To draw a sample from the distribution, we then take a uniform random number ξ and use it to select one of the possible outcomes using the CDF, doing so in a way that chooses a particular outcome with probability equal to its own probability.

This idea is illustrated in Figure D.3, where the events' probabilities are projected onto the vertical axis and a random variable ξ selects among them.

It should be clear that this draws from the correct distribution - the probability of the uniform sample hitting any particular bar is exactly equal to the height of that bar. In order to generalise this technique to continuous distributions, consider what happens as the number of discrete possibilities approaches infinity. The PDF from Figure D.1 becomes a smooth curve, and the CDF from Figure D.2 becomes its integral. The projection process described in the previous paragraph is still the same, although if the function is continuous, the projection has a convenient mathematical interpretation - it represents inverting the CDF and evaluating the inverse at ξ. This technique is thus called the **inversion method**. More precisely, we can draw a sample X_i from a arbitrary PDF $p(x)$ with the following steps

---

[4] BSDF: Bidirectional Scattering Distribution Function

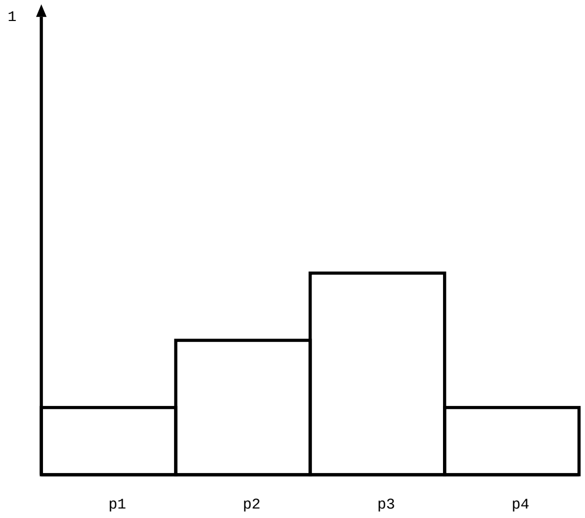

Figure D.1: A discrete PDF for Four Events with Probability p. The sum of their probability $\sum_i p_i$ is necessary one.

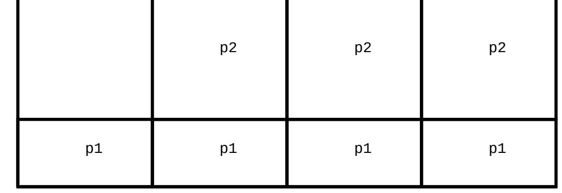

Figure D.2: A discrete PDF for Four Events with Probability p. The sum of their probability $\sum_i p_i$ is necessary one.

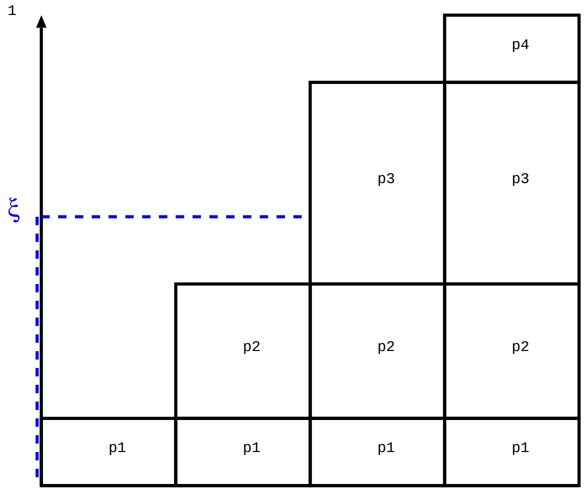

Figure D.3: To use the inversion method to draw a sample from the distribution described by the PDF in Figure D.2, a canonical. uniform random variable is plotted on the vertical axis. By construction, the horizontal extension of ξ will intersect the box representing the i'th outcome with probability p_i If the corresponding event is chosen for a set of random variables ξ, then the resulting distribution of events will be distributed according to the PDF.

1. Compute the CDF [5] $P(x) = \int_0^x p(x')dx'$
2. Compute the inverse $P^{-1}(x)$
3. Obtain a uniformly distributed random number ξ
4. Compute $X_i = P^{-1}(\xi)$

D.1.3.2 Example: power distribution

As an example how this procedure works, consider the task of drawing samples from a **power distribution** $p(x) \propto x^n$. The PDF of the power distribution is

$$p(x) = cx^n \tag{D.1.23}$$

for some constant c. The first task to tackle is to find the PDF for the function. In most cases, this simple involves computing the value of the proportionality constant c, which can be found using the constraint that $\int p(x)dx = 1$:

$$\begin{aligned} \int_0^1 cx^n dx &= 1 \\ \left| c\frac{x^{n+1}}{n+1} \right|_0^1 &= 1 \\ \frac{c}{n+1} &= 1 \\ c &= n+1 \end{aligned} \tag{D.1.24}$$

---

[5] In general, the lower limit of integration should be $-\infty$,although if $p(x) = 0$ for $x \leq 0$ this equation is equivalent

Therefore $p(x) = (n+1)x^n$. We can integrate this to get the CDF.

$$P(x) = \int_o^x p(x')dx = x^{n+1} \tag{D.1.25}$$

An inversion is simple $x^{\frac{1}{n+1}}$. Therefore, given a uniform random variable ξ, samples can be drawn from the power distribution as

$$X = \xi^{\frac{1}{n+1}} \tag{D.1.26}$$

D.1.3.3 Example: exponential distribution

When evolving situation with participating media, it is frequently useful to draw samples from a distribution $p \propto e^{-ax}$. As before, the first step is to normalise this distribution so that it integrates to one. In this case, the range of values x we'd like the generated samples to convert $[0, \infty)$ rather then $[0, 1)$ so

$$\int_0^\infty ce^{-ax} = \left| \frac{c}{a} e^{-ax} \right|_0^\infty = \frac{c}{a} = 1 \tag{D.1.27}$$

Thus we know that $c = a$, and our PDF is $p(x) = ae^{-ax}$. Now, we integrate to find $P(x)$

$$P(x) = \int_0^x ae^{-ax'}dx' = 1 - e^{-ax} \tag{D.1.28}$$

This function is easy to invert:

$$P^{-1}(x) = \frac{\ln(1-x)}{a} \tag{D.1.29}$$

and we can draw samples thusly

$$X = -\frac{ln(1-\xi)}{a} \tag{D.1.30}$$

This equation can be further simplified by making the observation that xi is a uniformly distributed random number, so is $1-\xi$, so we can safely replace $1-\xi$ by ξ without changing the distribution. Therefore, our final sampling strategy is

$$X = -\frac{ln(\xi)}{a} \tag{D.1.31}$$

D.1.3.4 Example: piecewise - constant 1-dim function

An interesting exercise to work out how to sample from one-dimensional piecewise-constant functions (step function). Without loss of generality, we will just consider piecewise-constant defined over $[0, 1]$

Assume that the one-dimensional function's domain is split into N equal-sized pieces of size $\Delta = 1/N$. These regions start and end a points $x_i = i\Delta$, where ranges from 0

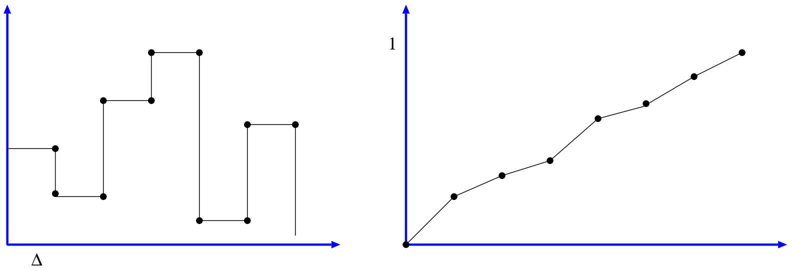

Figure D.4: (left) Probability density function for a piecewise-constant 1D function and (right) cumulative distribution function defined by this PDF

to N, inclusive. Within each region, the value of the function $f(x)$ is constant Figure: D.4 The value of $f(x)$ is

$$f(x) = \begin{cases} v_0 : & x_0 \leq x \leq x_1 \\ v_1 : & x_1 \leq x \leq x_2 \\ \vdots \end{cases} \tag{D.1.32}$$

The integral $\in f$ is

$$c = \int_0^1 f(x)dx = \sum_{i=0}^{N-1} \Delta\ v_i = \sum_{i=0}^{N-1} \frac{v_i}{N} \tag{D.1.33}$$

So it is easy to construct the PDF $p(x)$ for $f(x)$ as $f(x)/c$. By direct application of the relevant formulae, the CDF is a piecewise linear function defined at points x_i by

$$\begin{aligned} P(x_0) &= 0 \\ P(x_1) &= \int_{x_0}^{x_1} p(x)dx = \frac{v_0}{N\ c} = P(x_0) + \frac{v_0}{N\ c} \\ P(x_2) &= \int_{x_0}^{x_2} p(x)dx = \int_{x_0}^{x_1} p(x)dx + \int_{x_1}^{x_2} p(x)dx = P(x_1) + \frac{v_1}{N\ c} \\ P(x_i) &= P(x_{i-1}) + \frac{v_{i-1}}{N\ c} \end{aligned} \tag{D.1.34}$$

Between two points x_i and x_{i+1}, the CDF is linearly increasing with slope v_i/c. Recall that in order to sample $f(x)$ we need to invert the CDF to find the value x such that

$$\xi = \int_0^x p(x')dx' = P(x) \tag{D.1.35}$$

Because the CDF is monotonically increasing, the value of x must be between the x_i and x_{i+1} such that $P(x_i) \leq \xi$ and $\xi \leq P(x_{i+1})$.

Bibliography

[Alexander et al., 1983] Alexander, D. R., Johnson, H. R., and Rypma, R. L. (1983). Effect of molecules and grains on Rosseland mean opacities. *ApJ*, 272:773–780.

[Balsara, 1995] Balsara, D. S. (1995). Von Neumann stability analysis of smooth particle hydrodynamics - suggestions for optimal algorythms. *J. Comp. Phys.*, 121:357.

[Bate, 1995] Bate, M. R. (1995). *The role of accretion in Binary star formation*. Phd Thesis, Cambrige University, UK.

[Beck et al., 1992] Beck, H. K. B., Gail, H.-P., Henkel, R., and Sedlmayr, E. (1992). Chemistry in circumstellar shells. I. chromospheric radiation fields and dust formation in optically thin shells of M-giants. *Astron. & Astrophys.*, 265:626–642.

[Benz, 1990] Benz, W. (1990). *Smooth particle hydrodynamics - a Review*. Proc. of the NATO advanced research workshop on the Numerical Modelling of Nonlinear Stellar Pulsations Problems and Prospects, ed. J. R. Buvhler, dordrecht: Kluwer Academic Publishers, p. 269.

[Bjorkman and Wood, 2001] Bjorkman, J. E. and Wood, K. (2001). Radiative equilibrium and temperature correction in Monte Carlo radiation transfer. *ApJ*, 554(1):615–623.

[Bowen, 1988a] Bowen, G. (1988a). Dynamical modelling of long-period variable star atmospheres. *ApJ.*, 329:299–317.

[Bowen, 1988b] Bowen, G. H. (1988b). *The mechanism of mass loss from pulsating cool stars*. In Stalio, R. and Willson, L. A., editors, Pulsation and mass loss in stars, pages 3-25, Kluwer Academic Publisher.

[Boyarchuk et al., 2002] Boyarchuk, A. A., Bisikalo, D. V., Kuznetsov, O. A., and Chechetkin, V. M. (2002). *Mass Transfer in Close Binary Stars*. Taylor & Francis, London, UK.

[Burrows et al., 2001] Burrows, A., Hubbard, W. B., Lunine, J, I., and Liebert, J. (2001). The theory of brown dwarfs and extrasolar gian planets. *Rev. Mod. Phys.*, 73:719–765.

[Carter and Cashwell, 1975] Carter, L. L. and Cashwell, E. D. (1975). *Particle-Transport Simulation with the Monte Carlo Method*. Technical Information Center, Office of Public Affairs U.S. Energy Research and Development Administration, USA.

[Chaisson and McMillan, 2002] Chaisson, E. and McMillan, S. (2002). *Astronomy today.* fourth edition, Prentice Hall, Upper Saddle River, New Jersey, USA.

[Chandrasekhar, 1960] Chandrasekhar, S. (1960). *Radiative transfer.* Mineola, NY Dover Publications, USA.

[Collins, 2003] Collins, G. W. (2003). *The Fundamental of Stellar astrophysics.* Web Edition.

[Croat et al., 2005] Croat, T. K., Stadermann, F. J., and Bernatowicz, T. J. (2005). Presolar graphite from AGB stars: Microstructure and s-process enrichment. *ApJ*, 631:976–987.

[Evrard, 1988] Evrard, A. E. (1988). Beyond N-body: 3D cosmological gas dynamics. *Mon. Not. Roy. Astron. Soc.*, 287:57.

[Feast, 1989] Feast, M. (1989). *The use of pulsating stars.* in fundamental problems of Astronomy, E. G. Schmidt ed., Cambridge University Press, Cambridge, UK.

[Feast, 2001] Feast, M. (2001). *In Encyclopedia of Astronomy and Astrophysics.* Nature publishing group, Hampshire, UK.

[Feder et al., 1966] Feder, J., Russell, C. K., Lothe, J., and Pound, G. M. (1966). Homogeneous nucleation and growth of droplets in vapours. *Advances in Physics*, 15(57):111–178.

[Ferguson et al., 2002] Ferguson, J. W., Alexander, D. R., Allard, F., Barman, T., Bodnarik, J. G., Hauschildt, P., Heffner-Wong, A., and Tamanai, A. (2002). Low-Temperature opacities. *ApJ*, 623:585–596.

[Flannery, 1975] Flannery, B. (1975). The location of the hot spot in cataclymic variable stars as determined from particle trajectories. *Mon. Not. Roy. Astron. Soc.*, 170:325.

[Fleischer, 1994] Fleischer, A. J. (1994). *Hydrodynamics and dust formation in the circumstellar shells of Miras and Long-Period variables.* PhD Thesis, Technische Universität Berlin, Berlin, FRG.

[Fleischer et al., 1992] Fleischer, A. J., Gauger, A., and E., S. (1992). Circumstellar dust shells around long-period variables. I : Dynamical models of C-stars including dust formation, growth and evaporation. *Astron. & Astrophys.*, 266:321.

[Frantsman and Eglitis, 1988] Frantsman, Y. L. and Eglitis, I. E. (1988). The C / O - ratio in N stars: observations and theory. *SvA*, 14:L109–L111.

[Gail et al., 1984] Gail, H.-P., Keller, R., and Sedlmayr, E. (1984). Dust formation in stellar winds I. A rapid computational method an application to graphite condensation. *Astron. & Astrophys.*, 133:320–322.

[Gail and Sedlmayr, 1985] Gail, H. P. and Sedlmayr, E. (1985). Dust formation in stellar winds, II. carbon condensation in stationary, spherically expanding winds. *Astron. & Astrophys.*, 148:183–190.

[Gail and Sedlmayr, 1987] Gail, H. P. and Sedlmayr, E. (1987). Dust formation in stellar winds, III. self-consistent models for dust-driven winds around C-stars. *Astron. & Astrophys.*, 171:197–204.

[Gail and Sedlmayr, 1988] Gail, H.-P. and Sedlmayr, E. (1988). Dust formation in stellar winds. IV - Heteromolecular carbon grain formation and growth. *Astron. & Astrophys.*, 206:153.

[Gail and Sedlmayr, 2009] Gail, H.-P. and Sedlmayr, E. (2009). *Physics and Chemistry of Circumstellar dust shells*. in press.

[Garrod, 1995] Garrod, C. (1995). *Statistical mechanics and thermodynamics*. Oxford University Press,Inc., Oxford, UK.

[Gauger et al., 1990] Gauger, A., Gail, H.-P., and Sedlmayr, E. (1990). Dust formation, growth and evaporation in a cool pulsating circumstellar shell. *Astron. & Astrophys.*, 235:345.

[Gingold and Monaghan, 1977] Gingold, R. A. and Monaghan, J. J. (1977). Smoothed particle hydrodynamics: Theory and application to non-spherical stars. *Mon. Not. Roy. Astron. Soc.*, 181:375.

[Gingold and Monaghan, 1982] Gingold, R. A. and Monaghan, J. J. (1982). Kernel estimates as a basis for general particle methods in hydrodynamics. *J. Comp. Phys.*, 46:429.

[Gow, 1977] Gow, C. (1977). Spectrophotometry of cool carbon stars. *PASP*, 89:510–518.

[Groenewegen et al., 1995] Groenewegen, M. A. T., van de Hoek, L., and de Jong, T. (1995). The evolution of galactic carbon stars. *Astron. & Astrophys.*, 293:381–395.

[Haniff, 1989] Haniff, C. (1989). *Astrophysical applications of stellar pulsation*. in Astron. Soc. Pacific Conf. vol. 83, R. S. Stobie and P. A. Whitelock ed., Astronomical society of the Pacific, San Francisco, USA.

[Hartmann and MacGregor, 1980] Hartmann, L. and MacGregor, K. B. (1980). Momentum and energy deposition in late-type stellar atmospheres and winds. *ApJ.*, 242:260–282.

[Hernquist and Katz, 1989] Hernquist, L. and Katz, N. (1989). TreeSPH: a unification of SPH with the hierarchical tree method. *Astrophys. J. supll.*, 70:419.

[Holzer and MacGregor, 1985] Holzer, T. E. and MacGregor, K. (1985). *Mass loss mechanisms for cool, low-gravity stars*. In Morris, M. and Zuckerman, B., editors, Mass Loss from red giants, pages 229-255. D. Reidel Pub. Com.

[Hoskin et al., 2001] Hoskin, M., Kovalevsky, J., Margon, B., Moore, P., Mould, J., Nomoto, K., Pounds, K., Priest, E., S. E., and Altena, W. V. (2001). *Encyclopedia of Astronomy and Astrophysics*. John Navas Nature Publishing Group.

[Hurley et al., 2000] Hurley, J. R., Pols, O. R., and Tout, C. A. (2000). Comprehensive analytic formulae for stellar evolution as a function of mass and metallicity. *Mon. Not. Roy. Astron. Soc.*, 315(3):543–569.

[Iben, 1981] Iben, I. J. (1981). Single and binary star evolution. *ApJS*, 76:55–114.

[Iben and Renzini, 1983] Iben, I. J. and Renzini, A. (1983). Asymptotic giant branch evolution and beyond. *ARA& A*, 21:271–342.

[J. Feder et al., 1966] J. Feder, J., Russell, K. C., Lothe, J., and Pound, G. M. (1966). Homogeneous Nucleation and Growth of Droplets in Vapours. *Advances in Physics*, 15:111 – 178.

[Jørgensen and Johnson, 1992] Jørgensen, U. G. and Johnson, H. R. (1992). Radiative force on molecules and its possible role for mass loss in evolved AGB stars. *Astron. & Astrophys.*, 265:168–176.

[Jura, 1986] Jura, M. (1986). The role of dust in mass loss from late-type stars. *Irish astr. J*, 17:322–330.

[Jura, 1991] Jura, M. (1991). High-luminosity single carbon stars in stellar and galactic evolution. *Astron. & Astrophys.*, 2:227–247.

[Kim et al., 1994] Kim, S.-H., Martin, P., and Hendry, P. D. (1994). The size distribution of interstellar dust particles as determined from extinction. *ApJ*, 422:164–175.

[Kippenhahn and Weigert, 1967] Kippenhahn, R. and Weigert, A. (1967). Entwicklung in engen doppelsternsystemen I. massenaustausch vor und nach beendigung des zentralen wasserstoff-brennens. *Zeitschrift für Astrophysik*, 65.

[Kirkpatrick et al., 1999] Kirkpatrick, J. D., Allard, F., Bida, T., Zuckerman, B., Becklin, E. E., Chabrier, G., and Baraffe, I. (1999). An improved optical spectrum and new model fits of the likely brown dwarf GD165B. *ApJ.*, 519:834–843.

[Kling et al., 2000] Kling, A., Barão, F., Nakagawa, M., Távora, L., and Vaz, P. (2000). *Advanced Monte Carlo for radiation physics, particle transport simulation and applications*. Spriger Verlag, Berlin, Germany.

[Knapp and Morris, 1985] Knapp, G. R. and Morris, M. (1985). Mass loss from evolved stars. III. Mass loss rates for 50 stars from CO J = 1 - 0 observations. *ApJ.*, 292:640–669.

[Kruszewski et al., 1968] Kruszewski, A., Gehrels, T., , and Serkowski, K. (1968). Wavelength dependence of polarization. xii. red variables. *ApJ*, 73:677–687.

[Kwok, 1975] Kwok, S. (1975). *From red giants to planetary nebulae*. In Iben, Jr., I. and Renzini, A., editors, Physical processes in red giants, vol. 88, pages 421-425, Astrophys. Space Sci. Library.

[Lambert et al., 1986] Lambert, D., Gustafsson, B., Eriksson, K., and Hinkle, K. H. (1986). The chemical composition of carbon stars. I. Carbon, nitrogen, and oxygen in 30 cool carbon stars in the galactic disk. *ApJ.*, 62:373–425.

[Lamers and Cassinelli, 1999] Lamers, H. J. G. L. M. and Cassinelli, J. P. (1999). *Introduction to stellar winds*. Cambridge University Press, Cambridge, UK.

[Lapeyre et al., 2003] Lapeyre, B., Pardoux, E., and Sentis, R. (2003). *Introduction to Monte-Carlo methods for transport and diffusion equations*. Oxford University Press,Inc., Oxford, UK.

[Lattanzio and Wood, 2003] Lattanzio, C. and Wood, P. (2003). *Evolution, nucleosynthesis and pulsation of AGB stars*. In Habing, H. and Olofsson, H., editors, Asymptotic Giant Branch Stars, pages 23-104, Springer.

[Lattanzio, 1989] Lattanzio, J. C. (1989). Carbon dredge-up in low-mass stars and solar metallicity stars. *ApJ*, 344:L25–L27.

[Lattanzio et al., 1986] Lattanzio, J. C., Monaghan, J. J., Pongracic, H., and Schwarz, M. P. (1986). Controlling penetration. *SIAM J. Sci. Stat. Comp.*, 7:591.

[Liebert, 2007] Liebert, J. W. (2007). Irradiated brown dwarfs with close but detached white dwarf companions. *Bulletin of the American Astronomical Society*, 38:185.

[Lifang et al., 2004] Lifang, L., Zhanwen, H., and Fenghui, Z. (2004). Structure and evolution of low-mass W UMa-type systems. *Mon. Not. Roy. Astron. Soc.*, 351:137–146.

[Loewenstein and Mathews, 1986] Loewenstein, M. and Mathews, W. G. (1986). Adiabatic particle hydrodynamics in 3 dimensions. *J. Comp. Phys.*, 62:414.

[Lubow and Shu, 1975] Lubow, S. H. and Shu, F. H. (1975). Gas dynamics of semi detached binaries. *ApJ.*, 198:383.

[Lucy, 1968] Lucy, L. B. (1968). The structure of contact binaries. *ApJ.*, 151:1123.

[Lucy, 1971] Lucy, L. B. (1971). The formation of resonance lines in extended atmospheres. *ApJ*, 163:95–110.

[Lucy, 1976] Lucy, L. B. (1976). Mass loss by cool carbon stars. *ApJ*, 205:482–491.

[Lucy, 1977] Lucy, L. B. (1977). A numerical approach to the testing of the fission hypothesis. *The Astronomical Journal*, 82:12.

[Lucy, 1999] Lucy, L. B. (1999). Computing radiative equilibria with Monte Carlo techniques. *Astronom. & Astrophys.*, 344:282–288.

[Maarten et al., 2002] Maarten, B., Stamatellos, D., Davies, J. I., Whitworth, A. P.and Sabatini, S., Roberts, S., Linder, S. M., and Evans, R. (2002). Radiative equilibrium in Monte Carlo radiative transfer using frequency distribution adjustment. *New Astron.*, 10:523–533.

[Mamon et al., 1988] Mamon, G. A., Glassgold, A. E., and Huggins, P. J. (1988). The photodissociation of CO in circumstellar envelopes. *ApJ*, 328:797–808.

[Mastrodemos and Morris, 1998] Mastrodemos, N. and Morris, M. (1998). Bipolar preplanetary nebulae: Hydrodynamics of dusty winds in binary systems I. Formation of accretion disks. *ApJ.*, 497:303–329.

[Mastrodemos and Morris, 1999] Mastrodemos, N. and Morris, M. (1999). Bipolar preplanetary nebulae: Hydrodynamics of dusty winds in binary systems.II. Morphology of the circumstellar envelopes. *ApJ.*, 523:357–380.

[Mauron and Huggins, 2006] Mauron, N. and Huggins, P. J. (2006). Imaging the circumstellar envelopes of AGB stars. *Astron. & Astrophys*, 452:257–268.

[Maxted et al., 2001] Maxted, P. F. L., Napiwotzki, R., Dobbie, P. D., and Burleigh, M. R. (2001). Survival of a brown dwarf after engulfment by a red giant star. *Nature*, 442:543–545.

[Mie, 1908] Mie, G. (1908). Beiträge zur optik trüber medien, speziell kolloidaler metallösungen. *Annalen der Physik*, 25:377–445.

[Mihalas, 1970] Mihalas, D. (1970). *Stellar Atmosphere*. W.H. Freeman and Company, San Francisco, USA.

[Millar, 2003] Millar, T. (2003). *Molecule and dust grain formation*. In Habing, H. and Olofsson, H., editors, Asymptotic Giant Branch Stars, Springer, pages 247-289.

[Mitrović and Stephan, 1980] Mitrović, J. and Stephan, K. (1980). Equilibrium radii of vapour bubbles and liquid droplets. *Heat and Mass Transfer*, 13:171–176.

[Miyama et al., 1984] Miyama, S., Hayashi, C., and Narita, S. (1984). Criteria for collapse and fragmentation of rotating, isothermal clouds. *ApJ*, 279:621.

[Monaghan, 1988] Monaghan, J. J. (1988). An introduction to SPH. *Comp. Phys. Comm.*, 48:89.

[Monaghan, 1992] Monaghan, J. J. (1992). Smoothed particle hydrodynamics. *Ann. Rev. Astron. Astrophys.*, 30:543.

[Monaghan and Gingold, 1983] Monaghan, J. J. and Gingold, R. A. (1983). Shock simulation by the particle method SPH. *J. Comp. Phys.*, 52:374.

[Monaghan and Lattanzio, 1985] Monaghan, J. J. and Lattanzio, J. C. (1985). A Refined Particle method for Astrophysical Problems. *Astron. & Astrophys.*, 149:135.

[Morris et al., 2006] Morris, M., Sahai, R., Matthews, K., Cheng, J., Lu, J., Claussen, M., and Sánchez-Contreras, C. (2006). *A Binary-Induced Pinwheel Outflow from the Extreme Carbon Star, AFGL 3068.* in Planetary Nebulae in our Galaxy and Beyond, Proceedings of the International Astronomical Union, Symposium 234. Michael J. Barlow and Roberto H. Méndez, editors. Cambridge: Cambridge University Press, pages 469-470.

[Nakajima et al., 1995] Nakajima, T., Oppenheimer, B. R., Kulkarni, S. R., Golimowski, D. A., Matthews, K., and Durrance, S. T. (1995). Discovery of a cool brown dwarf. *Nature*, 378:463–465.

[Nelson and Papaloizou, 1993] Nelson, R. P. and Papaloizou, J. C. B. (1993). Three-dimensional hydrodynamics simulations of collapsing prolate clouds. *Mon. Not. Roy. Astron. Soc.*, 265:905.

[Nelson and Papaloizou, 1994] Nelson, R. P. and Papaloizou, J. C. B. (1994). Variable smoothing lengths and energy conservation in smoothed particle hydrodynamics. *Mon. Not. Roy. Astron. Soc.*, 270:1.

[Neumann and Richtmyer, 1950] Neumann, J. and Richtmyer, R. D. (1950). A method for the numerical calculation of hydrodynamic shocks. *J. Appl. Phys*, 21:232–237.

[Oppenheimer et al., 1995] Oppenheimer, B. R., Kulkarni, S. R., Matthews, K., and Nakajima, T. (1995). Infrared spectrum of the cool brown dwarf GL:229B. *Science*, 270:1478 – 1479.

[Oran and Boris, 1987] Oran, E. S. and Boris, J. P. (1987). *Numerical simulation of reactive flow*. Elsevier Science Publishing Co., Inc., New York, USA.

[Peraiah, 2002] Peraiah, A. (2002). *An Introduction to Radiative Transfer - Methods and applications in Astrophysics*. Cambridge University Press, Cambridge, UK.

[Pijpers, 1990] Pijpers, F. P. (1990). A model for the wind of the M supergiant VX Sagittarii. *Astron. & Astrophys.*, 238:256–264.

[Pijpers and Habing, 1989] Pijpers, F. P. and Habing, H. J. (1989). Driving the stellar wind of AGB stars by acoustic waves; exploration of a simple model. *Astron. & Astrophys.*, 215:334–346.

[Pinte et al., 2006] Pinte, C., Menard, F., Duchene, G., and Bastien, P. (2006). Monte Carlo radiative transfer in protoplanetary disks. *Astron. & Astrophys.*, 459(3):797–804.

[Pringle, 1985] Pringle, J. E. (1985). *in Interacting binary systems (Chapter 1)*. J. E. Pringle and R. A. Wade, editors , Cambridge Univ. Press, Cambridge, UK.

[Rasio and Lombardi Jr., 1998] Rasio, F. A. and Lombardi Jr., J. C. (1998). Smoothed particle hydrodynamics calculations of stellar interactions. *J. Comput. Appl. Math.*, 109(1-2):213–230.

[Richtmyer and Morton, 1967] Richtmyer, R. D. and Morton, K. W. (1967). *Difference methods for initial-value problems*. John Wiley & Sons, New York, USA, 2nd edition.

[Salpeter, 1974a] Salpeter, E. E. (1974a). Formation and flow of dust grains in cool stellar atmospheres. *ApJ.*, 193:585–592.

[Salpeter, 1974b] Salpeter, E. E. (1974b). Nucleation and growth of dust grains. *ApJ.*, 193:579–584.

[Sawada et al., 1986a] Sawada, K., Matsuda, T., and Hachisu, I. (1986a). Accretion shocks in a close binary system. *Mon. Not. Roy. Astron. Soc.*, 221:679–686.

[Sawada et al., 1986b] Sawada, K., Matsuda, T., and Hachisu, I. (1986b). Spiral shocks on a Roche lobe overflow in semi-detached binary system. *Mon. Not. Roy. Astron. Soc.*, 219:75–88.

[Schirrmacher et al., 2003] Schirrmacher, V., Woitke, P., and Sedlmayr, E. (2003). On the gas temperature in the shocked circumstellar envelopes of pulsating stars III. dynamical models for AGB star winds including time-dependent dust formation and non-LTE cooling. *Astron. & Astrophys.*, 404:276–282.

[Schönberner, 1983] Schönberner, D. (1983). Late stages of stellar evolution. II. Mass loss and the transition of asymptotic giant branch stars into hot remnants. *ApJ.*, 272:708–714.

[Schüssler and Schmitt, 1981] Schüssler, I. and Schmitt, D. (1981). Comments on smoothed particle hydrodynamics. *Astron. Astrophys.*, 97:373.

[Sedlmayr, 1985] Sedlmayr, E. (1985). Die entstehung des interstellaren staubs. *Mit. Astron. Gesel.*, 63:75–88.

[Serkowski and Shawl, 2001] Serkowski, K. and Shawl, S. J. (2001). Polarimetry of 167 cool variable stars: Data. *ApJ*, 122:2017–2041.

[Shore, 2003] Shore, S. N. (2003). *The tapestry of modern astrophysics*. John Wiley & Sons, New York, USA.

[Steinmetz, 1996] Steinmetz, M. (1996). GRAPESH: Cosmological smoothed particle hydrodynamics simulations with the special-purpose hardware GRAPE. *Mon. Not. Roy. Astron. Soc.*, 278:1005.

[Steinmetz and Müller, 1993] Steinmetz, M. and Müller, E. (1993). On the capabilities and limits of smoothed particle hydrodynamics. *Astron. & Astrophys.*, 263:391.

[Thacker et al., 1998] Thacker, R. J., Tittley, E. R., Pearce, F. R., Couchman, H. M. P., and Thomas, P. (1998). Smoothed particle hydrodynamics in cosmology: a comparative study of implementations. *Mon. Not. Roy. Astron. Soc.*, 000:1–30.

[Thomas and Couchman, 1992] Thomas, P. A. and Couchman, H. M. P. (1992). Simulating the formation of a cluster of galaxies. *Mon. Not. Roy. Astron. Soc.*, 257:11.

[Toro, 1997] Toro, E. F. (1997). *Riemann Solvers and Numerical Methods for Fluid Dynamics*. Springer Verlag, Berlin, Germany.

[Tsuji, 1981] Tsuji, T. (1981). Intrinsic properties of carbon stars.I. effective temperature scale of N-type carbon stars. *J. Astrophys. Astr.*, 2:95–113.

[van der Veen and Rugers, 1989] van der Veen, W. E. C. J. and Rugers, M. (1989). A comparison between.

[Vehkamäki, 2006] Vehkamäki, H. (2006). *Classical Nucleation Theory in Multicomponent System*. Springer Verlag, Berlin, Germany.

[Winters, 1994] Winters, J. M. (1994). *Internal structure and optical appearance of circumstellar dust shells around cool carbon giants*. PhD Thesis, Technische Universität Berlin, Berlin, FRG.

[Woitke et al., 1996] Woitke, P., Goeres, A., and Sedlmayr, E. (1996). On the gas temperature in the shocked circumstellar envelopes of pulsating stars II. shock induced condensation around r coronae borealis stars. *Astron. & Astrophys.*, 313:217 – 228.

[Yang et al., 2001] Yang, Y., Liu, Q., and Leung, K. (2001). Uy Ursae Majoris: A W-subtype W UMa system with a small mass ratio. *Astron. & Astrophys.*, 370:507–512.

Picture Credits & URI

[1] Margarita Karovska (Harvard-Smithsonian Center for Astrophysics) and NASA / CXC/SAO. Chandra x-ray mira http://chandra.harvard.edu/photo/2005/mira/more.html.

[2] Margarita Karovska (Harvard-Smithsonian Center for Astrophysics) and NASA. Hubble mira http://hubblesite.org/newscenter/archive/releases/1997/26/image/a/.

[3] C. E. Hansen and J. B. Simon. Visualization of multiple star evolution http://rainman.astro.uiuc.edu/ddr/stellar/archive/sse.pdf.

[4] National ignition & Photon Science. https://lasers.llnl.gov.

[5] R. Powell. Hertzsprung-russel diagram http://www.atlasoftheuniverse.com/hr.html.

[6] Doug Welch. Macho project http://wwwmacho.anu.edu.au.

Danksagung

Mein Dank gilt zunächst Herrn Prof. Dr. Erwin Sedlmayr, für die Betreuung, dieser Arbeit am Zentrum für Astronomie und Astrophysik der TU Berlin und für die vielen hilfreichen Anregungen und Hinweise.

Weiterhin möchte ich Frau Prof. Dr. Heike Rauer dafür danken, dass sie sich als Berichterin zur Verfügung gestellt hat, sowie Herrn Prof. Dr. Tobias Brandes dafür, dass er sich bereit erklärt hat, den Vorsitz über den Promotionsausschuß zu übernehmen.

Ich danke ebenfalls allen Kollegen am ZAA der TU-Berlin für die interessanten und hilfreichen Diskussionen.

Ein besonderen Dank richte ich an meine Mutter und meine Schwester für ihre tatkräftige Hilfe und natürlich an meine geliebte Frau Ana Teresa, für ihr Verständnis, ihre Unterstützung und Motivation. Sie vermochte es mir die Schönheit eines völlig anderen Kosmos zu offerieren. Vielen Dank dafür.

Curriculum Vitae

PERSÖNLICHE DATEN

Name	Carsten Köllein
Geburtsdatum	August 22, 1972
Geburtsort	Berlin/Deutschland
Staatsangehörigkeit	Deutsch

SCHULBILDUNG

1979 - 1989	Besuch der Polytechnischen Oberschule Berlin, Prenzlauer Berg
09/89 - 12/91	Berufsausbildung Informationselektroniker mit der Spezialisierungsrichtung terrestrischer- bzw. extraterrestricher Empfangsanlagen beim VEB Rundfunk-Fernsehtechnik Berlin.
08/90 - 06/92	Hochschulreife am Abendgymnasium Berlin - Weißensee
04/92 - 07/92	Fortbildungslehrgang Pneumatik, Elektropneumatik computergesteuerte Messtechnik und SPS
09/92 - 11/93	Zivildienst: Ausbilder für lebensrettende Sofortmassnahmen und Erste Hilfe

STUDIUM

10/93 - 10/01	Physikstudium an der Technischen Universität Berlin. Diplomarbeit - Max-Planck Institut für Gravitationsphysik

PROMOTION

Sep. 2005 - Feb. 2009	Zentrum für Astronomie und Astrophysik der Technischen Universität Berlin.